Dissertation
submitted to the
Combined Faculties of the Natural Sciences and Mathematics
of the Ruperto-Carola-University of Heidelberg, Germany
for the degree of
Doctor of Natural Sciences

Put forward by
Dipl.-Phys. Matthias J. Frank
Born in: Eschenbach i. d. Opf, Germany
Oral examination: 24 July 2012

Observational Dynamics of Low-Mass Stellar Systems

The Mass Content of Ultra-Compact Dwarf Galaxies and Diffuse Globular Clusters

Referees: Prof. Dr. E. K. Grebel
Prof. Dr. R. Spurzem

Abstract

Using spectroscopy and imaging obtained with ground-based telescopes and the Hubble Space Telescope (HST), we study the dynamics of ultra-compact dwarf galaxies (UCDs) and diffuse Galactic globular clusters (GCs).
We present, for the first time, the spatially resolved kinematics of a UCD. We obtain a velocity dispersion profile fully consistent with a constant mass-to-light ratio (M/L) that in turn agrees well with its stellar population M/L. We find no evidence for an extended dark matter halo nor for a massive central black hole. While this does not exclude a galaxian origin for the UCD, we conclude that its internal kinematics are fully consistent with it being a massive star cluster.
Results from the gravity-sensitive 2.3 μm CO index of UCDs do not support a scenario explaining their high M/L with an overabundance of low-mass stars.
A comparison the photometric and dynamical mass of the GC Palomar 4 yields good agreement with Newtonian dynamics and adds to the evidence against Modified Newtonian dynamics (MOND).
We find mass segregation in Palomar 4 and Palomar 14 that may be primordial given their long relaxation times, or that suggests that these clusters were once significantly more compact.

Zusammenfassung

Basierend auf spektroskopischen und photometrischen Daten, die mit bodengebundenen Teleskopen und dem Hubble Weltraumteleskop gewonnen wurden, wird die Dynamik ausgedehnter Kugelsternhaufen in der Milchstraße und ultrakompakter Zwerggalaxien (UCDs) untersucht.
Zum ersten Mal wird die Kinematik eines UCDs räumlich aufgelöst. Das UCD zeigt ein Geschwindigkeitsdispersionsprofil in gutem Einklang mit einem konstanten Masse zu Leuchkraft-Verhältnis (M/L), welches wiederum gut mit dem M/L der Sternpopulation des UCDs übereinstimmt. Es gibt keine Hinweise auf das Vorhandensein eines ausgehnten Dunkle Materie-Halos, noch eines massereichen schwarzen Lochs. Während dies einen galaktischen Ursprung des UCDs nicht ausschließt, ist seine interne Dynamik in guter Übereinstimmung mit der eines massereichen Sternhaufens.
Die Messung des oberflächenschwerkraftsensitiven 2.3 μm CO Index von UCDs liefert keine Hinweise auf ein Szenario, welches die hohen M/L von UCDs mit einer Überhäufigkeit massearmer Sterne erklärt.
Ein Vergleich der photometrischen und dynamischen Masse des Kugelsternhaufens Palomar 4 zeigt gute Übereinstimmung in Newtonscher Dynamik und stärkt die Beweislast gegen modifizierte Newtonsche Dynamik (MOND).
Die Massensegregation, die in Palomar 4 und 14 gemessen wird, könnte angesichts der langen Relaxationszeit beider Kugelsternhaufen primordial sein, oder bedeuten dass beide Kugelsternhaufen einst deutlich kompakter waren.

Contents

1 Introduction

1.1 Stellar systems at the star cluster – galaxy interface

On 8 May 1764, Charles Messier observed the nebular structure that would later become the fourth object of his catalogue (Messier 1774) and recognised it as a 'cluster of very small, or faint, stars'[1]. This made Messier 4 the first globular cluster (GC) ever resolved into stars (Frommert et al. 2006). It took one and a half centuries more and one Great Debate (Shapley & Curtis 1921), until the nature of galaxies as truly extragalactic 'island universes' was established. Since this time, the known stellar systems in the universe could be relatively easily classified into either galaxies or star clusters, based on their morphology (late-type galaxies, i.e. spirals and irregulars) and their physical extent in the case of an early-type, i.e. spheroidal or elliptical, morphology. Galaxies, cosmological structures, which formed in dark matter halos and grew via mergers with and accretion of other galaxies, have half-light radii ranging from hundreds of pc to tens of kpc. Star clusters, which formed from molecular clouds inside these galaxies, have typical half-light radii of a few to a few tens of pc. This distinction is reflected, for example, in Tammann's (1994) widely adopted definition of dwarf galaxies, to be 'fainter than $M_B \leq -16$ mag and *more extended than globular clusters*'.

However, in recent years several discoveries blurred the boundary between the regime of galaxies and star clusters:

- Ultra-compact dwarf galaxies (UCDs; Section 1.2) began to fill the parameter space (in size, mass and luminosity) between classical globular clusters on the one side and compact and dwarf ellipticals on the other side (see Fig. 1.1, where UCDs are represented by star symbols).

- Ultra-faint and extended dwarf spheroidal satellites (shown as green crosses in Fig. 1.1) were discovered in wide-field photometric surveys around our Galaxy and M 31 (e.g. Zucker et al. 2004; Willman et al. 2005; Belokurov et al. 2006b; Martin et al. 2006) and, apart from containing large amounts of dark matter, resemble diffuse globular clusters.

- More and more extended star clusters were detected around nearby galaxies (e.g. Larsen & Brodie 2000; Brodie & Larsen 2002; Huxor et al. 2005; Da Costa et al. 2009). With absolute V-band magnitudes of $-8 \lesssim M_V \lesssim -4$ mag and projected half-light radii of $5 \lesssim r_h \lesssim 25$ pc they

[1] 'Amas de très-petites étoiles'

populate the 'extended side' of the star cluster distribution (see e.g. fig. 8 of Brodie et al. 2011).

- Finally, if also late-type morphologies are considered, tidal dwarf galaxies, which formed in gas-rich galaxy mergers (e.g. Barnes & Hernquist 1992; Duc & Mirabel 1998) and are thought to be mostly dark-matter-free present another challenge to the picture of galaxies residing in dark-matter halos on the one side and star clusters on the other side.

As a result, astronomical conferences are being dedicated to the stellar systems at the interface between star clusters and galaxies (e.g. Mieske & Gieles 2011) and the question 'What is a galaxy?' is being actively discussed in the literature (e.g. Forbes & Kroupa 2011; Willman & Strader 2012).

The consensus is that a galaxy is at least gravitationally bound and contains stars, although this excludes any conjectured 'dark galaxies' (Verde et al. 2002), and several additional requirements have been proposed as *sufficient* defining criteria. Willman & Strader (2012) proposed that (I) galaxies are objects, whose properties cannot be explained by a combination of baryons and Newton's laws of gravity, and as a more observationally accessible proxy criterion, that (II) galaxies show a spread in metallicity [Fe/H]. Forbes & Kroupa (2011) proposed that galaxies (III) have a two-body relaxation time greater than the Hubble time, that (IV) galaxies have half-light radii $\geq 100\,\mathrm{pc}$, (V) contain complex stellar populations, (VI) contain non-baryonic dark matter, or (VII) host a satellite system.

A working classification scheme is highly desirable as it allows one to draw general conclusions on a whole class of objects from the study of a few of its representatives, as well as a meaningful analysis of the bulk properties of a given class and the study of trends and correlations among different properties. Classification, therefore in many disciplines, most prominently in biology, has been at the foundation of our modern scientific view of the world. Moreover, a 'wrong' classification scheme can bias the interpretation of bulk studies, illustrated by Willman & Strader (2012) with the example of ωCen that, due to its historical classification, is included in samples of globular clusters, but not in samples of dwarf galaxy nuclei.

Nevertheless, scientific progress also comes from detailed studies of individual specimen that try to decipher their inner workings, their evolution and their origin. As is demonstrated by genetic sequencing in biology, the results from such in-detail studies of individuals may eventually also help to revise and improve the prevailing classification schemes.

In this spirit, this Thesis presents the results of observational studies aiming at the internal dynamics of several individual low-mass stellar systems at the border of the galaxy and star cluster regime, the ultra-compact dwarf galaxies and extended Galactic globular clusters that are highlighted in Fig. 1.1. The systems under study all are galaxies under criterion (III) from above, they all are star clusters under criteria (IV) and (VII).

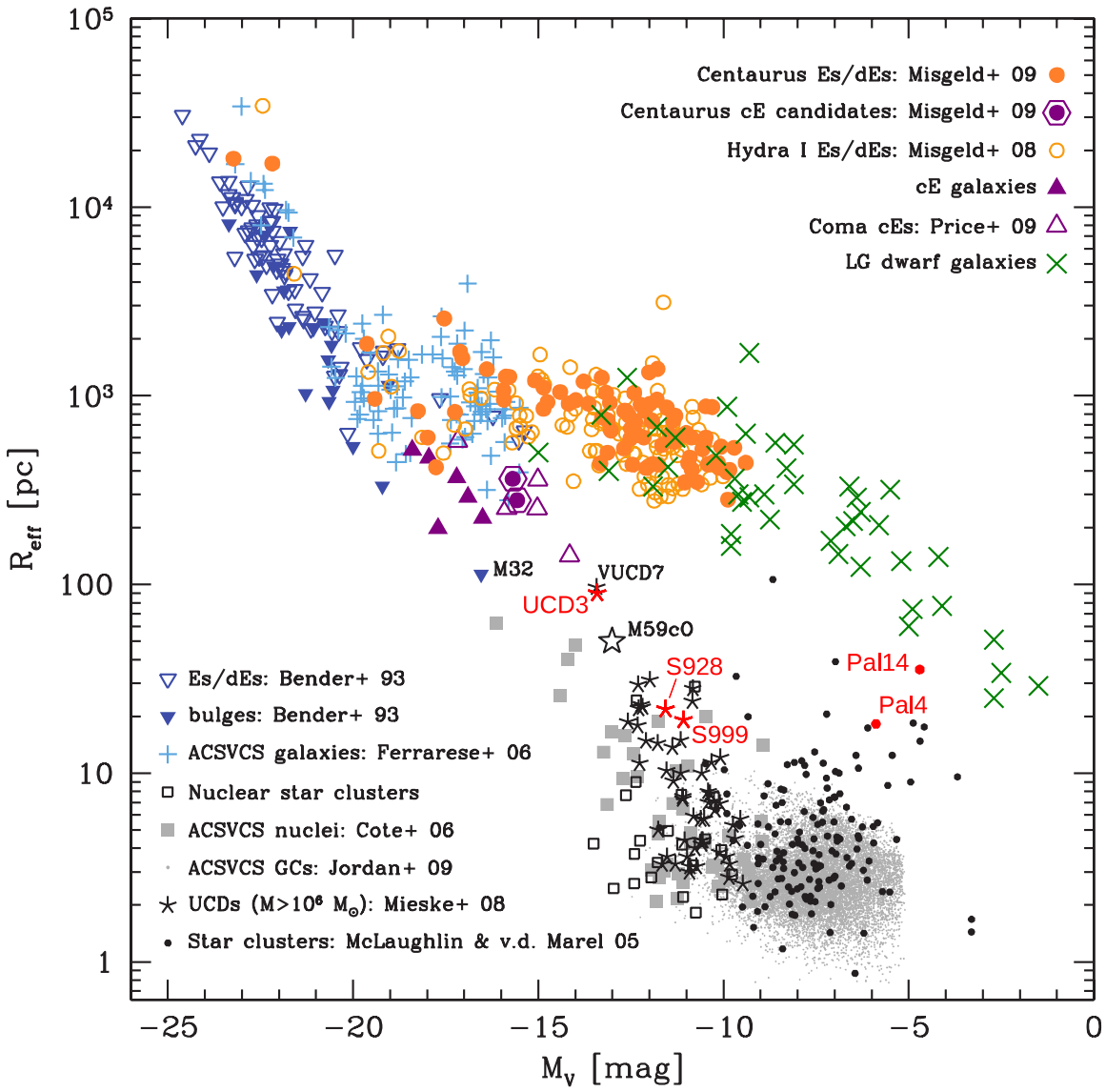

Figure 1.1: Sizes and luminosities of dynamically hot stellar systems. This figure is reproduced from the recent compilation by Misgeld & Hilker (2011). The objects studied in this Thesis, the ultra-compact dwarf galaxies UCD 3 (Chapter 2), S 928 and S 999 (Chapter 3) and the Galactic globular clusters Palomar 4 (Pal 4; Chapter 4) and Palomar 14 (Pal 14; Chapter 5) are highlighted and labelled in red. The size and luminosity of Pal 4 and Pal 14 were updated to the values obtained in this Thesis for Pal 4 and by Sollima et al. (2011) for Pal 14.
Blue and orange symbols represent giant and dwarf ellipticals (open blue triangles) and bulges of S0 galaxies (filled blue triangles) from the compilation of Bender et al. (1993), giant and dwarf ellipticals in the Virgo (blue pluses; Ferrarese et al. 2006), Centaurus (filled orange circles; Misgeld et al. 2008) and Hydra I galaxy clusters (open orange circles; Misgeld et al. 2008). Local Group dwarf ellipticals and dwarf spheroidals from various literature sources (see table 1 in Misgeld & Hilker 2011) are shown as green crosses. Purple symbols represent compact ellipticals (filled and open triangles; Mieske et al. 2005; Smith Castelli et al. 2008; Chilingarian et al. 2008b; Price et al. 2009; Chilingarian & Bergond 2010), and compact elliptical candidates (hexagons; Misgeld et al. 2008). The prototypical compact elliptical M 32 is included in the bulge sample of Bender et al. (1993) and is labelled. Nuclear star clusters (Böker et al. 2004; Rossa et al. 2006) are shown as open black squares and nuclei of early-type galaxies in the Virgo cluster (Côté et al. 2006) as filled grey squares. Globular clusters in the Milky Way, the Magellanic Clouds and the Fornax dwarf spheroidal are shown as black dots (McLaughlin & van der Marel 2005), globular clusters in the Virgo cluster are shown as grey dots (Jordán et al. 2009). Finally, ultra-compact dwarf galaxies are shown as star symbols (from a compilation by Mieske et al. 2008 and from Chilingarian & Mamon 2008), and the brightest objects of this class, VUCD7, UCD3 and M59cO are labelled.

1.2 Ultra-compact dwarf galaxies

In spectroscopic surveys of the Fornax cluster Hilker et al. (1999) and Drinkwater et al. (2000) discovered a population of compact stellar systems that are more luminous than any Galactic globular cluster, but significantly more compact than compact ellipticals or dwarf ellipticals of comparable luminosity. These objects constituted the prototypes of the morphological class of 'ultra-compact dwarf galaxies'[2] (UCDs; Phillipps et al. 2001), which can be loosely defined as predominantly old (e.g. Chilingarian et al. 2011), early-type stellar systems with half-light radii of $15 \lesssim r_h \lesssim 100$ pc and absolute luminosities of $-13.0 \lesssim M_V \lesssim -11$ mag, or alternatively, masses of $2 \times 10^6 \gtrsim \mathrm{M} \gtrsim 2 \times 10^8$ $\mathrm{M}_\odot$ (Mieske & Kroupa 2008).

Following their initial discovery, systematic searches for UCDs were conducted, and UCDs were also discovered in other all-target spectroscopic surveys of galaxy clusters. These studies yielded a larger number of known UCDs in the Fornax cluster (at a distance of d = 19 Mpc; Hilker et al. 2007; Mieske et al. 2007a; Gregg et al. 2009) and objects of this type have also been found in other nearby galaxy clusters, such as Virgo (d = 17 Mpc; Haşegan et al. 2005; Jones et al. 2006; Brodie et al. 2011), Centaurus (d = 43 Mpc; Mieske et al. 2007b), Coma (d = 100 Mpc; Price et al. 2009; Madrid et al. 2010; Chiboucas et al. 2011), Hydra I (d = 54 Mpc; Wehner & Harris 2007; Misgeld et al. 2011) and Perseus (d = 71 Mpc; Penny et al. 2012).

More recently objects of this type have also been discovered in less rich environments, around the dominant giant galaxies in nearby loose groups, namely NGC 5128 (Centaurus A, d = 4 Mpc; Rejkuba et al. 2007; Taylor et al. 2010), M 104 (Sombrero, d = 9 Mpc; Hau et al. 2009), NGC 4546 and NGC 3923 (d = 13 Mpc and d = 21 Mpc, respectively; Norris & Kannappan 2011), NGC 4494 (d = 16 Mpc; Foster et al. 2011), as well as in the compact groups HCG 22 and HCG 90 (both at d = 33.1 Mpc; Da Rocha et al. 2011) and in the fossil group NGC 1132 (d = 100 Mpc; Madrid 2011).

Up to now, no UCDs are known that exist in isolation, but this is perhaps not surprising: due to their small sizes, most UCDs appear unresolved from the ground and thus evade detection in wide-field imaging surveys such as the Sloan Digital Sky Survey (SDSS; Abazajian et al. 2003) or Pan-STARRS (Kaiser et al. 2002). The identification of UCDs therefore has been based on all-target spectroscopic surveys of galaxy groups or clusters (where UCD candidacy of unresolved sources was inferred by proximity to the cluster galaxies on the sky) or by follow-up spectroscopic observations of candidates identified as marginally resolved objects in the surroundings of galaxies imaged by the Hubble Space Telescope (HST). If isolated UCDs exist at all, there is a small chance to discover them by their radial velocity in blind spectroscopic surveys of unresolved sources with colours of late spectral type stars, such as SEGUE (Yanny et al. 2009) or the stellar surveys conducted with LAMOST (Chu & Zhao 1998).

1.2.1 Formation Scenarios

Several scenarios for the formation and nature of UCDs have been proposed in the literature.

UCDs could be the remnant nuclei of tidally stripped galaxies. Based on numerical simulations of this 'threshing' scenario, Bekki et al. (2001) and Bekki et al. (2003) showed that the tidal stripping of nucleated dwarf ellipticals, as well as of nucleated low-surface brightness spiral galaxies,

[2] Alternative names for these objects exist in the literature, such as 'Dwarf-Globular transition objects' (DGTOs; Haşegan et al. 2005), or simply 'ultra-compact objects' (UCOs; Mieske et al. 2002) or 'compact stellar systems' (CSSs; Firth et al. 2009). Kissler-Patig (2004) criticised the term UCDs, arguing that if these objects were the remnant nuclear star clusters of tidally stripped galaxies (see Section 1.2.1), they would in fact be 'ultra-diffuse' (for a star cluster) rather than 'ultra-compact'. Nevertheless, the term 'UCDs' has become the most widely adopted name, and it will be used throughout this Thesis, without advocating its possible implication that these objects necessarily descend from galaxies.

on eccentric orbits and in close passages (pericenter distances of 5–70 kpc) of the Fornax cluster centre, can result in naked nuclei that resemble observed UCDs. Qualitatively similar results were obtained by Bassino et al. (1994), who studied the formation of globular clusters from nucleated dwarf galaxies. In particular, depending on the eccentricity and pericenter distance of the orbit and the dark-matter distribution of the original nucleated galaxy, the resulting UCDs can also retain low-surface brightness envelopes, similar to the extended halos observed around some UCDs (Evstigneeva et al. 2008).

Based on the spatial distribution of UCDs in the Fornax cluster (see below), Drinkwater et al. (2004) argued that UCDs may descend from a entirely novel primordial population of progenitor galaxies that formed at early times around the central cluster galaxies.

UCDs could also be massive star clusters. Mieske et al. (2002) proposed that UCDs represent the high-luminosity tail of the (intra-cluster) GC population. Fellhauer & Kroupa (2002) proposed that UCDs could be the result of mergers of stellar superclusters (i.e. aggregates of many young star clusters; Kroupa 1998) that formed in gas-rich galaxy-galaxy mergers. The massive star cluster W3 in the merger remnant galaxy NGC 7252 may be an example for the latter scenario (Fellhauer & Kroupa 2005). With a mass of $\sim 10^8$ $M_\odot$ and a half-light radius of 18 pc it resembles typical UCDs, except for its young age of only ~ 0.5 Gyr.

1.2.2 Properties of UCDs

Beyond the search for UCDs and the confirmation of UCD candidates, studies of these objects, mainly in the Fornax and Virgo clusters, have focused on collecting information on their bulk properties and discussing these mainly in the context of the 'threshed nuclei' and 'star clusters' scenarios.

In Fornax, the spatial and kinematic distribution of UCDs is distinct from that of nucleated and non-nucleated dwarf galaxies and the GC systems of the central cluster galaxies (e.g. Drinkwater et al. 2003, 2004; Mieske et al. 2004, 2012; Gregg et al. 2009). Since simulations of the threshing scenario require highly eccentric orbits to form UCDs and since the remnant nuclei will remain on these orbits, Drinkwater et al. (2004) argued that the more concentrated distribution of UCDs compared to nucleated dwarfs disfavours these as the UCD progenitors, and that UCDs therefore may represent the progeny of a novel class of galaxies. A potential caveat of this argument is that there is a selection bias. The observed nucleated dwarfs are those that were *not* tidally stripped, and therefore these could be on orbits less susceptible to threshing, or could have fallen into the cluster at a later time. Gregg et al. (2009) showed that the spatial distribution of UCDs in Fornax is compatible with that of the intra-cluster GCs, i.e. GCs not associated with one of the central cluster galaxies. Also in other clusters, the specific frequency of UCDs is found to be very similar to that of GCs, consistent with UCDs being the bright end of the GC luminosity distribution (Mieske et al. 2012).

At a given luminosity, UCDs are more extended than the nuclei of galaxies (e.g. De Propris et al. 2005; Evstigneeva et al. 2008). This is also apparent in Fig. 1.1 and has been put forward as an argument against the threshing model. However, also in the threshing simulations, a certain degree of expansion of the remnant nuclei is seen (see e.g. fig. 4 of Bekki et al. 2003), but to date this has not been quantified. Moreover, one nucleus in the small sample studied by De Propris et al. (2005) is as extended as the UCDs in their study. Its host galaxy shows residual spiral structure, and so these authors conclude that UCDs may be the remnant nuclei of spiral galaxies. In contrast to GCs, whose sizes and luminosities are uncorrelated, and in common with galaxies, UCDs show a trend of increasing size with increasing luminosity (Mieske et al. 2006a; Evstigneeva et al. 2008). Brodie et al. (2011), who include also extended but faint clusters (half-light radii of $5 \lesssim r_h \lesssim 25$ pc and luminosities of $M_V \lesssim -8$ mag) in their study, argue that such a size-luminosity relation does

not exist and that extended clusters and UCDs show a continuous distribution in luminosity that parallels that of concentrated GCs. However, they also note that there is a very sparsely populated prominent gap in luminosity ($-8 < M_V < -11$ mag) between faint extended clusters and UCDs (see their fig. 8). While this may be a consequence of the target selection in spectroscopic surveys of UCDs and star clusters, it at least warrants caution regarding the claim of a continuous distribution in luminosity from extended clusters to UCDs.

Stellar population studies (e.g. Maraston et al. 2004; Mieske et al. 2006a, 2007a; Evstigneeva et al. 2007; Hau et al. 2009; Taylor et al. 2010; Chilingarian et al. 2011) showed that UCDs have generally sub-solar metallicities of $-2 \lesssim [\mathrm{Fe/H}] \lesssim 0$ dex and are predominantly old ($\gtrsim 9$ Gyr), although there are a few younger UCDs with ages of 0.5 to several Gyr, such as the already mentioned UCD-like young massive cluster W3 in NGC 7252. Both, the metallicities and the ages derived in these studies, are luminosity-weighted, single stellar population equivalent quantities, and to date the observationally challenging question whether UCDs contain multiple stellar population has not been addressed.

Like the GC systems of many galaxies, also the GC populations of the Virgo and Fornax clusters show a bimodality in colour (Mieske et al. 2006b, 2010). These bimodalities are known to reflect an actual bimodality in the metallicity distribution in many systems, although in the GC systems of some galaxies, they may also result from the non-linear dependence of colour on metallicity, which can cause a unimodal metallicity distribution to appear bimodal in optical colours (e.g. Chies-Santos et al. 2012, and references therein). In terms of colours, UCDs in the Virgo cluster coincide with the blue peak of the cluster's GC distribution and UCDs in the Fornax cluster, being significantly redder, coincide with the red peak of the GC distribution. The same correlations hold also when spectroscopic metallicity, instead of colour, is considered and could indicate a fundamental difference in the origin of UCDs in the Virgo and Fornax clusters (Mieske et al. 2006a). Paudel et al. (2010) compared the stellar population properties of nuclei of 34 Virgo dwarf ellipticals (dE) and ten Virgo UCDs. In agreement with previous studies of the Virgo cluster, they found that dE nuclei are on average more metal-rich than UCDs. However, they showed that in the high-density regions of the cluster, where most of the UCDs reside, there is no difference in metallicity between nuclei and UCDs. Hence, they argued that the difference in metallicity in the cluster-wide sample can be explained by dEs being able to retain retain gas for a longer time and therefore form younger and more chemically enriched generations of stars in the lower-density regions of the cluster. UCDs in Virgo could therefore descend from dE nuclei in which the star formation, due to the higher environmental density, was shut down at earlier epochs. On the other hand, Mieske et al. (2006a) based on their finding that nuclei in the Fornax cluster are significantly more metal-poor and potentially older than the UCDs in this cluster, argue that UCDs in Fornax may be the successors of merged stellar superclusters produced in violent galaxy-galaxy mergers.

The relative abundance of α elements and iron is an indicator for the formation time-scale of a stellar population. α elements are produced by Type II supernovae that accompany the formation of neutron stars in the core-collapse of short-lived massive stars. Iron-peak elements, on the other hand, are produced in Type Ia supernovae. These result from carbon-oxygen white dwarfs that accrete matter from a companion giant star and reach the Chandrasekhar mass of $1.4\,\mathrm{M}_\odot$, or, in the so-called double-degenerate scenario, from the merger of two white dwarfs in a binary whose total mass exceeds the Chandrasekhar limit. Carbon-oxygen white dwarfs are the final evolutionary stages of stars with initial masses lower than 6-8 $\mathrm{M}_\odot$. Therefore, they only exist in stellar populations older than 50 Myr (e.g. Salaris & Cassisi 2005) and even then only in low numbers, as the initial stellar mass function (IMF) is dominated by lower-mass stars. Thus enrichment with iron-peak elements via Type Ia supernovae occurs on time-scales of hundreds of Myr to several Gyr. Consequently, and indicative of their rapid formation, Galactic GCs (e.g. Thomas et al. 2011), as

well as massive elliptical galaxies (Trager et al. 1998; Kuntschner 2000), are known to have stellar populations enhanced in [α/Fe] elements compared to the solar ratio. Dwarf ellipticals and also the nuclei of nucleated dEs in the majority have sub-solar to solar [α/Fe] ratios and therefore are thought to have experienced prolonged star formation (e.g. Geha et al. 2003; Evstigneeva et al. 2007). Evstigneeva et al. (2007) find that the majority of a sample UCDs in Virgo shows super-solar [α/Fe] ratios, compatible with a star-cluster origin of UCDs. Firth et al. (2009) find a more diverse picture for a small sample of Fornax UCDs, with at least one UCD, UCD3 (see Chapter 2) having at most solar [α/Fe]. UCDs in NGC 5128 (Centaurus A) appear significantly less enhanced in α-elements than the Virgo and Fornax samples (Taylor et al. 2010) and therefore more closely resemble dE nuclei.

In summary, the bulk properties of UCDs thus far have not provided clear evidence for or against UCDs being either a star clusters or threshed nuclei. Consequently, a consensus seems to emerge in the literature, that the morphological class of UCDs comprises objects from different evolutionary tracks (e.g Hilker 2009; Da Rocha et al. 2011; Norris & Kannappan 2011; Brodie et al. 2011), even though the fraction of threshed nuclei among UCDs may be very low (Mieske et al. 2012).

1.2.3 High mass to light ratios

One of the most intriguing properties of UCDs are their high dynamical mass to light ratios (M/L) that are on average $\sim$30-50 per cent higher than the predictions of canonical stellar population models (e.g. Kruijssen & Mieske 2009). While there are UCDs for which the dynamical and stellar population M/L largely agree with each other (e.g. Chilingarian et al. 2011), there are also extreme cases, for which the dynamical M/L is up to ~ 3 times higher than expected from the stellar population synthesis (e.g. Haşegan et al. 2005; Mieske & Kroupa 2008; Taylor et al. 2010).

The V-band M/L$_V$ of a simple stellar population increases with increasing age and with increasing metallicity (e.g. Maraston 2005). In order to compare the M/L$_V$ of objects with different metallicities, Mieske & Kroupa (2008) introduced a mass-to-light ratio normalised to solar metallicity:

$$\mathrm{M/L}_{V,\mathrm{normalised}} = \frac{\mathrm{M/L}_{V,\mathrm{obs}}}{\mathrm{M/L}_{V,\mathrm{SSP},[\mathrm{Fe/H}]}} \times \mathrm{M/L}_{V,\mathrm{SSP},0} \tag{1.1}$$

where $\mathrm{M/L}_{V,\mathrm{obs}}$ is the observed dynamical M/L$_V$ of an object, $\mathrm{M/L}_{V,\mathrm{SSP},[\mathrm{Fe/H}]}$ is the simple stellar population (SSP) mass to light ratio predicted for 13 Gyr stellar population with the metallicity [Fe/H] of the observed object, and $\mathrm{M/L}_{V,\mathrm{SSP},0}$ is the SSP prediction for a 13 Gyr solar-metallicity stellar population. The choice of 13 Gyr is arbitrary, but is justified as most GCs and UCDs are indeed old. Moreover, the ratio of the M/L$_V$ of populations with different metallicity is largely independent of age for ages $\gtrsim 5$ Gyr. The SSP predictions depend on the adopted stellar mass function and on the details of the spectral synthesis library and its calibration. Mieske & Kroupa (2008) therefore adopted the average of the widely used Bruzual & Charlot (2003) and Maraston (2005) models that are based on the IMF by Chabrier (2003) and Kroupa (2001), respectively.

Figure 1.2 shows this metallicity-independent mass to light ratio $\mathrm{M/L}_{V,\mathrm{normalised}}$ as a function of dynamical mass for Milky Way and M31 GCs, GCs and UCDs in NGC 5128 (Centaurus A) and UCDs in the Fornax and Virgo clusters. Since UCDs and extragalactic GCs are marginally resolved under good seeing conditions, aperture corrections have to be applied when calculating the dynamical mass or the $\mathrm{M/L}_{V,\mathrm{obs}}$ of an object. The velocity dispersion measured from the integrated light of an object is not simply the luminosity-weighted integrated intrinsic velocity dispersion, but the light lost due to the finite size of the spectrograph's aperture (i.e. slit or fibre) has to be taken into account. This requires the knowledge of the intrinsic surface brightness profile and therefore, in practise, space-based imaging of the object. The $\mathrm{M/L}_{V,\mathrm{obs}}$ entering into Fig. 1.2 are based on

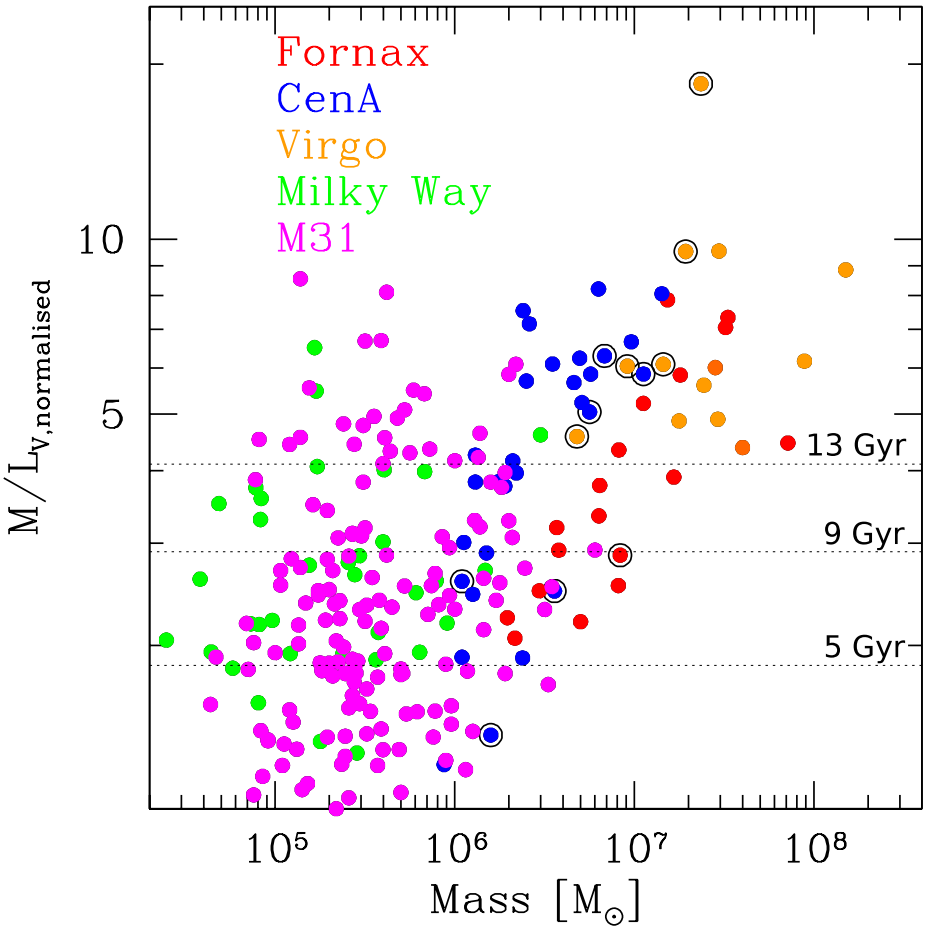

Figure 1.2: The normalised mass to light ratios of GCs and UCDs in the Milky Way (shown as green circles), M 31 (magenta), NGC 5128 (Centaurus A; blue) and in the Virgo (orange) and Fornax (red symbols) clusters. Objects for which only a metallicity based on optical colours is available, are indicated by a black circle around the coloured symbol. This figure is an updated version of fig. 2 of Mieske & Kroupa (2008) and was kindly provided by Steffen Mieske. Compared to the version shown in Mieske & Kroupa (2008) based on literature sources listed in their table 2, this updated figure includes the sample of M31 GCs studied by Strader et al. (2009) and new metallicity and dynamical mass measurements for several NGC 5128 GCs and UCDs (Beasley et al. 2008; Taylor et al. 2010). Dashed horizontal lines indicate the M/L_V predicted for simple stellar populations (SSPs) with ages of 5, 9 and 13 Gyr, taken as the average of the Bruzual & Charlot (2003) and Maraston (2005) models. It can be seen that UCDs ($M > 2 \times 10^6$ $M_\odot$) have higher M/L_V and in many cases these exceed the expectation of the oldest SSP models. There are also a few low-mass GCs with high M/L_V, which can be understood as the effect of binaries and unbound stars. The low M/L_V of many old GCs are likely the result of their dynamical evolution (see text).

the measured velocity dispersions and HST-based light-profiles and the mass-modelling described in Hilker et al. (2007) and Mieske et al. (2008).

Several points should be noted about Fig. 1.2. At first glance, it is surprising that many GCs, which at least in the Milky Way are known to be older than $\gtrsim 9$ Gyr have normalised M/L$_V$ lower than ~ 3. This can be explained by the preferential loss of low-mass stars due to mass segregation in GCs with half-mass relaxation times significantly shorter than their age. These stars have high specific M/L$_V$ and therefore their loss lowers the global M/L$_V$ of the cluster (Kruijssen & Mieske 2009). Also several GCs with M$\lesssim 6\times10^5\,$M$_\odot$ have M/L$_V$ higher than the oldest SSP models. This may be caused by an overestimation of the dynamical mass due to the inflation of the velocity dispersion measured from a small sample of stars by the presence of binaries and unbound stars (see also Section 4.5.2). An illustrative example in this context is the Galactic GC Palomar 13. For this cluster, Côté et al. (2002) inferred a dynamical M/L$_V$ of $40^{+24}_{-17}\,$M$_\odot\,$L$_\odot^{-1}$ from the radial velocities of 21 probable member stars. Bradford et al. (2011) obtained radial velocities of 61 probable member stars in several epochs, which allowed them to identify binaries, and derived a M/L$_V$ of $2.4^{+5.0}_{-2.4}\,$M$_\odot\,$L$_\odot^{-1}$ for this cluster.

Both these effects should not affect the measurement of the dynamical masses of UCDs. Their relaxation times exceed a Hubble time (by several orders of magnitude for the most extended systems, e.g. Mieske et al. 2008), and thus their stars should not be mass-segregated. Moreover, their internal velocity dispersions are of order of $25-45\,$km s^{-1} and are measured from their integrated light that samples a large number of stars. The inflation of velocity dispersions due to binaries however, is problematic only in systems with low intrinsic velocity dispersions and measurements based on small samples of individual radial velocities (e.g. Minor et al. 2010). We will come back to the possible effect of unbound stars on the dynamical masses of UCDs below.

There is, however, one major concern when comparing the observed M/L$_V$ of UCDs to SSP predictions: if UCDs were the remnant nuclei of galaxies, it is likely that they contain multiple stellar populations. As mentioned before, the stellar population parameters available for UCDs are luminosity-weighted SSP-equivalent values, which were almost exclusively derived in the optical wavelength range[3]. If a young population is present on top of an underlying old population, the integrated light in the optical will be dominated by the young population, even if the young population contributes only a few percent of the stellar mass. Therefore, based on spectroscopic population parameters, the mass-weighted age of UCDs may be underestimated. Assuming a reasonable enrichment history with younger populations being at least as enriched as older populations, their mass-weighted metallicities may be overestimated by the spectroscopic value. Moreover, also purely old, metal-poor ([Fe/H]$\lesssim -1.2\,$dex) stellar populations can mimic a young population in integrated-light spectroscopy, if they contain blue horizontal branch stars (Ocvirk 2010). If metallicities are inferred from broad-band photometric colours, as for the UCDs marked by black circles in Fig. 1.2, any young population that may be present will lead to significantly bluer colours and an underestimation of the metallicity, if an old age is assumed.

Younger and/or more metal-poor populations have a lower M/L$_V$. Therefore underestimating the metallicity or age will lead to an underestimation of the true mass-weighted stellar population $\mathrm{M/L}_{V,\mathrm{SSP,[Fe/H]}}$, or equivalently cause too large a correction term in Eq. (1.1), leading to a high $\mathrm{M/L}_{V,\mathrm{normalised}}$. However, if one uses only spectroscopic metallicities (that may be over- but *not* underestimated in the presence of younger stellar populations), and adopts an old age for safety, even if spectroscopy may indicate differently, one will not overestimate, but potentially underestimate, the $\mathrm{M/L}_{V,\mathrm{normalised}}$ of UCDs. Hence, the high M/L of UCDs with spectroscopic metallicities, which are available for the majority of the objects in Fig. 1.2, cannot be explained as the result of

[3] An exception is the study of Evstigneeva et al. (2007), who included the near-infrared Ca triplet in their metallicity measurement

the presence of multiple stellar populations.

Regardless of the origin of UCDs, their high M/L are not readily explained. If UCDs are threshed nuclei, they would reside in the centre of the (remnant) dark matter halo of the original galaxy. However, in order to affect the stellar kinematics of such compact objects, dark matter halos with extremely high central densities would be required, two orders of magnitude higher than the central dark matter densities of the, presumably cored, dark-matter halos of dwarf spheroidals (e.g. Gilmore et al. 2007; Dabringhausen et al. 2010). This holds also, assuming realistic halo masses, for the central dark matter densities in the cuspy Navarro et al. (1997) or Moore et al. (1999) halos (Murray 2009). A possible way to alleviate this problem could be the enhancement of the central dark matter concentration during the formation of the progenitor nuclei via the infall of gas (Goerdt et al. 2008; Baumgardt & Mieske 2008).

Another possibility in the tidal stripping scenario is that the M/L_V of the remnant UCDs are enhanced due to the presence of unbound stars around the UCDs. In this case, the integrated-light velocity dispersion would no longer be that of a system in virial equilibrium and the inferred dynamical mass would be systematically too high. Based on *N*-body simulations Fellhauer & Kroupa (2006) showed that this effect can enhance the measured M/L_V of UCDs with masses of $10^7\,M_\odot$ by a factor of up to 10, if the line-of-sight coincides with the UCD's trajectory. The measured M/L_V is not affected, if the line-of-sight is perpendicular to the orbital plane, or if the UCD is compact and massive ($M\sim 10^8\,M_\odot$). Assuming that the orbital planes of UCDs are randomly oriented, it is difficult to explain that almost all UCDs with $M\gtrsim 10^7\,M_\odot$ in Fig. 1.2 show an enhanced M/L_V. Moreover, unbound stars would eventually escape into the host halo, and as the majority of UCDs are old ($\gtrsim 9$ Gyr), it is unlikely that they were only threshed within the last few Gyr.

UCDs could also harbour massive black holes, either because a black hole and a nucleus of comparable mass coexisted in the progenitor galaxy (Graham & Spitler 2009), or because UCDs are in fact 'hyper-compact stellar systems' bound to recoiling super-massive black holes that were ejected from the cores of giant galaxies (Merritt et al. 2009). The black hole masses expected in these scenarios, and required to explain the high M/L of UCDs, could substantially exceed those of intermediate-mass black holes that may (e.g. Gebhardt et al. 2002; Gerssen et al. 2002; Noyola et al. 2008; Lützgendorf et al. 2011) or may not (Baumgardt et al. 2003; Anderson & van der Marel 2010; van der Marel & Anderson 2010) be present in GCs.

These three scenarios can in principle be tested by obtaining spatially resolved kinematics of UCDs. Due to their compact sizes, low velocity dispersions, large distances and therefore faint magnitudes, however, this remains observationally challenging even with current 8 m class telescopes, because it requires high spatial and spectral resolution. A first study of the spatially resolved kinematics of UCDs will be presented in Chapter 2.

An alternative scenario to such extra, dark constituents of the UCDs' masses and to recent tidal interactions is that the stellar populations of UCDs themselves are not 'normal', showing an overabundance of underluminous stellar objects. This has been proposed in the form of an overabundance of either stellar remnants (top-heavy mass function; Dabringhausen et al. 2008, 2009, 2010) or of low-mass stars (bottom-heavy mass function; Mieske & Kroupa 2008). Chapter 3 will present a first test of this latter, bottom-heavy mass function scenario.

1.3 Galactic Globular Clusters

The globular cluster system of the Milky Way extends out to more than 100 kpc and contains more than 150 known GCs (e.g. Harris 1996, 2010 edition), with more GCs being discovered in current wide-field infra-red imaging surveys (e.g. Minniti et al. 2011; Longmore et al. 2011; Moni Bidin et al. 2011) and a few clusters probably still awaiting their discovery (e.g. Ivanov et al. 2005). GCs

have masses of $10^4 \lesssim M \lesssim 2.5 \times 10^6$ $M_\odot$. In terms of mass, GCs are not clearly delineated from the class of young or open clusters, such as Westerlund 1 ($\sim 10^5$ $M_\odot$; Clark et al. 2005). Since all GCs in the Galaxy are old ($\gtrsim$ 9Gyr), historically the distinction between GCs and open clusters is also based on the old age. Inter-mediate age, massive clusters that are found in other galaxies, such as the LMC or M 33 are therefore sometimes referred to as 'rich' or 'populous' clusters rather than GCs. Also the distinction between GCs and UCDs is somewhat arbitrary and the upper mass limit of 2×10^6 $M_\odot$ stated above is simply the mass of the most massive Galactic GC, ωCen (NGC 5139; the van de Ven et al. 2006), and is generally adopted as the lower mass limit for UCDs for the same reason.

In Section 1.1 it has been mentioned that physical size alone is not sufficient to distinguish extended GCs from ultra-faint dSphs and both classes overlap also in luminosity. If size and luminosity together are considered, the two classes stand apart in that GCs have higher surface brightnesses (e.g. van den Bergh 2008). The most striking difference, of course, are the dynamical masses. Ultra-faint dSphs are thought to be the most dark-matter dominated stellar systems known with V-band mass-to-light ratios of 10^2 - 3×10^3 $M_\odot L_\odot^{-1}$ (Walker 2012, and references therein). While also GCs were conjectured to have formed inside their own dark matter halos (Peebles 1984), current observations of their density profiles and velocity dispersions suggest that there is no detectable amount of dark matter in GCs (e.g. Baumgardt et al. 2009; Conroy et al. 2011; Hankey & Cole 2011; Da Costa 2012, see also Chapter 4).

The Galactic GC system is not a homogeneous population of objects. A sub-population of metal-rich GCs ([Fe/H]> -1.5 dex) is associated with the Galactic bulge or disc, but also metal-poor ($-2 <$[Fe/H]< -1.5 dex) GCs show an over-density in the bulge region (e.g. van den Bergh 1999). Also in the halo GC population several components can be distinguished. About one quarter of these belongs to the so-called 'outer halo', at Galactocentric distances larger than 15 kpc (e.g. van den Bergh & Mackey 2004). Several of these outer halo clusters are also attributed to the 'young halo' sub-population because they seem to be 1-2 Gyr younger than the old, inner halo GCs of similar metallicity (e.g. Dotter et al. 2010). A number of authors have suggested that the young and/or outer halo GCs were accreted by the Milky Way via the infall of dwarf satellite galaxies (e.g. Mateo 1996; Côté et al. 2000; Mackey & Gilmore 2004; Lee et al. 2007; Forbes & Bridges 2010), similar to the halo assembly scenario already proposed by Searle & Zinn (1978), whereas the classical old GCs probably formed during an early and rapid dissipative collapse of the Galaxy's halo, first proposed by (Eggen et al. 1962).

For a long time, GCs were believed to be examples of truly simple stellar populations. Having formed from a single molecular cloud, they were thought to contain a population of coeval, chemically homogeneous stars. However, in recent years, an increasing number of GCs has been found to contain several populations, (e.g. Sarajedini & Layden 1995; Lee et al. 1999; Bedin et al. 2004; Piotto et al. 2007). In the majority of these clusters the different stellar subpopulations stand out by a difference in light element abundances, and younger populations are thought to have formed from material polluted by the first generation of stars (see Gratton et al. 2012, for an overview). However, in ωCen and M 54 the sub-populations differ also significantly (by $\gtrsim 0.1$ dex) in the iron abundance, and by several Gyr in age. Both clusters have been proposed to be the nuclei of accreted dwarf galaxies (Lee et al. 1999; Hughes & Wallerstein 2000; Majewski et al. 2000; Hilker & Richtler 2000; Tsuchiya et al. 2003; Bekki & Freeman 2003, ωCen); (M 54 Bassino & Muzzio 1995; Layden & Sarajedini 2000). At least in the case of M 54, the former host galaxy is still observable as the Sagittarius dwarf galaxy that is currently being disrupted (Ibata et al. 1995). Therefore, these two clusters may be more similar to UCDs than to classical GCs. Interestingly, the massive outer halo cluster NGC 2419, that similarly was proposed to be the former nucleus of an accreted dwarf galaxy (van den Bergh & Mackey 2004), appears to show no significant spread in the iron

abundance (Cohen et al. 2011).

1.3.1 Dynamical evolution of GCs

The dynamical evolution of GCs is driven by internal processes and influenced by the ambient Galactic potential in which the clusters evolve. A detailed description of these processes can be found in chapters 7 and 8 of Binney & Tremaine (2008), which formed the basis for this Section.

The early evolution of a star cluster is dominated by the mass-loss due to stellar winds and core-collapse supernovae with massive stellar progenitors, leading to an expansion of the cluster. Since lower-mass stars evolve more slowly, and since they retain a larger fraction of their initial masses, the importance of stellar evolution for the dynamical evolution of the clusters decreases with time.

Two-body relaxation arises from encounters of stars, in which these exchange kinetic energy. Stars that lose kinetic energy sink into the cluster centre, while stars that gain kinetic energy populate orbits further away from the cluster's centre. This diffusion of kinetic energy to the outer parts of the cluster eventually leads to the core collapse, a run-away contraction of the cluster's core. The time-scale for two-body relaxation depends on the stellar density and therefore varies significantly from a cluster's centre to its outer parts. An approximation of the two-body relaxation time at the half-mass radius is given by (Binney & Tremaine 2008, eq. 7.108)

$$t_{rh} = \frac{0.17N}{ln\,(\lambda N)} \sqrt{\frac{r_h^3}{G\mathrm{M}}}, \tag{1.2}$$

where N is the number of stars in the cluster, r_h its deprojected half-light radius, M is its total mass, λ in the Coulomb logarithm is ≈ 0.1 and G is Newton's constant.

In clusters, where a spectrum of stellar masses is present, the system evolves towards equipartition of kinetic energies: massive stars preferentially lose kinetic energy to lower-mass stars in two-body encounters. This is observed as mass segregation, more massive stars show a more concentrated radial distribution than lower-mass stars. As a consequence, the mass function of the cluster becomes shallower in the cluster centre, but also globally as stars at large radii are more easily lost to the Galactic potential (Vesperini & Heggie 1997; Baumgardt & Makino 2003) and the cluster's mass-to-light ratio decreases as mentioned in the discussion of Fig. 1.2. Mass segregation occurs more quickly for more massive stars, and in a two-mass system with stars of masses m_1 and m_2 ($m_1 < m_2$), the time-scale for mass segregation is

$$t_{ms} \propto \frac{m_1}{m_2}\, t_{rh} \tag{1.3}$$

(Kruijssen 2009). For stars that are very massive compared to the average stellar mass $\langle m \rangle$, the situation turns into dynamical friction and these stars sink to the centre quickly. This early segregation of massive stars in the cluster's centre speeds the cluster's dynamical evolution and in clusters with a spectrum of stellar masses, core collapse occurs more quickly than in single-mass clusters, and can take place after only a fraction of the initial half-mass relaxation time (e.g. Gürkan et al. 2004). In a two-mass system dynamical evolution occurs faster, the larger the ratio between massive and lower-mass stars (Khalisi et al. 2007). In globular clusters, however, the range of stellar masses is quickly limited by stellar evolution: massive stars lose mass and turn into white dwarfs or neutron stars. The latter can escape from low-mass clusters, whose escape velocity is lower than the initial kick velocities of neutron stars (Kruijssen 2009). Therefore, after a few tens of Myr, the ratio of the maximum stellar mass to the average stellar mass ($\langle m \rangle \approx 0.4\,\mathrm{M}_\odot$) becomes ~ 4 in a globular cluster. According to the simulations of Gürkan et al. (2004), it takes several half-mass relaxation times until such a cluster goes into core collapse. Most of the Milky Way's GCs have half-mass

relaxation times significantly shorter than their ages and mass segregation is observed in these clusters. However, by comparing the slope of the stellar mass function observed in Galactic GCs with numerical simulations, Baumgardt et al. (2008) found that several GCs are more strongly depleted in low-mass stars than expected from dynamical evolution if a Kroupa (2001) IMF is adopted. They argued that this could indicate primordial mass segregation in this clusters. We will return to the question of primordial mass segregation in Chapters 4 and 5.

Due to relaxation, some stars will gain velocities larger than the cluster's escape velocity and evaporate from the cluster. For a cluster evolving in an external tidal field, stars may also be lost from the cluster if they have energies large enough to cross the Roche surface of the cluster, where gravitational attraction of the cluster and that of the Galaxy are equal. The extent of a GC therefore is limited to the Roche or Jacobi radius, which can be approximated as (Binney & Tremaine 2008, eq. 8.14)

$$r_J = \left(\frac{G\mathrm{M_C}}{2V_G^2}\right)^{1/3} R_G^{2/3}, \tag{1.4}$$

where $\mathrm{M_C}$ is the cluster's mass, V_G is the circular velocity of the Galaxy and R_G is the Galactocentric radius of the cluster. Clusters on outer, circular orbits experience a steady loss of mass, while for clusters on eccentric orbits, mass loss primarily occurs near the perigalacticon (Baumgardt & Makino 2003). Clusters crossing the Galactic disk or coming close to the Galactic bulge experience more violent disk or tidal shocks that heat the cluster and speed up its dynamical evolution (e.g. Gnedin & Ostriker 1997).

The loss of stars from Galactic GCs is evident as tidal tails around several clusters, such as Palomar 5 (Odenkirchen et al. 2001), NGC 5466 (Belokurov et al. 2006a; Grillmair & Johnson 2006), Palomar 14 (Jordi & Grebel 2010; Sollima et al. 2011), M53 and NGC 5053 (Chun et al. 2010). Based on the discovery of a large number of field stars in the Galactic halo that show the strong CN absorption bands typical for GC stars, Martell & Grebel (2010) argued that up to 50 per cent of the field stars in the halo may originally have formed in GCs.

1.3.2 Remote GCs as probes for testing gravitational theories

Apart from being tracers of the assembly of the Galactic halo, GCs have also been recognised as valuable probes for testing fundamental physics (e.g. Scarpa et al. 2003). Baumgardt et al. (2005) proposed to use diffuse outer halo GCs to distinguish between classical and modified Newtonian dynamics (MOND; Milgrom 1983a,b; Bekenstein & Milgrom 1984). MOND is very successful in explaining the flat rotation curves of disk galaxies without any assumption of unseen dark matter, although it faces problems reproducing gravitational lensing from galaxy clusters and the anisotropies in the cosmic micro-wave background (Famaey & McGaugh 2011). According to MOND, Newtonian dynamics breaks down for accelerations lower than $a_0 \simeq 1 \times 10^{-8}\ \mathrm{cm\,s^{-2}}$ (Begeman et al. 1991; Sanders & McGaugh 2002) and the Newtonian acceleration $\mathbf{a}_{\mathrm{Newton}}$ is replaced by $\mu\left(a/a_0\right)\mathbf{a}$, where $\mathbf{a}$ is the acceleration acting on a particle, a is its Euclidean norm and $\mu\left(x\right)$ is an arbitrary smooth function, which satisfies $\mu\left(x\right) = x, x \ll 1$ and $\mu\left(x\right) = 1, x \gg 1$.

In remote Galactic GCs, the external acceleration due to the Galaxy experienced by the cluster stars is below this critical limit of a_0, and the radial velocity dispersion profiles of such clusters can thus be used to distinguish between MOND and Newtonian dynamics (see e.g. Sollima & Nipoti 2010, who derived King-like models for GCs in MOND). It should be noted that Scarpa et al. (2003, 2007), Scarpa & Falomo (2010) and Scarpa et al. (2011) reported a flattening of the velocity dispersion profile at accelerations comparable to a_0 also in GCs with Galactocentric distances $\lesssim$ 20 kpc. However, as the external acceleration in these clusters is well above a_0, such flattened velocity dispersion profiles in 'inner' GCs are more commonly attributed to the effects of tidal

heating and unbound stars or to contamination by field stars (e.g. Drukier et al. 1998; Lane et al. 2010a,b; Küpper et al. 2010a).

Two GCs in the outer halo have been studied extensively in the context of testing MOND, the massive cluster NGC 2419 and the diffuse cluster Pal 14. Based on radial velocities of 40 member stars of NGC 2419 and assuming isotropic stellar orbits, Baumgardt et al. (2009) derived a dynamical mass of $9\pm2\times10^5\,\mathrm{M}_\odot$, compatible with the photometric expectation from a simple stellar population with a Kroupa (2001) IMF. Moreover, they found no flattening of the velocity dispersion profile at low accelerations that could point to MONDian dynamics or dark matter in this cluster. Ibata et al. (2011a) studied an extended radial velocity sample of 178 stars of NGC 2419 and found that, while radial anisotropy is required in both Newtonian and MONDian dynamics to explain the observed kinematics, the data favour Newtonian dynamics, with their best-fitting MONDian model being less likely by a factor of $\sim 40,000$ than their best-fitting Newtonian model. Sanders (2012a) challenged this conclusion, arguing that in MONDian dynamics non-isothermal models, approximated by high-order polytropic spheres, can reproduce the cluster's surface brightness and velocity dispersion profiles. This led Ibata et al. (2011b) to extend the analysis of their data to polytropic models in MOND. Again, they concluded that the best-fitting MONDian model is less likely by a factor of ~ 5000 than the best-fitting Newtonian model, and that the data therefore pose a challenge to MOND, unless systematics are present in the data (but see also Sanders 2012b).

In the most diffuse outer halo clusters, i.e. clusters with large effective radii, low masses and therefore low stellar densities, also the internal acceleration due to the cluster stars themselves is below a_0 throughout the cluster. In these clusters, not only the shape of the velocity dispersion profile, but also the *global* velocity dispersions can be used to discriminate between MONDian and Newtonian dynamics. Baumgardt et al. (2005) showed that the expected global velocity dispersions in case of MOND exceed those expected in the classical Newtonian framework by up to a factor of 3 in these clusters (see their table 1). This result was reinforced by more accurate numerical simulations including the external field effect by Haghi et al. (2011). For the diffuse halo cluster Pal 14, Jordi et al. (2009) measured radial velocities of 16 of the cluster's member stars and found a good agreement between the cluster's photometric and dynamical mass in classical Newtonian dynamics, while the velocity dispersion is significantly lower than predicted in MOND (Haghi et al. 2009). Gentile et al. (2010) challenged this conclusion and argued on the basis of a Kolmogorov-Smirnov (KS) test that the sample of radial velocities (or, alternatively, the sample of studied diffuse outer halo GCs) is too small to rule out MOND. Küpper & Kroupa (2010) reanalysed the Jordi et al. (2009) radial velocity data including a heuristic treatment of binaries and mass segregation, and argued that Pal 14 either has to have a very low binary fraction of less than 10 per cent or otherwise is in a 'deep freeze' state, with an intrinsic velocity dispersion (after correction for binarity) low enough to challenge Newtonian dynamics in the opposite sense of MOND. Sollima et al. (2012), on the other hand, in a Monte-Carlo analysis based on the same radial velocity data and including the effects of binaries, of the external field and of velocity anisotropy, found that the cluster is compatible with Newtonian dynamics also when the constraint of the binary fraction is relaxed to $\lesssim 30$ per cent and that the data favour Newtonian over MONDian dynamics. Finally, tidal tails around Pal 14, already seen at low significance in Sloan Digital Sky Survey (SDSS; Abazajian et al. 2009) data by Jordi & Grebel (2010), were recently detected in deeper wide-field imaging by Sollima et al. (2011), indicating that the cluster is currently losing mass at a considerable rate. This may further complicate the interpretation of the small sample of radial velocities as unbound stars may contaminate the sample (e.g. Küpper et al. 2011b).

Chapter 4 will present a comparison of the dynamical and photometric mass of the diffuse outer halo cluster Pal 4, discussing the results in the context of testing MOND. The dynamics of Pal 14, in particular the question, whether it is mass-segregated, will be the subject of Chapter 5.

1.4 This Thesis

This Thesis is structured as follows: Chapter 2 presents the spatially resolved kinematics of the most-massive known UCD in the Fornax cluster, UCD3. An observational test for a bottom-heavy stellar mass function in two Virgo cluster UCDs with extremely high M/L_V, based on the gravity-sensitive 2.3 μm CO absorption band is presented in Chapter 3. Chapter 4 reports on the dynamical and photometric mass and the stellar mass function of the outer halo cluster Pal 4. Evidence for mass segregation in the halo cluster Pal 14, based on the analysis of its stellar mass function, is presented in Chapter 5. Chapter 6 summarises the results of this Thesis and Chapter 7 gives an outlook.

2

Spatially Resolved Kinematics of an Ultra-Compact Dwarf Galaxy[1]

2.1 Introduction

As discussed in Section 1.2.3, one of the most striking properties of UCDs is that on average, their dynamical mass to light ratios are ∼30-50 per cent higher than the predictions of canonical stellar population models (e.g. Kruijssen & Mieske 2009). Moreover, their V-band mass to light ratios M/L_V are on average twice as large as those of Galactic GCs of comparable metallicity (e.g. Mieske et al. 2008; Dabringhausen et al. 2008; Taylor et al. 2010). Depending on their origin, this may indicate that UCDs mark the onset of dark matter domination in small stellar systems (Baumgardt & Mieske 2008; Goerdt et al. 2008), or harbour massive central black holes (Merritt et al. 2009), or exhibit an unusual initial stellar mass function (Mieske & Kroupa 2008; Dabringhausen et al. 2009, 2010).

The nature of UCDs is still uncertain. Do they represent the most massive star clusters (e.g. Fellhauer & Kroupa 2002; Mieske et al. 2004)? Or are they the result of the environmental transformation of galaxies (e.g. Bekki et al. 2003)?

Spatially resolved kinematics of UCDs open up a way to new insights on this matter, complementary to those gained from the study of the spatial and velocity distributions of UCD populations as a whole (e.g. Mieske et al. 2004), of their structural properties (De Propris et al. 2005; Evstigneeva et al. 2008), of their integrated internal velocity dispersions (e.g. Hilker et al. 2007), or of their stellar population content (e.g. Taylor et al. 2010; Paudel et al. 2010).

Integral-field spectroscopy has become a well established technique to study the kinematics of stellar systems and has been employed in large surveys of massive galaxies, such as SAURON (de Zeeuw et al. 2002) or ATLAS3D (Cappellari et al. 2011). However, resolving the kinematics of objects with angular half-light radii on the order of 1 arcsec, takes seeing-limited optical integral field spectroscopy to its limits. On the other hand, present-day adaptive optics-aided, near infra-red integral field units (IFUs; e.g. Gemini/NIFS, McGregor et al. 2003; VLT/SINFONI, Eisenhauer

[1]The work presented in this chapter was done in collaboration with Michael Hilker, Steffen Mieske, Holger Baumgardt, Eva Grebel and Leopoldo Infante. The principal results on the kinematics of UCD3 were published in Frank et al. (2011). The modelled intrinsic line-of-sight velocity distributions discussed in Section 2.4.2 were calculated by Holger Baumgardt.

et al. 2003), provide only a moderate spectral resolving power of $R = \Delta\lambda/\lambda \lesssim 4000$, corresponding to an instrumental resolution $\sigma_{\rm ins} \gtrsim 32\,{\rm km\ s^{-1}}$. This severely limits the ability to accurately sample the velocity distribution of typical UCDs with velocity dispersions of $\sim 25\,{\rm km\ s^{-1}}$.

In this Chapter we present, for the first time, the spatially resolved kinematics of an UCD. The target of our study, UCD3, is one of the originally discovered objects (Hilker et al. 1999), which subsequently led to the definition of the class of UCDs. Nevertheless, UCD3 is not an average UCD in several ways: With $M_V = -13.55$ mag, it is the brightest known UCD in the Fornax cluster, separated by ~ 0.8 mag from the rest of the cluster's UCD population. In projection, it is relatively close to the central cluster galaxies NGC 1399 and NGC 1404 with projected distances of 46 kpc and 13 kpc, respectively. It is unusually red, with a spectroscopic metallicity of [Fe/H]~ -0.2 dex (Chilingarian et al. 2008a). Most importantly, it has a large half-light radius of $r_{\rm h} = 87$ pc, corresponding to ~ 0.95 arcsec at a Fornax cluster distance of 18.97 Mpc (Freedman et al. 2001), and is one of the few UCDs where an extended, low surface-brightness envelope has been detected (Evstigneeva et al. 2008), making it possible to resolve the UCD from the ground with seeing-limited instruments.

2.2 Observations and data reduction

UCD3 was observed in ESO programme 078.B-0496 (PI: Infante) under excellent seeing with the ARGUS IFU (Kaufer et al. 2003) of the Flames/GIRAFFE (Pasquini et al. 2002) spectrograph mounted on UT2 at the VLT. ARGUS consists of an array of 14×22 lenslets. In the employed '1:1' scale the spatial sampling is 0.52×0.52 arcsec per lenslet (or 'spaxel'), yielding a field of view of 11.5×7.3. We used the LR04 grism, providing a spectral resolution of R$\sim$9600, which corresponds to a instrumental resolution of $\sigma_{\rm ins} \sim 13\,{\rm km\ s^{-1}}$, over the range $5015-5831$ Å . The observations were executed in service mode over the period of almost one year and consisted of eight exposures of 2775 seconds each. A log of the observations is provided in Table 2.1. The first two columns list the observation number and Modified Julian Date of the observation. The remaining three columns contain the full-width at half-maximum (FWHM) of the seeing point-spread function (PSF) as measured by the Differential Image Motion Monitor (DIMM), on the guide probe and based on a model of the reconstructed images (see Section 2.2.2). Table entries in bold face indicate the six observations with the best modelled seeing that were used for our final analysis.

Table 2.1: Log of observations.

		Seeing FHWM		
No.	MJD	DIMM	Guide probe	Model
	54,120+	(arcsec)	(arcsec)	(arcsec)
1	**0.102284**	**0.6**	**$\sim$0.5**	**0.66**
2	0.128211	0.7	$0.5-0.6$	0.79
3	**5.090816**	**1.0**	**0.4–0.6**	**0.50**
4	**5.128742**	**1.2**	**$>$0.4–0.6**	**0.67**
5	**6.069953**	**0.8**	**0.6**	**0.65**
6	6.106291	0.7	$0.6-0.7$	0.70
7	**251.241424**	**0.7**	**–**	**0.53**
8	**330.143332**	**1.6**	**$<$0.5**	**0.58**

2.2.1 Basic data reduction

The basic data reduction and the extraction of wavelength-calibrated spectra was carried out using the Giraffe Baseline Data Reduction System (GIRBLDRS; Blecha et al. 2000), standard IRAF tasks and custom PYTHON routines.

The long integration times of our science frames of $3/4$ hours allow a considerable number of cosmic ray hits to accumulate during the exposures. The GIRBLDRS pipeline provides the possibility to perform a cosmic ray rejection based on identifying outlying pixels in a set of several exposures of the same. This method is not applicable to our observations, as they were recorded in a period of several months, a time span over which the wavelength and distortion solution of the spectrograph cannot be assumed to be stable. Therefore, prior to the other reduction steps, we used the LACOSMIC routine (van Dokkum 2001) to mask pixels affected by cosmic rays. The routine works on single bias-subtracted frames and performs a Lagrangian edge detection to identify the steep edges around cosmic ray hits. It produces a bad pixel mask, as well as a 'fudged' image, in which bad pixels are replaced by the median of their nearest neighbours. It would be appropriate to treat pixels affected by cosmic rays as 'missing data' and propagate this bad pixel information through the entire data reduction, in order to correctly weight pixels from the different data cubes in the final combination step. Unfortunately, when given the cosmic ray maps as input bad pixel maps, the subsequent GIRBLDRS pipeline recipes reproducibly crashed, presumably because the extraction recipe is not designed to handle cases where, at some wave length, all of the pixels in one fibre profile are bad. Therefore, we used the 'fudged' output images of LACOSMIC for the further reduction.

The observations were then reduced following the procedure outlined in the GIRBLDRS manual[2] using the calibration frames taken closest in time to the observations. The reduction produces 315 spectra for each observation. These are wavelength-calibrated and resampled to a common wavelength scale and arranged in a two-dimensional fits file. Of these, 297 spectra correspond to ARGUS lenslets (the spectra of three lenslets fall outside of the detector), 14 spectra correspond to dedicated sky fibres that are placed around the IFU and 5 correspond to simultaneous calibration lamp spectra.

A master sky spectrum for each observation was estimated from IFU spectra outside an aperture of $r \geq 7$ spaxels around the UCD's centre and the 14 dedicated sky fibres. These spectra were averaged using the IRAF task SCOMBINE with a 3σ-clipping rejection of outliers. The resulting master sky was then subtracted from all ARGUS spectra of that observation using the IRAF task SKYTWEAK and allowing for residual shifts in the wavelength calibration. Using the IRAF package ONEDSPEC the spectra from the individual observations were corrected for heliocentric velocities and the observations from all nights were resampled to a common logarithmic wavelength scale. The ARGUS spectra were then organised into three-dimensional data cubes with two spatial dimensions corresponding to the position on the sky and one wavelength dimension.

2.2.2 Combination of data cubes and spatial binning

Preserving spatial resolution is crucial to our goal of resolving the kinematics of UCD3. In order to prevent a blurring of the spatial information when combining the different observations, accurate information of their relative positions on the sky is required. Moreover, we need to quantify the spatial resolution, i.e. the seeing, of the individual observations. An estimate of the FWHM of the seeing measured by the DIMM of the VLT is recorded in the fits headers of each data frame and is given in the third column of Table 2.1. However, Sarazin et al. (2008) showed that the DIMM seeing can significantly differ from the actual seeing inside the UT2 dome. While the observing

[2] available online at `http://girbldrs.sourceforge.net`

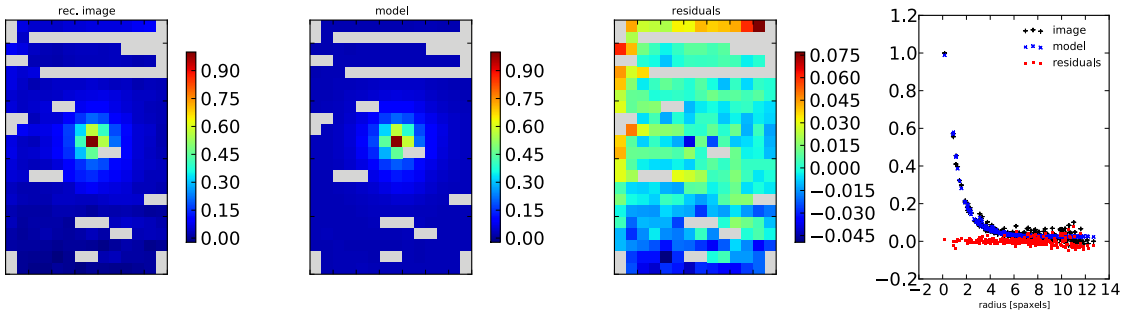

Figure 2.1: An example of the forward-modelling used to determine the centroid and PSF of our observations. The reconstructed image, i.e. the sum of the data cube along the wavelength dimension, of one observation is shown in the first panel. Individual pixels correspond to the 14×22 spaxels of ARGUS, grey pixels reflect bad spaxels. The second panel shows the best-fitting model consisting of an ACS/HRC image that was convolved with a Gaussian PSF and integrated over the ARGUS spaxels, and a constant sky background. The difference of the reconstructed image and the model is shown in the third panel. The right panel shows the pixel values of the reconstructed image, the model image and the residuals as a function of radius from the inferred UCD centre. The model reproduces the observations very well. The larger deviations at the top of image are cause by a 'glow' feature that affects spectra at one edge of the FLAMES CCD (cf. the FLAMES User Manual).

astronomers fortunately included a raw estimate of the seeing based on the UT2 guide probe in the observational logs of all but one of our observations (fourth column of Table 2.1), an objective measurement of the PSF is clearly preferable.

To measure accurate centroids and the PSF of our observations, we modelled the reconstructed images, i.e. the data cubes collapsed along the wavelength dimension. The model consisted of an HST/ACS high resolution channel (HRC) image in the F606W filter (shown in the upper left panel of Figs. 2.3 and 2.4 and obtained in HST programme 10137; Evstigneeva et al. 2007) that we convolved with a Gaussian PSF and then rebinned to the IFU's spatial scale. The use of an actual image as basis for the modelling, instead of the intrinsic surface brightness profile of the UCD (Evstigneeva et al. 2007), has the advantage that it also includes the background object (see Section 2.5) that is apparent as an irregular structure towards the south of UCD3. The PSF of the HST with a FWHM of ~ 0.1 arcsec is small compared to that of our observations and the F606W filter of the ACS/HRC covers the wavelength range of our observations, although it extends further to the red. Therefore, the ACS/HRC image can be thought of as a version of our reconstructed images seen without the 'convolution' by the earth's atmosphere. Figure 2.1 shows an example of this modelling, where the position in x- and y- direction, the FWHM of the Gaussian PSF and a constant background level were varied as free parameters. The first three panels show the reconstructed image, the best-fitting model image and the residuals. Grey pixels in the images correspond to bad spaxels that will be discussed further below. The right panel shows the pixel values of these three images as a function of radius from the inferred UCD centre. The small residuals show that the model reproduces our observations quite well. The inferred best-fitting PSF FWHM for each observation is given in the last column of Table 2.1.

Based on the measured seeing, we chose the six observations with best seeing, $0.50 \leq$ PSF FWHM ≤ 0.67 arcsec, with a mean of 0.60 arcsec. These observations are indicated by bold face in Table 2.1. We stacked these data cubes by resampling them to a common coordinate grid, at the same time removing the effect of atmospheric dispersion as we will describe in the following.

Atmospheric dispersion is caused by the variation of the refractive index of air with wavelength. It results in a wavelength-dependent offset of the apparent position of an observed object

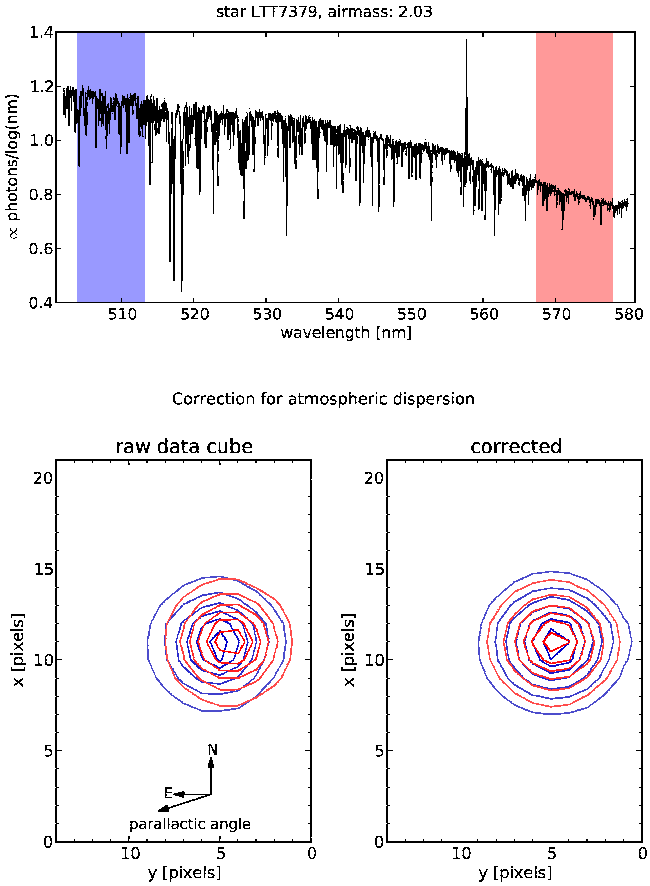

Figure 2.2: A test of the removal of differential atmospheric refraction using a star that was observed at a airmass of ~ 2. Upper panel: The spectrum of the star obtained by summing over all spaxels in the data cube. No sky-subtraction was done for this experiment, as evident from the presence of the strong 5577 Å OI emission line. The blue and red shaded areas are the wavelength ranges used for the reconstructed images in the lower panels. Lower panels: The left panel shows isophotes of the reconstructed images obtained by summing the original data cube over the wavelength ranges indicated in the upper panel. It is obvious that the redder and bluer image are offset relative to each other in the direction of the parallactic angle that is indicated at the bottom of the panel. The right panel shows the isophotes obtained in the same wavelength ranges from a data cube that was corrected for atmospheric dispersion. The offset is no longer present, illustrating that the correction works very well.

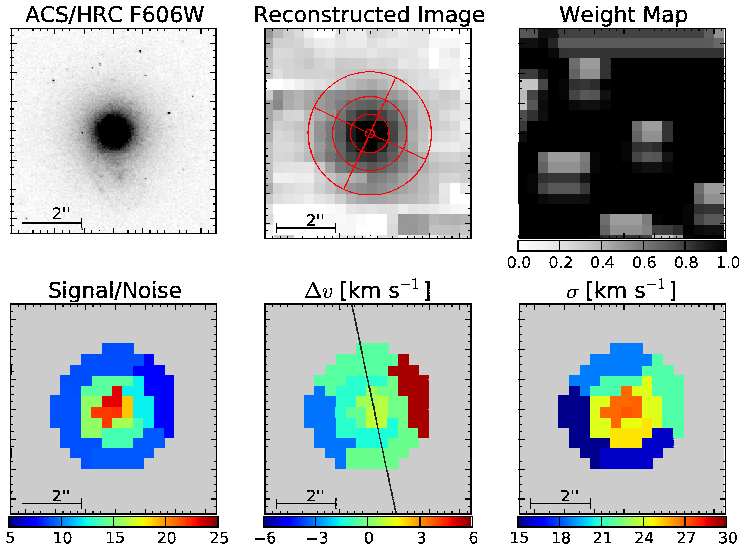

Figure 2.3: The upper row shows an ACS/HRC F606W image of the UCD, the image reconstructed from the merged data cube and the weight map, which illustrates the effect of bad spaxels in the input data cubes. The polar grid overlaid on the reconstructed image indicates the subdivisions used for the spatial binning of the spaxels. The position angle of the quadrant subdivisions was chosen such that the rotation of the UCD is visible. The bottom row shows the mean signal to noise ratio in each spatial bin per spectral bin (of 11 km s $^{-1}$ or ~ 0.2 Å), the recovered velocity field with a line indicating the axis of rotation (see Section 2.4.1) and the velocity dispersion map. The extraction of the kinematics will be described in Section 2.3. The scale of the images is indicated by the 2 arcsec scale bar at the lower left, 1 arcsec corresponds to ~ 92 pc at the distance of the Fornax cluster.

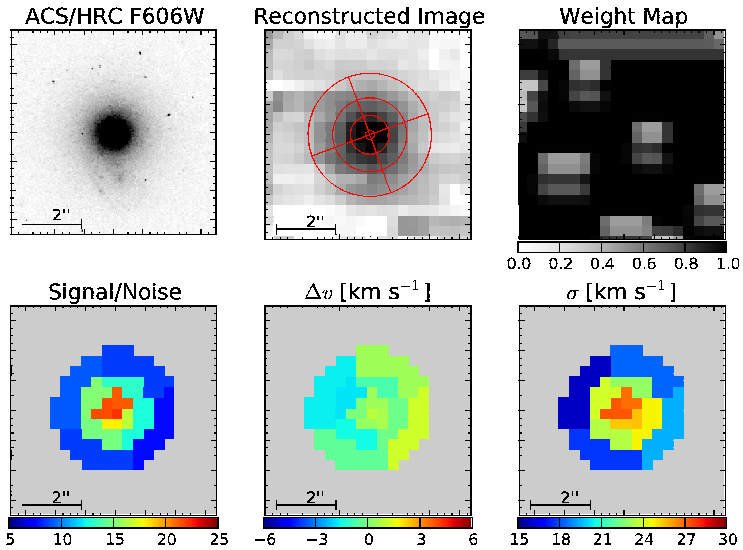

Figure 2.4: Same as Fig. 2.3, but for a binning rotation differing by 45 degrees from the one used in Fig. 2.3. It can be seen that the velocity map is almost flat when spaxels are combined in this orientation.

in the direction of the parallactic angle. To remove this curvature from our data cubes, we used the empirical relation given by Filippenko (1982) for the angular offset as a function of wavelength, airmass (< 1.1 for all of our observations), and the temperature, pressure, and water vapour pressure of the atmosphere. The airmass, and the ambient temperature and pressure are recorded in the fits file headers of VLT observations. For the water vapour pressure, we used a generic value of 7 mm Hg. For our observations, we calculated the spatial offset between the minimum and maximum wavelengths to be $\leq$0.5 spaxels, or ≤ 0.26 arcsec. This is small, but is on a scale comparable to that of the PSF. Therefore, when resampling the data cubes to a common spatial grid, we shifted the position of each spatial slice (i.e. a slice of constant wavelength) in the direction of the parallactic angle according to the Filippenko (1982) relation.

The effect of atmospheric dispersion is stronger for a higher airmass. To test the correction routine in a case where a the effect is more clearly visible, we queried the ESO archive for stars observed with ARGUS in the same setup as our observations, but at high airmass. Fig. 2.2 illustrates the correction for one such star, LTT 7379, that was observed at an airmass of ~ 2. The top panel of Fig. 2.2 shows the spectrum obtained by combining all spaxels in the observation. The lower panels of Fig. 2.2 show the isophotes of two passbands, a bluer and a redder passband that are also indicated by the shaded regions in the upper panel. Before the correction (lower left panel), it is evident that the blue and red portion of the image of the star are offset by ~ 1 spaxel or ~ 0.52 arcsec in the direction of the parallactic angle (represented by the vector at the bottom of the panel). The right lower panel of Fig. 2.2 shows the situation on the data cube after the correction for atmospheric dispersion, where the positions of the blue and red portion of the stellar image coincide. This demonstrates that the correction routine works very well.

The actual resampling of our observed data cubes was done using the drizzle algorithm (Fruchter & Hook 2002) implemented in the IRAF task IMLINTRAN by treating each spatial slice of the data cubes as an image. The drizzle algorithm, in its simplest form, is based on the assumption that the flux across a pixel is constant. It calculates the fraction of the area of a given input pixel that overlaps with a given output pixel and adds the same fraction of the flux of the input pixel to the output pixel. For input and output pixels of equal size, the maximum number of input pixels that can contribute to an output pixel is four, making the drizzle algorithm very locally confined. Given our goal of preserving spatial information, this property is an advantage over more sophisticated higher order interpolation schemes, where the value of an output pixel may depend on the values of input pixels further away. Moreover, the simplicity of drizzle allows for a straight-forward treatment of bad spaxels. These bad spaxels comprised a hot column on the detector (see the Flames User Manual), as well as spectra that were strongly affected by the stray light from neighbouring simultaneous calibration lamp spectra. To treat bad spaxels properly as 'missing data' we set their value to 0 in the input data cubes and created weight cubes with a value of 1 in good spaxels and 0 in bad spaxels. These input weight cubes were then resampled and stacked in the same way as the data cubes and the resulting combined weight cube was divided into the combined data cube. This division by the weight cube is analogous to e.g. a weighted mean and ensures the correct weighting of the relative contributions of the input data cubes in the presence of bad spaxels.

To minimise the loss of spatial resolution due to resampling, we chose a moderate amount of super-sampling by using output pixels smaller by a factor of 1.5 on each side. The upper middle and right panels Fig. 2.3 show the reconstructed images of the resulting combined data and weight cubes. Due to pointing offsets between the individual observations, and due to the removal of atmospheric dispersion, the bad spaxels that are apparent in the individual data cubes (see Fig. 2.1) are partially filled in the combined data cube.

Since the spectra in individual spaxels can be very noisy, especially in the outer regions of the UCD, it is beneficial for the measurement of the kinematics to combine neighbouring spectra. A

commonly used technique to group spaxels in IFU observations is the adaptive Voronoi tessellation described by Cappellari & Copin (2003). This procedure groups spectra together in locally confined, compact spatial bins such that each bin reaches a specified minimum signal to noise ratio (S/N). However, the steeply declining luminosity profile of the UCD causes an equally steep decline in S/N. When applied to our data, Voronoi binning therefore produces spatial bins that are aligned radially around the centre: one inner spaxel contributes most of the signal, and outer spaxels that are added to the given bin to achieve a compact shape. Therefore, the Voronoi binning scheme is only of limited use, as we are interested in the radial variation of the UCD's kinematics, rather than their azimuthal variation. After some experimentation, we chose a simple geometrical scheme for binning the limited number of spaxels receiving significant flux from the UCD: the spaxels were grouped into radial annuli, which in turn were subdivided into quadrants. This is shown as red polar grid overlaid on the reconstructed image in Figs. 2.3 and 2.4. While this scheme cannot avoid a decrease in S/N with radius (see the lower left panels of Figs. 2.3 and 2.4), it preserves radial resolution and produces bins that are spatially confined in accordance with the reasoning that neighbouring regions of the UCD should have similar spectra. Moreover, the subdivision of the annuli into quadrants allows a cross-check in the extracted kinematics, as different quadrants in the same annulus should give similar velocity dispersions.

2.3 Kinematic Measurements

The kinematics were recovered from each spectrum using the penalised pixel-fitting (PPXF) code of Cappellari & Emsellem (2004). The code fits the observed spectra with a linear combination of template spectra that are convolved with a trial line-of-sight velocity distribution (LOSVD) which is parametrised as Gauss-Hermite series (van der Marel & Franx 1993). Given the moderate S/N of our spectra, we chose to extract only the first two moments of the LOSVD, the velocity v and velocity dispersion σ. As spectral templates for the fitting we used spectra of field stars and members of the NGC 6475 open cluster from the UVES Paranal Observatory Project (UVESPOP, Bagnulo et al. 2003) library. The library consists of reduced and calibrated high-resolution ($R \sim 80000$) stellar spectra recorded with VLT/UVES (Dekker et al. 2000) and spanning a range of spectral-types and metallicities. We used a sub-sample of 46 late-type stars (spectral types F0 to M1, luminosity classes II-V), of which the ppxf algorithm would select a subset of $\lesssim 8$ significant templates during the fitting of each observed spectrum.

The spectra were brought to a common radial velocity and rebinned to the same logarithmic wavelength scale as our ARGUS data. To degrade the template library to the resolution of our observations, we constructed an empirical model of the spectral line-spread function (LSF) as a function of wavelength (e.g. Chilingarian et al. 2007) and convolved the UVESPOP templates with this LSF. The empirical LSF was measured using PPXF to fit UVESPOP templates to the spectra the late-type stars that were observed with the ARGUS LR04 setup and we reduced and processed in the same way as our observations of UCD3. The determined LSF is shown in Fig. 2.5. From top to bottom, the panels show the shift in velocity Δv, the velocity dispersion σ and the h3 and h4 moments of the ARGUS LSF. Red crosses correspond to the results from the individual late-type stars, black squares and error bars correspond to the mean and standard deviation of these measurements. The shift in velocity Δv in velocity is consistent with zero over the entire wavelength range, indicating that there is no distortion between the wavelength calibrations of the ARGUS stars and UVESPOP templates. The deviations of h3 and h4 from zero suggest small deviations from a Gaussian instrumental profile. The mean of the velocity dispersion moment of the LSF is $\sigma \sim 15\,\mathrm{km\,s^{-1}}$, which implies an effective resolution of the ARGUS LR04 setting of R $\sim$ 8600, somewhat smaller than the R $\sim$ 9600 specified in the instrument manual. This is likely a conse-

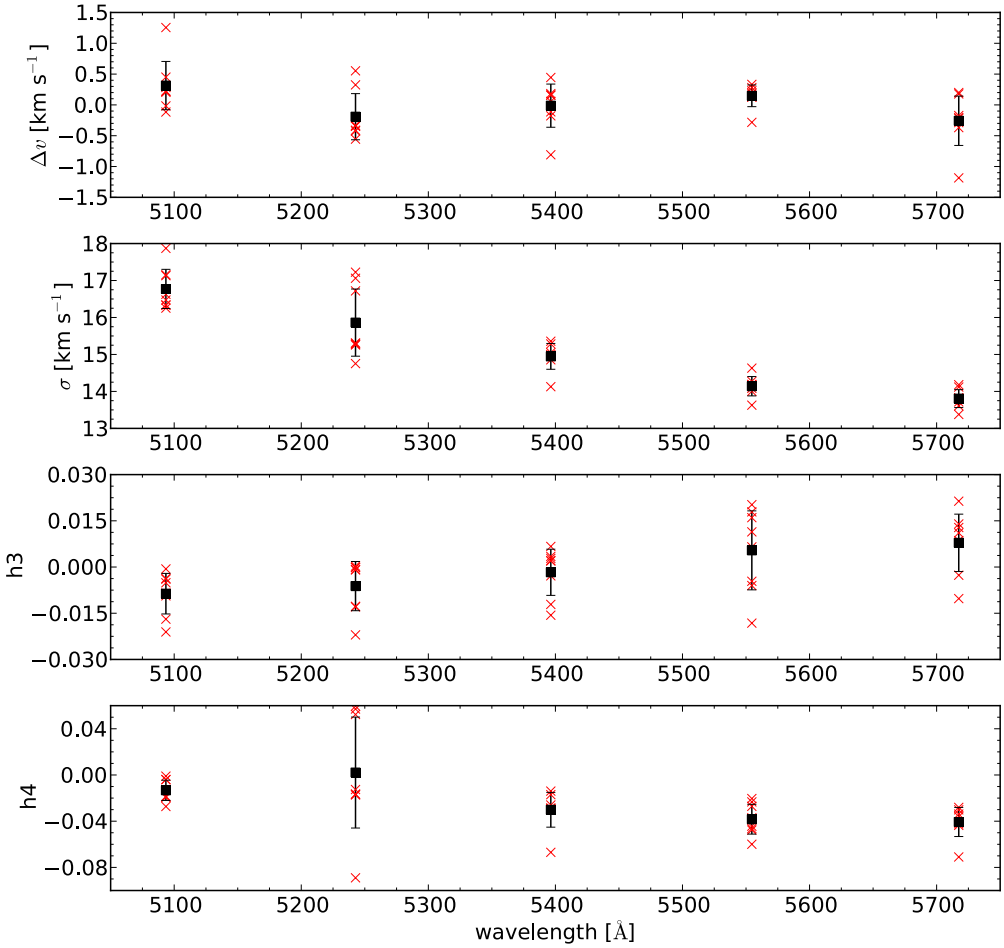

Figure 2.5: The moments of the line-spread function of the ARGUS LR04 as a function of wavelength measured in wavelength intervals that divide the covered wavelength range (5015−5831 Å) into five equally spaced regions. From top to bottom, the panels show the shift in velocity Δv, the velocity dispersion σ and the h3 and h4 moments of the ARGUS LSF. The LSF was determined by fitting late-type stars observed with ARGUS with UVESPOP template spectra. Red crosses correspond to the results from individual stars. The means and standard deviations of these measurements are shown as black squares and error bars, respectively. The mean LSF was used to bring the UVESPOP template library to the same instrumental resolution as our observations.

quence of the broadening introduced in the processing of the spectra, since any resampling of the data degrades their resolution. During the pipeline extraction the spectra were resampled once in order to bring all spectra of a given observation to a common wavelength sampling. The spectra were resampled once more, when bringing the spectra of all observations to a common logarithmic wavelength scale.

PPXF performs a χ^2 minimisation and therefore requires an estimate of the uncertainties of the observed spectra. The magnitude of the noise in our spectra varied gradually with wavelength. Therefore it was modelled by using the DER_SNR algorithm (Stoehr et al. 2007) to estimate the noise at each wavelength and then fitting a linear function to these estimates. The resulting noise spectra are shown as green lines in the spectra in Figs. 2.6 and 2.7. They were used as an input for ppxf to ensure the correct relative weighting of pixels in the χ^2-minimisation. They were also used as the basis for generating 100 Monte Carlo realisations of each spectrum by adding random noise with a normal distribution with a dispersion equal to the noise spectra. These Monte Carlo realisations were then fit with PPXF and uncertainties on the measured velocity and velocity dispersion for each spectrum were obtained as the standard deviations of these quantities in the 100 realisations.

The fitting was done in the wavelength range from 5156 Å to 5691 Å. We masked out spectral regions containing a strong emission line doublet in some of the spaxels, most likely originating from a background galaxy slightly offset from the UCD's position (cf. Section 2.5; Evstigneeva et al. 2007), the imperfectly subtracted 5577 Å OI sky line, as well as regions particularly affected by the calibration lamp stray light. For consistency the same mask (represented by the grey wavelength intervals in Figs. 2.6 and 2.7) was applied to all spectra, regardless of whether they were affected by these blemishes or not.

The spectra and best-fitting models in all of the 13 spatial bins are shown in Fig. 2.6 (for the central spaxel and inner spatial bins) and Fig. 2.7 (for outer spatial bins). The left panels of each row show the observed spectrum (black curve), the best-fitting model (blue curve), and a fourth order multiplicative polynomial used in the fit to absorb the relative flux calibration of our observations and the UVESPOP spectra. The residuals from the fits are shown as grey curves at the bottom of the left panels, green lines indicate the uncertainties according to the noise model described above. Wavelength ranges shaded grey correspond to regions that were masked out in the fit. The right panel of each row shows the spaxels that were combined in the given spatial bin to produce the spectrum.

The signal to noise ratio of our spectra decreases with increasing radius (see the S/N maps in Figs. 2.3 and 2.4). In order to test whether this causes a systematic bias in the extracted kinematics, we degraded the spectrum of the central spaxel to lower S/N levels by adding Gaussian noise with an amplitude determined by the noise model described above. Figure 2.8 shows the velocity (upper panel) and velocity dispersion (lower panel) extracted from the resulting spectra. Black squares correspond to the mean of the results from 100 different realisations at a given S/N level, error bars indicate the standard deviation of these 100 results. The relative velocity and the velocity dispersion of the original spectrum are indicated by blue dashed lines. Reassuringly, the extracted kinematics do not depend on the signal to noise level down to a S/N of 3, which is by a factor of two lower than the lowest S/N (~ 7) in our spectra.

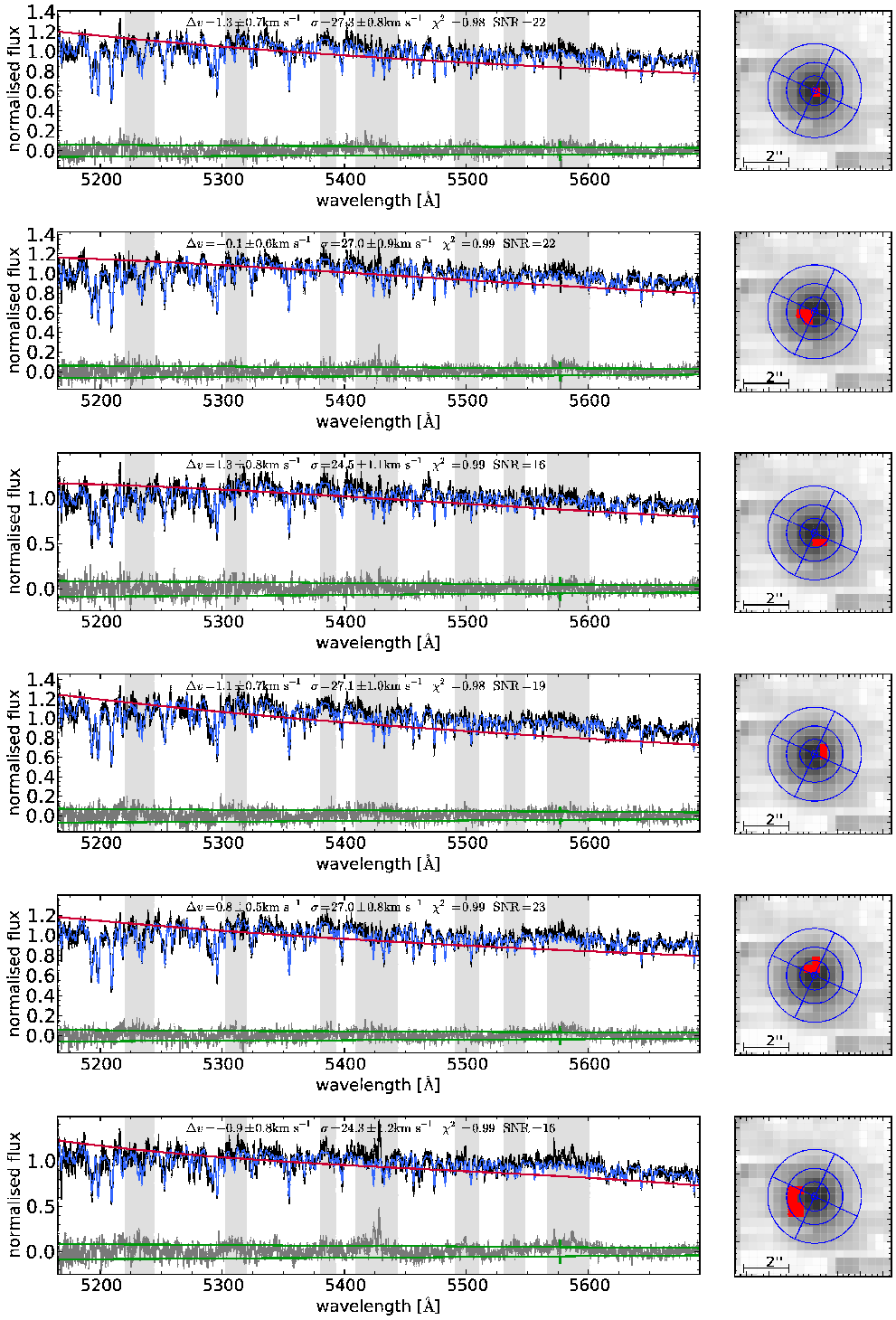

Figure 2.6: Left panels: The observed spectrum (black curve), best-fitting model (blue curve), fourth order multiplicative polynomial (red curve) used in the fit, residuals (grey curve) and modelled amplitude of the noise (green curve). Grey regions were masked out in the fitting. The best-fitting velocity (relative to the mean velocity of the UCD) Δv, velocity dispersion σ, χ^2 of the fit and S/N of the spectrum are reported at the top. Right panel: The spaxels that were combined to produce the observed spectrum are shown in red and overlaid on the reconstructed image. The corresponding binning scheme is indicated by the blue polar grid.

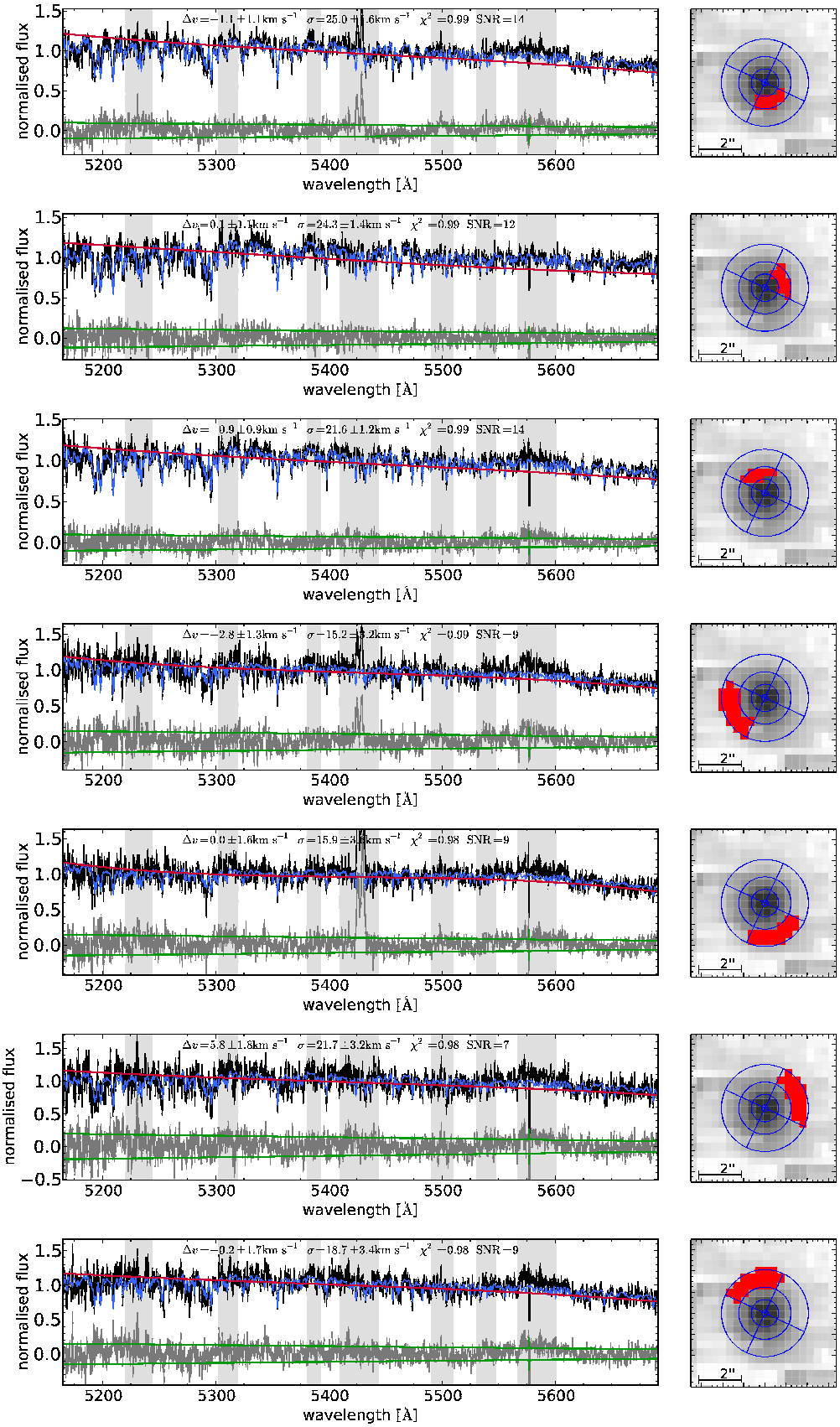

Figure 2.7: Same as Fig. 2.6, but for spectra in the outer two annuli of our geometrical binning scheme.

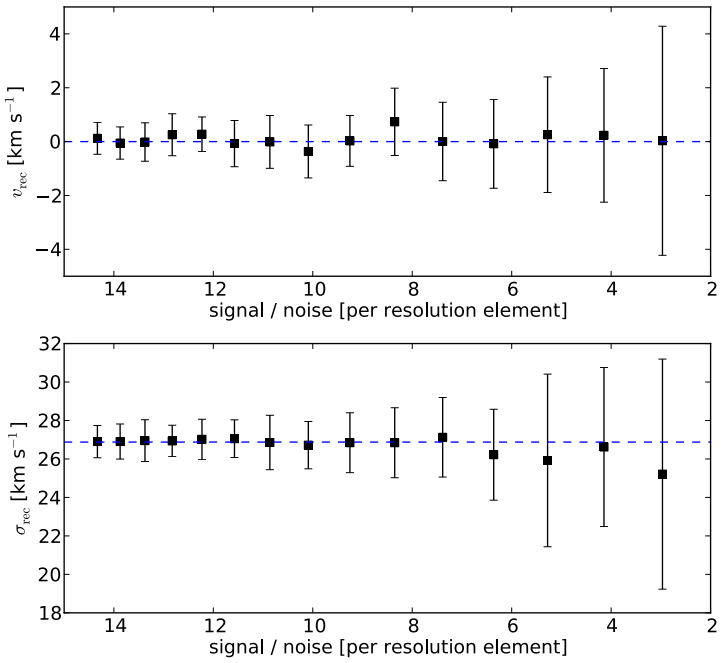

Figure 2.8: A test of the dependence of extracted velocity (upper panel) and velocity dispersion (lower panel) on the signal to noise ratio. The means and standard deviations of the results of 100 realisations per S/N level are shown as black squares and error bars. Dashed lines indicated the relative velocity and the velocity dispersion of the original spectrum. The results indicate that there is no systematic bias of the extracted kinematics down to a S/N of 3.

2.4 Internal Dynamics

2.4.1 Rotation

The velocity field of the UCD shows the signature of weak rotation. To recover the projected kinematic axis, we initially varied the position angle of the quadrants in the spatial binning. The second panels in the bottom rows of Fig. 2.3 and Fig. 2.4 show the velocity map obtained in binning orientations rotated by 45 degrees with respect to each other. In Fig. 2.3, the binning sectors are aligned so that the rotational axis lies approximately along the centre of two opposing sectors. In Fig. 2.4, the rotational signal is suppressed as the rotational axis approximately coincides with one of the azimuthal subdivisions. Once the approximate orientation of the rotational axis was found, a sinusoid of the form

$$v(r) = v_0 + A\sin(\phi - \mathrm{PA}) \tag{2.1}$$

was fitted simultaneously to the velocities recovered from that orientation and from the quadrants rotated by 45 degrees. This is shown in the left panel of Fig. 2.9. In Eq. (2.1), v_0 is the systemic velocity, A is the amplitude of the rotation, ϕ is the azimuth of each bin, and PA is the position angle of the rotational axis. In the outer annulus (r$\geq$ 1.2 arcsec; upper left panel of Fig. 2.9), the fit yielded a PA of 12 ± 15 degrees and an amplitude of 2.8 ± 0.7 km s^{-1}. Due to the unknown inclination of the rotational axis and due to the fact that the maximum of the rotation curve velocity need not be reached at r$\sim$ 1.5 arcsec, this represents a lower limit on the true rotational velocity. The rotation curve of the UCD along the approximate direction of the maximum gradient is shown in the right panel of Fig. 2.9.

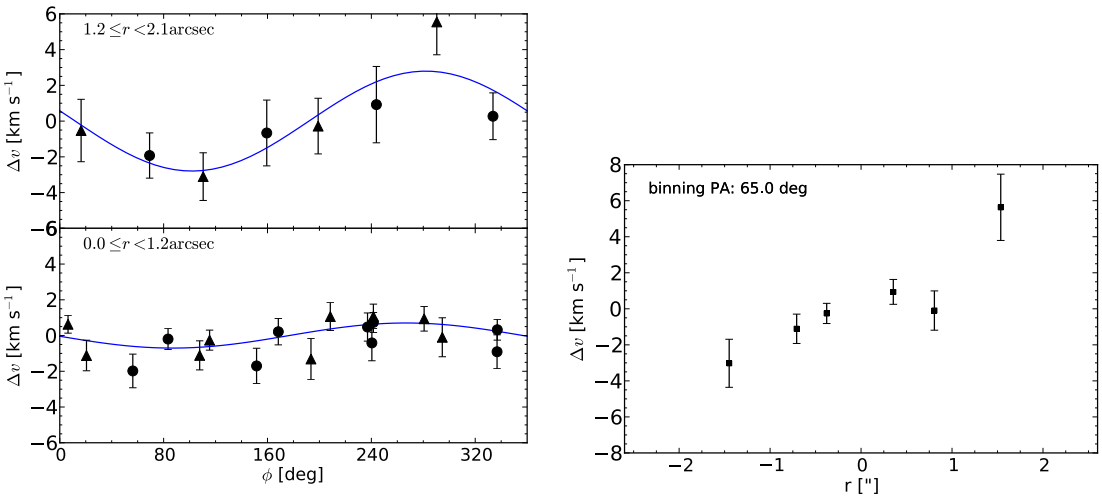

Figure 2.9: The signature of rotation in the UCD. Left: The top panel shows the measured velocity versus the luminosity-weighted azimuth ϕ of each bin in the outer annulus (r$\geq$ 1.2 arcsec) of the spatial binning shown in Fig. 2.3 (triangles) and the binning orientation with quadrants rotated by 45 degrees shown in Fig. 2.4 (circles). The blue curve represents the best-fitting sinusoid (Eq. (2.1)) to the velocities measured in both orientations of the quadrants (i.e. triangle and circle symbols). The bottom panel shows the same for the inner annuli (r$<$ 1.2 arcsec). Right: The rotation curve of the UCD along the direction approximately perpendicular to the kinematic axis.

2.4.2 Dispersion profile

The velocity dispersion profile of UCD3, i.e. the measured velocity dispersion versus the luminosity-weighted radial coordinate of each spatial bin, is shown as black squares in Fig. 2.10. Except for the innermost radius, where there is only one spaxel, the four measurements at a given radius correspond to the four quadrants in a given annulus. The velocity dispersion decreases continuously with increasing radius. There is no sign of a disturbed profile, or for an increase of the dispersion at large radii, which could have been expected if the unbound stars were present due to a recent tidal interaction of the UCD, a scenario proposed to explain the high dynamical masses of some UCDs (cf. Section 1.2.3; Fellhauer & Kroupa 2006).

Along with the observed velocity dispersion profile, Fig. 2.10 shows a model assuming that mass follows light. Open black circles correspond to the model prediction in the radial annuli of our binning, the solid black curve simply connects these model points for clarity.

The model shown here and in the following are based on the best-fitting two-component luminosity distribution determined by Evstigneeva et al. (2007), a Fornax cluster distance of 18.97 Mpc (Freedman et al. 2001) and assuming an isotropic velocity distribution and spherical symmetry. They were constructed using the code described in Hilker et al. (2007). The code takes into account the convolution with the seeing PSF and predicts the full line-of-sight velocity distribution (LOSVD) in each of our radial annuli. Briefly, the code deprojects the input surface density profile into a three-dimensional density profile using Abel's integral equation. It then calculates the cumulative mass function M($< r$), and the potential energy $\phi(r)$, and from these the energy distribution function assuming isotropic orbits for the stars. It then creates an N-body representation (populated with 10^5 test particles) of the UCD using the deprojected density profile and the distribution function. These test particles are then convolved with a Gaussian corresponding to the estimated seeing PSF and the fractions of the Gaussians that fall into a each annulus of our binning scheme are calculated. Using these fractions as weighting factors for the velocities of the test particles, the

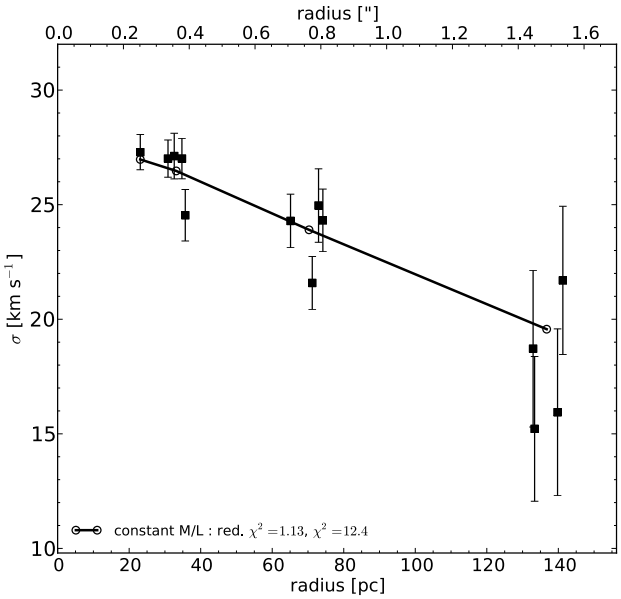

Figure 2.10: The observed velocity dispersion profile and a mass model assuming a constant mass to light ratio. Squares represent the measured velocity dispersions and their uncertainties. The best-fitting constant mass to light ratio model, evaluated in the radial annuli of our binning scheme is shown as open circles, connected by a solid line for clarity. The model shows very good agreement with the data, as is also indicated by a reduced χ^2 (see text) of 1.13.

code calculates the line-of-sight velocity distribution in each radial annulus.

While our measurement of the observed velocity dispersion assumed a Gaussian LOSVD, the actual LOSVD need not be strictly Gaussian. In the case of the models including a massive black hole (see Section 2.4.3), where a significant fraction of the observed stars move in the potential of the central point source, the integrated velocity distribution can even become highly non-Gaussian (cf. Merritt et al. 2009). The modelled LOSVDs in the four annuli based on a model including a massive black hole with a mass of 10 per cent of the UCD's stellar mass are shown in the left panels of Fig. 2.11. From top to bottom, the panels correspond to annuli in order of increasing radius. Black curves show the LOSVDs predicted by the model. The red curve shows a Gaussian with a dispersion equal to that of the LOSVD. Compared to this Gaussian, the LOSVDs in the inner two annuli (upper two panels), where the influence of the black hole is significant, show a more acute peak at the mean systemic velocity.

We modelled the effect introduced by the assumption of a Gaussian LOSVD in our kinematic measurements, while the actual LOSVD may be non-Gaussian. For this, we created artificial spectra by convolving UVESPOP template spectra with the full modelled LOSVDs predicted in each annulus and measured the velocity dispersion in the same way as for the observed spectra. The recovered velocity dispersions are shown as a function of the signal to noise ratio in the right panels of Fig. 2.11. For each signal to noise level, we created 100 artificial spectra by adding normally distributed noise to the original convolved spectrum. For each set of 100 realisations, the mean and standard deviation of the recovered velocity dispersions are shown as black squares and error bars, respectively. The dashed red lines indicate the dispersions of the original modelled LOSVD. It can be seen, that the velocity dispersion that is measured assuming a Gaussian LOSVD may differ significantly from the dispersion of the intrinsic LOSVD, if the latter deviates from Gaussianity.

We performed simulations analogous to the one shown in Fig. 2.11 for all our models. This

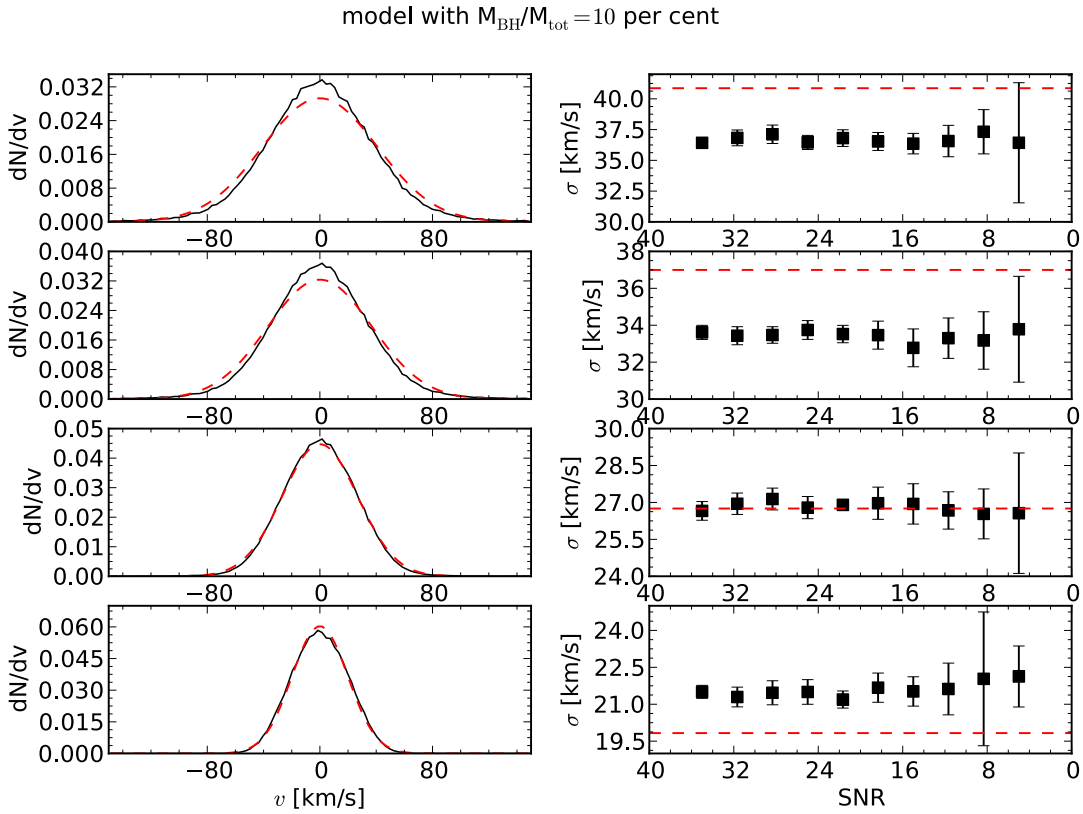

Figure 2.11: An illustration of the post-processing of the modelled intrinsic LOSVDs. This step was done to obtain the velocity dispersion that would be measured with our data for given intrinsic LOSVD. Shown is the case of the model containing a black hole with 10 per cent of the UCD's mass (see Section 2.4.3). In order of increasing radius from top to bottom, the panels correspond to the radial annuli, in which we measured the kinematics. The left panels show the modelled LOSVD as black solid curves. Red dashed curves represent Gaussians with the same dispersion as the intrinsic LOSVD. The right panels show the velocity dispersion that was measured from template spectra that were convolved with the intrinsic LOSVD, as a function of signal to noise of these convolved spectra. Black squares represent the mean of 100 Monte Carlo realisations of each spectrum at a given signal to noise level, error bars correspond to the standard deviation of these 100 realisations. Dashed red horizontal lines show the dispersion of the input LOSVD and correspond to the Gaussians shown as red dashed curves in the left panels. The recovered velocity dispersion differs from the dispersion of the intrinsic LOSVD, if the latter deviates from a Gaussian shape. This is most obvious om the inner two radial annuli (upper two panels), where the influence of the massive black hole is strongest. No significant trend with the signal to noise ratio is seen.

produces modelled velocity dispersion profiles as they would be measured for a given mass model. The results of these simulations were used in all comparisons of the observed and modelled velocity dispersion profiles, such as the model points shown by open circles in Fig. 2.10.

Using the fact that the velocity dispersion σ scales with the mass as $\sigma^2 \propto \mathrm{M}$ (virial theorem), the best-fitting mass (or equivalently the best-fitting M/L, for a given observed luminosity L) for each model was calculated by scaling the model to the data (cf eq. 51 given by Cappellari 2008), so that

$$\chi^2 = \sum_i (\sigma_{\mathrm{m,i}} - \sigma_{\mathrm{obs,i}})^2 / (\Delta^2_{\mathrm{obs,i}}) \tag{2.2}$$

is minimised, where $\sigma_{\mathrm{obs,i}}$ are the observed velocity dispersions, $\Delta_{\mathrm{obs,i}}$ are their associated uncertainties and $\sigma_{\mathrm{m,i}}$ are the velocity dispersions that would be measured for a given mass model at the same radii.

Confidence regions around the best-fitting parameters were estimated from the increase in the χ^2 compared to its minimum value. For one parameter of interest, the 68, 90 and 99 per cent confidence regions are given by an increase $\Delta\chi^2 = \chi^2 - \chi^2_{\mathrm{min}}$ of 1, 2.71 and 6.63, respectively (e.g. Press et al. 2007). For an arbitrary $\Delta\chi^2$, the confidence level can be found by numerical integration of the χ^2 distribution function.

The simplest possible model, assuming that mass follows light (or equivalently, a constant M/L), which is shown as black solid line in Fig. 2.10, provides an excellent fit to the observed dispersion profile. With this model, the best-fitting mass of the UCD is $\mathrm{M} = 8.2 \pm 0.2 \times 10^7\,\mathrm{M}\odot$, which corresponds to a mass to light ratio of $\mathrm{M}/\mathrm{L}_{V,\mathrm{dyn}} = 3.6 \pm 0.1\,\mathrm{M}_\odot\,\mathrm{L}_\odot^{-1}$.

The M/L is in good agreement with the stellar population M/L_V of $3.7 \pm 0.2\,\mathrm{M}_\odot\,\mathrm{L}_\odot^{-1}$ that was recently measured via the fitting of synthetic spectra to observations by Chilingarian et al. (2011). However, regarding the stellar population M/L of UCD3, we note that there is a disagreement on the age of UCD3 in the literature: Lick/IDS absorption indices suggest an age of $\sim 2-5\,\mathrm{Gyr}$ (Mieske et al. 2006a; Firth et al. 2009). This would render UCD3 one of the youngest known UCDs and imply a stellar $\mathrm{M}/\mathrm{L}_V \lesssim 2\,\mathrm{M}_\odot$, which in turn would still require a substantial amount of dark mass according to our measured dynamical $\mathrm{M}/\mathrm{L}_{V,\mathrm{dyn}}$. On the other hand, studies based on spectral fitting yield ages of $\gtrsim 12\,\mathrm{Gyr}$ (Chilingarian et al. 2008a, 2011), placing UCD3 within the typical range of ages found for most UCDs, which would make our dynamical $\mathrm{M}/\mathrm{L}_{V,\mathrm{dyn}}$ fully consistent with a standard stellar mass function and no dark mass. As a possible cause for the discrepant ages, Firth et al. (2009) point out that the young age inferred from absorption indices could be an artifact introduced by the presence of hot horizontal branch stars.

2.4.3 Constraints on the non-luminous matter content

Dark matter

As a possible explanation for the, on average, high dynamical mass to light ratios of UCDs, a substantial dark matter content is discussed in the literature (e.g. Haşegan et al. 2005; Baumgardt & Mieske 2008). A potential formation channel would then be the tidal stripping of nucleated galaxies, leaving behind a remnant nucleus with properties comparable to those of a UCD (Bekki et al. 2003). Simulations show that the resulting UCDs can be dark matter dominated, if the central concentration of dark matter was enhanced prior to the stripping through, for example, the adiabatic infall of gas (Goerdt et al. 2008; Baumgardt & Mieske 2008).

In order to test this scenario, we included in the mass model a dark matter component with a density profile mimicking the dark matter distribution predicted for the final evolutionary stage by the simulations of Goerdt et al. (2008). Their fig. 5 shows a final dark matter density approximately proportional to $r^{-2.5}$ for radii $200\,\mathrm{pc} \lesssim r \lesssim 2\,\mathrm{kpc}$. We chose as an analytic expression in our model

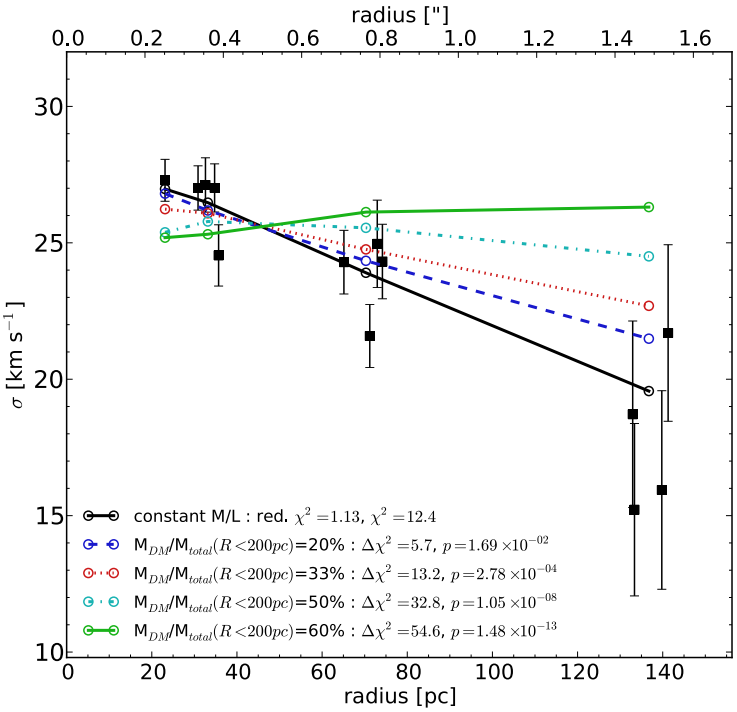

Figure 2.12: Comparison of the observed velocity dispersion profile (black squares) with models including a dark matter halo with a radial density profile of the shape given in Eq. (2.3). The blue dashed, red dotted, cyan dash-dotted and green solid curves represent the best-fitting models with a dark matter fraction of 20, 33, 50 and 60 per cent within a three-dimensional radius, respectively. The solid black curve shows the constant M/L model without dark matter. The difference in χ^2 with respect to this best-fitting model, $\Delta\chi^2$, along with the resulting probability for the model to represent the data is reported in the legend for each model. The best-fitting mass to light ratios are 3.4 ± 0.1, 3.24 ± 0.08, 2.85 ± 0.07, and $2.67\pm0.07\,M_\odot\,L_\odot^{-1}$ for $M_{DM}/M_{total}(R<200pc)$ of 20, 33, 50 and 66 per cent, respectively. It is obvious that the radial velocity dispersion profile predicted in the presence of dark matter is shallower than the observed profile.

a density profile of the form

$$\rho(r) = \rho_0(1+r^2/r_s^2)^{-1.25}, \tag{2.3}$$

where r is the three-dimensional radius, which shows the same slope at large radii and converges to a central density ρ_0 at $r=0$. As a scale radius we adopted $r_s = 200\,\mathrm{pc}$, which is the approximate radius below which the profile in the simulations of Goerdt et al. (2008) starts to flatten.

Models calculated for different fractions of dark matter within a three-dimensional radius of 200 pc are shown in Fig. 2.12. The blue dashed, red dotted, cyan dash-dotted and green solid curves represent a dark matter fraction of 20, 33, 50 and 60 per cent, respectively. The constant M/L model from Fig. 2.10 is shown for comparison as solid black curve. As expected, an extended dark matter halo causes a shallower velocity dispersion profile. All of the dark matter models reproduce the observations worse than the mass follows light model. The increase in χ^2 with respect to the latter model, $\Delta\chi^2$, as well as the corresponding probabilities are reported in the legend of Fig. 2.12. The model with a dark matter fraction of 20 per cent is compatible with the data at the 3σ level. For this model, the best-fitting mass to light ratio is $M/L_{V,\mathrm{dyn}} = 3.4\pm0.1\,M_\odot\,L_\odot^{-1}$ and the stellar mass is $M_{\mathrm{stellar}} = 7.6\times10^7\,M_\odot$. As mentioned above, age estimates of UCD3 in the literature are discrepant.

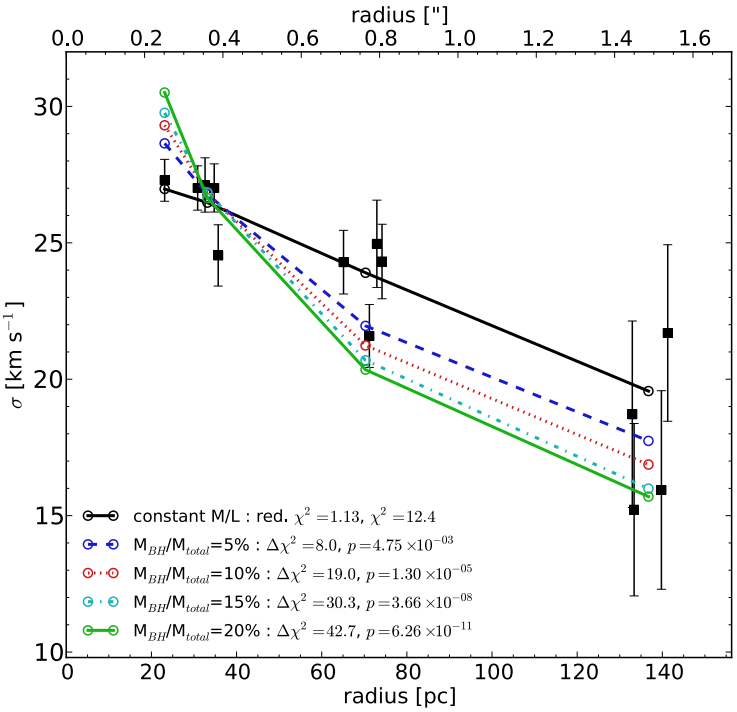

Figure 2.13: Comparison of the observed velocity dispersion profile (black squares) with models including a massive black hole in addition to the constant mass to light ratio stellar component. The blue dashed, red dotted, cyan dash-dotted and green solid curves represent the best-fitting models with a black hole mass of 5, 10, 15 and 20 per cent of the UCD's total mass. The solid black curve shows the constant M/L model without a black hole. The difference in χ^2 with respect to this best-fitting model, $\Delta\chi^2$, along with the resulting probability for the model to represent the data is reported in the legend for each model. The best-fitting mass to light ratios are 2.72 ± 0.07, 2.30 ± 0.06, 1.96 ± 0.05, and $1.78 \pm 0.05\,\mathrm{M}_\odot\,\mathrm{L}_\odot^{-1}$ for $\mathrm{M_{BH}/M_{total}}$ of 5, 10, 15, and 20 per cent, respectively. The radial velocity dispersion profile predicted by models including a massive black hole are steeper than the observed profile.

If the UCD was only $\sim 2-5$ Gyr old as suggested by the potentially biased measurement of Firth et al. (2009), its stellar population $\mathrm{M/L}_V$ would be $\lesssim 2\,\mathrm{M}_\odot$, lower than the best-fitting $\mathrm{M/L}_{V,\mathrm{dyn}}$ of $2.7 \pm 0.1\,\mathrm{M}_\odot\,\mathrm{L}_\odot^{-1}$ found with the 60 per cent dark matter model. Therefore, if the UCD was indeed young, its dynamical mass could be explained with a dark matter halo only if a very substantial amount of dark matter is invoked. However, the shape of the 60 per cent dark matter model is clearly too flat to reproduce the observations and its $\Delta\chi^2$ of 55 with respect to the constant M/L model corresponds to a probability for this model of only 1.5×10^{-13}.

Massive black hole

Unseen mass in UCDs could also be present in the form of a massive black hole. In massive galaxies, nuclear star clusters can coexist with central black holes with comparable masses (Graham & Spitler 2009). Therefore, if UCDs represent the remnant nuclei of originally much more massive galaxies, at least some of them could contain a black hole which contributes a substantial fraction of the total mass. Also if UCDs represent compact star clusters around recoiling super-massive black holes that were ejected from the centres of massive galaxies (Merritt et al. 2009), they would contain

a black hole with a mass comparable to or exceeding that of the stellar component. Therefore, we explored a family of mass models which, in addition to the constant M/L stellar component, included massive black holes. The resulting model dispersion profiles are shown in Fig. 2.13. The blue dashed, red dotted, cyan dash-dotted and green solid curves represent the best-fitting models with a black hole mass of 5, 10, 15 and 20 per cent of the UCD's total mass, respectively. The black solid curve shows the constant M/L model for comparison. It is evident, that the black hole models predict too steep a dispersion profile to reproduce the observations. Already the model with a black hole of 5 per cent of the UCD's mass, which yields a best-fitting stellar $M/L_{V,dyn}$ of $2.7 \pm 0.1\,M_{\odot}$, is excluded at the $> 3\sigma$ confidence level. The probabilities (reported in the legend of Fig. 2.13 along with the difference in χ^2 with respect to the constant M/L model) are even lower by several orders of magnitude for the models including more massive black holes.

2.5 Background object

As mentioned above, the HST/ACS image of the UCD (see the upper left panel of Fig. 2.3) reveals an irregular extension towards the south of the UCD. Based on the irregular pattern in the residual image obtained by subtracting a smooth model of the UCD's light from this image Evstigneeva et al. (2007) conjectured that the light comes from a background spiral galaxy. In our observations, the sky region south of the UCD's centre stand out by the presence of two strong emission lines centred around a wavelength of ~ 5425 Å and separated by 4.5 Å . These lines are clearly visible in the spectra shown in Figs. 2.6 and 2.7. The middle panel of Fig. 2.14 shows a reconstructed image obtained by summing only over the wavelength range around the two emission lines and subtracting a reconstructed image in an adjacent equally wide wavelength range. For comparison the left panel of Fig. 2.14 shows the reconstructed image obtained when summing over the entire wavelength range. The low pixel values in this middle panel near the centre of the UCD indicate that the light from the UCD was over-subtracted. Nevertheless, the location of this excess flux caused by the emission lines is clearly visible and coincides with the irregular extension of the UCD seen on the HST/ACS image.

We could not identify the line transition responsible for the emission line doublet, which would have allowed us to measure the redshift of the object. However, we derived a velocity map (relative to the unknown systemic velocity) by fitting the emission line doublet in each spaxel with

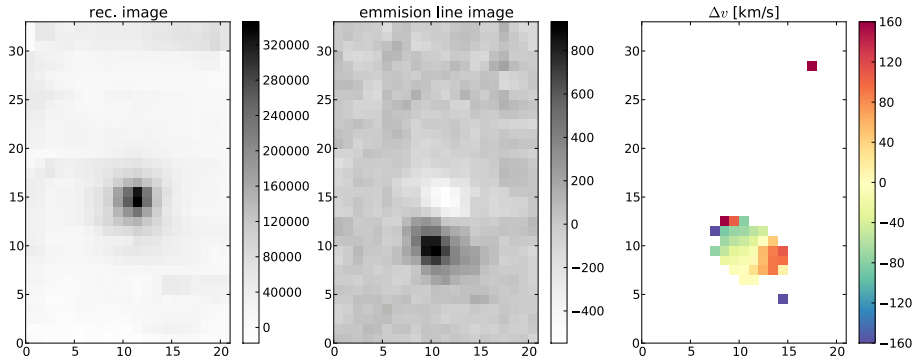

Figure 2.14: Shown is the reconstructed image of our observations a reconstructed image based on the wavelength region that includes the emission lines and a radial velocity map obtained by fitting the emission line doublet with two Gaussians. The velocity map reveals rotation with a lower limit on its amplitude of the rotational velocity of the object is consistent with it being a massive galaxy.

a significant excess flux with a model consisting of two Gaussians that are separated by 4.5 Å . This velocity map is shown in the right panel of Fig. 2.14 and reveals rotation with an amplitude of $\gtrsim 80\,\mathrm{km\,s^{-1}}$. This rotational is consistent with the emission being due to a massive background galaxy. The irregular extension of seen in projection close to the UCD is therefore not associated with the UCD.

2.6 Conclusions

We have demonstrated that the resolution of the internal kinematics of the brightest and most extended UCDs is feasible with seeing-limited integral-field spectroscopy, making it a promising tool to constrain the formation scenarios and hence the nature of UCDs.

The analysis of UCD3, the brightest known UCD in the Fornax cluster, reveals weak rotation and a radial dispersion profile in excellent agreement with an isotropic velocity distribution and a constant mass to light ratio. The mass of the UCD, measured under these assumptions, is $8.2 \pm 0.2 \times 10^7\,\mathrm{M}\odot$ and the implied mass to light ratio of $\mathrm{M/L}_{V,\mathrm{dyn}} = 3.6 \pm 0.1\,\mathrm{M}_\odot\,\mathrm{L}_\odot^{-1}$ is in excellent agreement with the stellar population mass to light ratio of $\mathrm{M/L}_V = 3.7 \pm 0.2\,\mathrm{M}_\odot\,\mathrm{L}_\odot^{-1}$ based on the most recent determination of the UCD's stellar population age and metallicity by Chilingarian et al. (2011).

The shape of the radial velocity dispersion profile does not show any sign for tidal disturbance. Moreover, it excludes the presence of a black hole with a mass $\gtrsim 5$ per cent of the total mass, and of dark matter contributing $\gtrsim 20$ per cent of the mass within a three-dimensional radius of 200 pc. Hence UCD3 does not show any of the attributes that would strongly suggest that the UCD is the remnant nucleus of a larger galaxy or a remnant star cluster around a recoiling super-massive black hole. While this result does not exclude such scenarios, the internal kinematics of UCD3 are fully consistent with it being a massive globular cluster.

3

A bottom-heavy stellar mass-function in UCDs?[1]

3.1 Introduction

In Section 1.2.3, we discussed the high M/L$_V$ of UCDs and attempts to explain these with the presence of dark matter, of massive black holes, or of unbound stars. We also mentioned that an alternative scenario to such extra, dark constituents of the UCDs' masses and to recent tidal interactions is that the stellar populations of UCDs themselves are not 'normal', showing an overabundance of underluminous stellar objects compared to the canonical IMF.

The universality of the IMF has been debated ever since Salpeter (1955) found the distribution of stellar masses, $\xi(m) = dN/dm$, where dN is the number of stars in a mass interval $[m, m+dm]$, in the solar neighbourhood to follow a power-law of the form

$$\xi_{\rm Salpeter}(m) \propto m^{-\alpha_{\rm Salpeter}}, \tag{3.1}$$

where $\alpha_{\rm Salpeter} = 2.35$. A recent overview of potential variations of the IMF is given by Bastian et al. (2010) and can be summarised as follows: The 'integrated galaxial IMF' (IGIMF; Weidner & Kroupa 2005) may be subject to variations due to the cut-off in stellar masses imposed by the finite total mass of the contributing star-forming complexes. Moreover, the present-day mass function in individual star clusters, apart from stellar evolution (i.e. mass-loss of individual stars) can also be influenced by dynamical processes such as the preferential removal of low-mass stars in mass-segregated clusters (cf. Sections 1.2.3 and 1.3.1). However, the *initial* stellar mass function can be thought of being universal over cosmic time (possibly disregarding the very first population III stars; Bromm & Larson 2004). This means that stellar evolution, largely independent of the environment, starts from stellar masses drawn from the same distribution function. This *canonical* IMF can be approximated as a broken power law (Kroupa 2001, 2002) of the form

$$\xi_{\rm Kroupa}(m) \propto \begin{cases} m^{-\alpha_1}, & 0.08 \leq m/\,{\rm M}_\odot \leq 0.5 \\ m^{-\alpha_2}, & m > 0.5\,{\rm M}_\odot, \end{cases} \tag{3.2}$$

[1] The work presented in this Chapter was done in collaboration with Steffen Mieske, Michael Hilker, Eva Grebel and Pavel Kroupa. The dynamical masses and normalised mass to light ratios listed in Table 3.1 were contributed by Steffen Mieske and derived using the mass modelling and aperture correction routine described in Mieske et al. (2008)

where $\alpha_1 = 1.3$ and $\alpha_2 = 2.3$. Alternatively, it can be expressed as a log-normal distribution for low-mass stars (Chabrier 2003) of the form

$$\xi_{\rm Chabrier}(m) \propto \begin{cases} \frac{1}{m} \exp\left(-\frac{(\log(m/\mathrm{M}_\odot)-\log 0.08)^2}{0.9522}\right), & m < 1\,\mathrm{M}_\odot \\ m^{-\alpha_{\rm Salpeter}}, & m \geq 1\,\mathrm{M}_\odot. \end{cases} \tag{3.3}$$

In both cases, $\xi_{\rm Kroupa}$ and $\xi_{\rm Chabrier}$, the normalisation of the mass function in the different intervals is given by the requirement that the mass function be continuous at the breaks at $m = 0.5\,\mathrm{M}_\odot$ or $m = 1\,\mathrm{M}_\odot$, respectively. According to Dabringhausen et al. (2008), it is not possible to distinguish between the two functional forms of the IMF given in Eqs. (3.2) and (3.3) within the uncertainties of currently available observational data.

Claimed deviations from this canonical mass function in extragalactic star clusters (e.g. NGC 1705-1, Sternberg 1998; M82-F, Smith & Gallagher 2001) have frequently been revoked when more data became available (e.g. Bastian et al. 2007) or on the grounds of more detailed modelling (e.g. Goodwin & Bastian 2006).

Recently, a number of studies presented indications for a variation of the IMF in massive galaxies. Comparisons of the masses of giant galaxies measured via gravitational lensing with their luminosities favoured the more bottom-heavy Salpeter IMF over Kroupa or Chabrier IMFs (e.g. Grillo & Gobat 2010; Spiniello et al. 2011). Spatially resolved kinematics of a large sample of massive galaxies were obtained recently by the ATLAS3D survey (Cappellari et al. 2011). Based on mass models of these galaxies, Cappellari et al. (2012) found that the mass to light ratio of their stellar component increases with increasing stellar mass and differs from the expectation from population synthesis models based on a Kroupa or Chabrier IMF. They argued that this discrepancy can be explained with either a bottom-heavy or top-heavy stellar mass function. In addition to these indirect indications for a variation of the IMF based on the comparison of measured and expected masses of the stellar components of galaxies, van Dokkum & Conroy (2010, 2011) presented direct evidence for such a variation. By measuring the strength of gravity-sensitive features in the integrated spectra of massive early-type galaxies they found a significant overabundance of low-mass stars in the cores of these galaxies, indicating a bottom-heavy stellar mass function.

For UCDs, Dabringhausen et al. (2008, 2009, 2010) proposed that they could form with a top-heavy stellar mass function, in which case their high M/L would be due to an overabundance of stellar remnants, such as white dwarfs, neutron stars, or stellar mass black holes. Mieske & Kroupa (2008) proposed that UCDs could have a bottom-heavy stellar mass function, i.e. an overabundance of low-mass stars that have high specific mass to light ratios compared to giants.

To test their top-heavy mass function scenario, Dabringhausen et al. (2012) modelled the expected number of low-mass X-ray binaries (LMXBs) in GCs and UCDs based on the assumption that LMXBs form exclusively in encounters of neutron stars with giant stars. Comparing these predictions with literature data on the number of X-ray sources that have GCs and UCDs as optical counterparts, they found that the high number of observed X-ray sources in UCDs cannot be explained by LMXBs, if a Kroupa IMF is assumed. This may indicate that there is an overabundance of neutron stars in UCDs, and that the stellar mass function of UCDs could indeed be top-heavy. This conclusion depends on whether the one-to-one correspondence between X-ray sources and LMXBs is a valid assumption and on whether LMXBs form only in encounters and not for example also from primordial binaries.

In contrast to this statistical approach that correlates the number of X-ray sources with the GC or UCD luminosity, the scenario of a bottom-heavy stellar mass function can be tested directly for individual objects by making use of spectral features that differ in dwarf and giant stars. Assuming that the high dynamical masses of UCDs are entirely due to a bottom-heavy stellar mass func-

tion, Mieske & Kroupa (2008) predicted that the UCDs with the highest M/L ratios should have a significantly weaker absorption in the gravity-sensitive 2.3 μm CO band.

In general, lower-mass dwarf stars show stronger spectral lines of neutral atoms and weaker lines of ionised species than higher-mass giant stars of comparable temperature (cf. Conroy & van Dokkum 2012). This is a direct consequence of ionisation equilibrium, which is described by the Saha equation (e.g. Unsöld & Baschek 2005, eq. 7.10): the higher electron density in the atmospheres of dwarf stars, which in turn is a consequence of their higher surface gravity, makes recombinations of ions and electrons more likely. Therefore neutral atoms are more abundant in dwarf star atmospheres than in those of giant stars. When molecules are considered, the analogue to the ionisation equilibrium of neutral atoms and ions is the dissociation equilibrium. In general this causes a higher abundance of molecules in dwarf star atmospheres and therefore stronger molecular bands in the spectra of dwarfs compared to those of giants (Russell 1934). The CO molecule is an exception to this picture and dwarf star spectra are known to have weaker CO absorption features than giants of the same temperature. This can be understood as the consequence of two effects. The binding energy of CO is large compared to that of most other molecules in stellar atmospheres (Russell 1934). Therefore, also in giant star atmospheres most of the carbon is bound in CO, and the abundance of CO in dwarfs and giant is similar. The second effect is the higher continuous absorption coefficient in dwarf stars. At a given CO abundance, this causes the depth of the CO absorption lines to be weaker in the spectra of cool dwarfs than in those of cool giants (Bell & Tripicco 1991).

This Chapter presents a first test for a bottom-heavy stellar mass function in UCDs. The test is based on a measurement of the photometric 2.3 μm CO index as proposed by Mieske & Kroupa (2008). The Chapter is structured as follows: Section 3.2 describes the observations and the basic data reduction. Section 3.3 describes the extraction of the spectra, and measurement of the CO index, and discusses systematics that can affect the measurement, and a method devised to circumvent these problems. Our results and their significance is discussed in Section 3.4.

3.2 Observations and basic data reduction

We obtained low-resolution K-band spectroscopy of two UCDs around M 87 in the Virgo cluster, whose normalised mass to light ratios $M/L_{V,\mathrm{norm}}$ are among the highest values measured for UCDs so far, and a sample of four comparison GCs/UCDs in NGC 5128 (Centaurus A). Table 3.1 lists the observed targets, their celestial coordinates, radial velocities and metallicities from the literature, and their dynamical masses M_{dyn} and mass to light ratios normalised to solar metallicities $M/L_{V,\mathrm{norm}}$ (defined by Eq. (1.1)). The metallicities are based either on spectroscopy or on broad-band photometric colours. In the latter case the combination (or combinations, if several colours were used) of the photometric bands is given as a subscript. The target selection originally was designed such that the comparison NGC 5128 objects have similar metallicities as the Virgo UCDs and dynamical M/L_V that agree with the expectation from stellar population models. However, the metallicity estimates available then were based on broad-band photometric colours (see Table 3.1). In the meantime, Beasley et al. (2008) presented spectroscopic metallicities for three of the NGC 5128 targets. According to their study, all three objects are significantly more metal-rich than previously estimated. Since spectroscopic metallicities are known to be more reliable than metallicities inferred from broad-band photometry, we adopt the Beasley et al. (2008) metallicities for these three objects. Taylor et al. (2010) presented new measurements of the dynamical masses of the same three NGC 5128 targets. For two of the objects, HCH99-21 and HGHH92-C23, their inferred dynamical mass is 20-30 per cent higher than previously measured by Rejkuba et al. (2007). Both measurements are based on data of comparable quality, namely high-resolution UVES spectra with

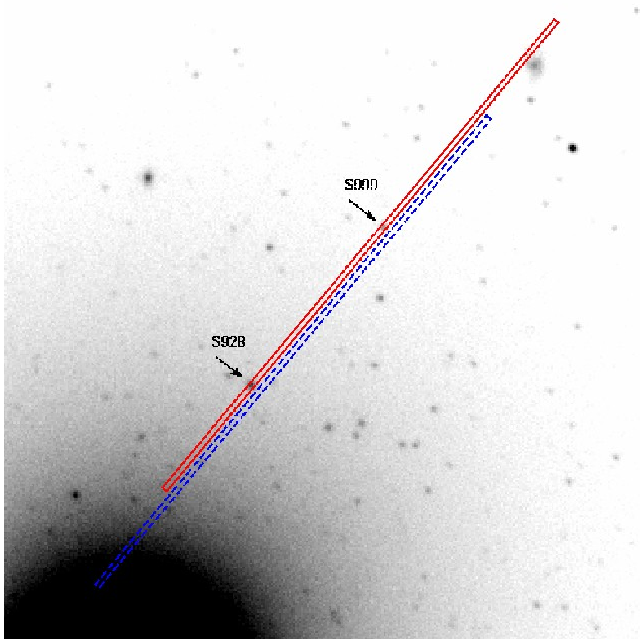

Figure 3.1: Position of the two UCDs on the sky shown on a $\sim 2 \times 2$ arcmin g-band image from the Sloan Digital Sky Survey (Abazajian et al. 2009). In the image north is up and east is left. The two targets, S928 and S999, are indicated by the arrows. Both UCDs were observed simultaneously in one 1×120 arcsec slit. The approximate location of the slit is shown as a red box (to scale) for an A nodding position. The blue dashed box indicates a B nodding position that is offset by 24 arcsec along the direction of the slit. For clarity in the plot, it is shown also artificially offset in the direction perpendicular to the slit. The centre of M 87 is towards the south-east.

relatively low signal to noise (S/N). Taylor et al. (2010) measured the velocity dispersions via pixel-fitting, which is potentially more reliable than the cross-correlation measurement used by Rejkuba et al. (2007). Therefore we adopted the Taylor et al. (2010) velocity dispersion measurements. With these metallicities and velocity dispersion measurements, we calculated updated dynamical masses and normalised mass to light ratios that are given in Table 3.1. This was done in the same way and using the same literature surface brightness profiles as described in Mieske & Kroupa (2008). As a result, also the $M/L_{V,\mathrm{norm}}$ of one of the NGC 5128 objects (HGHH92-C23), with a value of 8.1 is significantly higher than the value of ~ 4 predicted by the Bruzual & Charlot (2003) and Maraston (2005) population synthesis models for an old stellar population of solar metallicity (cf. Section 1.2.3).

The spectroscopic data were obtained in ESO programme 081.B-0282 (PI: Mieske) using the short-wavelength (SW) arm of the ISAAC spectrograph (Moorwood et al. 1998). ISAAC is mounted on one of the Nasmyth foci of the 8.2 m UT3 at the VLT. We used the spectrograph's low resolution grating and a slit width of 1 arcsec, which yields a resolving power of $R = \lambda/\Delta\lambda = 450$ in the K-band ($\lambda \sim$1.82 - 2.5μm). The targets were observed in the nod-on-slit mode with typically a AAABBBBBBAAA... nodding sequence. The nod-throw between A and B positions was 24 arcsec, with additional small offsets between subsequent blocks A and B exposures to limit the influence of bad detector pixels. Figure 3.1 shows the position of the two Virgo cluster UCDs, S928 and S999, on the sky. They lie in projection close to M 87 and are separated from each other by only 40 arcsec on the sky. This made it possible to observe both targets simultaneously in the 120 arcsec slit. The position of the slit in an A and a B nodding cycle of a representative observation are indicated in Fig. 3.1; for clarity, the B position is shown also artificially offset in the direction

perpendicular to the slit.

A log of our observations is given in Table 3.2. The first three columns list the observed target, modified Julian date of the observation and the number of exposures and integration time per exposure. The fourth column gives an estimate of the signal to noise ratio of the extracted spectra per resolution element of 7.2 Å obtained with the DER_SNR algorithm (cf. Section 2.3; Stoehr et al. 2007). In the case of the lowest S/N spectra, the reported S/N ratios should be taken as a crude estimate. The observations were carried out in service mode and after each sequence of science observations, a telluric standard star that is reported in the fifth column of Table 3.2 was observed as part of the observatory's calibration plan.

Table 3.1: Observational Targets

Target	RA (J2000)	Dec (J2000)	v_r (km/s)	[Fe/H] (dex)	M_{dyn} ($10^7\,M_\odot$)	$M/L_{V,norm}$ ($M_\odot L_\odot^{-1}$)
HCH99-21 = GC0242	13 25 34.65	−43 03 27.7	662.9 ± 1.5^{a}	$-2.0^{c}_{VI,BV}$, -0.48 ± 0.25^{f}	$0.22^{(e)}$	$4.0^{(e)}$
HGHH92-C23 = GC0330	13 25 54.58	−42 59 25.4	673.7 ± 0.9^{a}	$-1.5^{c}_{VI,BV}$, -0.36 ± 0.09^{f}	$1.4^{(e)}$	$8.1^{(e)}$
HGHH92-C37 = GC0378	13 26 10.58	−42 53 42.7	611.7 ± 0.3^{a}	$-0.95^{c}_{VI,BV}$,-0.46 ± 0.09^{f}	$1.1^{(e)}$	$1.9^{(e)}$
HHH86-C38 = GC0397	13 26 23.78	−42 54 01.1	405.1 ± 0.7^{a}	$-1.2^{c}_{VI,BV}$	$1.1^{(a)}$	$2.6^{(e)}$
S999	12 30 45.91	+12 25 01.8	1465.9 ± 5.1^{b}	-1.93^{b}_{gz}, $-1.38^{b}_{CT_1}$	$2.3^{(b)}$	$18.5^{(b)}$
S928	12 30 47.70	+12 24 30.8	1282.5 ± 5.0^{b}	-1.54^{b}_{gz}, $-1.34^{b}_{CT_1}$, -1.37^{d}	$1.9^{(b)}$	$9.5^{(b)}$

Nomenclature for the NGC 5128 clusters: HCH99=Holland et al. (1999), HGHH92=Harris et al. (1992), HHH86=Hesser et al. (1986). The GC numbers are according to Woodley et al. (2007). Celestial coordinates are in hours, minutes, and seconds for right ascension and in degrees, arcmin, and arcsec for declination, respectively. Metallicities are based on either broad-band photometric colours, in which case the employed bands are indicated as subscript, or on spectroscopy. Dynamical masses M_{dyn} and normalised mass to light ratios $M/L_{V,norm}$ were calculated in the same way as described in Mieske & Kroupa (2008). For these quantities, superscripts in parentheses refer to the velocity dispersion measurement used in the calculation. References: [a] Rejkuba et al. (2007); [b] Haşegan et al. (2005); [c] Mieske & Kroupa (2008); [d] Cohen et al. (1998); [e] Taylor et al. (2010); [f] Beasley et al. (2008)

Table 3.2: Log of the ISAAC observations.

Target	MJD 54,500+	Exposure times [seconds]	S/N [1 / 7.2 Å]	Telluric standard
S928, S999	99.11042	24×112.0	2.6, 2.7	Hip064716
HGHH92-C23	99.15862	20×60.0	50.4	Hip087287
S928, S999	110.99720	24×112.0	2.9, 2.3	Hip070506
S928, S999	111.05007	24×112.0	2.9, 2.6	Hip057432
HGHH92-C37	111.10254	24×113.0	21.3	Hip066957
HHH86-C38	111.15167	24×113.0	18.4	Hip088857
HCH99-21	111.21577	24×113.0	12.1	Hip092957
S928, S999	146.04962	24×112.0	2.5, 2.2	Hip096939
S928, S999	164.99092	24×112.0	2.9, 2.4	Hip057963
S928, S999	343.33501	24×112.0	3.6, 2.5	Hip070182
S928, S999	403.15481	24×112.0	2.4, 1.8	Hip044105
S928, S999	403.20649	24×112.0	3.0, 2.4	Hip059099 obs. 1
S928, S999	406.17488	24×112.0	2.0, 1.2	Hip059099 obs. 2
S928, S999	407.28098	24×112.0	2.2, 1.6	Hip072505
S928, S999	410.28207	24×112.0	3.1, 2.5	Hip088201

3.2.1 Basic data reduction

The read-out electronics of ISAAC's SW arm, a Rockwell Hawaii detector, suffer from cross-talk that introduces electrical ghosts in the data. These are visible as an additional signal in the data, which is to first order proportional to the sum of the fluxes in the corresponding row and the row 512 pixels away (see the ISAAC Data Reduction Guide[2]). Therefore, prior to all other reduction steps, we preprocessed all calibration and science frames to remove this signal. This was done in a way identical to that implemented by the GHOST recipe in the now superseded eclipse-based ESO instrument pipeline: from each row, a value 1.34×10^{-5} times the sum of the counts in this row and the row 512 pixels away, was subtracted. A residual of the ghost can still be seen in the frames containing bright telluric standard stars, but we estimated that the ghost signal is removed to within 5-8 percent. The further basic data reduction was carried out using version 5.10.2 of the ISAAC instrument pipeline based on the ESO Common Pipeline Library.

Master-flats were derived from daytime calibration frames using the ISAAC_SPC_FLAT pipeline recipe. The ISAAC_SPC_STARTRACE recipe was used to measure the geometric distortion solution of the instrument from the monthly star-trace observations.

Each set of science and telluric standard exposures was combined using the ISAAC_SPC_JITTER recipe and the calibrations closest in time to the observations. This recipe flat-fields and then averages the frames of each A or B cycle, and subtracts the averaged frames in A and B positions from each other. As the position of a target on an A frame corresponds to an empty patch of sky on a B frame and vice versa (see Fig. 3.1), this constitutes the first pass of sky subtraction and removes the thermal background and sky emission lines from the frames. The recipe then resamples the sky-subtracted frames to an undistorted, wavelength calibrated coordinate system, and shifts A and B frames to the same position and combines all the groups. This produces one undistorted, wavelength-calibrated combined frame for each observation. The recipe also attempts to extract one-dimensional spectra of point sources. This step failed to identify the faint spectra of our targets

[2]Available at: `http://www.eso.org/sci/facilities/paranal/instruments/isaac/doc/drg/html/drg.html`

in most science exposures. For this reason, we also disabled the recipe's option that attempts to refine the offsets between nodding positions based on the location of the identified spectra.

The wavelength solution used by the ISAAC_SPC_JITTER recipe can be obtained either beforehand from Xe and Ar arc-lamp exposures, that are recorded as part of the daytime calibrations (the pipeline offers a ISAAC_SPC_ARC RECIPE to achieve this), or directly in the ISAAC_SPC_JITTER step based on the OH sky emission lines that are abundant in the *K*-band. The latter method proved much more reliable. A cross-correlation of telluric absorption features in our response function (see Section 3.3.2) with a library telluric spectrum[3], which was degraded to a resolution of $R \sim 450$, showed that the wavelength solution based on sky emission lines is accurate within 0.66 pixels, or 4.7 Å r.m.s, whereas the r.m.s scatter for wavelength solutions obtained from the Xe or Ar arc-lamps was 10.2 pixels. The calibrations from either the Xe or Ar lamp frames were consistent with each other, so the difference between the sky-line- and arc-lamp-based calibration is likely due to a different dispersion solution at night and during the day. This may be either because of a change in ambient temperature or because of flexure in the optical path.

The result of this basic data reduction is a wavelength-calibrated, undistorted two-dimensional combined frame for each of the science observations that has a wavelength dimension and a spatial dimension, i.e. the position in the slit. The typical FWHM of the spectra in spatial direction in these frames was ~ 6 pixels at the central wavelength and varied slightly from larger values at short wavelengths to lower values at long wavelengths. This may be partially due to the variation of the point spread function with wavelength. However, a variation of the shape of the spectrum profile with wavelength that showed signs of two components (instead of a single Gaussian-like component) at the shortest wavelengths suggests that the geometric distortion solution obtained from the star trace calibrations deviates from the geometric distortion in our science frames. In this case, the spectra of the individual frames may still be marginally curved or tilted and may not perfectly align when resampled onto the combined frames.

3.3 Spectrum extraction and measurement of the CO index

We will see in the following that the extraction of one-dimensional spectra from the two-dimensional combined frames is the critical step for a reliable measurement of the CO index from spectra with a low signal to noise ratio. In this Section we will first describe the classical approach to extracting and analysing the spectra. In Section 3.3.4 we will discuss the problems of this approach and the modifications made to ensure an unbiased measurement.

3.3.1 Spectrum extraction

To extract one-dimensional spectra from the combined frames, we initially used the APALL task contained in the IRAF package APEXTRACT. This task allows one to interactively identify and to trace the spectra. The tracing, i.e. the determination of the location of the spectrum as a function of wavelength is necessary since the removal of geometric distortion in the data reduction is not perfect and therefore the spectra in the combined frames are not perfectly aligned with the chip's rows. The task APALL then performs a second pass of sky subtraction by fitting a polynomial model to the sky background on both sides of the spectrum and subtracting this model.

To extract a one-dimensional spectrum, the task offers either direct summation over an aperture around the location of the spectrum, or a variance-weighted extraction (Horne 1986). While the

[3] Available at `http://www.eso.org/sci/facilities/paranal/instruments/isaac/tools/spectroscopic_standards.html` and produced by NSF/NOAO based on data obtained with the NSO/Kitt Peak Fourier Transform Spectrometer.

direct summation, over large enough an aperture, produces a statistically unbiased spectrum, for faint targets a variance-weighted or optimal extraction is superior in terms of obtained signal to noise. For the optimal extraction, the APALL task estimates the variance in each pixel from a constant read-out noise term and a Poissonian term based on the input signal. However, in *K*-band spectra of faint targets, the variance in the signal is entirely dominated by the sky background. This sky background, to first order, is already subtracted in the combined frames, and therefore the APALL task cannot take into account the variation of the noise with wavelength. However, this variation is substantial: the thermal background steeply increases with wavelength and strong sky emission lines cause a variation of the photon noise on small wavelength scales.

For this reason, and to have more direct control over the individual steps of the extraction we implemented our own code for the extraction. It resembles IRAF's APALL task, but allows for an input variance map to take into account the variation of the photon noise with wavelength. Since the ISAAC pipeline does not propagate uncertainties from the raw frames to the combined frame, we estimated the variance in the following way: for each raw science and standard star frame, we created 100 realisations of the data by adding random noise that consisted of a Gaussian component for the read-out noise and a Poissonian component for the photon shot-noise. These artificial frames were then combined in the same way as the observed data using the ISAAC_SPC_JITTER recipe to yield 100 realisations of each original combined frame. The variance was then estimated as the dispersion of these 100 realisations[4].

Our extraction then followed closely the optimal extraction method that is described in detail by Horne (1986). In an iterative procedure, at each wavelength a linear fit to the background on both sides of the spectrum was subtracted. The two-dimensional data were then divided by an estimate of the one-dimensional spectrum (provided by a summation extraction in the first iteration). This results in a profile image, i.e. an image that has the shape of the spectrum in the combined frame, but contains no spectral features. This profile image was then modelled by fitting low-order polynomials to rows of pixels in dispersion direction, i.e. along the spectrum. A new estimate of the one-dimensional spectrum is then calculated using the profile and the variance map to weight pixels in order to achieve the maximum signal to noise. Using the profile information, outlying pixels (produced e.g. by cosmic rays or chip defects) at each wavelength are identified and masked out and the procedure is repeated.

As mentioned above, the imperfect distortion solution causes the spectra in the combined frames to be not perfectly aligned with the image's rows. While the use of polynomials along rows in principle can deal with such small tilts or curvatures, we found it beneficial to use the Marsh (1989) modification to the algorithm. This amounts to also tracing the spectra and fitting the trace, i.e. the location of the spectrum as a function of wavelength, by another low-order polynomial. The polynomials that describe the profile along dispersion direction are then evaluated at given distances from the trace instead of in a given image row (for details see Marsh 1989). Especially for the faint spectra, this stabilised the profile fit, because the polynomials in dispersion direction that describe the profile can be of very low order because they no longer need to absorb the spectrum's tilt or curvature.

The orders of the polynomials describing the profile and the trace, as well as the width of the extraction region, were fine-tuned using the high signal to noise spectra of the telluric standard stars. Via trial and error, the parameters were set such that the number of free parameters (i.e. polynomial

[4]On the technical side, the creation and reduction of the noise realisations requires the processing of $\sim 4 \times 10^4$ frames. The simulations discussed in Section 3.3.4 required the processing of even substantially larger amounts of data frames. Fortunately, most of the processing steps lend themselves to parallelization since sets of frames corresponding to one observation can be processed independently. To speed up the processing in these situations, we frequently used the IPCLUSTER tool of the IPYTHON package (Pérez & Granger 2007) to create a transparent cluster of workstations at the Astronomisches Rechen-Institut, which would run tasks scheduled in a queue during nighttime and weekends.

Table 3.3: Telluric standard stars.

Telluric standard	MJD 54,500+	S/N [1 / 7.2 Å]	Spectral type & luminosity class	K [mag]	model SED
Hip064716	99.15106	96	B1/B2V	8.6	23,950 K
Hip087287	106.32559	63	B2IV	8.4	22,300 K
Hip070506	111.03759	72	B3IV	8.8	19,000 K
Hip057432	111.09075	63	B5V	8.9	15,400 K
Hip066957	111.14420	60	B5V	9.2	15,400 K
Hip088857	111.19739	44	B3V	7.0	19,000 K
Hip092957	111.25654	55	B3V	8.0	19,000 K
Hip096939	146.17073	127	B5	8.1	15,400 K
Hip057963	165.03172	108	B4IV	7.2	17,200 K
Hip070182	343.37683	107	G2Vw	7.5	G2V template
Hip044105	403.19509	48	B5	6.2	15,400 K
Hip059099 obs. 1	403.24853	69	B9	6.8	10,700 K
Hip059099 obs. 2	406.21613	127	B9	6.8	10,700 K
Hip072505	407.32302	93	B9V	6.8	10,700 K
Hip088201	410.32318	113	B3V	7.5	19,000 K

degrees and number of polynomials used to describe the profile) were as low as possible, while ensuring that the extracted spectrum matches that obtained via the parameter-free direct summation extraction. The latter provides a good reference since it gives a statistically unbiased estimate of the spectrum (Horne 1986), while the high signal to noise ratio of the standard star spectra makes a weighting of the pixels unnecessary. The adopted parameters were: a third order polynomial to describe the location of the spectrum as a function of wavelength, 19 third-order polynomials spaced evenly in a 39 pixel extraction window to describe the profile image, and the linear fit to the sky evaluated in a 100 pixel wide region, excluding the inner 39 pixels of the extraction window.

Overall, our own extraction procedure slightly improved the quality of the extracted spectra compared to the initial APALL extraction. While this may partially be due to employing the correct variance map in the weighting, it is as likely due to the extensive testing and fine-tuning of each extraction step in our procedure.

3.3.2 Telluric correction and stacking of observations

The science spectra were then corrected for telluric absorption and for instrument response, which effectively flux-calibrates the spectra on a relative scale. We determined the telluric and flux calibration as the ratio of a model spectral energy distribution (SED) and the observed spectrum of each telluric standard star. The telluric standard stars used are listed in Table 3.3. The first three columns give the stars identifier, the time of observation, and the signal to noise ratio per spectral element in the extracted spectrum. The exposure times for the standard stars were 2×5.0 s in all cases. Columns three and four give the spectral type and luminosity class, and the K band magnitude of the star according to the SIMBAD database[5].

The fifth column of Table 3.3 lists the used model SED for each star. The model for the B-type stars consisted of a black body spectrum with a temperature (listed in the Table) according to the spectral type and luminosity class (Allen 1977). Spectra of B-type stars are almost devoid of

[5] `http://simbad.u-strasbg.fr/simbad/`

features, but still contain hydrogen lines. In the K-band the strongest of these, and the only one visible in our telluric standard spectra, is the Brγ line at 2.166 μm. This line was present in all of the B-type telluric standard star spectra and in some of the cases was seen in emission instead of absorption, an effect that is known to occur in some luminous early-type stars (Hanson et al. 1996). We removed this line from the spectra by fitting it with a Gaussian line profile on top of a locally linear continuum and subtracting this Gaussian from the spectrum. For the G2V star, we used as a model the flux-calibrated G2V template spectrum from Pickles (1998). The resolution of this library, with $R \sim 500$ is very similar to that of our ISAAC setup, so that no further convolution with a line-spread function was applied.

After multiplying the spectra of our science targets with the telluric correction and instrument response (i.e. the ratio of the model SED and the telluric star spectrum), we stacked the individual observations of the Virgo cluster UCDs that were observed multiple times. The stacking was done by averaging the spectra of the eleven observations with the IRAF task SCOMBINE and rejecting the highest and lowest pixel at each wavelength to remove potential remaining bad pixels.

Finally, the spectra were shifted to the rest frame velocity using the radial velocities from the literature (cf Table 3.1). The final spectra are shown in Fig. 3.2 in order of increasing metallicities. The objects are reported on the left of the panels. The signal to noise ratio is relatively low (cf. Table 3.2). This is expected from the design of our study that does not aim at measuring individual spectral features. Instead, it aims at measuring the integrated flux in the broad CO continuum and feature bands that are shown as shaded wavelength intervals in Fig. 3.2.

3.3.3 Measurement of the CO-Index

There exists a multitude of definitions of indices to quantify the CO band absorption at $\sim 2.3\mu$m (see the lower panel of Fig. 3.2). An overview and comparison of different *spectroscopic* CO indices is given by Mármol-Queraltó et al. (2008). The measurement of any of these spectroscopic indices requires a relatively high signal to noise ratio, which cannot be achieved within reasonable exposure times for our targets on current 8 m-class telescopes.

Therefore we use the *photometric* CO index. This index is historically based on two narrow band filters (Frogel et al. 1975; Persson et al. 1977; Frogel et al. 1978) and therefore is in fact a narrow-band photometric colour. We use the idealised definition of the index's passbands, namely a rectangular shaped response curve centred on 2.36 μm (feature band) and 2.2 μm (continuum band) with widths of 0.08 μm and 0.11 μm (Frogel et al. 1975). Thus, this idealised index is measured from a spectrum by simply integrating it over the corresponding bands:

$$\mathrm{CO} = -2.5\log\frac{\int_{2.32\mu\mathrm{m}}^{2.4\mu\mathrm{m}} f_\lambda d\lambda}{\int_{2.145\mu\mathrm{m}}^{2.255\mu\mathrm{m}} f_\lambda d\lambda}, \tag{3.4}$$

where f_λ is the normalised flux as a function of wavelength.

Since the idealised rectangular response curves deviate from those of the historical photometric CO filter system, the historical CO index, $\mathrm{CO}_{\mathrm{Frogel}}$, differs from our idealised CO index by a zeropoint CO_0:

$$\mathrm{CO}_{\mathrm{Frogel}} = \mathrm{CO} - \mathrm{CO}_0 \tag{3.5}$$

The CO index measured for our targets using Eq. (3.4) versus the metallicity is shown as filled squares in Fig. 3.3. The colour of the squares gives the normalised mass to light ratio according to the colour scale shown on the right. The individual objects are labelled. Uncertainties on the CO index were estimated by repeatedly measuring the CO index according to Eq. (3.4) n times, using

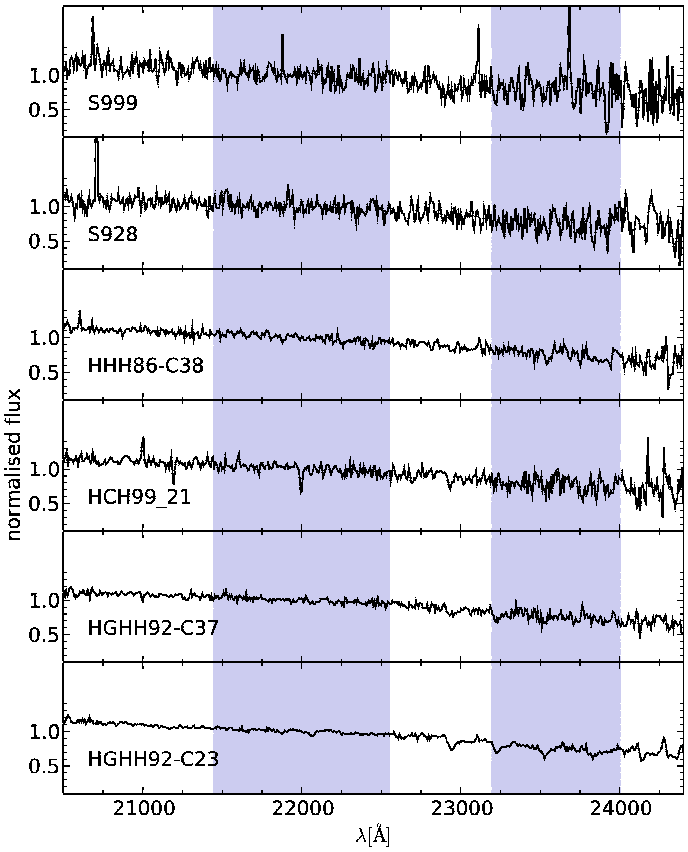

Figure 3.2: Fully reduced spectra and stacked spectra of our targets. The spectra are corrected for radial velocity (using the values given in Table 3.1) and shown in order of increasing metallicity. The object to which the spectrum corresponds is reported at the left of each panel. The areas shaded blue represent the continuum (left) and feature (right) band passes of the CO index (see Section 3.3.3). The spectra generally have low S/N (cf. table Table 3.2) and only in the case of HGHH92-C23 the characteristic sequence of CO absorption bands around 2.3 μm is unambiguously identifiable by eye.

only every n-th pixel (starting at a pixel i=1...n) to define the spectrum. The uncertainty can then be approximated as the standard deviation of these measurements divided by $\sqrt{n}$. The (narrower) feature band is $\sim$ 100 pixels wide and we chose $n = 10$, i.e. ten repeat measurements using only every tenth pixel to define the spectrum. As metallicities we adopted the spectroscopic values from the literature for HCH99-21, HGHH92-C23 and -C37 and S928 (cf. Table 3.1). For S999, the adopted value is the mean of the two photometric metallicities. The error bars on metallicity in Fig. 3.3 represent the uncertainties on the spectroscopic metallicity for HCH99-21, HGHH92-C23, and -C37, and the range of literature metallicity estimates for S928 and S999. Figure 3.3 also shows a line corresponding to the empirical relation between [Fe/H] and the CO index given by Frogel et al. (2001), which is based on integrated light measurements of the photometric CO index by Aaronson et al. (1978) and metallicities from the Harris (1996) catalogue. Since the zeropoint CO_0 from Eq. (3.5) is a priori unknown, the empirical relation only defines the slope of the [Fe/H]-CO index relation and leaves the ordinate offset undefined. We fixed the zeropoint by minimising

$$\chi^2 = \sum \frac{\left(\mathrm{CO}_i - CO_{\mathrm{Frogel}}\left([\mathrm{Fe/H}]\right)\right)^2}{\left(\Delta \mathrm{CO}_i\right)^2}, \tag{3.6}$$

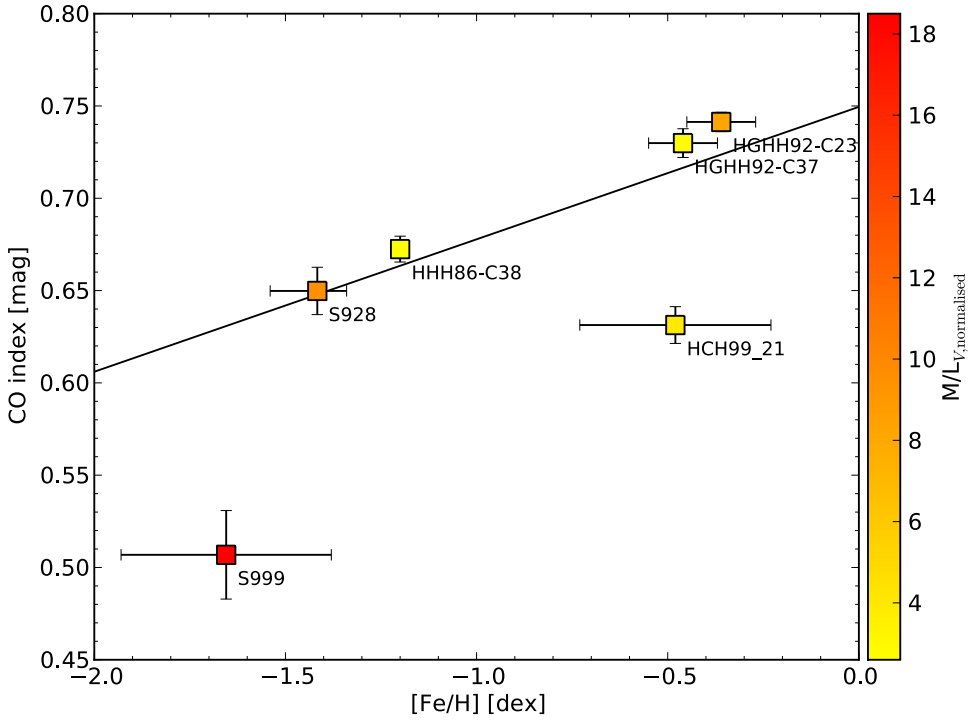

Figure 3.3: The CO index measured with the classical spectrum extraction method versus the metallicity of our targets. Filled squares correspond to the individual targets that are also indicated by labels. The colour of the squares refers to the normalised mass to light ratio of the object on the colour scale given on the right side. The black line has the slope of the empirical relation for Galactic globular clusters between $\mathrm{CO}_{\mathrm{Frogel}}$ and [Fe/H] given by Frogel et al. (2001). The offset in CO-direction corresponds to the zeropoint of the CO index and was defined by a χ^2-fit (Eq. (3.6)) to all our data points. It is intriguing that the CO index of S999, the object with the highest normalised mass to light ratio, deviates significantly from the remaining sample. The deviation is in the direction that would be expected, if the object's high M/L is caused by an overabundance of dwarf stars.

where CO_i and $\Delta\mathrm{CO}_i$ are our measurements and their uncertainties and $CO_{\mathrm{Frogel}}([\mathrm{Fe/H}])$ is the empirical relation given by eq. (5) of Frogel et al. (2001). Given the inhomogeneous nature of the [Fe/H] measurements (see Table 3.1), we chose to treat the metallicities as fixed, minimising only in the CO direction. This is equivalent to assigning equal weights to all metallicity measurements. We obtained a zeropoint of $\mathrm{CO}_0 = 0.61 \pm 0.02$ mag, somewhat higher than the zeropoint of 0.56 mag found by Kroupa & Gilmore (1994), who determined the zeropoint from similarly flux-calibrated *stellar* spectra relative to photometric CO measurements from the literature.

Figure 3.3 shows that the CO index of S999, the UCD with the highest measured mass to light ratio, deviates significantly from the remaining sample. This deviation is in direction of a weaker CO absorption, exactly as would be expected in the case of a bottom-heavy stellar mass function. Taken at face value this would be an intriguing result. However, the fact that the spectrum of S999 has the lowest signal to noise ratio of our spectra warrants caution. S999 remained a significant outlier independent of the extraction method, i.e. our own code, as well as APALL implementation of the variance-weighted and direct summation extraction, for a reasonable choice of extraction parameters. However, when a very small extraction window of $\lesssim 4$ pixels was used, the CO index measured for S999 was similar to that of the other objects. An extraction window smaller than the 6 pixel FWHM of the spectra is not expected to be a good choice of parameters, because the relative amount of flux it captures is very sensitive to the accuracy of the trace and because the discrete

sampling of the profile by the detector pixels may introduce a stochastic bias if only a few pixels in the centre of the profile are used. Nevertheless, the result obtained with this small extraction window also does not lend support to the authenticity of the discrepant CO index of S999.

3.3.4 Possible systematics and artificial spectrum tests

Both Virgo cluster UCDs were observed simultaneously in the same slit and S928 shows normal CO absorption with respect to the remaining sample. Therefore, it is unlikely that e.g. temporal variations in the telluric absorption of the atmosphere between the science and telluric star exposures, or a bad fit of the telluric standard's SED due to an erroneous spectral type, are responsible for the measured effect in S999. Such systematics would enter multiplicative into both spectra and therefore would also affect the CO index S928 in the same magnitude and direction. However, there are also possible additive effects that may affect both spectra differently due to either a dependence on the position in the slit or simply because of the lower signal in the S999 spectrum, that would cause a small additive bias to yield a larger deviation in the CO index. The ISAAC instrument manual reports that the bias level of the SW detector can vary with time. In this case, the subtraction of nodding A and B frames would not perfectly remove the bias level, which would result in an additive remnant in the combined frames. The surface brightness of the M 87 halo strongly varies on the scale of the slit length (see Fig. 3.1). Therefore, in the subtraction of A and B nodding positions, the light from M 87 is either over- or under-subtracted, again leading to an additive remnant in the combined frames. On the other hand, any possible additive effects are principle eliminated in the second pass of sky subtraction during the spectrum extraction, unless they vary more strongly with the position in the slit than the linear fit to the sky background in this sky subtraction.

For photometric data, it is common practise to use artificial star tests to estimate the uncertainties and the completeness of measured stellar magnitudes (see e.g. Sections 4.2.3 and 5.2.1). In these tests, artificial stellar images of a given magnitude and of a shape determined by a model of the point-spread function are added to the raw frames. Their magnitudes are then measured in the same way as for actual stars and the results are compared to the inserted magnitudes. A corresponding procedure is also conceivable for spectroscopic data, although likely because of the complexity of these data, it is not commonly used. To verify our intriguing result on the CO index of S999, we implemented such a procedure, which we describe in the following.

Since we aim at reproducing the observations as closely as possible, we chose to use for each artificial spectrum simulation all eleven observations of the Virgo cluster, amounting to $11 \times 24 = 264$ raw frames. We randomly selected the position for an artificial spectrum 'on the sky' to be inserted into the data. This step is not trivial due to pointing differences between the individual observations and due to the employed offsets along the slit direction between subsequent sets of A or B exposures. The artificial spectrum should not coincide with the spectra of the two UCDs or their negative image that is produced when the nodded A and B frames are subtracted from each other. We therefore generated random trial positions on a coordinate system defined by the first exposure of an arbitrary reference observation. We then used the information on the pointing and offset present in the fits headers of the raw frames to transform this trial position to the coordinate system of each exposure. If the position was within 5 pixels of one of the observed spectra or their negative image in one of the exposures, we rejected the trial position and accepted it otherwise.

The pipeline-produced wavelength and geometric distortion solution of each observation define mappings from the x- and y-coordinates on the detector to the wavelength λ and the position along

the slit in an undistorted coordinate system, $\hat{y}$:

$$\begin{aligned} \text{wavelength solution} &: (x,y) \mapsto \lambda \\ \text{distortion solution} &: (x,y) \mapsto \hat{y} \end{aligned} \tag{3.7}$$

Equation (3.7) can be inverted by iteration, to obtain a mapping between $(\lambda,\hat{y})$ and (x,y) that is required to insert a given artificial spectrum into the raw frames.

For the artificial spectrum, i.e. the flux as a function of $(\lambda,\hat{y})$, we chose a Gaussian profile in the spatial direction with a FWHM of 6 pixels, corresponding to the FWHM of the observed spectra in the combined frames. In the wavelength direction, we chose a Maraston (2005) synthetic spectrum of a stellar population with an age of 14 Gyr and a metallicity of [Fe/H]$= -1.35$ dex, shifted to the radial velocity of S999 of $1466\,\mathrm{km\,s^{-1}}$, and divided by the telluric correction and instrument response of each observation. Using the same telluric correction and instrument response in the insertion step and in the following reduction implies that the artificial spectrum tests do not test for possible multiplicative systematics.

We then inserted the artificial spectrum using the inverse transformation of Eq. (3.7) into each of the 264 raw frames of our observations. We reduced these raw frames in the same way as our data, by first producing combined frames from the sets of 24 exposures of each observation as described in Section 3.3.1, extracting a one dimensional spectrum from each of the 11 observations and then stacking these spectra after multiplying them with the telluric correction and instrument response (Section 3.3.2). We then measured the CO index from the resulting stacked spectrum. We repeated the procedure, varying the position 'on the sky' of the artificial spectrum and its amplitude.

The resulting difference between the CO index of the inserted synthetic spectrum and the measured CO index for a set of representative artificial spectrum tests is shown in Fig. 3.4. Black crosses are the mean of 407 artificial spectra at five different amplitudes. The amplitudes reported are proportional to the total flux of the spectra on an arbitrary normalisation. From left to right, the signal to noise, decreases. The shaded region corresponds to the approximate flux level of the spectrum of S928 (towards the high-flux, left edge of the region) and the spectrum of S999 (towards the low-flux edge of the region) on this amplitude scale. Black error bars and red error bars indicate the intervals containing 68.3 and 99.7 per cent of the simulation results, respectively, and can be interpreted as 1σ and 3σ confidence intervals. It is apparent, that at high signal to noise ratios, the CO index of the inserted synthetic spectrum is reproduced very well. However, at flux levels comparable to those of the faint Virgo UCD spectra, not only the uncertainty increases, but there is also a systematic towards measuring a lower CO index. This suggests, that the low CO index of S999 is due to systematics, rather than an overabundance of low-mass stars. Figure 3.5 shows the differences between the inserted and recovered CO index as a function of position in the slit for an amplitude of 10 (corresponding approximately to the flux level of the S999 spectrum). The position in the slit refers to the coordinate system of the first exposure of an arbitrary observation chosen as a reference. It can be seen that there is no smooth trend of the deviation with the position that would be expected if the systematics were due to an imperfect subtraction of the background light from the M 87 halo. However, the systematics are clearly correlated with position on a scale of several tens of pixels. While the cause of the systematics is unclear, this correlation suggests that it may be related to medium-scale imperfections of the detector.

Equipped with our artificial spectrum simulations, we performed extensive experiments to test whether modifications to spectrum extraction procedure (Section 3.3.2) make it less susceptible to the systematics. We varied the extraction parameters, i.e. the orders of the polynomials used to trace the spectrum and to describe the spectrum profile, the width of the extraction and sky windows, and the spacing of the polynomials describing the spectrum profile. We also tested a sky subtraction that,

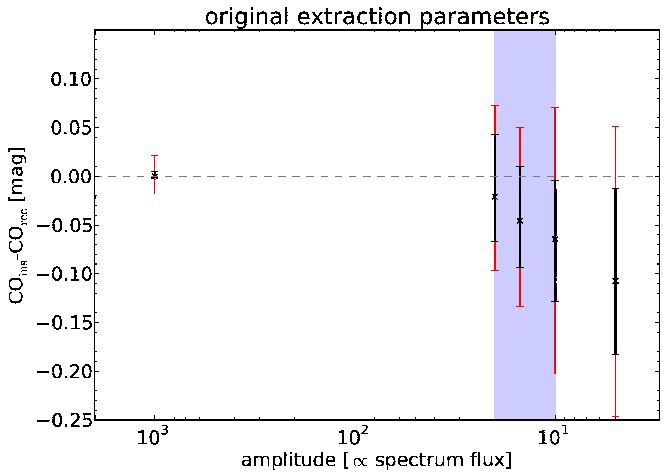

Figure 3.4: Results of the artificial spectrum tests for the extraction method discussed in Section 3.3.1, whose parameters were tailored to reproduce the result of a direct summation extraction in the case of the high signal to noise spectra of the telluric standard stars, while using a minimum number of free parameters. Shown is the difference between inserted and recovered CO index as a function of amplitude of the inserted spectra. Crosses denote the mean of 407 simulations at each amplitude. The ranges containing 68.3 per cent and 99.7 per cent of the simulation results are indicated as thick black and thin red error bars. A deviation of zero is indicated by the dashed horizontal line. From left to right the signal to noise ratio decreases. The shaded area corresponds to the approximate flux level of S928 on the high-flux side and S999 on the low-flux side. It is apparent that the measurement systematically depends on the amplitude of the artificial spectra. At the flux levels of our Virgo UCD spectra, the mean of the recovered CO index is systematically too low, indicating that the deviation of the CO index of S999 is due to systematics.

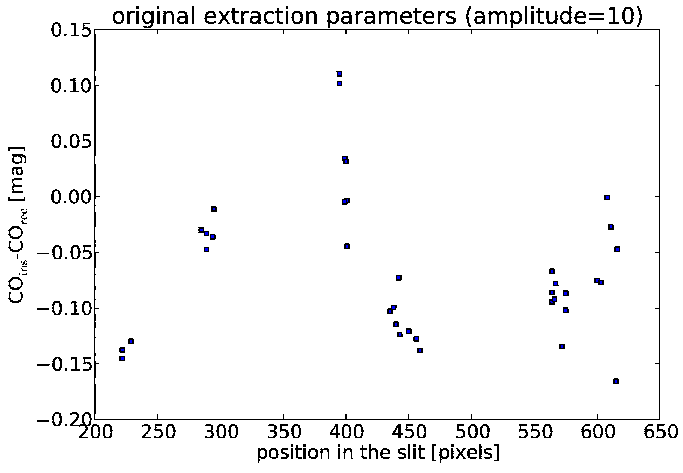

Figure 3.5: The deviations between the inserted and recovered CO index and their dependence on the position in the slit. The position refers to the position in pixels on the first exposure of an arbitrary reference observation. Individual points correspond to sets of simulated artificial spectra with an amplitude of 10 (see Fig. 3.4), which corresponds approximately to the flux level of the S999 spectrum. The deviations are correlated with the position on a scale of several tens of pixels, but no smooth trend is visible. The latter would suggest an imperfect subtraction of the M 87 background as a cause for the systematics.

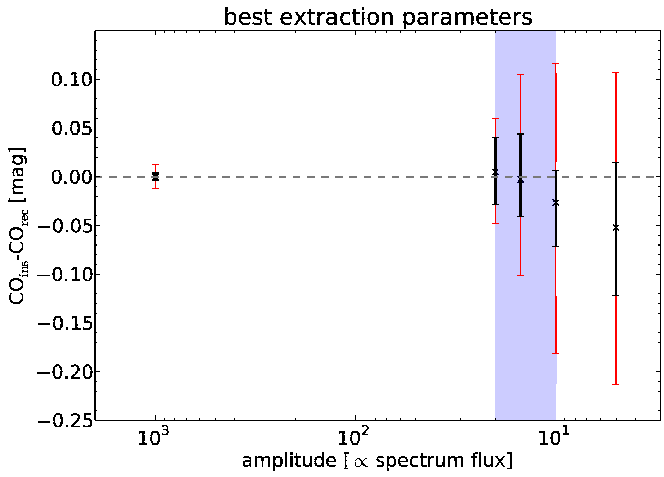

Figure 3.6: Same as Fig. 3.4, but for extraction parameters that were fine-tuned in order to minimise the deviation between the inserted and recovered CO index of the artificial spectra. While the systematics are smaller than with the original extraction parameters (Fig. 3.4), they are still clearly present at the approximate flux level of the spectrum of S999, which corresponds to the right edge of the shaded region.

instead of a linear fit to the background on both sides of the spectrum, estimates the background from a robust mean of the pixel values in the sky window (cf. Press et al. 2007, chapter 15). And we experimented with imposing regularity constraints on the shape of the profile at each wavelength by requiring that it be described by a sum of Gaussians, whose centres, relative amplitudes and widths were described by low-order polynomials along the wavelength direction. We found that none of these modified extraction procedures produced entirely unbiased results. The results for the best (in terms of producing the least systematics) extraction parameters of our original routine are shown in Fig. 3.6. In this figure, the systematic deviations of recovered CO index from the inserted value at low flux levels are smaller than in Fig. 3.4, but are still clearly present.

A method that successfully recovers the inserted CO index was finally found by deviating entirely from the classical order of spectroscopic data analysis. A schematic of this classical method that we discussed in the previous Sections is shown in the left panel of Fig. 3.7. The critical step of spectrum extraction (highlighted in red in the schematic) takes place after the basic data reduction and therefore occurs relatively early in the processing. However, the measurement of the photometric CO index involves a severe amount of stacking and binning in the subsequent steps. Therefore, applying all possible binning steps to the data first could stabilise the fragile extraction (we acknowledge Thorsten Lisker, priv. comm., a discussion with whom inspired this approach). To achieve this, we used the steps that are shown as a schematic in the right panel of Fig. 3.7: We multiplied each row of the combined frames produced in the basic data reduction with the telluric and instrument response function, and then averaged these frames of each of the eleven observations of the Virgo UCDs using the IRAF task IMCOMBINE, rejecting the highest and lowest of the eleven pixels at each position to reject outliers. We then summed these two-dimensional spectra along the columns corresponding to the continuum and feature wavelength bands of the CO index (Eq. (3.4)). This produces two collapsed two-dimensional frames with a spatial dimension (position along the slit) and a spectral dimension that is only one pixel long. On these frames, we subtracted a linear fit to the background determined from sky windows on both sides of the spectrum profiles. We then measured the flux of the length-one spectra by summing in the position direction over the resulting sky-subtracted spectrum profiles. The borders of the summation window were defined by the loca-

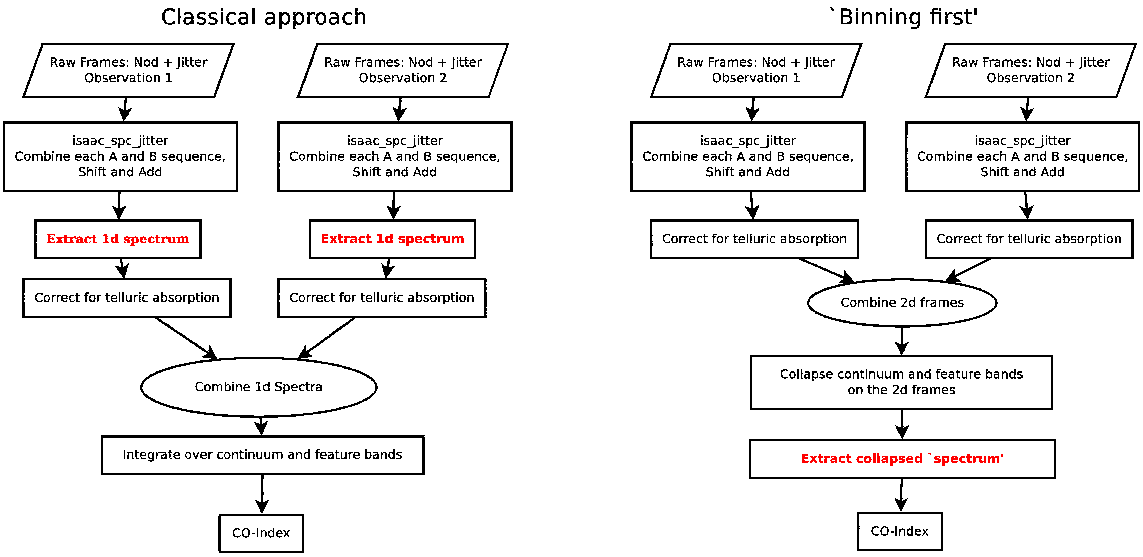

Figure 3.7: Schematic of the classical spectrum extraction and the 'binning first' method. While in the classical method, 1d-spectra are extracted from the combined frames of each observation (the representative case of two observations is shown), in the 'binning first' method, we defer the actual extraction until after all possible binning steps. In the case of the NGC 5128 targets, which were observed only once, the combination step (the fifth step in the classical and the fourth step in the 'binning first' method) is omitted.

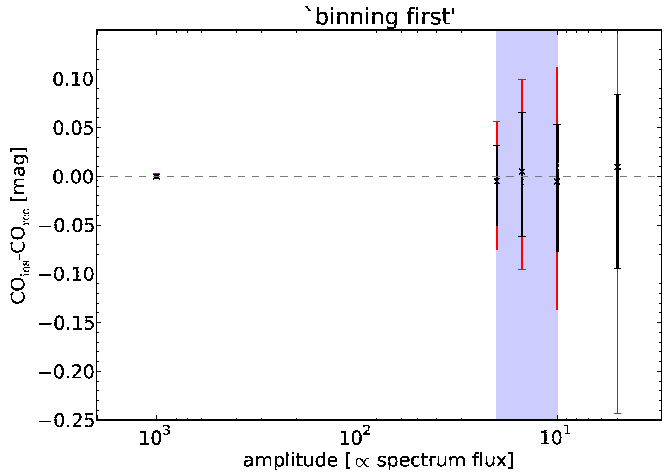

Figure 3.8: Results of the artificial spectrum tests when using the 'binning first' method (see text and Fig. 3.7) to measure the CO index. As in Figs. 3.4 and 3.6, crosses denote the mean difference between the inserted and recovered CO index of 407 simulations at each amplitude and ranges containing 68.3 per cent and 99.7 per cent of the simulation results are indicated as thick black and thin red error bars. Compared to the methods using the classical order of spectroscopic analysis, the 'binning first' method is not affected by the systematics that are seen in Figs. 3.4 and 3.6. At the flux level of the observed S928 and S999 spectra (indicated by the shaded region), the mean of the artificial spectrum results is in excellent agreement with the inserted value.

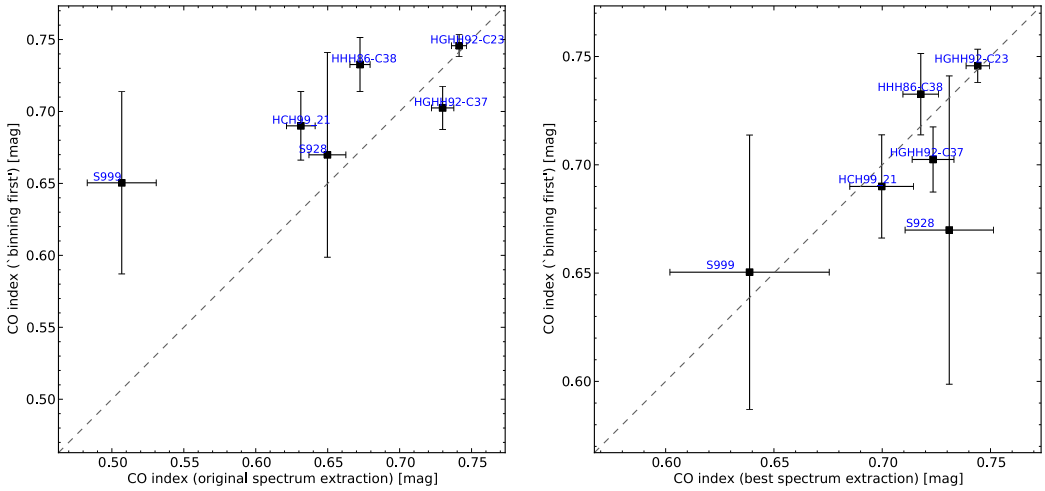

Figure 3.9: Comparison of the CO index of the Virgo UCDs and the NGC 5128 GCs/UCDs measured with different techniques. In both panels the ordinate corresponds to the measurement obtained with the 'binning first' method, which showed no systematic biases in the artificial spectrum tests. The left panel compares this to the measurement obtained with the classical approach to measuring spectral indices and with extraction parameters optimised for a low number of free parameters and high signal to noise standard star spectra. The right panel compares the 'binning first' result to the classical spectrum extraction with extraction parameters optimised to yield low systematics in the artificial star tests. As suggested by the artificial spectra simulations, the original measurement is significantly biased towards a low CO index. The 'best' spectrum extraction shown in the right panel shows better agreement with the 'binning first' method, even though the artificial spectrum tests showed that systematics are still present with this method.

tion where the flux had dropped to 1/8 of its value at the peak of the profile. The latter method was empirically determined to yield the most stable results on the artificial spectra. Figure 3.8 shows the results of applying this method to the artificial spectra. It is apparent that the systematic dependence of the recovered CO index on the spectrum amplitude that was seen in Figs. 3.4 and 3.6 is no longer present. Therefore, this 'binning first' method yields an unbiased measurement of the CO index.

We measured the CO index of our science targets using this 'binning first' method and adopted the results as our final measurement. Uncertainties on the CO index were estimated as the standard deviations of the results from applying the method also to the 100 realisations that were created to derive variance maps for each combined frame in Section 3.3.1. A comparison of the results obtained with the 'binning first' method and with the classical method is shown in Fig. 3.9. The left panel shows the 'binning first' measurement versus the measurement using the original extraction parameters that were tailored to reproduce with a minimum number of free parameters an unbiased spectrum for the high signal to noise standard star observations. As was suggested by the artificial spectrum tests, the original method is systematically biased towards measuring a low CO index. The right panel of Fig. 3.9 shows the 'binning first' CO index versus that obtained with the classical method and extraction parameters specifically tailored to minimise the systematics in the artificial spectrum tests. The results of both methods agree within their uncertainties. Nevertheless, since the artificial spectrum tests revealed that systematics were still present in this latter method, we concluded that the more reliable 'binning first' results are preferable even though their statistical uncertainties are somewhat larger.

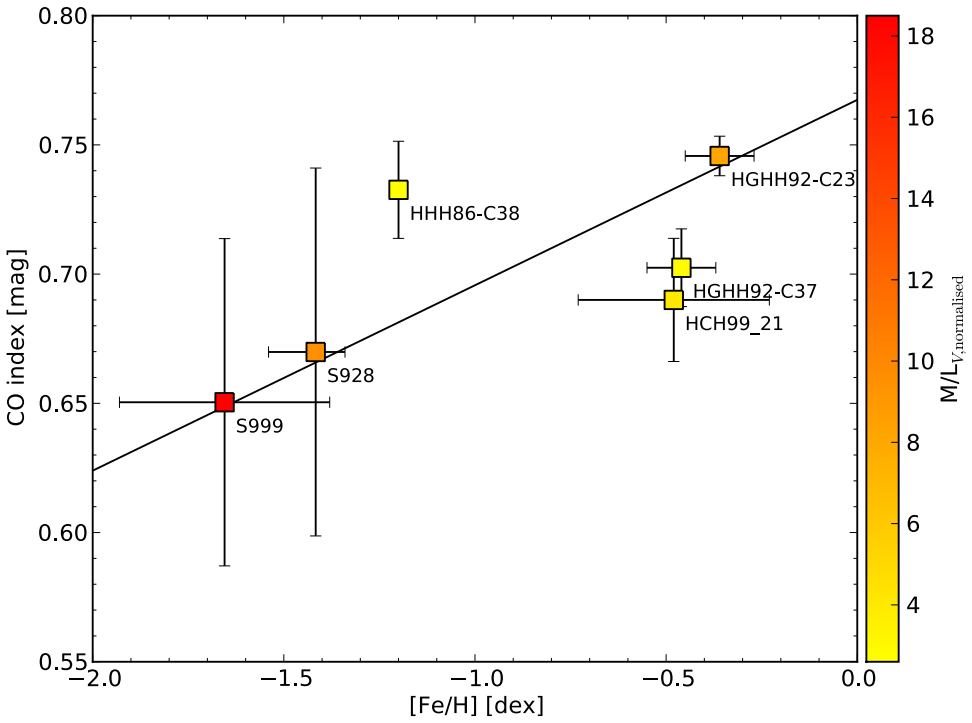

Figure 3.10: The CO index measured with the 'binning first' method versus the metallicity of our targets. Filled squares correspond to the individual targets that are also labelled. The colour of the squares refers to the normalised mass to light ratio of the object on the colour scale given on the right side. The black line has the slope of the empirical relation for Galactic globular clusters between CO and [Fe/H] given by Frogel et al. (2001). The offset in CO-direction corresponds to the zeropoint of the CO index, CO_0, and was defined by a χ^2-fit to all our data points (Eq. (3.6)). Compared to our initial results, the UCD with the highest mass to light ratio, S999, no longer shows a significantly lower CO index than this average relation. Also the CO index of the other observed objects is compatible within $\lesssim 3\sigma$ with this average relation.

3.4 Discussion

Our final measurement of the CO index of the Virgo UCDs and the NGC 5128 GCs/UCDs versus their metallicity is shown in Fig. 3.10. Uncertainties on the CO index were estimated using 100 Monte Carlo realisations of each observation as described in the previous section. As in Fig. 3.3, the colour of the data points gives the normalised mass to light ratio according to the colour scale shown on the right and the individual objects are labelled. The adopted metallicities are the same as in Section 3.3.3, error bars represent the uncertainties of the spectroscopic metallicities for HCH99-21, HGHH92-C23 and -C37, and the range of metallicity measurements in the case of S928 and S999. The line shown in Fig. 3.10 has a slope corresponding to the empirical relation between [Fe/H] and the CO index of Galactic globular clusters (Frogel et al. 2001, eq. (5)). Its offset in CO-direction, or equivalently the zeropoint CO_0 between our idealised CO index and the one measured by photometric narrow band filters (Eq. (3.5)), was determined via the χ^2-minimisation given by Eq. (3.6). This yielded a zeropoint of $CO_0 = 0.62 \pm 0.01$ mag.

All of our observed targets show a CO index compatible within $\lesssim 3\sigma$ with the empirical relation. In particular, compared to the initial results shown in Fig. 3.3, the UCD with the highest measured mass to light ratio, S999, shows no longer a significantly weaker CO index. Also S928 and HGHH929-C23, which have a mass to light ratio higher than predicted by population synthe-

sis models, are in excellent agreement with the empirical trend of the CO index with metallicity. Hence, our results lend no support to the scenario proposed by Mieske & Kroupa (2008) that the high dynamical mass to light ratios in UCDs could be caused by an overabundance of low-mass stars.

Mieske & Kroupa (2008) gave an empirical estimate of the expected deviation of the CO index, if the high mass to light ratios of UCDs were due to low-mass stars. This first-order estimate is based on the average K-band mass to light ratio of globular clusters, $\mathrm{M/L}_K = 2.75\,\mathrm{M}_\odot\,\mathrm{L}_\odot^{-1}$, and an empirical estimate of the K-band mass to light ratio of a population of low-mass stars (a population of stars with a mass function of slope $0 < \alpha < 1.3$ and masses of $m < m_{\mathrm{cut}}$, with a high-mass cut-off at $m_{\mathrm{cut}} = 0.5\text{-}0.7\,\mathrm{M}_\odot$), for which they obtained $\mathrm{M/L}_{K,\mathrm{lms}} = 4.5\text{-}9\,\mathrm{M}_\odot\,\mathrm{L}_\odot^{-1}$. They used these mass to light ratios to infer the fraction of the low-mass stellar population required to explain the high mass to light ratios of UCDs. By assuming a CO index for the low-mass stellar population of $\mathrm{CO}_{\mathrm{Frogel,lms}} = -0.05\,\mathrm{mag}$ and the $\mathrm{CO}_{\mathrm{Frogel}}([\mathrm{Fe/H}])$ relation given by Frogel et al. (2001) for a canonical IMF stellar population, they predicted that the CO index should show a deviation of $\gtrsim 0.05\,\mathrm{mag}$ for the UCDs with the highest mass to light ratios, if the latter were due to low-mass stars.

Our observations were designed to achieve the necessary accuracy of $< 0.05\,\mathrm{mag}$ on the CO index measurement for the faintest targets, S928 and S999, and the statistical uncertainties on our initial measurement are within this expected range (cf. Fig. 3.3). However, as we have shown, systematic biases affect this classical approach to analysing the spectra. On the other hand, the results obtained with the unbiased method that we devised unfortunately do not reach the required precision. Therefore, while our non-detection of a deviating CO index in S928 and S999 does not support the bottom-heavy mass function scenario, it also does not place a strong constraint to exclude this scenario.

A stronger constraint comes from the NGC 5128 GCs/UCDs that have uncertainties smaller than the expected deviations. HGHH92-C23, which has a high normalised mass to light ratio of $\mathrm{M/L}_{V,\mathrm{norm}} = 8.1$, has a higher CO index than the similar metallicity objects HGHH92-C37 and HCH99-21. This difference is in the opposite sense of the deviation predicted by the bottom-heavy mass function scenario. As the measurements of the three objects are compatible within $\sim 2-3\sigma$, the bottom-heavy mass function scenario cannot be ruled out with high confidence, but is clearly also not supported by our data.

4

The velocity dispersion and mass function of the outer halo globular cluster Palomar 4[1]

4.1 Introduction

This chapter presents the internal velocity dispersion, the stellar mass function and total stellar mass of the remote halo globular cluster Palomar 4 (Pal 4). With a Galactocentric distance of 103 kpc (see Section 4.4.2) Pal 4 is the second to outermost halo GC after AM 1 (at 123 kpc according to the 2010 edition of the Galactic GC data base by Harris 1996). Pal 4 also is among the most extended Galactic GCs: its half-light radius of 18 pc (Section 4.4.1) is more than five times larger than that of 'typical' GCs (e.g. Jordán et al. 2005). The cluster thus has a size comparable to some of the Galaxy's ultra-faint dwarf spheroidal satellites, but is at the same time brighter by ~ 2 mag in V than these (e.g. Belokurov et al. 2007).

As discussed in Section 1.3.2, the velocity dispersion profile of remote GCs can be used to distinguish between classical and modified Newtonian dynamics (MOND). This is because the external acceleration due to the Galaxy experienced by stars in such clusters is lower than the critical acceleration $a_0 \simeq 1 \times 10^{-8}\mathrm{cm\,s^{-2}}$ (e.g. Sanders & McGaugh 2002), below which MOND predicts a deviation from Newtonian dynamics. Section 1.3.2 summarised the previous work in this context, that focused on the massive outer halo cluster NGC 2419 (Baumgardt et al. 2009; Ibata et al. 2011a,b; Sanders 2012a,b) and on the diffuse outer halo GC Pal 14 (Haghi et al. 2009; Jordi et al. 2009; Gentile et al. 2010; Küpper & Kroupa 2010; Sollima et al. 2012). The data on both these clusters favour Newtonian dynamics, but at the same time are not sufficient to confidently rule out MOND. The study of Pal 4 that is presented here continues these efforts to test MOND using *diffuse* GCs in the outer Galactic halo. In these clusters, also the internal acceleration due to the cluster stars themselves is below a_0 throughout the cluster. Therefore, not only the shape of the

[1] The results presented in this chapter are being published as Frank et al. (2012). The work was done in collaboration with Michael Hilker, Holger Baumgardt, Patrick Côté, Eva Grebel, Hosein Haghi, Andreas Küpper and S. G. Djorgovski. The Keck LRIS and HIRES data presented in Sections 4.2.1 and 4.2.2 were reduced by Patrick Côté. The model predictions for Newtonian and MONDian dynamics are the work of Hosein Haghi and based on the N-body simulations presented in Haghi et al. (2011). The simulations on the effects of binaries and mass segregation on the measured velocity dispersion presented in Section 4.5.2 were contributed by Andreas Küpper. Katrin Jordi kindly provided a table of the SDSS-based surface density profile of Pal 4 derived in Jordi & Grebel (2010).

velocity dispersion profile (like in the case of NGC 2419), but also the *global* velocity dispersion of Pal 4 (just like that of Pal 14) can be used to discriminate between MONDian and Newtonian dynamics (Baumgardt et al. 2005; Haghi et al. 2011).

Regarding its horizontal branch, Pal 4 forms a so-called 'second parameter pair' with the equal-metallicity inner halo GC M 5 (e.g. Catelan 2000). Pal 4 has a red horizontal branch and M 5 a blue one. One of the differences between M 5 and Pal 4 is their age. Pal 4 was found to be ∼1-2 Gyr younger (∼10-11 Gyr) than M 5 (Stetson et al. 1999; VandenBerg 2000). As mentioned in Section 1.3, such relatively young halo clusters are thought to have been accreted from disrupted dwarf satellites. In this context, Law & Majewski (2010) discuss Pal 4's possible association with the Sagittarius stream, but conclude that this is unlikely based on current observational data and models of the stream's location. In deep wide-field imaging of the cluster and its surroundings, Sohn et al. (2003) find indications for the presence of extra-tidal stars, but no significant detection of a stream. They attribute this extra-tidal overdensity to internal evaporation and tidal loss of stars at the cluster's location in the Galaxy.

The most recent determination of the chemical composition of Pal 4 was presented by Koch & Côté (2010). According to their abundance analysis of the same spectra that we use here for our kinematical study, Pal 4 has a metallicity of [Fe/H]$= -1.41 \pm 0.17$ dex and an α-element enhancement of [α/Fe]$= 0.38 \pm 0.11$ dex. The metallicity is compatible with a previous spectroscopic measurement of [Fe/H]$= -1.28 \pm 0.20$ dex by Armandroff et al. (1992).

This chapter is organised as follows. Section 4.2 describes describe the spectroscopic and photometric data and their reduction. Section 4.3 presents stellar radial velocities and the cluster's systemic velocity and velocity dispersion. The cluster's surface brightness profile, mass function and total stellar mass is derived in Section 4.4 that also presents evidence for mass segregation in the cluster. A discussion of the results is given in Section 4.5.

4.2 Observations and Data Reduction

The analysis of the dynamical behaviour of Pal 4 is based on spectroscopic and photometric observations. The High Resolution Echelle Spectrograph (HIRES) on the Keck I telescope was used to obtain radial velocities and to derive the velocity dispersion of Pal 4's probable member stars. Pre-images for the spectroscopy were obtained with the Low-Resolution Imaging Spectrometer (LRIS) mounted on the Keck II telescope and used to derive the cluster's structural parameters. Both Keck datasets were obtained as part of a larger program dedicated to study the internal kinematics of outer halo GCs (for details of the program see Côté et al. 2002). Archival imaging data obtained with the Hubble Space Telescope's (HST) Wide Field Planetary Camera 2 (WFPC2) were analysed to determine the mass function and total mass of the cluster.

4.2.1 Keck LRIS Photometry

B and *V* images centred on Pal 4 were obtained with LRIS (Oke et al. 1995) on the night of 1999 January 14. In imaging mode, LRIS has a pixel scale of 0.215 arcsec pixel^{-1} and a field of view of 5.8×7.3 arcmin^2. A series of images were obtained in both *V* and *B*, with exposure times of 3×60s and 2×180s, respectively. Conditions during the night were photometric, and the FWHM of isolated stars within the frames was measured to be 0.″65–0.″75. The images were reduced in a manner identical to that described in Côté et al. (2002) using IRAF[2]. Briefly, the raw frames were bias-subtracted and flat-fielded using sky flats obtained during twilight. Instrumental magnitudes

[2]IRAF is distributed by the National Optical Astronomy Observatories, which are operated by the Association of Universities for Research in Astronomy, Inc., under cooperative agreement with the National Science Foundation.

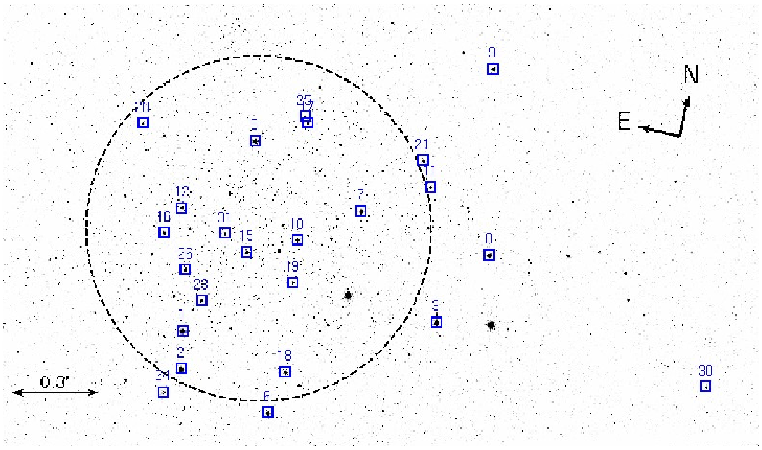

Figure 4.1: Position of spectroscopic target stars on the sky, overlaid on an archival HST Advanced Camera for Surveys (ACS) image (program 10622, PI: Dolphin). The numbering corresponds to the order of objects as listed in Table 4.1. The dotted circle marks Pal 4's half-light radius of 0.6 arcmin, corresponding to 18 pc at a distance of 102.8 kpc.

for unresolved objects in the field were derived using the DAOPHOT II software package (Stetson 1993), and calibrated with observations of several Landolt (1992) standard fields taken throughout the night. The V band magnitudes, which we used to calibrate the cluster's surface brightness profile (Section 4.4.1), were found to agree to within 0.02 ± 0.03 mag with those published by Saha et al. (2005) for stars contained in both catalogues. The final photometric catalogue contained 848 objects detected with a minimum point-source signal-to-noise ratio of S/N = 4 in both filters.

4.2.2 Spectroscopy

On three different nights in February and March 1999, spectra for 24 candidate red giants in the direction of Pal 4 were obtained using HIRES (Vogt et al. 1994) mounted on the Keck I telescope. The targets were selected from the LRIS photometric catalogue. The spectra were taken with the C1 decker, which gives a $0\farcs86$ entrance slit and a resolution of $R = 45000$, and cover the wavelength range from 445 to 688 nm. Their position within the cluster is shown in Fig. 4.1. The exposure times of the spectra were adjusted on a star-to-star basis depending on the individual magnitudes ($17.8 < V < 19.9$ mag), and varied between 300 and 2400 s with a median value of 1200 s. An observation log and the photometric properties of the target stars are given in Table 4.1, their coordinates are given in table 1 of Koch & Côté (2010), and their location in the colour-magnitude diagram (CMD) can be seen in fig. 1 of the same paper. Based on their location in the CMD, five of the sample stars are probable AGB stars, the remaining 19 stars lie on the RGB.

The spectra were reduced entirely within the IRAF environment, in a manner identical to that described in Côté et al. (2002). The radial velocities of the target stars were obtained by cross-correlating their spectra with those of master templates created from the observations of IAU standard stars, which were taken during the seven observing runs (13 nights) that were devoted to the HIRES survey of globular clusters in the halo. From each cross-correlation function, we measured the heliocentric radial velocity, v_r, and $R_{\rm TD}$, the Tonry & Davis (1979) estimator of the strength of the cross-correlation peak. Since an important factor in the dynamical analysis of low-mass clusters is an accurate determination of the radial velocity uncertainties, $\varepsilon(v_r)$, 53 repeat measurements for 23 different stars, distributed over different target GCs, were accumulated during the same observing runs. The r.m.s. of the repeat measurements was used to calibrate a relation between $\varepsilon(v_r)$ and $R_{\rm TD}$. Following Vogt et al. (1995), we adopt a relationship of the form $\varepsilon(v_r) = \alpha/(1+R_{\rm TD})$, where

$R_{\rm TD}$ is the Tonry & Davis (1979) estimator of the strength of the cross-correlation peak, and find $\alpha \simeq 9.0\,{\rm km\,s^{-1}}$. The resulting radial velocity uncertainties for our Pal 4 target stars range from 0.23 to 1.31 $\rm km\,s^{-1}$ (see Table 4.1).

4.2.3 HST Photometry

We used archival HST images of Pal 4 obtained with the WFPC2 in GO program 5672 (PI: Hesser, cf. Stetson et al. 1999). The dataset consists of F555W (V) and F814W (I) band exposures and is the deepest available broad-band imaging of the cluster. The individual exposure times are 8×30 s, 8×60 s and $8\times\sim1800$ s in each filter, amounting to total exposure time of ~4.1 h per filter.

PSF-fitting photometry was obtained using the HSTPHOT package (Dolphin 2000). In order to refine the image registration, HSTPHOT was first run on the individual images and the resulting catalogues were matched to one of the deep F555W images as a reference using the IRAF tasks XYXYMATCH and GEOMAP. The derived residual shifts were used for a refined cosmic ray rejection with HSTPHOT's CRMASK task, and as an input for the photometry from all images. The latter was obtained by running HSTPHOT simultaneously on all frames with a deep F555W image as the reference or detection image.

To select bona-fide stars from the output catalogue, the following quality cuts were applied (for details, see the HSTPHOT user manual): a type parameter of 1 (i.e. a stellar detection), abs(sharpness)< 0.2, $\chi < 2.0$, and in both filters a crowding parameter < 1.5 mag and a statistical uncertainty in the magnitude < 0.2 mag. The resulting CMD, containing 3878 stars, is shown in Fig. 4.2. To assess the photometric uncertainties and completeness of the catalogue, HSTPHOT was used to perform artificial star tests with ~ 275000 fake stars. We used the program's option to create artificial stars with distributions similar to the observed stars, both in the CMD, and on the WFPC2 chips, in order to efficiently sample the relevant parameter space. In artificial star mode, the program inserts, star by star, stellar images with given magnitudes and position in all of the frames (using the empirically adjusted PSF for each frame that is constructed during the photometry run) and then performs photometry on this stellar image. It yields as a result a catalogue containing the inserted magnitudes and positions, as well as the recovered photometry for each fake star. We applied the same quality cuts to the artificial star catalogue as were used to select bona-fide stars in the observed catalogue. Photometric uncertainties in a given region of the CMD and on the sky were then estimated from the differences between inserted and recovered magnitudes. The photometric completeness was estimated from the ratio of the number of recovered to the number of inserted artificial stars. The completeness, within the colour limits used for our analysis of the cluster's mass function (see Section 4.4.3), as a function of F555W magnitude is shown in the top panel of Fig. 4.3. The different curves correspond to the completeness in different radial ranges, containing each one fourth of the observed stars. At the faint end, the completeness in the inner two annuli drops somewhat faster with decreasing luminosity, which reflects the effect of crowding caused by the higher surface density of stars in the cluster's centre.

The geometric coverage of the WFPC2 photometry was quantified in the following way. For both filters, we ran multidrizzle (Koekemoer et al. 2006) on all frames in that filter, to obtain geometric distortion-corrected combined frames. As a small-scale dither pattern was used in the observations, we then created a coverage mask by selecting all pixels that received, in both filters, at least 25 per cent of the total exposure time. This information can be retrieved from the weight map extension of the drizzled frames. As HSTPHOT uses a single deep exposure as a detection image for the photometry, we additionally required that pixels flagged as covered in the coverage mask were covered also by one of the four chips in that exposure. For this, in order to avoid possible completeness artifacts near chip borders, the chips were assumed to be smaller by 5 pixels on each side. The area covered by the WFPC2 photometry as a function of distance from the cluster's centre

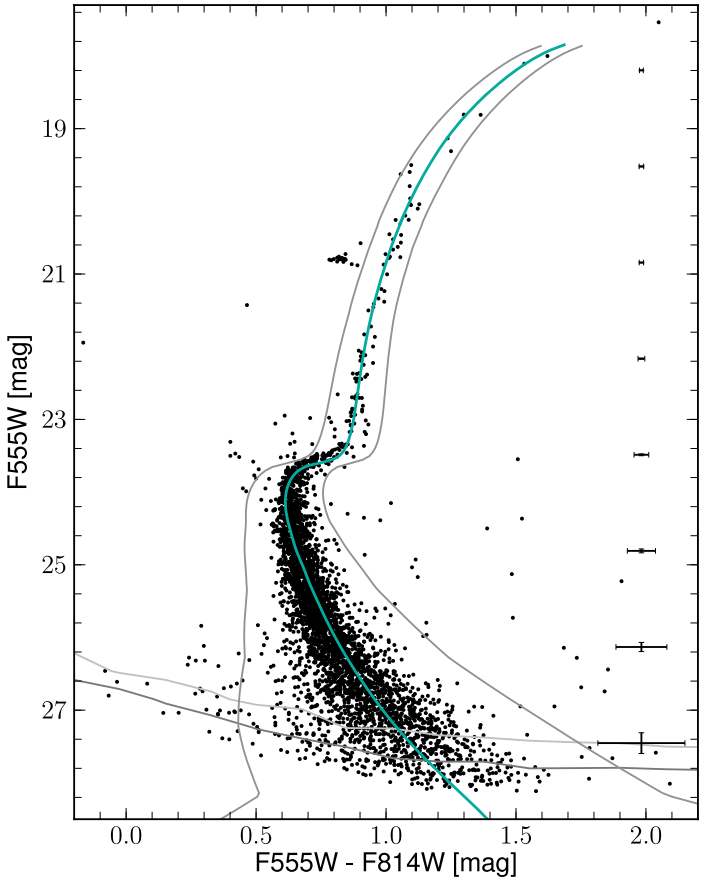

Figure 4.2: Observed colour-magnitude diagram of Pal 4. Errorbars on the right represent the photometric errors derived from artificial star tests. The grey lines at the faint end represent the 80 per cent (light grey) and 50 per cent (dark grey) completeness contours. The isochrone (cyan line) corresponds to an age of 11 Gyr, a metallicity of [Fe/H]=−1.41 dex and an α-enhancement of [α/Fe]=+0.4 dex, shifted to the cluster's distance of 20.06 mag at a reddening of E(B-V) = 0.023 mag. Thin grey curves to the left and to the right of the isochrone represent the colour limits used for our analysis of the cluster's mass function (see Section 4.4).

was then expressed as the ratio of the area covered by the coverage mask to the total area of a given radial annulus around the cluster's centre. This is shown in the bottom panel of Fig. 4.3. The stellar positions in the photometric and artificial star catalogues were transformed to the same drizzled coordinate system and to be consistent, stars falling on pixels marked as 'not covered' in the coverage mask were rejected. In order to select radial subsamples of stars, we determined the cluster's centre by fitting one-dimensional Gaussians to the distributions of stars projected onto the x and y axes (e.g. Hilker 2006). Since the cluster's centre is close the PC chip's border in the WFPC2 pointing, for the purpose of determining the centre, we performed photometry on more suitable archival data taken with the Wide Field Channel (WFC) of HST's Advanced Camera for Surveys (ACS) in GO program 10622 (PI: Dolphin, cf. Saha et al. 2011). We used HSTPHOT's successor DOLPHOT on the program's F555W (two exposures of 125 s each) and F814W (2×80 s) exposures to obtain a photometric point source catalogue, determined the centre form these data and transformed its coordinates to the coordinate system of the WFPC2 catalogue.

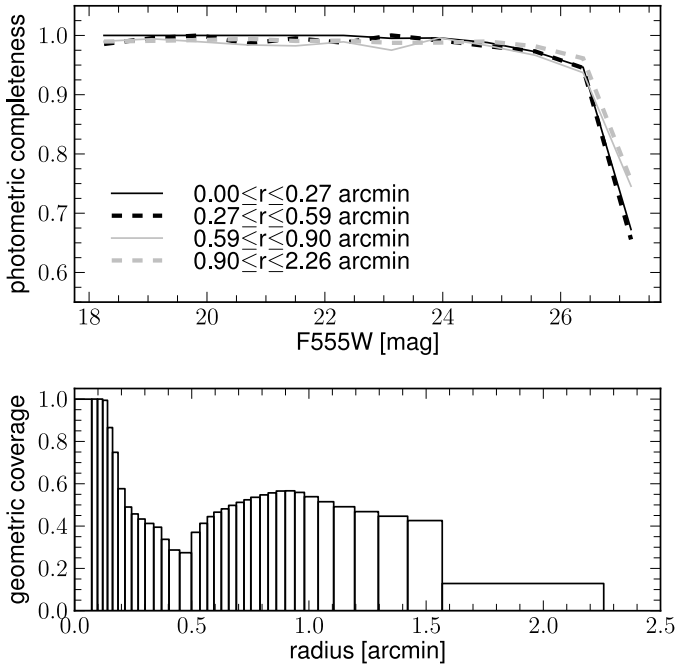

Figure 4.3: Photometric and geometric completeness of the WFPC2 photometry. Top: The photometric completeness inside the colour limits used for our analysis (see Fig. 4.2) as a function of F555W magnitude derived from the artificial star tests is shown for four radial ranges as denoted in the plot. The radial ranges are defined to contain one fourth of the observed stars each. Bottom: The geometric coverage of the WFPC2 catalogue as a function of radius in radial bins containing each one 36th of the observed stars. The fraction represents the area covered by the WFPC2 pointing in a given radial annulus divided by the total area of the annulus.

4.2.4 Foreground contamination

As Pal 4 lies on "our side" of the Galaxy at high Galactic latitude (l ∼202 deg, b ∼72 deg), the expected contamination by foreground stars in our spectroscopic and photometric samples is low. To estimate the fraction of foreground contamination, we used the Besançon model of the Galaxy (Robin et al. 2003) to obtain a photometric and kinematic synthetic catalogue. The model was queried for stars out to 200 kpc in the direction of Pal 4. For better number statistics, we used a solid angle of 50 square degrees and the model's 'small field' mode that simulates all stars at the same location and thus ensures that any spatial variation in the foreground that could be present in such a large field is neglected. The remaining model parameters, such as the extinction law and spectral type coverage, were left at their default values.

For a generous estimate of possible foreground contaminants in our spectroscopic sample, we selected from the obtained synthetic catalogue stars with magnitudes and colours in the range of the spectroscopic targets ($17.5 \leq V \leq 20.0$ mag, $0.8 \leq B-V \leq 1.7$ mag, cf. Table 4.1). The top panel of Fig. 4.4 shows the resulting distribution of stars per square degree as a function of radial velocity. Red vertical lines denote the velocity range of the cluster's systemic velocity plus and minus three times its velocity dispersion (derived in Section 4.3). Within this velocity range, ∼3 stars per deg^2 lie inside the colour and magnitude range. Scaled to the solid angle covered by the spectroscopic sample (assuming a circular aperture with a radius equal to the largest cluster-centric distance of our sample stars, ∼ 100 arcsec), this amounts to ∼ 0.01 stars. It is thus unlikely that the

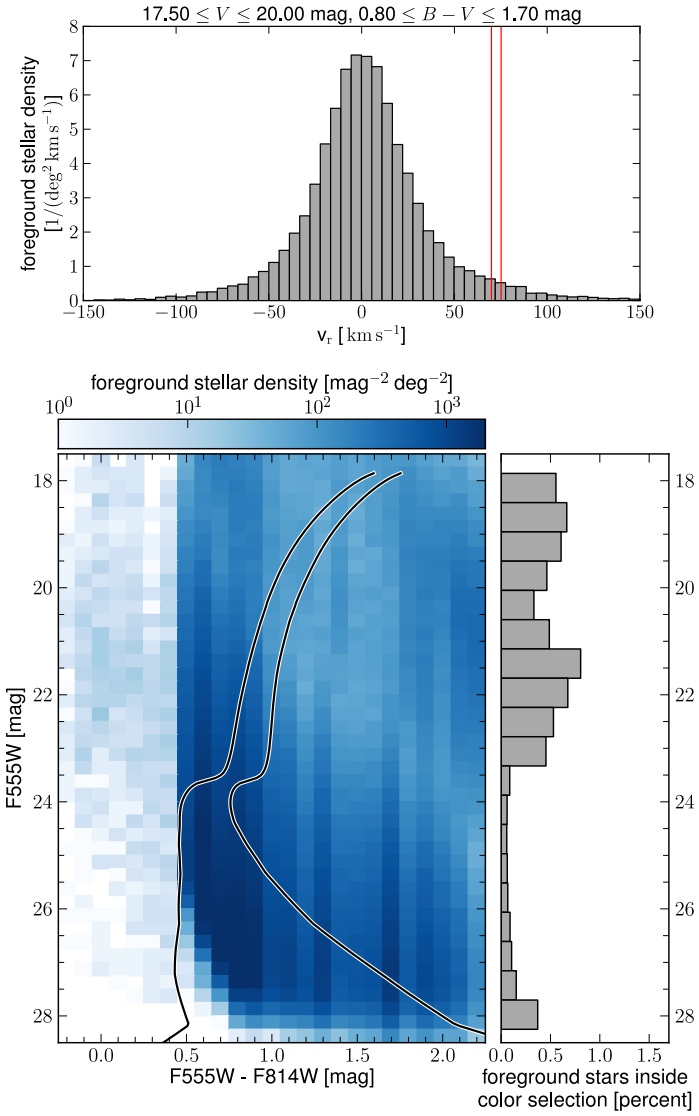

Figure 4.4: Expected contamination by foreground stars based on the Besançon model. Top: The distribution of foreground stars having magnitudes and colours in the range of our spectroscopic targets as a function of radial velocity. Red vertical lines denote the velocity range of interest. Bottom: The left panel shows the density of foreground stars in the colour-magnitude diagram. The black-on-white lines correspond to the region of the CMD used to estimate the mass function of Pal 4 (Section 4.4.3). Within these colour-limits, the fraction of expected foreground stars in the photometric sample, averaged over 0.5 mag in F555W and shown in the right panel, is below one per cent.

spectroscopic sample contains any foreground stars.

To quantify the expected foreground contamination in the photometric catalogue, we transformed the V and I magnitudes of the synthetic foreground stars to F555W and F814W magnitudes, by inverting the Holtzman et al. (1995) WFPC2 to *UBVRI* transformations. Photometric errors and completeness were then taken into account in the following simple way: for each synthetic foreground star, we selected from our artificial star catalogue a random one of the 100 nearest artificial stars in terms of inserted magnitudes. Here 'nearest' refers to the Euclidean distance in the (F555W, F814W)-plane[3]. If the chosen artificial star was recovered, we added its photometric errors (i.e. recovered minus inserted magnitude) to the magnitudes of the synthetic star; if the artificial star was not recovered, we rejected the synthetic foreground star. To take into account the variation of completeness and photometric errors as a function of distance from the cluster centre, we assumed the synthetic foreground stars to be homogeneously distributed on the sky and performed the procedure independently on 30 radial sub-samples of the foreground and artificial star catalogues. This results in a foreground catalogue that reproduces the photometric errors and completeness limits of our WFPC2 catalogue and their variation with distance from the cluster centre. The density of foreground stars is shown in the bottom left panel of Fig. 4.4. The two-dimensional histogram was obtained with bins of 0.1 mag in colour and 0.25 mag in magnitude and scaled to units of stars per square degree on the sky and square magnitude in the CMD. Selecting stars only in the region of the CMD that was used to derive the mass function of Pal 4 (denoted by the black-on-white lines in the density plot; see Section 4.4.3) and scaling to the effective area of the WFPC2 field, ~ 4.76 arcmin^2, we calculated that the expected fraction of foreground stars in the photometric sample is below one per cent over the whole luminosity range and therefore negligible. This is shown in the bottom right panel of Fig. 4.4.

4.3 The systemic velocity and the velocity dispersion

Table 4.1 summarises the results of our radial velocity measurements for Pal 4 member stars. Columns (1)–(10) of this table record the names of each program star (second column from identification by Saha et al. 2005), distance from the cluster centre, V magnitude, $(B-V)$ colour (both from Saha et al. 2005), HIRES exposure time, the heliocentric Julian date of the observation, the Tonry & Davis $R_{\rm TD}$ value, the heliocentric radial velocity, and the error-weighted mean velocity. Six of the stars in our Pal 4 sample were observed twice, and two stars were observed three times. For most stars the difference in radial velocity between the individual measurements is below $1\,{\rm km\,s^{-1}}$. Two stars show a larger discrepancy of $1.65\,{\rm km\,s^{-1}}$ (Pal4-10) and $4.51\,{\rm km\,s^{-1}}$ (Pal4-12, a likely AGB star), potentially due to binarity. For the latter, the two velocity measurements differ by more than 5σ and the mean of the two measurements stands out in the velocity distribution (see Fig. 4.5). This suggests that the star should probably be excluded as an outlier. Nevertheless, as its mean velocity is still marginally consistent with the velocity distribution (see below), we will present our kinematical analysis with and without this star (named in the following 'star 12').

The mean heliocentric radial velocity and velocity dispersion of Pal 4 were calculated using the maximum likelihood formulae that Pryor & Meylan (1993) derived for a Gaussian velocity distribution and Gaussian uncertainties on the individual radial velocity measurements. Using the 23 clean member stars from Table 4.1 (i.e. excluding star 12), we obtain a mean cluster velocity

[3]Selecting the n nearest artificial stars from a large catalogue that are nearest to a given (F555W, F814W)-pair for a large number of such pairs can be done efficiently by initially constructing a k-d tree (e.g. Berg 2008) of the artificial star (F555W, F814W)-pairs. Since both the artificial star catalogue and the synthetic foreground catalogue contained $\sim 7\times10^5$ stars, this was done here and resulted in a considerable speedup in computation. The k-d tree was then queried for the 100 nearest neighbours for each of the foreground star (F555W, F814W)-pairs.

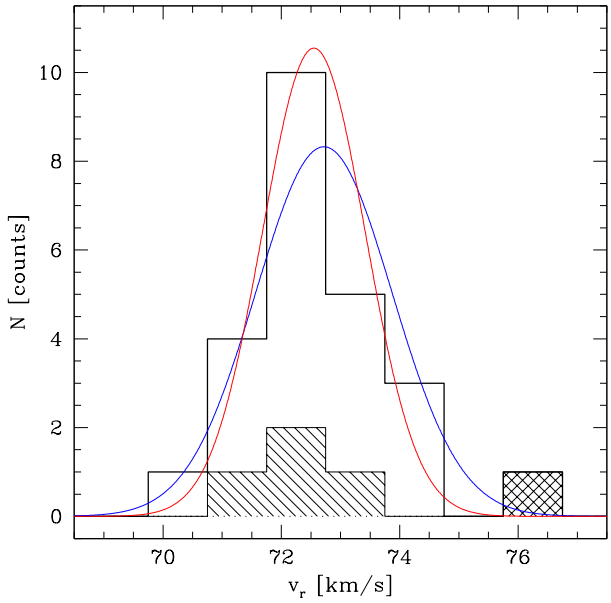

Figure 4.5: Histogram of radial velocities for all 24 sample stars. The hashed areas correspond to AGB stars, the cross-hashed area corresponds to star 12 at $\sim 76\,\mathrm{km\,s^{-1}}$. The blue and red curves are the maximum-likelihood Gaussian representations of the *intrinsic* velocity distribution for the total sample of 24 stars and for the sample without star 12, respectively that were derived using the Pryor & Meylan (1993) method (see text).

of $v_r = 72.55 \pm 0.22\,\mathrm{km\,s^{-1}}$ and an intrinsic velocity dispersion of $\sigma = 0.87 \pm 0.18\,\mathrm{km\,s^{-1}}$. When including star 12, the mean velocity is $v_r = 72.72 \pm 0.27\,\mathrm{km\,s^{-1}}$ and the velocity dispersion rises to $\sigma = 1.15 \pm 0.20\,\mathrm{km\,s^{-1}}$. The cluster's mean radial velocity is consistent with the determination by Armandroff et al. (1992), who obtained $v_r = 74 \pm 1\,\mathrm{km\,s^{-1}}$.

Table 4.1: Radial velocities of candidate red giants in Pal 4. (a)Probable AGB stars based on their location in the CMD.

ID	ID_{Saha}	radius (arcsec)	V (mag)	$(B-V)$ (mag)	T (s)	HJD 2,450,000+	R_{TD}	v_r (km s^{-1})	$\langle v_r \rangle$ (km s^{-1})
Pal4-1	S196	23.3	17.81	1.46	300	11220.9836	18.91	73.59±0.45	73.33±0.28
					300	11248.0317	16.50	72.84±0.52	
					300	11221.1684	18.06	73.45±0.47	
Pal4-2	S169	29.9	17.93	1.46	300	11220.9787	16.61	73.95±0.51	74.42±0.36
					300	11221.1634	16.31	74.90±0.52	
Pal4-3	S277	41.2	17.82	1.66	300	11221.1388	20.09	72.11±0.43	72.11±0.43
Pal4-5	S434	22.9	17.95	1.44	300	11221.1457	17.14	72.24±0.50	72.41±0.41
					300	11222.1754	11.36	72.78±0.73	
Pal4-6	S158	34.7	18.22	1.30	420	11220.9647	18.37	72.34±0.47	72.38±0.33
					420	11248.0018	10.42	72.47±0.79	
					420	11221.1152	15.36	72.39±0.55	
Pal4-7	S381	23.6	18.55	1.19	600	11221.0986	17.44	73.08±0.49	72.73±0.38
					600	11248.0382	14.08	72.21±0.60	
Pal4-8	S364	49.4	18.65	1.17	600	11220.9989	16.59	74.39±0.51	74.39±0.51
Pal4-9	S534	63.1	19.00	1.08	750	11221.0124	14.48	71.56±0.58	71.56±0.58
Pal4-10	S325	8.9	19.09	1.05	900	11220.9880	16.83	70.11±0.51	70.68±0.41
					900	11221.1720	11.86	71.76±0.70	

Continued on next page

Table 4.1 – continued

ID	ID_{Saha}	radius (arcsec)	V (mag)	$(B-V)$ (mag)	T (s)	HJD 2,450,000+	R_{TD}	v_r (km s^{-1})	$\langle v_r \rangle$ (km s^{-1})
Pal4-11[a]	S430	39.2	19.35	0.89	1200	11221.0705	10.12	73.08±0.81	73.08±0.81
Pal4-12[a]	S328	18.1	19.35	0.90	1200	11221.1041	13.09	78.70±0.64	76.22±0.43
					1200	11247.9845	14.50	74.19±0.58	
Pal4-15[a]	S307	2.2	19.38	0.88	1200	11221.0550	9.62	72.33±0.85	72.33±0.85
Pal4-16[a]	S306	19.9	19.43	0.88	1200	11221.0383	13.05	71.09±0.64	71.09±0.64
Pal4-17[a]	S472	28.9	19.45	0.85	1080	11222.0903	11.67	71.87±0.71	71.87±0.71
Pal4-18	S186	26.7	19.48	0.98	1200	11221.1275	12.23	71.17±0.68	71.17±0.68
Pal4-19	S283	10.4	19.53	0.95	1080	11222.0760	10.41	72.75±0.79	72.75±0.79
Pal4-21	S457	40.0	19.64	0.93	1200	11221.0869	9.53	74.41±0.86	74.41±0.86
Pal4-23	S235	15.9	19.70	0.93	1500	11222.1575	12.43	73.23±0.67	73.23±0.67
Pal4-24	S154	36.0	19.74	0.92	1500	11221.1612	13.50	73.00±0.62	73.00±0.62
Pal4-25	S476	29.9	19.77	0.91	1500	11222.1782	9.41	72.84±0.87	72.84±0.87
Pal4-26	S265	15.7	19.83	0.91	1500	11222.1389	11.20	72.44±0.74	72.44±0.74
Pal4-28	S426	35.9	19.87	0.91	1500	11222.1192	5.89	72.20±1.31	72.20±1.31
Pal4-30	S276	99.7	19.89	0.90	1800	11248.0166	9.50	71.33±0.86	71.33±0.86
Pal4-31	S315	7.5	19.89	0.93	1500	11222.1982	10.08	72.38±0.81	72.38±0.81

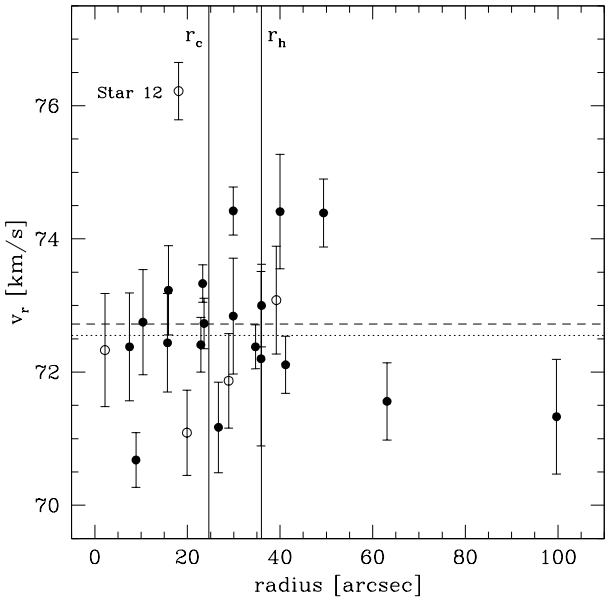

Figure 4.6: Radial distribution of stars with velocity measurements in Table 4.1. The open symbols mark probable AGB stars. The horizontal dotted line marks Pal 4's error-weighted mean systemic velocity without star 12, and the dashed line the velocity including star 12. The core and half-light radii are indicated by the vertical lines.

Figure 4.5 shows the distribution of radial velocities of the 24 cluster members (open histogram). The curves show the maximum-likelihood Gaussian representations of the intrinsic velocity distribution (with and without star 12) using the above values for v_r and σ. As can be seen, the observed radial velocity distribution is well approximated by a Gaussian except for the outlier star 12. For a Gaussian distribution and a sample of 24 stars, one would expect to find a star that is, like star 12, about 3σ away from the mean in only 5 per cent of all cases.

In Fig. 4.6 we show the radial distribution of our measured velocities (star 12 is labelled). The cluster's mean velocity is marked by the dotted (without star 12) and dashed (with star 12) horizontal line. One third of the 24 sample stars are located at radii equal to or greater than the half-light radius. Thus, the measured velocity dispersion is only slightly biased towards the central value. In this plot no clear trend of a decreasing or increasing velocity dispersion with radius is seen. However, our sampling beyond 50 arcsec radius is very sparse with only two measured velocities. Nevertheless, we derived the line-of-sight velocity dispersion profile with running radial bins, each bin containing eight stars. Figure 4.7 shows the resulting velocity dispersion profile. Within a radius of up to 24 arcsec we derived the velocity dispersion either excluding star 12 or including star 12. For the case excluding star 12, we can see a flat velocity dispersion profile that is in good agreement with the expectation from a single-mass, non-mass-segregated King model that is overplotted. When including star 12 one might argue for a declining velocity dispersion profile.

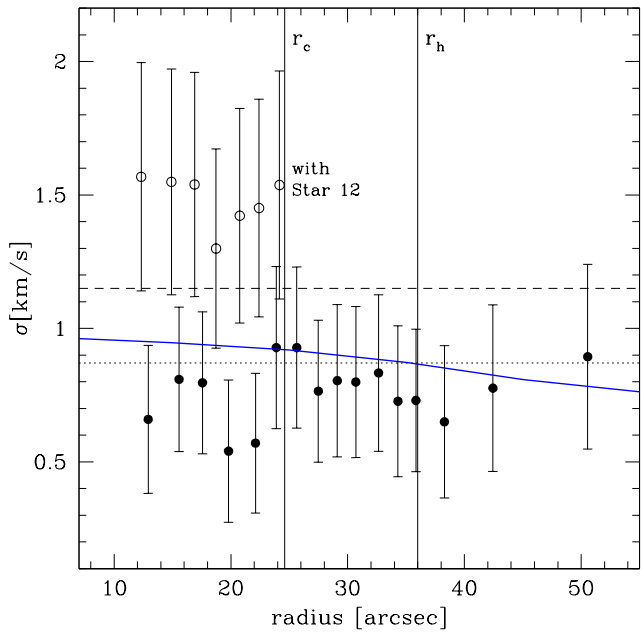

Figure 4.7: Velocity dispersion profile of Pal 4 using running bins with eight stars in each bin. The black filled symbols denote the velocity dispersion without star 12. The open symbols denote these bins where star 12 was included. The dashed and dotted horizontal lines are the average dispersion values if star 12 is included or excluded, respectively. The vertical lines are the core and half-light radii. Shown as blue solid curve is the dispersion profile expected in Newtonian dynamics for a cluster mass of $2.98 \times 10^4\,M_\odot$ and assuming that mass follows the light of the best-fitting King (1966) model derived in Section 4.4.1.

4.4 Photometric results

4.4.1 Surface brightness profile & structural parameters

In the literature there are only few surface brightness profiles and derivations of the structural parameters of Pal 4. As mentioned in the introduction of this Chapter, in a search for extra-tidal features Sohn et al. (2003) used deep wide-field imaging to study the stellar density distribution around Pal 4. Unfortunately, they did not derive a density profile or the cluster's structural parameters, but adopted the structural parameters from the Harris (1996) catalogue. This catalogue in its 2003 version quoted the structural parameters derived by Trager et al. (1995) from a compilation of surface photometry. In its updated 2010 version, the Harris (1996) catalogue refers to the reanalysis of the Trager et al. (1995) data presented by McLaughlin & van der Marel (2005). Recently, in a search for tidal tails around Galactic GCs, Jordi & Grebel (2010) derived surface density profiles for 17 GCs, including Pal 4. These are based on star counts in the Sloan Digital Sky Survey (SDSS DR7; Abazajian et al. 2009) catalogue and the PSF-fitting photometry of SDSS imaging of the inner regions of Galactic GCs by An et al. (2008). However, the authors note that Pal 4 is the most distant GC in their sample and thus the sample includes only stars on the upper RGB. Moreover the cluster's large distance and the relatively bright limiting magnitude and low spatial resolution of the SDSS make crowding an issue, at least in the cluster's inner region ($r \lesssim 1$ arcmin).

We therefore used our Keck LRIS photometry to measure the structural parameters for Pal 4. The point-source catalogue from our LRIS images covers an area of 42.8 arcmin^2 and contains 777 objects, after excluding stars fainter than $V = 24.5$ mag to minimise photometric incompleteness. Star counts based on these data were then combined with surface photometry for the innermost regions to construct a composite V-band surface brightness profile for the cluster, using the method

Table 4.2: Structural parameters of Pal 4. A distance of 102.8 ± 2.4 kpc (Section 4.4.2) was adopted and all literature values dependent on distance were recalculated using this distance. In calculating the total luminosity L_V, we used a V-band extinction of $A_V = 3.1 \times E(B-V) = 0.07$ mag (Section 4.4.2) and $M_{V,\odot} = 4.83$ mag (Binney & Merrifield 1998).

best-fitting King (1966) model			King (1966) model of McLaughlin & van der Marel (2005)	
central surface brightness $\mu_{V,0}$	23.26 ± 0.06	mag arcsec^{-2}	$23.01^{+0.26}_{-0.22}$	mag arcsec^{-2}
core radius r_c	0.43 ± 0.03	arcmin	$0.33^{+0.05}_{-0.04}$	arcmin
	13.0 ± 0.8	pc	$9.8^{+1.4}_{-1.3}$	pc
tidal radius r_t	3.90 ± 0.20	arcmin	3.30 ± 0.23	arcmin
	116.7 ± 6.6	pc	98.6 ± 7.2	pc
concentration c	0.96 ± 0.04		0.93 ± 0.1	
2d half-light radius r_h	0.62 ± 0.03	arcmin	$0.51^{+0.03}_{-0.02}$	arcmin
	18.4 ± 1.1	pc	$15.3^{+0.9}_{-0.8}$	pc
apparent magnitude V	14.23 ± 0.03	mag	$14.33^{+0.06}_{-0.03}$	mag
total luminosity L_V	19600 ± 1100	$L_\odot$	17900^{+1000}_{-1300}	$L_\odot$

best-fitting King (1962) profile			King (1962) profile of Jordi & Grebel (2010)	
central surface brightness $\mu_{V,0}$	22.96 ± 0.05	mag arcsec^{-2}	–	
core radius r_c	0.39 ± 0.02	arcmin	0.26 ± 0.10	arcmin
	11.7 ± 0.6	pc	7.8 ± 3.0	pc
tidal radius r_t	3.46 ± 0.16	arcmin	5.30 ± 0.65	arcmin
	103.6 ± 5.4	pc	158 ± 20	pc
2d half-light radius r_h	0.63 ± 0.03	arcmin	0.62 ± 0.24	arcmin
	18.8 ± 1.0	pc	18.7 ± 7.2	pc

best-fitting KKBH profile to combined LRIS, WFPC2 and Jordi & Grebel (2010) data		
central surface brightness $\mu_{V,0}$	22.88 ± 0.17	mag arcsec^{-2}
inner power-law slope γ	-0.04 ± 0.13	
core radius R_c	0.44 ± 0.04	arcmin
	13.1 ± 0.3	pc
edge radius R_t	2.77 ± 0.12	arcmin
	82.9 ± 1.9	pc
turn-over parameter μ	0.72 ± 0.05	
outer power-law slope η	2.3 ± 0.6	

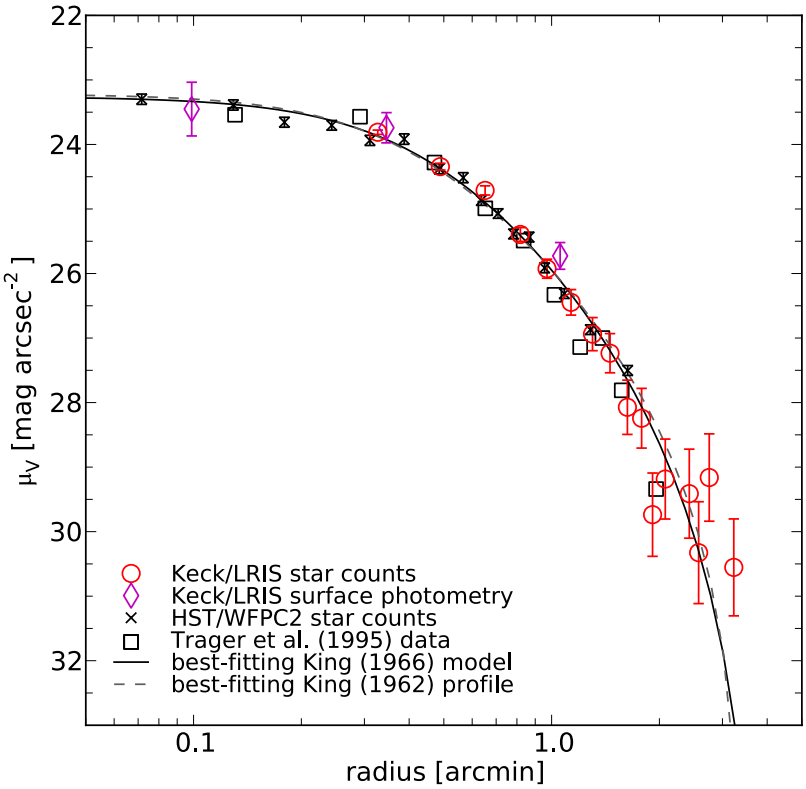

Figure 4.8: The surface brightness profile of Pal 4. Our LRIS data are represented by filled red circles (derived from star counts) and filled magenta diamonds (from direct surface photometry), the WFPC2 star counts are represented by black crosses. Open squares show the Trager et al. (1995) data based on star counts on photographic plates. The best-fitting King (1966) model to the Keck and HST data is shown as solid curve, the best-fitting King (1962) profile is shown as dashed curve.

described in Fischer et al. (1992). Figure 4.8 shows the resulting surface brightness profiles (filled red circles) and additionally three data points from direct surface photometry on the V-band image (filled magenta diamonds). As the deeper WFPC2 data sample a much greater number of stars in the cluster's centre, we also included a surface brightness profile derived from star counts in the WFPC2 catalogue and the V-band magnitudes that HSTPHOT calculates based on the Holtzman et al. (1995) WFPC2 to *UBVRI* transformations. We included stars down to 27 mag in F555W and corrected the star counts and flux for the radially varying completeness. The resulting profile is shown as black crosses in Fig. 4.8; due to the inhomogeneous geometric coverage of the WFPC2 catalogue, we define radial bins by the requirement that they hold equal numbers of stars. Thus, the Poissonian errorbars on the data points remain constant, while their radial spacing varies.

Both surface brightness profiles agree very well and also show good agreement with the Trager et al. (1995) surface brightness data, which are shown for comparison as open black squares. Figure 4.8 also shows the best-fitting King (1966, solid curve) model to our LRIS and WFPC2 data, which yields a central surface brightness of $\mu_{V,0} = 23.26 \pm 0.06$ mag arcsec^{-2}, a core radius of $r_c = 0.43 \pm 0.03$ arcmin and a tidal radius of $r_t = 3.90 \pm 0.20$ arcmin, corresponding to a concentration of $c = \log(r_t/r_c) = 0.96 \pm 0.04$ and a (two-dimensional) half-light radius of $r_h = 0.62 \pm 0.03$ arcmin. For comparability, we also fitted a King (1962) profile to our data (dashed curve), which yields core and tidal radii of $r_c = 0.39 \pm 0.02$ and $r_t = 3.46 \pm 0.16$ arcmin and a central surface brightness of 22.96 ± 0.05 mag arcsec^{-2} and reproduces the observations marginally worse in terms of the minimum χ^2. Table 4.2 summarises our fit results and shows also literature values for comparison. Our

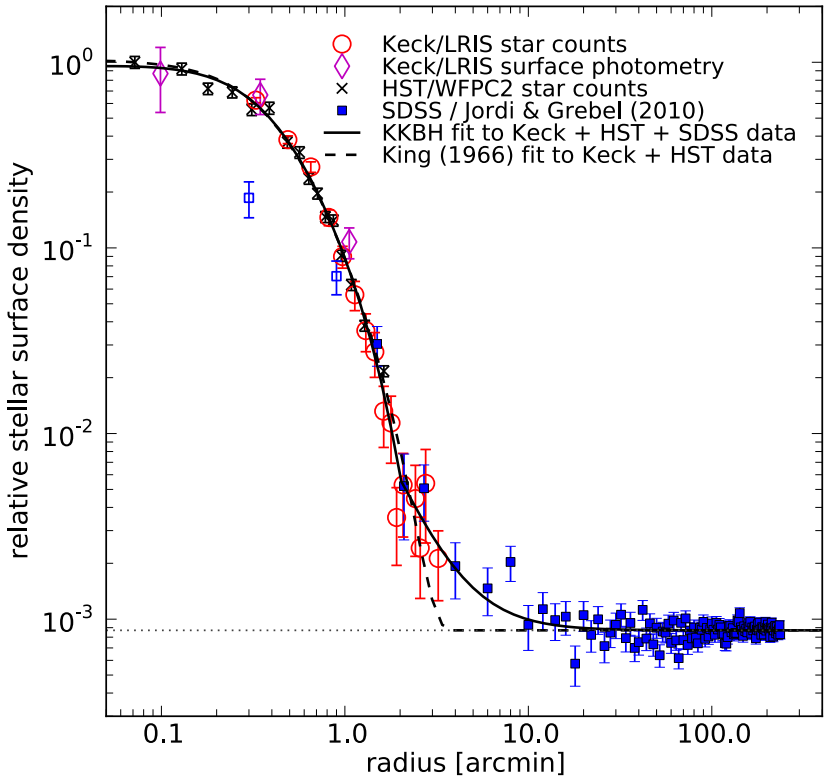

Figure 4.9: The cluster's surface density profile (normalised to the innermost point) based on the combined Keck, WFPC2 and SDSS data. In order to display the profile on a logarithmic scale we added a virtual background level, indicated as dotted horizontal line. As in Fig. 4.8, red circles and magenta diamonds represent the Keck data and black crosses represent the HST WFPC2 data. Blue squares represent the SDSS-based profile derived by Jordi & Grebel (2010). The two innermost data points of the SDSS-based profile (shown as open squares) were excluded, because they are systematically low due to crowding. The best-fitting KKBH profile to the combined dataset is shown as solid curve. For comparison, the dashed curve represents the best-fitting King (1966) model from the top panel. Pal 4 shows a clearly enhanced stellar density at radii > 3 arcmin.

best-fitting King (1966) model is somewhat more extended than the one derived by McLaughlin & van der Marel (2005), but otherwise is in good agreement with the latter in terms of central surface brightness, concentration and integrated total luminosity. Comparing our best-fitting King (1962) profile to that of Jordi & Grebel (2010), we find that the latter is more extended and diffuse. This is consistent with the SDSS data underestimating stellar density in the cluster's centre due to crowding as we will see below.

Sohn et al. (2003) noted an excess of stars beyond the cluster's formal tidal radius, for which they adopted $r_t = 3.33$ arcmin. As our Keck data reach out to a radius of only ~ 3.2 arcmin, we combine our profile with the SDSS-based profile of Jordi & Grebel (2010). We scaled their background-corrected surface density profile (K. Jordi, private communication) to match the Keck data in the radial range of $1.5 - 3.2$ arcmin, by interpolating the Keck data to the radii of the SDSS data points and requiring that the median ratio of the two profiles in the overlapping region be one. The merged profile is shown in Fig. 4.9. As before, diamonds and circles represent the Keck profile, crosses represent the WFPC2 profile. Blue squares represent the SDSS profile. As the SDSS data reach beyond the tidal radius the background-corrected stellar density in individual radial bins can scatter below zero. For the purpose of plotting the profile on a logarithmic scale, we therefore added an

artificial background level (shown as dotted horizontal line). The two innermost points of the SDSS data, shown as open squares, deviate from the Keck and WFPC2 profile reflecting the crowding in the SDSS data and we excluded them in our analysis. The dashed line represents the best-fitting King (1966) model from Fig. 4.8, and it is obvious that the observed density at large radii falls off less steeply than this model or any other similarly truncated model. We fitted the combined profile with a Küpper et al. (2010a, KKBH) template. These templates were designed to fit surface density profiles of GCs out to large cluster radii based on fits to a suite of N-body simulations of Galactic GCs on various orbits. They are a modification of the King (1962) profile including a term for a non-flat core and a term for tidal debris. The best-fitting KKBH profile, shown as solid line in Fig. 4.9 is found for core and edge radii of $R_c = 0.44 \pm 0.04$ arcmin and $R_t = 2.77 \pm 0.12$ arcmin, a core power-law slope of $\gamma = 0 \pm 0.1$ and an outer power-law slope of $\eta = 2.3 \pm 0.6$ that becomes dominant at $\mu R_t = 2.00 \pm 0.15$ arcmin. The shallow slope at large cluster radii may indicate that the cluster is in an orbital phase close to its apogalacticon, although projection effects may play a role in the appearance of the outer part of the density profile. Küpper et al. (2010a) find that the surface density profiles of star clusters, as seen in projection onto their orbital planes, are influenced by the tidal debris in this orbital phase: while the slope at large cluster radii, η, is about 4-5 in most orbital phases, it can reach values of 1-2 in apogalacticon due to orbital compression of the cluster and its tidal tails.

For the following analysis, we will adopt the best-fitting King (1966) model as the cluster's density profile and come back to the influence of tidal debris in Section 4.5.2.

4.4.2 Age determination

To derive the cluster's age, we determined the isochrone that best reproduces the locus of the principal evolutionary sequences from a subset of isochrones of the Dartmouth Stellar Evolution Database (Dotter et al. 2008a). Based on the chemical composition derived by Koch & Côté (2010) from coadded high-resolution spectra of red giants, we adopted [Fe/H]=-1.41 dex and an α-enhancement of $+0.4$ dex. We determined the best-fitting isochrone using a robust direct fit (similar to Stetson et al. 1999), to the colour-magnitude data. The subgiant branch is almost horizontal in the CMD. A minimisation in one dimension, interpreting the isochrone as 'colour as a function of magnitude' and comparing the separation in colour of each star to the colour uncertainty in that magnitude range, therefore runs into problems, because it is almost insensitive to stars on the subgiant branch. This holds even in the F814W vs. F555W-F814W plane, which is used by Stetson et al. (1999) for to avoid the even flatter sub-giant branch in the F555W vs. F555W-F814W plane. Therefore, we employed a χ^2 minimisation in the (F555W, F814W)-plane, where the uncertainties in both dimensions are uncorrelated, and minimised the squared sum of 2d-distances of each star to the isochrone. To be less sensitive to outliers, instead of χ^2, a robust metric that saturates at 5 σ was used.Distance and age were varied as free parameters, with the latter ranging from 8 Gyr to 15 Gyr in steps of 0.5 Gyr. We adopted a reddening of $\mathrm{E}(B\text{-}V) = 0.023$ mag estimated from Galactic dust emission maps[4] and filter-specific extinction to reddening ratios of $\mathrm{A}_{555\mathrm{W}}/\mathrm{E}(B\text{-}V) = 3.252$ and $\mathrm{A}_{\mathrm{F814W}}/\mathrm{E}(B\text{-}V) = 1.948$, taken from table 6 of Schlegel et al. (1998). From this, we obtained a best-fitting age of 11 ± 1 Gyr and an extinction-corrected distance modulus of 20.06 ± 0.05 mag. This places the cluster at a distance of 102.8 ± 2.4 kpc from the Sun. This is slightly closer than the 109.2 kpc derived by Harris (1996, edition 2010) from the mean observed V-band magnitude of horizontal branch stars from Stetson et al. (1999), but well within the range of other previous distance determinations of 100 kpc (Burbidge & Sandage 1958), 105 ± 5 kpc (Christian & Heasley 1986) and 104 kpc (VandenBerg 2000). The age estimate is consistent with Pal 4 being part of the

[4]Obtained from `http://irsa.ipac.caltech.edu/applications/DUST/`

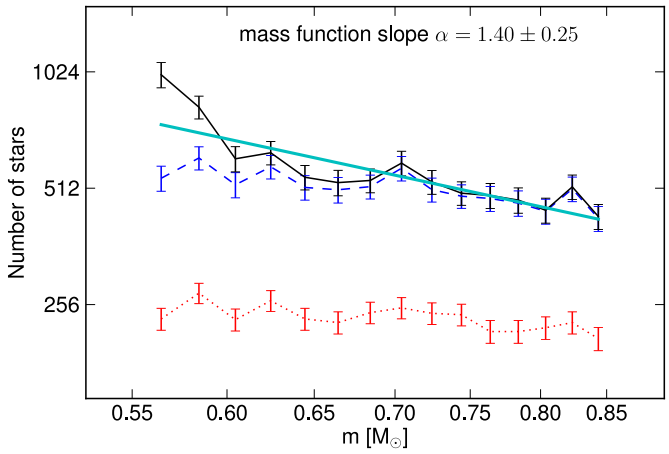

Figure 4.10: Mass function and power-law fit. The red dotted curve shows the number of observed stars per mass interval, errorbars represent the Poissonian errors on the star counts. The blue dashed curve represents the counts corrected for the missing area coverage, the black solid curve represents the counts additionally corrected for photometric completeness. The cyan line gives the best-fitting power law.

young halo population and $\sim$ 1.5–2 Gyrs younger than 'classical', old GCs, as also suggested by the differential analysis relative to M 5 by Stetson et al. (1999) and VandenBerg (2000).

4.4.3 Mass function

We determined the stellar mass function in the cluster in the mass range $0.55 \leq m/\mathrm{M}_\odot \leq 0.85$, corresponding to stars from the tip of the RGB down to the 50 per cent completeness limit in the cluster's core at the faint end (17.9 mag $\lesssim$ F555W $\lesssim$ 27.6 mag). We rejected stars that deviated in colour from the locus of the isochrone by more than $3\sigma_{\mathrm{col}}$, where σ_{col} is the colour uncertainty derived from the artificial star results in the corresponding region of the CMD. To avoid rejecting RGB stars, whose scatter around the isochrone is slightly larger than expected purely from photometric uncertainties, we additionally allowed for an intrinsic colour spread of 0.02 mag. This selection removed likely foreground stars, blue stragglers and horizontal branch stars (see Fig. 4.2). We then assigned to each of the remaining stars a mass based on the isochrone, by interpolating the masses tabulated in the isochrone to the star's measured F555W magnitude.

At the faint end, crowding affects the photometry and thus the completeness varies slightly with stellar density, or distance from the cluster centre. Moreover the geometric coverage of the WFPC2 photometry as a function of radius is very inhomogeneous (see Fig. 4.3). Therefore, we subdivided our photometric catalogue into n radial bins around the cluster centre, chosen such that each bin contains one n-th of the observed stars. This is optimal in terms of the Poissonian errors on the star counts, both of the observed stars and of the artificial stars, as the latter were distributed on the sky similarly to the observed stars. The number of radial subdivisions has to be chosen large enough such that completeness and stellar density are approximately constant within each annulus, because otherwise correcting for completeness would bias the results. In practise, we increased the number of bins, n, until the derived mass function slope and cluster mass (Section 4.4.5) did not vary any more with n. This was the case for $\mathrm{n} \geq 33$ and we chose $\mathrm{n} = 36$ radial bins for the final analysis. In each of these annuli, stars were counted in 12 linearly spaced mass bins (of width ~ 0.025 M$_\odot$). The counts were corrected for the missing area coverage and for photometric completeness in that radial range. Counts from the individual annuli were then summed and fit with a power law of the form $dN/dm \propto m^{-\alpha}$. From this, we obtained a mass function slope of $\alpha = 1.4 \pm 0.25$ (Fig. 4.10).

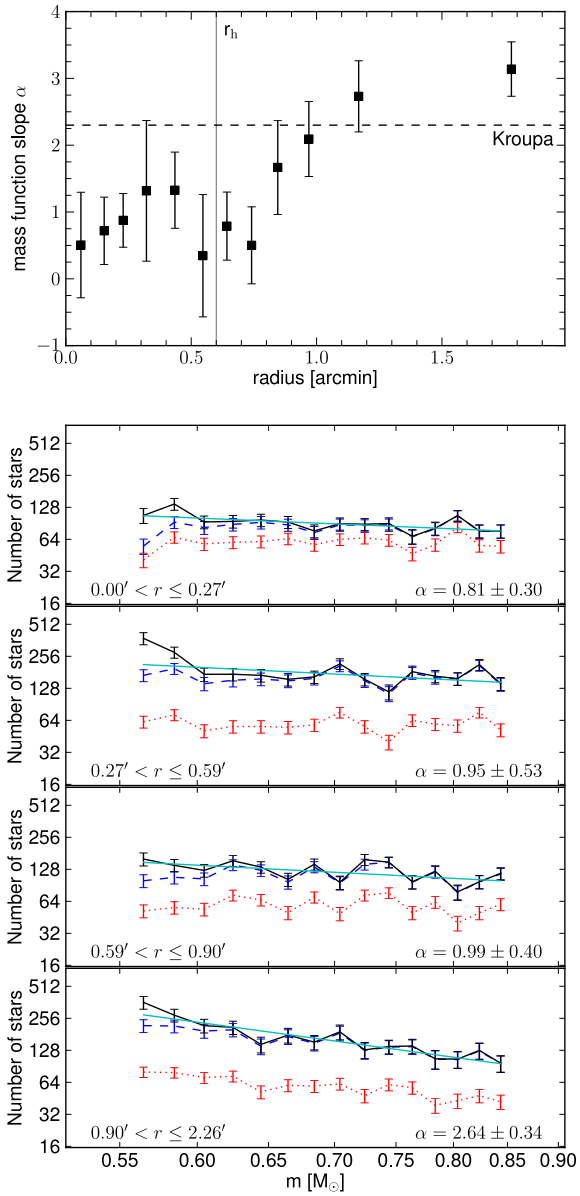

Figure 4.11: Top: The best-fitting mass function slope α in radial bins containing each one twelfth of the observed stars. Bottom: The mass function in radial bins in order of increasing distance from the cluster centre containing one fourth of the observed stars each. Dotted red curves represent the number of observed stars per mass interval, errorbars represent the Poissonian errors on the star counts. Blue dashed curves are the counts corrected for the missing area coverage in the given radial range. Black solid curves are additionally corrected for photometric completeness. Cyan lines represent the best-fitting power law functions to the completeness-corrected counts. The radial ranges and best-fitting power-law slopes are reported at the bottom of each panel.

This present-day mass function is significantly shallower than a Kroupa (2001) IMF (with $\alpha = 2.3$ in this range of masses) and is similar to the mass function in other Galactic GCs (e.g De Marchi et al. 2007; Jordi et al. 2009; Paust et al. 2010).

4.4.4 Mass segregation

To test for mass segregation, we derived the mass function as a function of radius. As the individual 36 radial annuli contain only ~ 120 stars each, deriving the mass function in each of them would produce very noisy results. It is thus necessary to bin several of these annuli – after the completeness-corrected counts have been obtained in each annulus individually. As a compromise between signal to noise and radial resolution, we show two different binning schemes: The top panel of Fig. 4.11 shows the best-fitting mass function slopes derived in radial bins containing each one twelfth of the observed stars. The bottom panel of the same figure shows the mass functions and power-law fits obtained in bins containing each one fourth of the observed stars. It is obvious that the mass function steepens with increasing radius, from $\alpha \lesssim 1$ inside $r \lesssim 1.3 \times r_h$ to $\alpha \gtrsim 2.3$ at the largest observed radii.

4.4.5 Total mass

In the mass range between $0.55 \leq m/\mathrm{M}_\odot \leq 0.85$, we measure a stellar mass of $5960 \pm 110\,\mathrm{M}_\odot$ within the radius covered by the WFPC2 pointing, $r < 2.26$ arcmin. We do not correct for the mass contained in blue stragglers and horizontal branch stars that fall outside of our colour selection. It is negligible due to their low number ($\sim$ 20 of each species in our pointing) and we estimate their contribution to be $\lesssim 0.2$ per cent of the total cluster mass.

Assuming the measured mass function slope of $\alpha = 1.40 \pm 0.25$ to hold down to 0.5 $\mathrm{M}_\odot$ and adopting a Kroupa (2001) mass function, with $\alpha = 1.3$, for masses $0.08 \leq m/\mathrm{M}_\odot \leq 0.5$, and $\alpha = 0.3$ for masses $0.01 \leq m/\mathrm{M}_\odot \leq 0.08$, the extrapolated stellar mass in the mass range $0.01 \leq m/\mathrm{M}_\odot \leq 0.85$ is $14500 \pm 1300\,\mathrm{M}_\odot$.

To account for the mass contributed by the remnants of higher-mass stars, we assume our observed slope α to hold up to 1.0 $\mathrm{M}_\odot$ and above that a high-mass Kroupa slope of $\alpha = 2.3$, and extrapolate the mass function to 60 $\mathrm{M}_\odot$. We follow the prescription of Glatt et al. (2011), assuming stars with initial masses $0.85 \leq m \leq 8\,\mathrm{M}_\odot$ to have formed 0.6 $\mathrm{M}_\odot$ white dwarfs, and stars with initial masses $8 \leq m \leq 60\,\mathrm{M}_\odot$ to have formed neutron stars of 1 $\mathrm{M}_\odot$. The extrapolation yields a mass in white dwarfs of $\mathrm{M_{WD}} = 8900 \pm 800\,\mathrm{M}_\odot$ and a mass in neutron stars of $\mathrm{M_{NS}} = 800 \pm 70\,\mathrm{M}_\odot$. In clusters with masses of several times 10^4 $\mathrm{M}_\odot$, neutron stars are expected to escape the cluster due to their high initial kick velocities, while virtually all white dwarfs are expected to be retained in the cluster (Kruijssen 2009). We therefore adopt $\mathrm{M_{WD}} = 8900 \pm 800\,\mathrm{M}_\odot$ as the mass of stellar remnants.

Based on the best-fitting King (1966) density profile, and approximating that mass follows light, 98.3 ± 0.4 per cent of the cluster's mass lies within $r = 2.26$ arcmin. Extrapolating out to the tidal radius, the total mass of Pal 4 amounts to $\mathrm{M_{phot}} = 29800 \pm 800\,\mathrm{M}_\odot$ including the corrections for low-mass stars and stellar remnants. We note that the uncertainty of the total mass is smaller than the individual uncertainties of the extrapolated high- and low-mass contributions because correlations were fully propagated. These correlations arise from the requirement that the mass function be continuous. As a steeper (shallower) mass function will have more (less) mass in low-mass stars and less (more) mass in high-mass stars and stellar remnants, the uncertainties of the two terms are anti-correlated.

With this mass and the total luminosity derived from the best-fitting King (1966) model, the photometric mass to light ratio of the cluster is $\mathrm{M_{phot}/L}_V = 1.52 \pm 0.09\,\mathrm{M}_\odot\,\mathrm{L}_\odot^{-1}$.

To obtain a conservative lower limit on the photometric mass of the cluster, we follow Jordi et al. (2009), assuming the cluster to be significantly depleted in low-mass stars with a declining mass function with $\alpha = -1.0$ for masses $0.01 \leq m/\mathrm{M}_{\odot} \leq 0.5$. For this hypothetical case, the extrapolation towards lower masses, inclusion of white dwarfs and extrapolation out to the tidal radius yields a total cluster mass of $\mathrm{M}_{\mathrm{decl,phot}} = 20100 \pm 600\,\mathrm{M}_{\odot}$.

4.5 Discussion

4.5.1 Newtonian and MONDian dynamical mass

In order to see if the observed velocity dispersion and mass of Pal 4 are more compatible with Newtonian or MONDian dynamics, we compare the observed global line-of-sight velocity dispersion with expected velocity dispersions for different cluster masses for the two cases. The expected line-of-sight velocity dispersions of Pal 4 are taken from Haghi et al. (2011), who performed *N*-body simulations of a number of outer halo globular clusters for both Newtonian and MONDian dynamics using the particle-mesh code N-MODY (Londrillo & Nipoti 2009).

Figure 4.12 shows the global line-of-sight velocity dispersion as a function of the cluster mass for the Newtonian (red open squares) and the MONDian case (black open circles). For cluster masses below $10^5\,\mathrm{M}_{\odot}$, the velocity dispersion in the MONDian case is significantly larger than

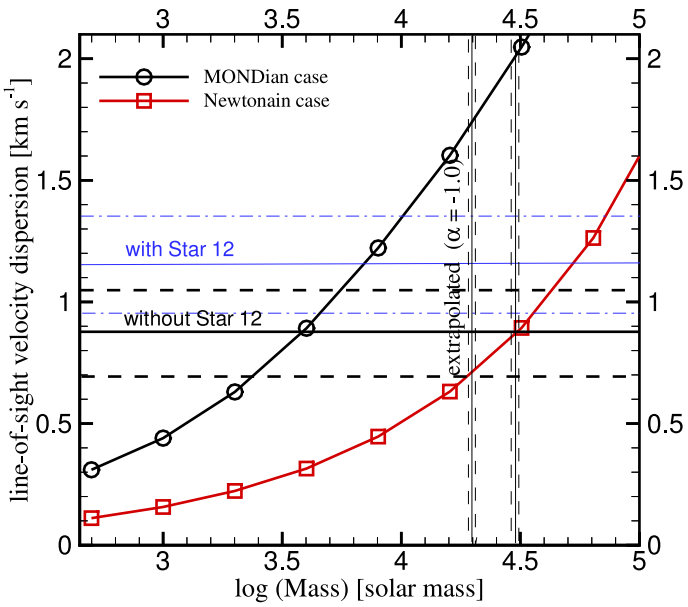

Figure 4.12: Theoretically predicted line-of-sight velocity dispersion as a function of mass for the Newtonian case (red open squares) and the MONDian case (black open circles). The predictions are taken from recent *N*-body simulations by Haghi et al. (2011). The observed velocity dispersion based on the 23 clean member stars and its uncertainty (Section 4.3) are shown by black solid and dashed horizontal lines, respectively. Blue solid and dashed lines represent the velocity dispersion and uncertainty obtained when including star 12. For the MONDian case the predicted cluster mass when excluding star 12 and its 1σ uncertainty are given by $\mathrm{M}_{\mathrm{MOND}} = 3900^{+1400}_{-1500}\,\mathrm{M}_{\odot}$, while in Newtonian dynamics they are $\mathrm{M}_{\mathrm{Newton}} = 32000 \pm 13000\,\mathrm{M}_{\odot}$. Including star 12, the predicted masses amount to $\mathrm{M}_{\mathrm{MOND}} = 6900^{+3100}_{-2300}\,\mathrm{M}_{\odot}$ and $\mathrm{M}_{\mathrm{Newton}} = 53000^{+18000}_{-16000}\,\mathrm{M}_{\odot}$ respectively. The vertical black lines indicate the observed total mass (solid line) and its uncertainty (dashed lines), $\mathrm{M}_{\mathrm{phot}} = 29800 \pm 800\,\mathrm{M}_{\odot}$, and the mass derived for a mass function significantly depleted in low-mass stars (see text), $\mathrm{M}_{\mathrm{decl,phot}} = 20100 \pm 600\,\mathrm{M}_{\odot}$.

for the Newtonian case since the acceleration of stars in Pal 4 is below the critical acceleration a_0 of MOND, making Pal 4 a good test case to discriminate between the two cases. For a line-of-sight velocity dispersion of $0.87 \pm 0.18\,\mathrm{km\,s^{-1}}$ (shown by black horizontal lines in the figure), obtained when excluding the probable outlier star 12 in Section 4.3, the theoretically predicted mass in MOND is $\mathrm{M_{MOND}} = 3900^{+1400}_{-1500}\,\mathrm{M_\odot}$ and in Newtonian dynamics $\mathrm{M_{Newton}} = 32000 \pm 13000\,\mathrm{M_\odot}$. This corresponds to mass to light ratios of $\mathrm{M_{MOND}/L_V} = 0.20 \pm 0.08\,\mathrm{M_\odot\,L_\odot^{-1}}$ and $\mathrm{M_{Newton}/L_V} = 1.63 \pm 0.67\,\mathrm{M_\odot\,L_\odot^{-1}}$. For the velocity dispersion including star 12, $\sigma = 1.15 \pm 0.20\,\mathrm{km\,s^{-1}}$ (shown by blue horizontal lines in Fig. 4.12), the theoretically predicted mass in MOND is $\mathrm{M_{MOND}} = 6900^{+3100}_{-2300}\,\mathrm{M_\odot}$, corresponding to $\mathrm{M_{MOND}/L_V} = 0.35^{+0.16}_{-0.12}\,\mathrm{M_\odot\,L_\odot^{-1}}$, while in Newtonian dynamics it is $\mathrm{M_{Newton}} = 53000^{+18000}_{-16000}\,\mathrm{M_\odot}$, corresponding to $\mathrm{M_{Newton}/L_V} = 2.70^{+0.93}_{-0.83}\,\mathrm{M_\odot\,L_\odot^{-1}}$.

In Section 4.4 we derived a cluster mass of $\mathrm{M_{phot}} = 29800 \pm 800\,\mathrm{M_\odot}$ based on the photometry of Pal 4 and assuming a Kroupa IMF for low stellar masses, and a mass of $\mathrm{M_{decl,phot}} = 20100 \pm 600\,\mathrm{M_\odot}$ for the case of a declining mass function for low-mass stars. Both values agree well with the expected value for the Newtonian case when excluding star 12. The photometric masses are however significantly larger than the cluster mass derived for the MONDian case. We note that even if the cluster did not contain any stars less massive than $0.55\,\mathrm{M_\odot}$ (or fainter than our 50 per cent completeness limit of $\lesssim 27.6$ mag in F555W), its mass of $15100 \pm 800\,\mathrm{M_\odot}$ would significantly exceed the MONDian prediction.

The excellent match between photometric and (Newtonian) dynamical masses also means that there is no need to invoke the presence of dark matter in Pal 4, although a small amount of dark matter cannot be excluded. As mentioned in the introduction, Pal 4 is similarly extended and luminous as some of our Galaxy's ultra-faint dwarf satellites. Its M/L of $\mathrm{M_{Newton}/L_V} \approx M_{\mathrm{phot}}/\mathrm{L_V} \approx 1.6\,\mathrm{M_\odot\,L_\odot^{-1}}$, however, suggests that it is very different from these dark matter dominated systems and a 'perfectly normal' globular cluster. This is also supported by the apparent lack of a metallicity spread in Pal 4, whereas such a spread is detected in most dwarf satellites (see the discussion in Koch & Côté 2010).

As shown by Gentile et al. (2010), velocity dispersions derived from a small sample of stars suffer from low number statistics. We therefore used Kolmogorov-Smirnov (KS) tests to determine the likelihood of the observed velocity distribution in Newtonian and MONDian dynamics given the photometric cluster mass of $\mathrm{M_{phot}} = 29800\,\mathrm{M_\odot}$ for our sample of radial velocities either including or excluding star 12. Figure 4.13 shows the resulting velocity distributions for the Newtonian and MONDian case and the two velocity distributions. In deriving the KS probabilities, we followed Gentile et al. (2010) by not fixing the systemic velocity, but shifting the model distributions in velocity such that the maximum probability was assumed. We note that a KS test in this form is slightly biased to favour MOND, or generally, any model predicting a higher velocity dispersion, because it neglects the broadening of the observed velocity distribution due to the radial velocity uncertainties. However, as the typical velocity uncertainties in our sample are small compared to the cluster's intrinsic velocity dispersion, the effect is small. For the Newtonian case, a KS test gives a probability of P=0.87 if excluding star 12 and P=0.68 if including star 12. In the MONDian case, the probabilities are P=0.19 and P=0.27 respectively.

Apart from the stochastic effect of the small sample, our velocity dispersion estimate is also subject to the effect of radial sampling. As two thirds of our sample stars are located within the cluster's half-light radius, the global velocity dispersion will be somewhat lower than our measured value. We do not correct for this effect, but note that it will be small compared to the statistical uncertainty because the cluster's expected velocity dispersion profile is fairly flat (see Fig. 4.7). As a lower global velocity dispersion will also lower the predicted masses, the discrepancy between the MONDian prediction and the photometric mass will be larger.

The Newtonian case is therefore favoured by the observational data. However, based on the

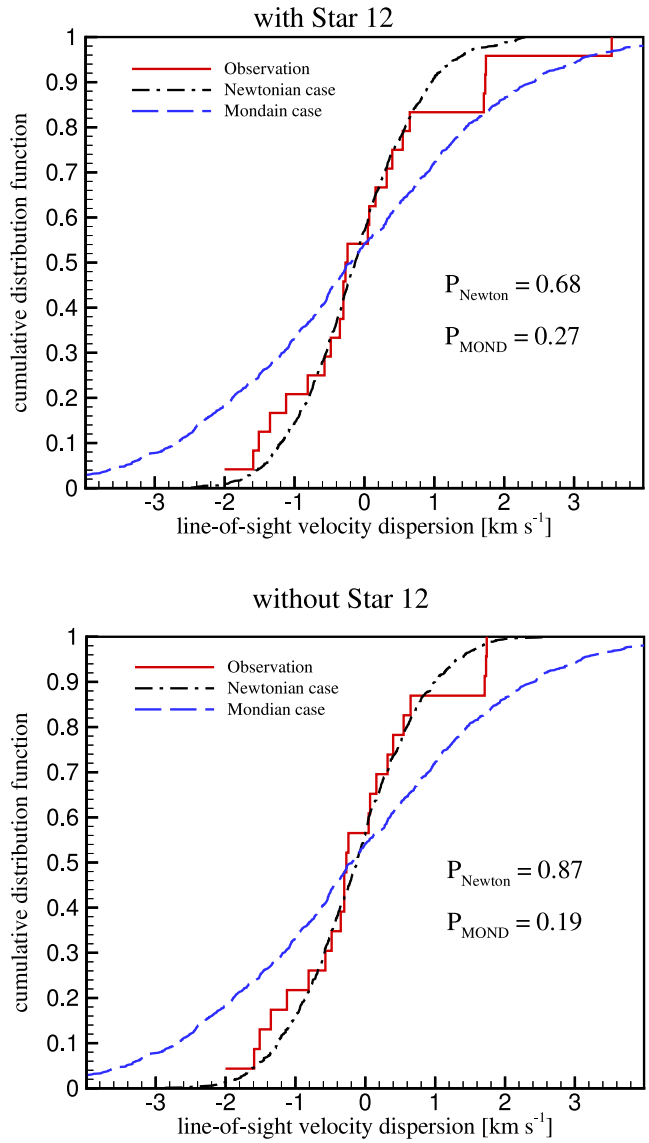

Figure 4.13: Cumulative distribution function (cdf) of radial velocities for the observed stars (red solid lines) and theoretical distributions assuming Newtonian (black dashed-dotted lines) and MONDian dynamics (blue dashed lines) and a cluster mass of $M_{phot} = 29800\,M_{\odot}$. In the upper panel, star 12 is included, in the lower panel it is excluded. The corresponding probabilities are shown inside the panels.

current data alone, MOND cannot be ruled out, so additional radial velocities will be necessary to distinguish between MONDian and Newtonian dynamics. The simulations done by Haghi et al. (2011) indicate that of the order of 40 radial velocities would be needed for Pal 4 to decrease the MONDian P-values below 0.05 if the internal cluster dynamics is Newtonian. Nevertheless, Pal 4 adds to the growing body of evidence that the dynamics of star clusters in the outer Galactic halo can hardly be explained by MOND, since the velocity dispersions of Pal 4 (this work), Pal 14 (Jordi et al. 2009; Sollima et al. 2012) and NGC 2419 (Baumgardt et al. 2009; Ibata et al. 2011a,b) are consistent with Newtonian dynamics and below the predictions of MOND.

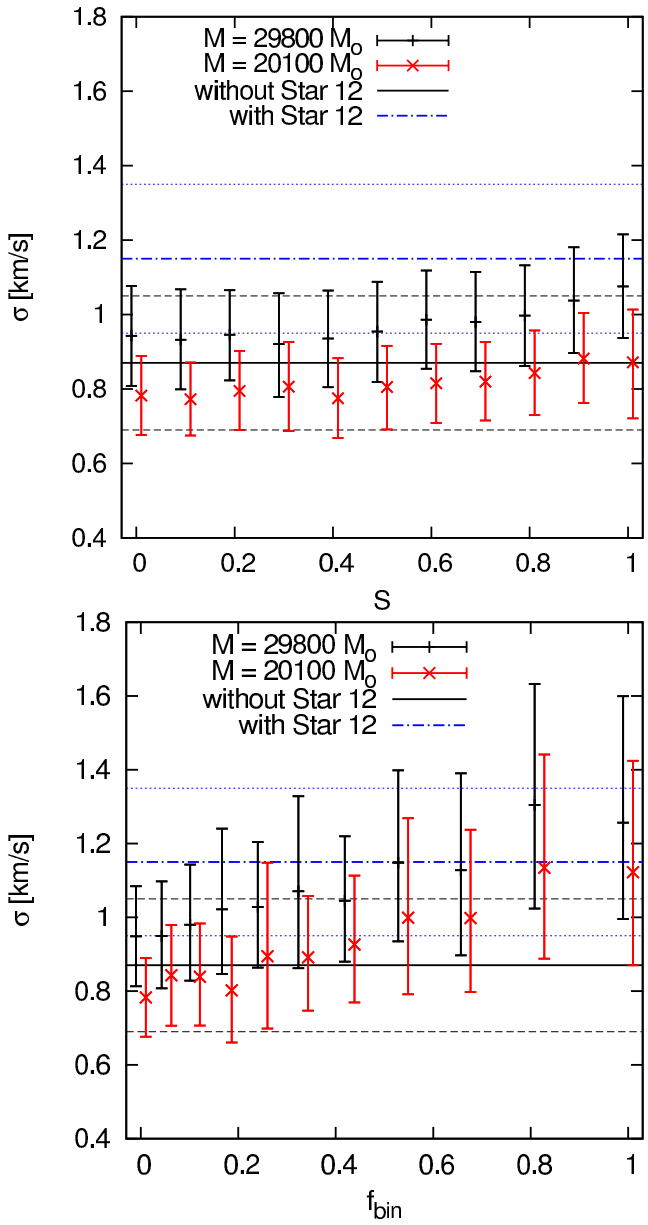

Figure 4.14: The effect of mass segregation (upper panel) and binarity (lower panel) on the measured velocity dispersion. Error bars show the range (68 per cent) of velocity dispersions of samples of 23 AGB/RGB stars drawn from models of Pal 4. Black solid and dashed horizontal lines represent the observed velocity dispersion and its uncertainty obtained from the 23 clean member stars, blue dash-dotted and dotted lines denote the dispersion and its uncertainty derived including star 12. Upper panel: Mass segregation can bias the measured velocity dispersion by up to 20 per cent since AGB/RGB stars are preferentially located deeper in the cluster potential with increasing degree of mass segregation, S. Lower panel: A high binary fraction, f_{bin}, can severely affect the measured velocity dispersion. Both effects may imply that Pal 4's true velocity dispersion is lower than the measured value, in which case the MONDian mass estimate would be more discrepant with the observed mass.

4.5.2 The effect of mass segregation, unbound stars and binarity

In our analysis we did not take into account the effects of mass segregation, of the presence of unbound stars, and of binaries.

Mass segregation will affect the interpretation of the radial velocity data in three ways: Massive stars, such as the red giant and asymptotic giant branch stars in our kinematic sample will reside more frequently in the cluster's centre, where the gravitational potential is deeper. Therefore they will show a higher velocity dispersion than the global one. On the other hand, energy equipartition will, at a given radius, cause higher mass stars to have lower velocities, lowering the observed velocity dispersion. Moreover, in a mass-segregated cluster, the half-mass radius is larger than the half-light radius. Therefore, when assuming that mass follows light and equating the half-mass radius to the observed half-light radius, a dynamical model will overpredict the velocity dispersion.

To quantify these effects, we used the MCLUSTER code (Küpper et al. 2011a) to set up cluster models of Pal 4 with the characteristics obtained in this investigation. We therefore used the best-fitting King (1966) model parameters (see Table 4.2), a metallicity of [Fe/H]$= -1.41$ dex and a cluster age of 11 Gyr. For the two photometric mass estimates, $\mathrm{M_{phot}} = 29800\,\mathrm{M_\odot}$ and $\mathrm{M_{decl,phot}} = 20100\,\mathrm{M_\odot}$, we generated a total of 126 evolved star clusters containing a number of about 200 RGB and AGB stars each, or 130 respectively in the case of the lower mass estimate. We set up 66 models with a varying degree of mass segregation, S. We increase S from zero (unsegregated) to 1.0 (completely segregated) in steps of 0.1, where the observed degree of mass segregation in Pal 4 corresponds approximately to a value of $0.8 < S < 0.9$, higher values of S are rather unrealistic. Velocity dispersions and their uncertainties were then extracted by repeatedly drawing 23 RGB and AGB stars from the inner 100 arcsec of the cluster models. In a similar approach as Sollima et al. (2012) chose for their analysis Pal 14's velocity dispersion, we rejected stars that differed by more than 2.5σ from the mean velocity of each sample to emulate the clipping of likely outliers, such as star 12, in the observations. As shown in the upper panel of Fig. 4.14, we find that, even in the case of extreme mass segregation, the obtained velocity dispersion rises by not more than 20 per cent compared to the non-segregated case. The velocity dispersion we obtained for Pal 4 may be biased by up to 10 per cent due to mass segregation. However, the error bars in Fig. 4.14 show only the 68 per cent most likely results. Significantly higher and lower velocity dispersion measurements are still possible with a sample of only 23 stars.

If any of the stars in the radial velocity sample are members of binary systems, the measured velocity dispersion will be increased by the fact that the stars are observed at a random orbital phase of the binaries. This effect can be significant for low-mass stellar systems like Pal 4 (see, e.g., Kouwenhoven & de Grijs 2008; McConnachie & Côté 2010; Bradford et al. 2011). The magnitude of this effect depends on the distribution of binary periods and orbital eccentricities and most importantly on the fraction of binaries in the cluster. We studied the effect of binarity by populating 60 further MCLUSTER models of Pal 4 with a varying fraction of binaries, f_{bin}. We used the same set-up as for the mass segregation models described above, but added binaries following a Kroupa period distribution and a thermal eccentricity distribution (Kroupa 1995). Since periods and eccentricities will be subject to internal dynamical evolution on a timescale of 11 Gyr, the binaries were evolved in time with the other stars in the cluster using the binary-star evolution routines by Hurley et al. (2002) that are implemented in MCLUSTER. As for the mass segregated models, velocity dispersions were calculated from random samples of AGB and RGB stars, rejecting velocity outliers. The results are shown in the lower panel of Fig. 4.14. Just like mass segregation, a high binary fraction can significantly affect the measured velocity dispersion, resulting in a dynamical mass estimate biased towards too high masses.

Finally, unbound stars may contaminate our radial velocity sample. First of all, energetically unbound stars, which have not yet escaped from the cluster (so-called potential escapers) may

inflate the velocity dispersion. However, Küpper et al. (2010a) showed that potential escapers mainly influence the velocity dispersion profile at large cluster radii. Moreover, also stars within the tidal debris may be misinterpreted as bound cluster members. Küpper et al. (2011b) showed that for clusters in an orbital phase close to apogalacticon the velocity dispersion may be inflated by unbound tidal debris stars, which get pushed close to the cluster due to orbital compression of the cluster and its tidal tails. The shallow slope of Pal 4's surface density profile at large cluster radii suggests that Pal 4 may be close to its apogalacticon, making such a contamination likely. On the other hand, this effect may be alleviated by the fact that, because of mass segregation, the unbound population will consist preferentially of low-mass stars, while our radial velocity sample consists of more massive red giant and asymptotic giant branch stars.

The combined effects of mass segregation, binaries and unbound stars render it possible that the intrinsic velocity dispersion in Pal 4 is lower than our measured value of $\sigma = 0.87 \pm 0.18\,\mathrm{km\,s^{-1}}$. If this was the case, it would further strengthen the case against MONDian dynamics in this cluster, as a decreased velocity dispersion will yield an even lower cluster mass predicted by MOND.

We note that also an anisotropic velocity distribution would affect the velocity dispersion profile of the cluster. While the total kinetic energy is always fixed to one half of the potential energy for a cluster in virial equilibrium, radial anisotropy will increase the velocity dispersion in the cluster's centre compared to the isotropic case and decrease it at large radii, and vice versa for tangential anisotropy. As our radial velocity sample, with 15 stars inside r_h and 8 stars outside r_h, covers a fair range of radii, the effect of anisotropy on our measured dispersion is expected to be only moderate. Correspondingly, Sollima et al. (2012) in their analysis of the similarly distributed radial velocity sample in Pal 14, find that the impact of even purely tangential and or maximally radial anisotropy on the measured velocity dispersion is small.

4.5.3 Primordial mass segregation

We found clear evidence for mass segregation between main sequence stars in Pal 4. This mass segregation could either have evolved through two-body relaxation and the dynamical friction of high-mass stars or it was already established at the time of the formation of the cluster (e.g. Hillenbrand & Hartmann 1998). For a half-light radius of 0.6 arcmin, corresponding to 18 pc, and for a cluster mass of $\mathrm{M} = 29800\,\mathrm{M}_{\odot}$, the half-mass relaxation time of Pal 4 is around 14 Gyr, i.e. of the same order as its age. Two-body relaxation is therefore very unlikely as the explanation for the mass segregation in Pal 4: according to the simulations of Gürkan et al. (2004), it takes several half-mass relaxation times until a cluster with a ratio of maximum to average stellar mass of $m_{\mathrm{max}}/\langle m \rangle \approx 4$, which is typical for a globular cluster, goes into core collapse. Unless Pal 4 was significantly more concentrated in the past, the mass segregation in Pal 4 was therefore most likely established by the star formation process itself.

Primordial mass segregation is found in several young Galactic (e.g. Sagar et al. 1988; Hillenbrand 1997; Hasan & Hasan 2011) and Magellanic Cloud star clusters (e.g. Fischer et al. 1998; Sirianni et al. 2002). There are also indications for primordial mass segregation in Galactic GCs: Koch et al. (2004) argue that the mass segregation they observed in Pal 5 may be primordial, if the cluster that is currently being disrupted was originally a low-concentration and low-mass cluster. Baumgardt et al. (2008) found that primordial mass segregation together with depletion of low-mass stars by external tidal fields is necessary to explain the present-day mass functions of stars in globular clusters. Pal 14, another diffuse and 'young halo' cluster has a flat stellar mass function with slope $\alpha = 1.27 \pm 0.44$ within the half-light radius (Jordi et al. 2009), which is very similar to the slope that we find for the centre of Pal 4. Zonoozi et al. (2011) modelled the evolution of Pal 14 over a Hubble time by direct N-body computations on a star-by-star basis and found that in order to reproduce its observed mass function, either strong primordial mass segregation was necessary,

or the initial mass function (IMF) was depleted in low-mass stars. Just like in Pal 4, the half-mass relaxation time of Pal 14 is comparable to its age, and Beccari et al. (2011) found a non-segregated population of blue stragglers in Pal 14, which they interpret as observational support for the fact that dynamical segregation has not affected the cluster yet. If one assumes that Pal 14 formed with a globally normal IMF, its flat central present-day mass function found by Jordi et al. (2009) then suggests that the cluster had primordial mass segregation. This might hold also for Pal 4. According to the simulations of Vesperini et al. (2009) long-lived initially mass-segregated clusters should show a looser structure than initially non-segregated clusters, as the former would lose more mass in the central regions during early stellar evolution. It is therefore an interesting question, if primordial mass segregation is common among diffuse GCs like Pal 4 and Pal 14.

5

Mass segregation in the diffuse halo cluster Palomar 14[1]

5.1 Introduction

The vast majority of the Galaxy's GCs have apparent half-mass two-body relaxation times much shorter than their respective ages (e.g. Harris 1996, 2010 edition). In these clusters, at least in their centres where the density is highest, two-body relaxation has shaped the distribution of stars: in two-body encounters, massive stars tend to lose kinetic energy to lower-mass stars and, as a result, massive stars sink into the cluster's centre, whereas low-mass stars gain energy allowing them to populate orbits further away from the cluster's centre. This is observed as mass segregation, more massive stars show a more concentrated radial distribution than lower-mass stars. As a consequence, the mass function of the cluster becomes shallower in the cluster centre but also globally, as stars at large radii are more easily lost to the Galactic potential (Section 1.3.1; Vesperini & Heggie 1997; Baumgardt & Makino 2003; Kruijssen 2009).

However, in a few GCs, such as the massive NGC 2419 and NGC 5139 (ωCen) and several low-mass, but extended, outer halo clusters, the dynamical half-mass relaxation time is comparable to or even exceeds the Hubble time. Dynamical effects like low-mass star depletion or mass segregation should not have affected such a cluster much, assuming that the cluster parameters such as half-mass radius and cluster mass have not changed dramatically within the last few Gyr and hence that its present-day two-body relaxation time is a representative measure of its relaxation time scale for its entire lifetime. One of these clusters is Palomar 14 (Pal 14; also known as AvdB after its discoverers Arp & van den Bergh 1960). Beccari et al. (2011) recently reported that the distribution of blue straggler stars in Pal 14 is not centrally concentrated with respect to less massive HB and RGB stars in this cluster. Blue stragglers (BS) are hydrogen-burning stars that are brighter and bluer than the main-sequence turn-off of their host population and are believed to form either through direct collisions (Hills & Day 1976) or through mass-transfer in binary systems (McCrea 1964). The radial distributions of BS in massive globular clusters (e.g. Mapelli et al. 2006; Lanzoni et al. 2007) as well as the detection of two distinct sequences of BS in M 30 (Ferraro et al. 2009) suggests that both mechanisms are at work in dense GCs. In a diffuse cluster like Pal 14, the low stellar density

[1]The work presented in this chapter was done in collaboration with Eva Grebel and Andreas Küpper.

and therefore low probability of collisions makes it likely that BS are primarily due to mass-transfer in primordial binary systems. Regardless of the formation channel, the masses of BS, or at least the total masses of their progenitor binary systems, likely exceed those of any other single star that can be identified in a cluster's colour-magnitude diagram (e.g. Shara et al. 1997; Geller & Mathieu 2011). Hence, Beccari et al. (2011) interpreted their finding as proof that two-body relaxation has not yet affected Pal 14, not even in its centre, and that the cluster is not mass-segregated, in agreement with the expectation from its long present-day half-mass relaxation time of $\sim 20\,\mathrm{Gyr}$ (Sollima et al. 2011).

On the other hand, Jordi et al. (2009) measured the slope of the stellar mass function in the mass range $0.53-0.79\,\mathrm{M}_{\odot}$ in the cluster's centre, and found a value of $\alpha = 1.3 \pm 0.4$, significantly shallower than a Salpeter or Kroupa initial mass function (IMF) with $\alpha \simeq 2.3$ in this mass range (Salpeter 1955; Kroupa 2001). Such a flattened present-day mass function would be expected if two-body relaxation had removed low-mass stars from the cluster's centre. However, if the cluster was indeed not mass-segregated, one would have to conclude that it already formed with a lack of low-mass stars, representing a rare example of a variation of the initial stellar mass function (for a recent overview of putative variations of the IMF, see Bastian et al. 2010).

As discussed in Section 1.3.2, the internal dynamics of Pal 14 have recently received considerable attention in the context of testing MOND. Its large Galactocentric distance of $\sim$66 kpc (Sollima et al. 2011) in combination with its low mass and density, and therefore the low external and internal acceleration experienced by its stars, make it an excellent test case for this theory (Baumgardt et al. 2005; Sollima & Nipoti 2010; Haghi et al. 2011). It is one of only three halo clusters that have been extensively studied in this context, the other two being the remote halo clusters NGC 2419 (Ibata et al. 2011a,b; Sanders 2012a,b) and Pal 4 (Chapter 4). For Pal 14, Jordi et al. (2009) measured radial velocities of 16 cluster members and found a good agreement between the cluster's photometric and dynamical mass in classical Newtonian dynamics, while the velocity dispersion is significantly lower than predicted in MOND (Haghi et al. 2009). Gentile et al. (2010) challenged this conclusion and argued on the basis of a Kolmogorov-Smirnov (KS) test that the sample of radial velocities is too small to rule out MOND. Küpper & Kroupa (2010) reanalysed the Jordi et al. (2009) radial velocity data including a heuristic treatment of binaries and mass segregation, and argued that Pal 14 has to have a very low binary fraction in order to be able to explain the low intrinsic velocity dispersion (after correction for binarity). In a Monte-Carlo analysis based on the same radial velocity data and including the effects of binaries, of the external field and of velocity anisotropy, Sollima et al. (2012) found that the cluster is compatible with Newtonian dynamics also when the constraint of the binary fraction is relaxed to $\lesssim$30 per cent and that the data favour Newtonian over MONDian dynamics. Tidal tails around the cluster, already seen at low significance in Sloan Digital Sky Survey (SDSS; Abazajian et al. 2009) data by Jordi & Grebel (2010), were recently detected in deeper wide-field imaging by Sollima et al. (2011), which may further complicate the interpretation of the small sample of radial velocities as unbound stars may contaminate the sample (e.g. Küpper et al. 2011b).

Pal 14 was also the subject of the first full collisional *N*-Body simulations of a GC over its entire lifetime by Zonoozi et al. (2011). These authors found that, while two-body relaxation does have an effect on the cluster's stellar mass function, the effect from two-body relaxation is too weak such that the shallow present-day mass function slope measured by Jordi et al. (2009) cannot be reproduced with models starting with a Kroupa (2001) IMF. The authors demonstrated that the observations can, in principle, be reproduced by models with primordial mass segregation, but that the necessary degree of mass segregation has to be very high. Alternatively, they argued that the cluster must have lost a good fraction of its low-mass stars in the early gas-expulsion phase, referring to an effect studied by Marks et al. (2008). However, also this scenario requires that the

cluster formed with a high degree of primordial mass segregation. Hence, in both cases Pal 14 has to be mass-segregated nowadays, otherwise the observational evidence for a flattened present-day mass function of this cluster are at odds with our current understanding of stellar dynamics or with the assumption of a universal IMF.

In this Chapter, we use archival HST data reaching down to $\sim$4 mag below the main-sequence turn-off to test if Pal 14 is mass-segregated in order to shed light on its dynamical state. The Chapter is structured as follows: the observational data and their analysis are described in Section 5.2.1. Section 5.3 reports our results on the state of mass segregation in Pal 14, followed by a discussion of our findings in Section 5.4.

5.2 Observations and Literature Data

5.2.1 HST/WFPC2 photometry

Our analysis is based on archival HST imaging, obtained with the Wide-Field Planetary Camera 2 (WFPC2) in program GO 6512 (PI: Hesser). The data were first published in the literature by Dotter et al. (2008b) and were also used by Jordi et al. (2009) to measure the slope of the cluster's overall central mass function. The data consist of F555W (V) and F814W (I) band images with the cluster approximately centred on the WF3 chip of the camera. With exposure times of 4×160 s, 1×900 s and 7×1000 s (amounting to 8540 s in total) in F555W and 4×230 s, 4×1100 s, 2×1200 s, 2×1300 s (10320 s in total) in F814W, this is the deepest available imaging of the cluster's core.

The data were reduced in the same way as described in more detail in Section 4.2.3. PSF-fitting photometry was obtained using the HSTPHOT package (Dolphin 2000). HSTPHOT was initially run on the individual images and the resulting catalogues were cross-matched in order to refine the image registration. The refined image registration was used for a cosmic ray rejection with HSTPHOT's crmask task, and as an input for the photometry from all frames using one of the deep F555W frames as reference image. The following quality cuts were applied to the resulting all-frames photometric catalogue to select clean stellar detections (for details, see the HSTPHOT user manual): a type parameter of 1 (i.e. a stellar detection), abs(sharpness)< 0.2, $\chi < 2.0$, and in both filters a crowding parameter < 1.5 mag and a statistical uncertainty in the magnitude < 0.2 mag. The resulting colour-magnitude diagram, containing 3201 stars, is shown in Fig. 5.1.

HSTPHOT was also used to perform artificial star tests with $\sim 700,000$ fake stars. Artificial stars were distributed similarly to the observed stars, both in the CMD, and on the WFPC2 chips, in order to efficiently sample the relevant parameter space. The same quality cuts as used for the observed stars were applied to the artificial star catalogue. Photometric uncertainties in a given region of the CMD and on the sky were then estimated from the differences between inserted and recovered magnitudes. Error bars on the right-hand side of Fig. 5.1 represent the uncertainty in magnitude and colour as a function of magnitude for main-sequence and RGB stars inside the colour selection indicated by the grey lines to both sides of the isochrone in the same figure. These colour limits were chosen to exclude stars that deviate in colour from the locus of the adopted isochrone (see Section 5.2.3) by more than $3\sigma_{\rm col}$, where $\sigma_{\rm col}$ is the colour uncertainty derived from the artificial star results in the corresponding region of the CMD. The photometric completeness was estimated from the ratio of the number of recovered to the number of inserted artificial stars. The completeness, within the colour selection, as a function of F555W magnitude and distance from the cluster centre is shown in the lower panel of Fig. 5.2. It is apparent that crowding does not or only marginally affect the photometry, as the completeness is essentially independent of the distance from the cluster centre, apart from a dip in completeness at ~ 0.35 arcmin caused by a bright star in the field.

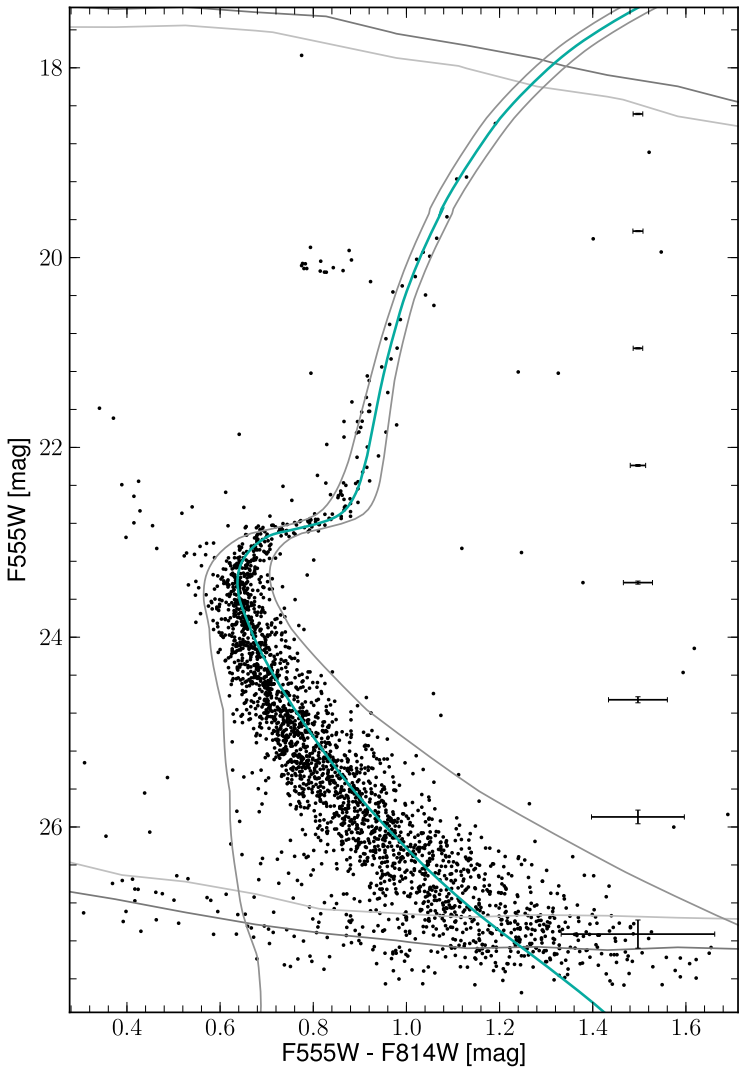

Figure 5.1: Observed colour-magnitude diagram of Pal 14. Error bars on the right represent the photometric errors derived from artificial star tests. The grey lines at the faint and bright ends represent the 80 per cent (light grey) and 50 per cent (dark grey) completeness contours; at the bright end (F555W$\lesssim$18 mag), completeness declines due to saturation even in the shorter exposures. The isochrone, taken from the Dartmouth Stellar Evolution Database (Dotter et al. 2008a) corresponds to an age of 11.5 Gyr, [Fe/H]$= -1.5$ dex and [α/Fe]$= +0.2$ dex (see Section 5.2.3). Thin grey curves to the left and to the right of the isochrone represent the colour limits used for our analysis of the cluster's mass function.

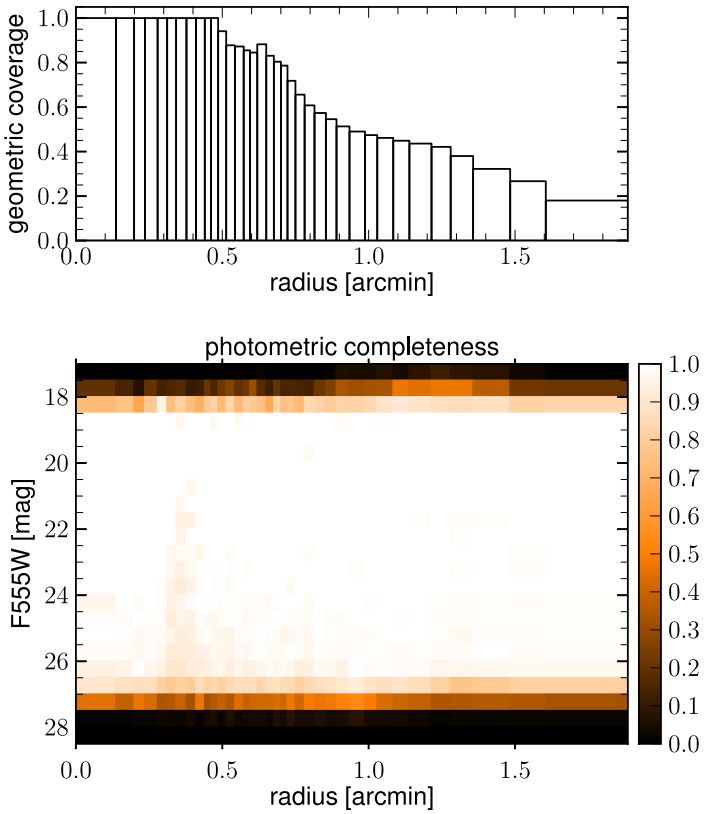

Figure 5.2: Geometric coverage and photometric completeness of the WFPC2 data as a function of radius from the cluster centre. The upper panel shows the geometric coverage of our photometric catalogue, i.e. the area covered by the WFPC2 pointing in a given radial annulus divided by the total area of that annulus. The annuli were defined to contain each one 36th of the observed stars in our catalogue. The lower panel shows the photometric completeness obtained from artificial star tests as a function of F555W magnitude (evaluated in bins of 0.5 mag) and radius; the radial bins are the same as in the upper panel. Completeness only marginally varies with radius, indicating that crowding does not strongly affect the photometry in this sparse cluster. The dip in completeness at $r \sim 0.35$ arcmin is caused by a very bright foreground star at this distance from the cluster centre.

The geometric coverage of the WFPC2 photometry, shown in the upper panel of Fig. 5.2, was quantified as the ratio of the area of covered pixels in a given radial annulus around the cluster's centre to the total area of that annulus. The covered pixels were selected on a distortion-corrected frame combined with multidrizzle (Koekemoer et al. 2006) by the requirement that the covered pixels receive at least 25 per cent of the total exposure time in both filters and be included in the reference frame used for photometry (see Section 4.2.3). The stellar positions in the photometric and artificial star catalogues were transformed to the coordinate system of the distortion-corrected, drizzled frame and stars falling on pixels marked as 'not covered' were rejected to avoid border effects. For the cluster's centre, we used the coordinates determined by Hilker (2006) that agree within the uncertainties with the centre determined by Beccari et al. (2011). Since the absolute astrometric accuracy of the HST is limited by the accuracy of its guide star catalogue, we registered the distortion-corrected coordinate frame to the SDSS DR7 catalogue (Abazajian et al. 2009), before transforming the coordinates of the centre to pixel coordinates in our photometric catalogue.

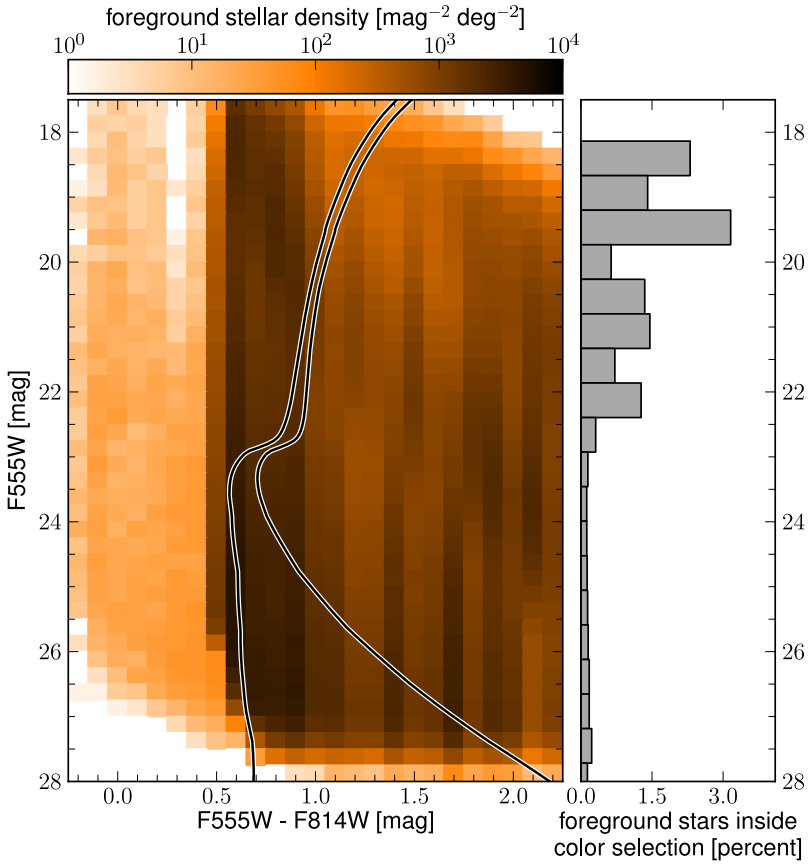

Figure 5.3: The left panel shows the density of foreground stars in the colour-magnitude diagram. The photometric uncertainties and completeness inferred from artificial star tests were imposed on the Besançon foreground catalogue. The density of foreground stars was evaluated in bins of 0.25 mag in F555W and 0.1 mag in colour. The colour scale indicates the density in units of foreground stars per square magnitude in the CMD and square degree on the sky. Black-on-white lines correspond to the region of the CMD used to estimate the mass function of Pal 14. Within these colour limits, the fraction of expected contaminants in the photometric catalogue, averaged over 0.5 mag in F555W is shown in the right panel. It is well below 1 per cent on the main sequence and up to 3 per cent on the sparsely populated RGB.

5.2.2 Foreground contamination

Since the WFPC2 photometry covers only the inner region of the cluster and no nearby comparison fields are available, we used the Besançon model of the Galaxy (Robin et al. 2003) to estimate the expected contamination by foreground stars in our field. We queried the model for stars out to 200 kpc in the direction of Pal 14. For better number statistics, we used a solid angle of 50 square degrees and the model's 'small field' mode that simulates all stars at the same location, so that any spatial variation in the foreground that could be present in such a large field is neglected. For the remaining model parameters, such as the extinction law and spectral type coverage, we used their default values. We transformed the V and I magnitudes of the resulting synthetic foreground catalogue to F555W and F814W magnitudes by inverting the Holtzman et al. (1995) WFPC2 filter to *UBVRI* transformations. The photometric uncertainties and completeness derived from artificial star tests were imposed on the foreground catalogue using the procedure described in Section 4.2.4. The radial variation of these properties was taken into account by assuming the foreground stars to

be distributed homogeneously over the sky and performing the procedure on radial sub-samples of artificial and foreground stars. The left panel of Fig. 5.3 shows the density of foreground stars in our pointing, evaluated in bins of 0.25 mag in F555W and 0.1 mag in colour and scaled to units of stars per mag in colour and magnitude in the CMD and per square degree on the sky. Given the small effective area of the WFPC2 pointing of 4.72 square arcmin the number of expected foreground stars in our catalogue is low. The ratio of expected foreground stars to observed stars inside our colour selection, averaged over bins of 0.5 mag in F555W, is below $\lesssim 3$ percent over the whole range of luminosities and even lower on the main sequence, as shown in the right panel of Fig. 5.3.

5.2.3 Adopted stellar population parameters

In Section 5.3.1 we will use an isochrone as a relation between stellar magnitude and mass, and thus require the knowledge of the distance, reddening, age and chemical composition of the cluster. There are two photometric studies of the cluster's population based on the same WFPC2 data we use here. Dotter et al. (2008b) analysed the photometry transformed to the Johnson-Cousins V and I filters, and applied offsets in the V and I zeropoints to match the ground-based standard star photometry of Stetson (2000). In this system, they obtained a best-fitting Dartmouth isochrone (Dotter et al. 2008a) for a distance of 79 kpc with [Fe/H]=-1.5 dex, [α/Fe]=$+0.2$ dex and an age of 10.5 Gyr. Jordi et al. (2009) used the WFPC2 instrumental magnitudes and the same set of Dartmouth isochrones and adopted the spectroscopic metallicity of [Fe/H]= -1.6 dex from Armandroff et al. (1992). They found a best-fitting isochrone with [α/Fe]=$+0.2$ dex, an age of 11.5$\pm$0.5 Gyr, and a distance of 71 ± 1.3 kpc.

From ground-based photometry, Hilker (2006) derived an age of 10 Gyr, [Fe/H]=-1.5 dex, [α/Fe]= $+0.3$ dex and a distance of 77 kpc based on Yonsei-Yale isochrones (Kim et al. 2002). Sollima et al. (2011) adopted [Fe/H]= -1.6 dex and [α/Fe]=$+0.3$ dex and found a distance of 71 ± 2 kpc as well as an older age of 13.2 ± 0.3 Gyr based on Padova isochrones (Marigo et al. 2008). While this age seems at odds with differential age dating, which suggests that Pal 14 is several Gyr younger than classical old GCs (Sarajedini 1997; Dotter et al. 2008b), differences in absolute ages may also result from differences in the 'age scale' of different sets of isochrones (e.g. Glatt et al. 2008; Marín-Franch et al. 2009).

Finally, from high-resolution spectroscopy of red giants, Çalışkan et al. (2012) recently derived a metallicity of [Fe/H]=-1.3 dex (the mean of their [FeI/H] and [FeII/H] values) and a [α/Fe]=$+0.3 \pm 0.2$ dex.

For our analysis in the WFPC2 instrumental magnitude system, we adopt the parameters derived by Jordi et al. (2009) in this system and specifically also their reddening of $E(\mathrm{F555W}-\mathrm{F814W}) = 0.063$ mag as well as their derived apparent distance modulus of $(m-M)_{\mathrm{F555W}} = 19.45$ mag. The adopted values are well within the scatter of parameters derived by other studies, but we keep in mind that there is some scatter, even when the parameters are derived from the same data and with the same set of isochrones. We will discuss the influence of these uncertainties on the mass function in Section 5.3.2.

5.3 Results

5.3.1 Mass segregation

We determined the stellar mass function in the cluster in the mass range $0.55 \leq m/\mathrm{M}_{\odot} \leq 0.85$, corresponding to stars with 19.5 mag $\lesssim$ F555W $\lesssim$ 27.1 mag, inside the colour selection shown in Fig. 5.1. Photometric completeness, which decreases at the faint end, is still $\gtrsim 70$ per cent in the lowest mass bin at all radii. The colour selection removed likely foreground stars, blue stragglers,

and horizontal branch stars. To each of the selected stars, we assigned a mass based on the adopted isochrone by interpolating the magnitude-mass relation defined by the isochrone to the star's measured F555 magnitude.

While the photometric completeness only marginally varies with distance from the cluster centre, both the geometric coverage and the stellar density do vary as a function of radius (Fig. 5.2). Since we are interested in the mass function within a given radial range in the cluster, rather than in our catalogue, it is necessary to apply a radially varying correction to the number of observed stars to ensure a correct weighting when combining stars from different radii to calculate the mass function. Correcting for the missing area in a given radial annulus necessarily has to assume that the cluster's stellar distribution is axially symmetric around the centre. This is justified, given that a distortion of the isophotes that marks the onset of the tidal tails is visible only at radii $\gtrsim 5$ arcmin (Sollima et al. 2011; Beccari et al. 2011), while our catalogue extends out to only 1.9 arcmin. We divided our photometric catalogue into n radial bins around the cluster centre, so that each of the bins contained one nth of the observed stars. This is optimal in terms of the Poissonian errors on the star counts. In each of the bins we calculated the corrections for photometric completeness and missing area. n has to be large enough to capture the variation of the geometric coverage and stellar density with radius, but should not be chosen larger than necessary to avoid statistical fluctuations caused by low numbers of artificial stars in the individual radial bins. We chose $n = 36$ bins for our analysis after verifying that increasing the number of subdivisions further did not influence any more the derived overall mass function or the integrated stellar mass within 1.9 arcmin.

With only 2354 observed stars within the colour selection and the magnitude limits reported above, the mass function in the individual 36 radial bins (containing 65 stars each) is poorly constrained. We therefore re-combined several of these bins after the correction for geometric coverage and photometric completeness and measured the mass function.

In the combined radial bins, we sorted stars by mass into 10 mass bins with a width of 0.03 $M_\odot$ and fitted the resulting histograms with a power-law of the form $dN/dm \propto m^{-\alpha}$. It is common practise and well justified in the case of large number counts n_i, to treat their uncertainties as Gaussian with dispersions of $\sqrt{n_i}$. In this case, a maximum likelihood fit is obtained by minimising χ^2 or, equivalently, by maximising the log likelihood function

$$\ln \mathscr{L} = k - \sum_{i=1}^{N} \frac{\left(f_i - n_i\, c_i^{-1}\right)^2}{2\left(\sigma_i\, c_i^{-1}\right)^2} \,, \tag{5.1}$$

where k is a constant, $f_i = \int_{m_i}^{m_{i+1}} dN$ is the model prediction in the i-th mass-bin (ranging from mass m_i to m_{i+1}), $\sigma_i = \sqrt{n_i}$ is the uncertainty of the observed number of stars n_i and c_i is the completeness (photometric and geometric) in the given bin. It is also well-known that number counts follow a Poisson distribution, which has to be taken into account in the case of small numbers (e.g. Mighell 1999). Therefore, we chose to maximise the Poissonian log likelihood function

$$\ln \mathscr{L} = -\sum_{i=1}^{N} \ln\left(\frac{\left(\mathrm{f_i}\, c_i\right)^{n_i} \exp\left(f_i\, c_i\right)}{n_i!}\right) , \tag{5.2}$$

where the completeness correction has been multiplied into the model term instead of divided into the n_i.

There are several methods to estimate confidence intervals from the likelihood function; one of them is the likelihood ratio method (e.g. Hudson 1971), which we used here: given the maximum likelihood, the p percent confidence interval for k parameters of interest is defined as the contour in parameter space where the likelihood function has dropped by a factor of $\exp\left(-Q_{\chi^2_k}(p)/2\right)$ with respect to its maximum. Here $Q_{\chi^2_k}(p)$ is the quantile function of the χ^2 distribution for k degrees

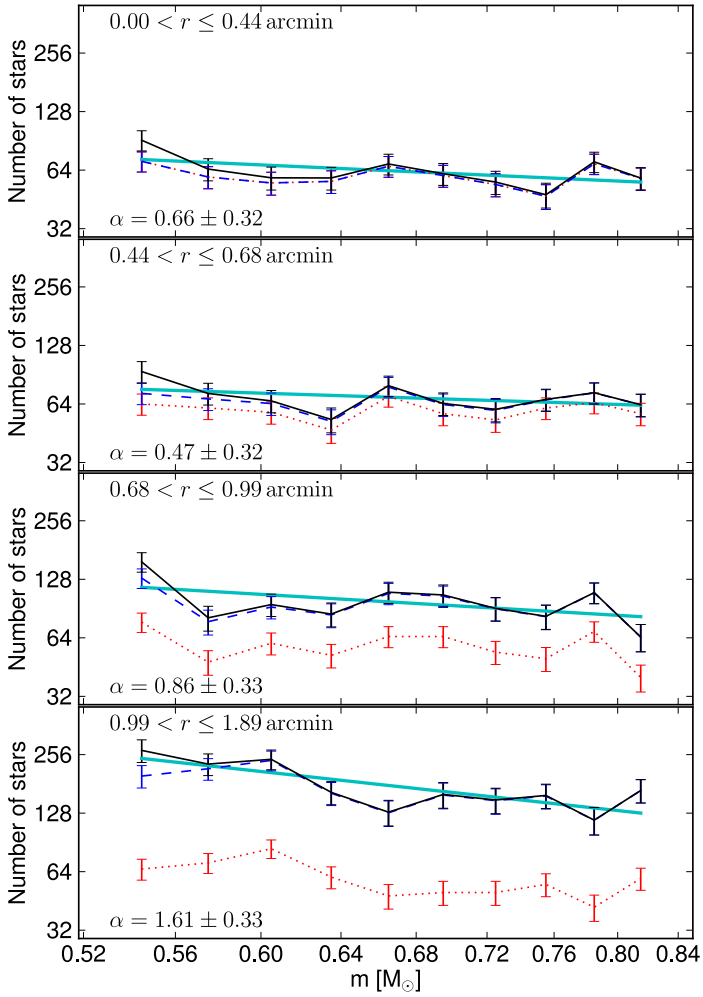

Figure 5.4: The mass function in radial bins containing one fourth of the observed stars each; the radial ranges are reported at the top of each panel. Red dotted lines correspond to the raw star counts, blue dashed lines to the star counts after correction for geometric coverage and black lines to the star counts additionally corrected for photometric incompleteness. The best-fitting power-law mass function, obtained with the maximum-likelihood scheme described in the text is shown as cyan line. The best-fitting mass function slope α and its $1\,\sigma$ uncertainty are reported at the bottom of each panel. In all radial ranges, the mass function is well reproduced by a power-law and that its slope is significantly shallower than a Kroupa (2001, ($\alpha = 2.3$)) mass function in this range of masses.

of freedom; for one parameter of interest, the 68.3 percent (or $1\,\sigma$) confidence interval is given by a decrease in the likelihood by a factor of $\exp(-1/2)$. The confidence limits derived in this way in principle need not be symmetric around the maximum likelihood solution. Nevertheless, our calculated upper and lower uncertainties on α are almost identical, indicating that the likelihood function is symmetric around its maximum. This is also supported by the fact that the results and uncertainties obtained with this Poissonian maximum likelihood fitting did not significantly differ from those obtained for comparison via a common χ^2-minimisation, despite the low number counts. Therefore, while the use of Eq. (5.2) is an improvement over the analysis described in Section 4.4.3 for the case of Pal 4, it is safe to assume that also the solutions obtained therein using χ^2-minimisation are close to the true maximum-likelihood solutions.

The amount of radial sub-divisions is clearly a trade-off between signal to noise and radial

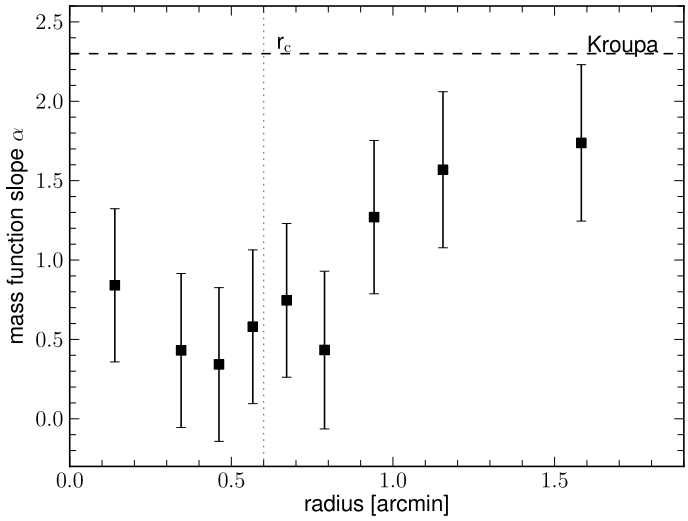

Figure 5.5: The best-fitting mass function slope and its uncertainties in nine radial bins containing equal numbers ($\sim$260) of observed stars. The radii of the data points correspond to the mean radius in the corresponding radial bin. The core radius r_c of the cluster is indicated by the dotted line. A trend of increasing α with increasing radius is obvious, although the slope stays below the Kroupa (2001) value (shown as dashed horizontal line) out to the maximum radius covered by the WFPC2 photometry.

resolution and we present two realisations of the binning. Figure 5.4 shows the mass distributions of observed stars (red dotted lines), the distributions corrected for missing area (blue dashed lines) and the distributions additionally corrected for photometric completeness (black solid lines), as well as the best-fitting power-law mass function, in radial ranges containing each one fourth of the observed stars (i.e. combining blocks of 9 of the 36 original radial bins). It can be seen that the mass function is well-reproduced by a power-law with a slope significantly shallower than a Kroupa (2001) mass function. Moreover, the slope α in the outer-most radial range ($1 \leq r \leq 1.9$ arcmin) is significantly steeper than in the inner two bins. This trend of increasing α with increasing radius is more clearly seen in Fig. 5.5, which shows the best-fitting mass function slope α as a function of radius for radial ranges containing each one ninth of the observed stars (i.e. combining blocks of 4 of the 36 original radial bins). In finer-grained binnings, the scatter and uncertainties of individual data points increase, but the trend remains present. To assess the significance of the trend, we fitted a linear relation to the data in Fig. 5.5. This yields a best-fitting relation of $\alpha(r) = (0.2 \pm 0.3) + r \times (0.9 \pm 0.4)\,\mathrm{arcmin}^{-1}$. A flat relation is excluded at $\sim$98 per cent confidence. This steepening of the mass function with increasing radius suggests that mass segregation is present in Pal 14.

5.3.2 Overall mass function and dependence on the adopted isochrone

The overall mass function slope of stars within 1.9 arcmin (i.e. subsuming the star counts from all radial bins) is $\alpha = 1.1 \pm 0.2$. This is somewhat shallower than the value of $\alpha = 1.3 \pm 0.4$ derived by Jordi et al. (2009) from the same data. Although consistent within the uncertainties, the difference is surprising, as we also adopted the best-fitting isochrone from Jordi et al. (2009) in our analysis. The difference likely stems from a difference in the completeness correction: we calculated the completeness based solely on artificial stars inside the colour selection used for the observed stars. If we instead calculate the completeness from the entire artificial star catalogue, we obtain in a larger completeness correction in the lowest mass bins, similar to the values given in table 3 of Jordi et al. (2009). However, as can be seen from the completeness contours in the CMD (Fig. 5.1), for faint

Table 5.1: Mean radii and two-sample KS tests of the radial distributions of BS, HB, RGB, and main sequence stars.

Sample	N_{obs}	$N_{foreground}$	$\langle r \rangle$ (arcmin)	KS-p HB	KS-p RGB	KS-p uMS	KS-p mMS	KS-p lMS
BS	23	0.5	0.65 ± 0.08	0.31	0.85	0.82	0.81	0.51
HB	14	0.1	0.55 ± 0.07		0.16	0.07	0.10	0.06
RGB	227	0.9	0.71 ± 0.03			0.46	0.54	0.06
uMS	507	0.9	0.71 ± 0.02				0.68	0.08
mMS	510	1.2	0.71 ± 0.02					0.06
lMS	508	1.6	0.75 ± 0.02					

stars bluer than the cluster's main sequence, detection is limited by the F814W filter. Therefore, the inclusion of artificial stars in that region of the CMD would result in an over-correction for completeness.

To estimate the systematic effects of the adopted stellar population parameters on the inferred mass function, we measured the mass function using our adopted 'measurement' isochrone from an artificial luminosity distribution that was generated based on the assumption that the cluster's actual stellar population parameters are different. For this experiment we chose a different isochrone from the (Dotter et al. 2008a) database that differed in age, [Fe/H], or [α/Fe] from our adopted values. We then drew 2000 stars in the range of $0.5 - 0.8\,M_{\odot}$ from a power-law mass function with slope α_{in} and converted the masses to a luminosity distribution according to this 'insertion' isochrone. The location of the main-sequence turn-off of the insertion isochrone in general differed from that of the measurement isochrone. However, any isochrone advocated as the best-fitting isochrone in an observational study will be one that reasonably well reproduces the cluster's main-sequence turn-off. Therefore, we shifted our measurement isochrone in magnitude and colour such that its turn-off point coincided with the insertion isochrone. In observations, these shifts would be equivalent to differences in the inferred distance and reddening and possibly the adopted magnitude zeropoints. Using this shifted measurement isochrone, we obtained the best-fitting slope of the mass function α_{rec} from the artificial luminosity distribution in the same way as for the observations. We find that over- or underestimating the cluster's age, metallicity or [α/Fe] by 1 Gyr or 0.2 dex respectively, results in systematic offsets between the inserted and measured mass function slope by $\Delta\alpha = \|\alpha_{rec} - \alpha_{in}\| = 0.05 - 0.15$. In the tested range of inserted mass function slopes, $\alpha_{in} = 0 - 3$, these offsets only weakly depend on the slope α_{in} itself. Therefore, the amplitude of the change in the mass function slope at different radii of the cluster is largely independent of the uncertainty in the stellar population parameters, while the absolute value of the slope may be considered subject to a systematic uncertainty of $\lesssim 0.15$.

5.3.3 Radial distributions

The argument of Beccari et al. (2011) for the cluster not being relaxed is based on the indistinguishable radial distribution of BS, HB, and RGB stars. It is therefore interesting to look at the radial distributions of cluster stars of different mass, and to extend this analysis to the main sequence. For this, we selected in the CMD blue straggler (BS), horizontal branch (HB), sub-giant branch, and red giant branch stars (the latter two are treated as one sample and simply called RGB). We divided the main sequence from the turn-off at F555W~ 23.4 mag down to 26.15 mag, where our photometry is complete to $\gtrsim 95$ per cent, arbitrarily into three regions containing approximately an equal number of stars, the upper (uMS, with masses of $0.73 \leq m \leq 0.80\,M_{\odot}$), middle (mMS, $0.67 \leq m \leq 0.73\,M_{\odot}$)

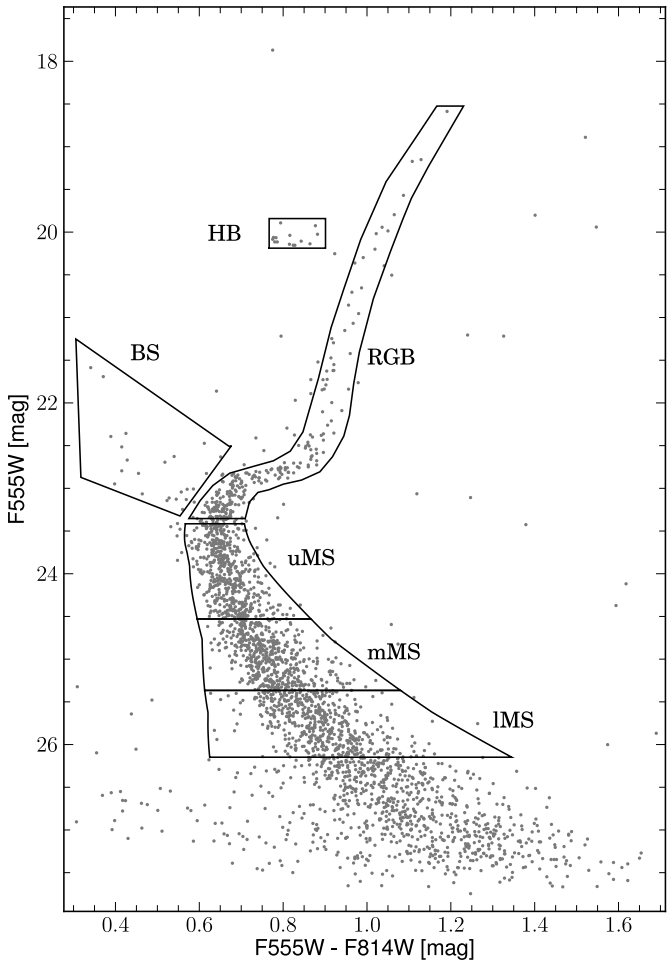

Figure 5.6: The cluster's CMD with selection boxes for sub-populations of different masses superimposed. The boxes show the selection of blue stragglers (BS), horizontal branch stars (HB), sub-giant and red giant branch stars (RGB), as well as the upper (uMS), middle (mMS) and lower (mMS) part of the main sequence. The faint-end limit of 26.15 mag corresponds to the $\sim$95 per cent completeness limit.

and lower (lMS, $0.60 \leq m \leq 0.67\,\mathrm{M}_{\odot}$) part of the main sequence. The selection boxes are shown in Fig. 5.6.

Two-sample KS-tests are widely applied in astronomy to test the hypothesis that two samples originate from the same underlying distribution function, and are based on the maximum separation of the cumulative distribution functions of two populations as a test statistic. In Fig. 5.7 we show the cumulative radial distribution functions of the different sub-populations. Apart from the question whether the observed distributions could stem from the same distribution function, we are also interested in the question which population, if different, is more centrally concentrated. An intuitive measure for this is the area A under the cumulative distribution function; the more concentrated the population, the larger A will be. Another intuitive measure is the average radius $\langle r \rangle$ of stars in a given sub-population. Both quantities, in fact, measure the same and are related by $A = r_{\mathrm{max}} - \langle r \rangle$, where r_{max} is the maximum radius out to which the distribution function is evaluated[2]. Table 5.1 summarises for each of the sub-populations the number of observed stars, the number of expected

[2]This can be seen by recalling that the cumulative radial distribution function for a sample of N stars at radii r_i (i=1...N, $r_i \leq r_{\mathrm{max}}$) increases by $1/N$ at each radius and is 1 in the range $r_N \leq r_{\mathrm{max}}$

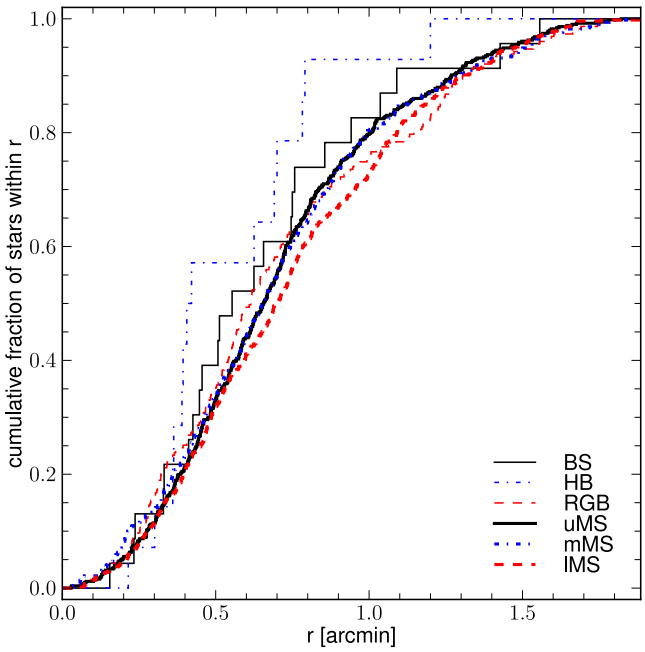

Figure 5.7: The cumulative radial distributions of the sub-populations selected in the CMD (Figure 5.6). Thin lines correspond to BS (black solid), HB (blue dashed-dotted) and RGB (red dashed lines), thick lines to the upper (black solid), middle (blue dash-dotted) and lower (red dotted) part of the main sequence. By eye, the most massive stars, BS and HB stars appear to be somewhat more concentrated, the lowest-mass lMS stars appear less concentrated than RGB, uMS and mMS stars. The significance of this impression was assessed via KS-tests and the average radii of each distribution (see text and Table 5.1).

foreground stars (cf. Section 5.2.2), the average radius $\langle r \rangle$ and the results of a KS-test comparing the radial distribution of the sub-population to those of the remaining ones. Uncertainties on $\langle r \rangle$ were estimated via several hundred bootstrapping realisations, i.e. drawing N stars with replacement from the N stars in the given sub-population.

Except for the BS stars, the radial distributions show at $\lesssim 2\,\sigma$ significance a trend expected in the case of mass segregation: stars with higher initial masses appear to be more centrally concentrated. Because the lifetime of stars in the RGB and HB phase is much shorter than the relaxation time, mass-loss due to winds on the RGB and during the helium flash can be neglected and stars can be assumed to be distributed approximately according to their initial masses. HB stars, having the highest initial masses apart from BS stars, appear more concentrated than RGB and MS stars; RGB, uMS and mMS stars have indistinguishable distributions, both based on a KS test and on their average radii. The stars on the lMS, with the lowest initial masses, show a more extended distribution than any of the higher-mass sub-populations.

In agreement with Beccari et al. (2011), we find no statistically significant difference between BS and HB stars and their radial distribution appears similar to that of RGB and MS stars, although it agrees with that of any of the populations within 1 σ.

5.4 Discussion

We have shown that the mass function in Pal 14 steepens with increasing distance from the centre. Moreover, HB stars appear more centrally concentrated than RGB and MS stars, and MS stars with

masses $0.60 \leq m \leq 0.67\,M_{\odot}$ appear to have a more extended distribution than higher-mass MS stars, RGB stars and HB stars. Both findings suggest that Pal 14 is mass-segregated.

In agreement with Beccari et al. (2011), we find that the distribution of BS stars shows no statistically significant difference with respect to that of any other population. It is possible that this is simply a consequence of the low number of BS stars (23 in our sample, 24 in the sample of Beccari et al. (2011). We note that the fraction of expected foreground contaminants is highest in the BS sample, although with 2 percent still very low, and that foreground contaminants, being randomly distributed on the sky over the extent of the cluster, will tend to flatten the radial distribution.

Other Galactic globular clusters, for which a non-segregated population of BS stars (compared to HB or RGB stars) has been found are NGC 5139 (ωCen; Ferraro et al. 2006), NGC 2419 (Dalessandro et al. 2008), and two clusters associated with the Sgr stream, Terzan 8 (Salinas et al. 2012) and Arp 2 (Salinas et al. 2012; Carraro & Seleznev 2011). For ωCen, Sollima et al. (2007) found no difference in the luminosity function of stars in fields at 12 and 20 arcmin from the cluster centre. There are also no indications for a significantly varying dynamical mass to light ratio out to ~ 3 half-light radii (van de Ven et al. 2006; Jalali et al. 2012) and also the velocity dispersion of MS stars as a function of their mass indicates that energy equipartition has not been established in its centre (Anderson & van der Marel 2010). Also for NGC 2419 there is no evidence for a radially changing luminosity function Bellazzini et al. (2012). Therefore, ωCen and NGC 2419 can be regarded as not being mass-segregated. For Terzan 8 no further data beyond the comparison of BS and HB and RGB stars by Salinas et al. (2012) are available. In Arp 2, which has the lowest present-day half-mass relaxation time among these GCs (8 Gyr, Salinas et al. 2012), the situation is similar to our result for Pal 14: the radial distribution of BS stars is not significantly different from that of HB and RGB stars, but MS stars have a more extended radial distribution (Carraro & Seleznev 2011), indicating that Arp 2 is mass-segregated. Hence, Arp 2 and Pal 14 may serve as examples that an indistinguishable radial distribution of BS and HB and RGB stars is not a sufficient criterion for a cluster to be non-segregated.

The large present-day half-mass relaxation time of Pal 14 may suggest that the observed mass segregation is primordial. Several mechanisms that can lead to a primordial, or early, mass segregation in clusters have been proposed. McMillan et al. (2007) propose a scenario, in which young star clusters assemble from less massive clumps that have significantly shorter relaxation time scales, and which therefore can be already mass-segregated at the time of the cluster assembly. The resulting merged cluster will inherit the mass segregation from its constituents. Olczak et al. (2011) found that early dynamical mass segregation also occurs in clusters without substructure, if they are initially sub-virial and therefore undergo a cold collapse. Another possibility is that mass segregation is created in the star-formation process itself due a more efficient accretion of gas through protostars that reside in the cluster's centre, where the density of gas is higher (Bonnell et al. 2001a,b). In this competitive accretion scenario it seems conceivable that stars are generally segregated by mass, but that the distribution of binaries (such as the BS progenitors) is not necessarily more centrally concentrated, although to our knowledge this has not been studied theoretically.

Primordial, or early, mass segregation is observed in several young Galactic (e.g. Sagar et al. 1988; Hillenbrand 1997; Hasan & Hasan 2011) and Magellanic Cloud star clusters (e.g. Fischer et al. 1998; Sirianni et al. 2002). Besides Pal 14, also the globular clusters Pal 5 (Koch et al. 2004), Pal 4 (Chapter 4) and potentially the rich cluster Lindsay 38 in the Small Magellanic Cloud (Glatt et al. 2011) show mass segregation despite having present-day half-mass relaxation times significantly larger than their age. Baumgardt et al. (2008) suggested that primordial mass segregation together with a depletion of low-mass stars is required to explain the shallow present-day mass functions of at least some Galactic GCs.

As mentioned in the introduction of this Chapter, this was also found by Zonoozi et al. (2011)

for Pal 14. Using collisional N-body simulations these authors showed that two-body relaxation alone is insufficient in order to deplete the mass function of low-mass stars and hence to establish the observed mass segregation if the cluster was born with an initial half-mass radius similar to its present-day value. However, it is also possible that the mass segregation in Pal 14 is due to two-body relaxation, if the cluster had a shorter relaxation time in the past. Sollima et al. (2011) found a present-day half-mass relaxation time for Pal 14 of ~ 20 Gyr based on its projected half-light radius of $r_{hp} = 46 \pm 3$ pc. Since the half-mass relaxation time scales with $r_{hp}^{3/2}$ (Eq. (1.2); Spitzer & Hart 1971), a half-mass relaxation time of a few Gyr would require the cluster to have been more compact by a factor of ~ 2 for most of its lifetime.

Pal 14 is the most extended Galactic GC, and its stellar distribution extends out to more than twice of its Jacobi radius (Eq. (1.4)), that Sollima et al. (2011) calculated to be $r_J = 170 \pm 10$ pc assuming a circular cluster orbit about the Galaxy. It is therefore plausible that it was more compact in the past since otherwise it is puzzling how such a diffuse cluster could have survived until the present day in the Galactic tidal field. Alternatively, it may have evolved in a less hostile environment of a satellite galaxy and was only recently accreted (Sollima et al. 2011). Çalışkan et al. (2012) concluded that the element abundance ratios of red giants in Pal 14 are consistent with a possible accretion origin of the GC from a dwarf spheroidal galaxy.

Baumgardt et al. (2010) used the ratio of the de-projected half-mass radius r_h to r_J to quantify how tidally filling a GC is and found two distinct populations among the Galactic GCs, a tidally under-filling group with $r_h/r_J < 0.05$ and a tidally filling group with $0.1 < r_h/r_J < 0.3$. Using $r_h = 4/3 \times r_{hp}$, and neglecting mass segregation by equating the half-light to the half-mass radius, yields a ratio $r_h/r_J = 0.35$ for Pal 14, making it one of the most tidally filling Galactic GCs, second only to Pal 5. The extended structure of Pal 5 was explained by Dehnen et al. (2004) as the result of its expansion due to heating induced by a tidal shock during a recent passage through the Galactic disk. Disk shocks in general dominate the evolution of diffuse clusters in the Galactic potential (Gnedin et al. 1999). Pal 5 is located at a Galactocentric distance of 18.5 kpc and is believed to be near its apogalacticon (Odenkirchen et al. 2003). Pal 14 has a current Galactocentric distance of 66 kpc, 3.5 times as large, but its orbit is unknown.

However, in order for disk shocks to become important, a cluster has to cross the Galactic disk within a Galactocentric radius of about 8 kpc, since disk shocks will be considerably weaker for a cluster crossing the outer disk where the stellar density is much lower (Vesperini & Heggie 1997). In addition, disk crossings will occur less frequently for a cluster on a nearly circular orbit at the Galactocentric distance of Pal 14. So Pal 14 would have to be on an eccentric orbit. In fact, assuming that its current distance of 66 kpc is close to its apogalactic radius, R_{apo}, Pal 14 would have to be on a highly eccentric orbit with $\varepsilon = (R_{apo} - R_{peri})/(R_{apo} + R_{peri}) = (66-8)/(66+8) \approx 0.8$ in order to have a perigalactic radius, R_{peri}, below 8 kpc. Such high eccentricities would imply severe tidal shocking during pericentre passages, being much more hazardous to the cluster than the disk shocks. Such tidal shocks could in fact temporarily unbind large parts of a cluster like Pal 14, since its Jacobi radius could be significantly smaller than the size of the cluster during a pericentre passage. While moving towards apogalacticon the Jacobi radius of the cluster would grow again and re-capture large parts of the temporarily unbound material (Küpper et al. 2010b).

It is therefore possible that the half-light radius of Pal 14 is significantly overestimated due to unbound stars. In N-body simulations of GCs on eccentric orbits in external tidal fields, Küpper et al. (2010a) found that beyond $0.5\,r_J$, the surface density profiles of the clusters can be entirely dominated by unbound stars. Since Pal 14 may not be on a circular orbit and may not currently be at its perigalacticon, the mean Jacobi radius, to which the cluster adjusts (Küpper et al. 2010a) may be smaller than the present-day value of $r_J = 170 \pm 10$ pc. Therefore the distribution of stars attributed to Pal 14 could already be dominated by unbound stars at radii smaller than $\lesssim 85$ pc, and

the half-light radius of the bound body of Pal 14 may be significantly smaller than the estimated half-light radius of 46 pc. In this case, the mystery how the diffuse cluster has survived to the present day has a simple solution: the cluster has *not* survived, and what we observe is an already largely disintegrated stellar system.

6 Summary

This Chapter briefly summarises the results obtained in this Thesis on ultra-compact dwarf galaxies (Section 6.1) and the remote Galactic globular clusters Pal 4 and Pal 14 (Section 6.2).

6.1 Ultra-compact dwarf galaxies

In Chapter 2 we presented the internal kinematics of UCD3, the brightest known ultra-compact dwarf galaxy (UCD) in the Fornax cluster, making this the first UCD with spatially resolved spectroscopy. We used observations obtained with the ARGUS Integral Field Unit of the VLT/FLAMES spectrograph under excellent seeing conditions (0.5 – 0.67 arcsec).

After correcting for differential atmospheric refraction, the individual data cubes were combined to an oversampled common grid in order to preserve as much spatial resolution as possible. We measured the UCD's velocity and velocity dispersion as a function of position by pixel-fitting the observed spectra with a linear combination of literature stellar spectra that we convolved to the ARGUS instrumental resolution. The velocity field of UCD3 shows the signature of weak rotation. Its velocity dispersion profile is fully consistent with an isotropic velocity distribution and the assumption that mass follows the light distribution obtained from HST imaging. Under these assumptions, we derived a dynamical mass of $\mathrm{M} = 8.2 \pm 0.2 \times 10^7\,\mathrm{M}_\odot$ for the UCD. This mass corresponds to a mass to light ratio of $\mathrm{M/L}_{V,\mathrm{dyn}} = 3.6 \pm 0.1\,\mathrm{M}_\odot\,\mathrm{L}_\odot^{-1}$, which is in excellent agreement with the stellar population mass to light ratio of $\mathrm{M/L}_{V,\mathrm{pop}} = 3.7 \pm 0.2\,\mathrm{M}_\odot\,\mathrm{L}_\odot^{-1}$ measured by Chilingarian et al. (2011).

The shape of the UCD's velocity dispersion profile is less well reproduced by models including dark matter or a central black hole. Hence, there is no evidence for the presence of an extended dark matter halo contributing a significant ($\gtrsim$20 per cent within $R < 200$ pc) mass fraction, nor for a central black hole more massive than $\sim$5 per cent of the UCD's mass. While this result does not exclude a galaxian origin for UCD3, we concluded that its internal kinematics are fully consistent with it being a massive star cluster, even though it is one of the most massive known UCDs.

In Chapter 3, we presented the first attempt to test whether a bottom-heavy stellar mass function causes the high M/L of UCDs. Based on low-resolution *K*-band spectra obtained with VLT/ISAAC of two Virgo cluster UCDs with very high measured M/L and comparison GCs/UCDs around Centaurus A, we measured the strength of the gravity-sensitive 2.3 μm CO absorption band in these

objects.

It became apparent that any classical spectrum extraction is subject to systematic biases in the low S/N spectra of the Virgo cluster UCDs. Performing extensive simulations by inserting artificial spectra in the original raw frames, reducing these and measuring the CO index from the resulting combined frames, allowed us to devise a method that is not susceptible to these biases: carrying out all binning steps first and then extracting the continuum and feature band of the CO index from the resulting collapsed spectra.

With this method, we found that the CO index in the high M/L UCDs is in agreement with that of the lower M/L comparison objects once the variation of the index with metallicity is taken into account. This suggests that the high M/L of the UCDs are not caused by an overabundance of low-mass stars. However, the uncertainties on the measured CO index of the high M/L UCDs are large compared to the expected deviations in the case of a bottom-heavy stellar mass function. Therefore, we cannot firmly exclude an overabundance of low-mass stars in these UCDs.

6.2 The remote Galactic globular clusters Pal 4 and Pal 14

In Chapter 4 we presented a comprehensive analysis of the stellar mass and internal dynamics of the outer halo cluster Pal 4.

Based on fitting isochrones to a deep CMD derived from archival HST/WFPC2 data and adopting literature values for metallicity, α-element enhancement and extinction, we measured the cluster's age and distance to be 11 ± 1 Gyr and 102.8 ± 2.4 kpc, respectively. Using Keck/LRIS and HST/WFPC2 imaging, we derived the cluster's density profile. Out to $r \lesssim 60\,pc$ it is well described by a King (1966) model with a core radius of $r_c = 13 \pm 0.8$ pc and a concentration of $c = 0.96 \pm 0.04$. Combining the LRIS and HST photometry with a SDSS-based literature density profile revealed an overdensity of stars beyond $r \gtrsim 90$ pc. Fitting the combined density profile with a Küpper et al. (2010a) template yielded a shallow outer power-law slope of $\eta = 2.3 \pm 0.6$ that may indicate that Pal 4 is close to its apogalacticon.

Transforming stellar magnitudes to masses using an isochrone with these parameters, we measured the cluster's mass function from the tip of the red giant branch down to main sequence stars of ~ 0.55 $M_\odot$ in the central $r < 2.26$ arcmin. The cluster shows mass segregation, with the mass function steepening from $\alpha \lesssim 1$ inside $r \lesssim 1.3 \times r_h$ to $\alpha \gtrsim 2.3$ outside of $r \gtrsim 1.7 \times r_h$. As the cluster's half-mass relaxation time is of the order of the Hubble time, this may suggest primordial, or early, mass segregation.

We obtained the total stellar mass of Pal 4, $M_{phot} = 29800 \pm 800$ $M_\odot$ by extrapolating the measured mass function towards lower-mass stars and stellar remnants and adopting a Kroupa mass function outside of $0.5 < m < 1.0$ $M_\odot$, as well as extrapolating the mass out to the cluster's tidal radius based on our surface density profile. Using radial velocities obtained from Keck/HIRES spectra of 23 member stars, we measured the cluster's velocity dispersion to be $0.87 \pm 0.18\,km\,s^{-1}$. The dynamical mass corresponding to this velocity dispersion in Newtonian dynamics, $M_{Newton} = 32000 \pm 13000\,M_\odot$, is in excellent agreement with the photometric mass. The dynamical mass predicted by MOND, $M_{MOND} = 3900^{+1400}_{-1500}\,M_\odot$, is significantly below the observed stellar mass. However, a KS test comparing the observed distribution of radial velocities with that predicted in MONDian dynamics showed that MOND is also compatible with the data at a probability of 20 per cent. Thus the observational data favour Newtonian dynamics, but an extended sample of radial velocities is needed to confidently rule out MOND, if the cluster is governed by Newtonian dynamics.

Together with the results of previous studies of Pal 14 and NGC 2419, Pal 4 adds to the growing evidence that the dynamics of outer halo clusters can hardly be explained by MOND.

In Chapter 5, we investigated the stellar mass function in the remote halo cluster Pal 14.

We obtained photometry from archival HST/WFPC2 imaging of the cluster's centre. Using an isochrone based on literature data on the distance, extinction, age, and chemical composition of the cluster, the measured stellar magnitudes were converted to masses. With these, we derived the present-day stellar mass function in the mass range $0.55 \leq m \leq 0.85\,\mathrm{M}_{\odot}$ as a function of distance from the cluster centre. Compared to a Kroupa IMF, Pal 14 is significantly depleted in low-mass stars. We found that the mass function is well described by a shallow power-law slope of $\alpha = 0.66 \pm 0.32$ in the cluster's core, while at larger radii the slope rises to $\alpha = 1.61 \pm 0.33$. This trend of an increasing mass function slope with increasing radius suggests that Pal 14 is mass-segregated. A flat relation of α as a function of radius is excluded at $\gtrsim 98$ per cent confidence.

We also found indications for mass segregation by analysing the radial distributions of different subpopulations of cluster stars. We showed that low mass main-sequence stars show, although at only $\lesssim 2\sigma$ significance, a radial distribution more extended than the populations of RGB and HB stars, as well as more massive main sequence stars. In agreement with Beccari et al. (2011), we find the radial distribution of BS stars to be statistically indistinguishable from that of any other subpopulation.

Our finding of mass segregation is in contrast with the claim of Beccari et al. (2011), who interpreted the indistinguishable radial distributions of blue straggler (BS) stars and HB and RGB stars as evidence for the cluster not being mass segregated. While with ωCen and NGC 2419 two of the handful of Galactic GCs that are known to have a non-segregated distribution of BS show also no sign for mass segregation, our results for Pal 14 and previous indications in the literature for Arp 2 show that comparing the radial distribution of a small sample of BS stars to RGB or HB stars is not a sufficient criterion for judging whether a cluster is mass segregated or not.

Like Pal 4, Pal 14 has a present-day half-mass relaxation time exceeding the Hubble time. For Pal 14 there also exists a full N-body simulation (Zonoozi et al. 2011) that showed that the shallow mass function can not have evolved via two-body relaxation when starting from a Kroupa IMF and an initially unsegregated cluster. We therefore argue that if the structure of Pal 14 did not change substantially during its lifetime, the observed mass segregation must be primordial, i.e. created by the star-formation process itself or must have developed dynamically shortly after the cluster's formation, either because the cluster formed sub-structured or sub-virially. For the cluster to have survived to the present day, its formation in this case is likely to have happened in a very remote environment, far away from the destructive tidal forces of the Milky Way. Alternatively, the cluster may have been significantly more compact in the past, in which case two-body relaxation caused the observed mass segregation. The required expansion of the cluster by a factor of ~ 2 in size might have been caused by severe tidal shocks during pericentre passages on a very eccentric cluster orbit about the Milky Way, like it has been similarly suggested for Pal 5 with disk shocks (Dehnen et al. 2004).

We expect the mass function to continue to steepen beyond the maximum radius covered by the WFPC2 photometry. The tidal tails of Pal 14 therefore should be dominated by low-mass stars and deep imaging reaching well below the main-sequence turn-off will be required to fully uncover the structure of these tails.

7 Outlook

In this Chapter we give an outlook on prospective studies of the dynamics low-mass stellar systems, UCDs (Section 7.1) and remote Galactic globular clusters (Section 7.2). In part, these studies are ongoing projects that were started during the past 3.5 years but are not included in this Thesis.

7.1 Ultra-compact dwarf galaxies

We demonstrated that with UCD3 one of the most massive known UCDs has kinematics compatible with being a star cluster. Moreover, a bottom-heavy stellar mass function is unlikely the explanation for the high M/L of UCDs. Nevertheless, the two big questions pertaining to UCDs remain essentially unanswered: Are UCDs the remnant nuclei of galaxies, or are they star clusters? And what causes their high dynamical mass to light ratios?

There are several areas in which progress can be made. With the study of UCD3, this Thesis sets a precedent for the feasibility of spatially resolving the most extended UCDs with seeing-limited integral-field spectrographs from the ground. There are several more UCDs whose kinematics can be studied with this technique. Figure 7.1 shows proposed observations of two such UCDs, NGC 4546 UCD1 and SUCD1 around the isolated galaxies NGC 4546 and the Sombrero (M 104) at distances of 13 and 9 Mpc respectively. These simulations were made assuming excellent seeing of 0.5 arcsec FHWM and a 0.3 arcsec plate scale and otherwise the same setup of the ARGUS Integral-Field Unit that was used in Chapter 2. The upper left panel of this Figure shows as dashed lines the literature surface brightness profiles of both UCDs (Norris & Kannappan 2011; Hau et al. 2009), and for comparison of UCD3. Solid lines correspond to the surface brightness after convolving with the seeing PSF and integrating over the IFU's spaxels. Both UCDs have smaller apparent half-light radii than UCD3, but their cores are more extended. Estimating the signal to noise ratio per spaxel and spectral bin (shown in the lower left panels) achievable in 6 hours of observing time indicates that kinematics can be measured out to a radius of ~ 0.6 arcsec. The right panel shows the predicted observed velocity dispersion profile assuming mass follows light, the presence of an additional Goerdt et al. (2008)-type dark matter halo, or of a massive black hole. The predicted velocity dispersion profiles were obtained using the Jeans modelling code of Cappellari (2008) with multi-Gaussian expansion representation of the literature surface brightness profiles (Cappellari 2002) as an input. While with these observations, it would be challenging to constrain the dark matter content

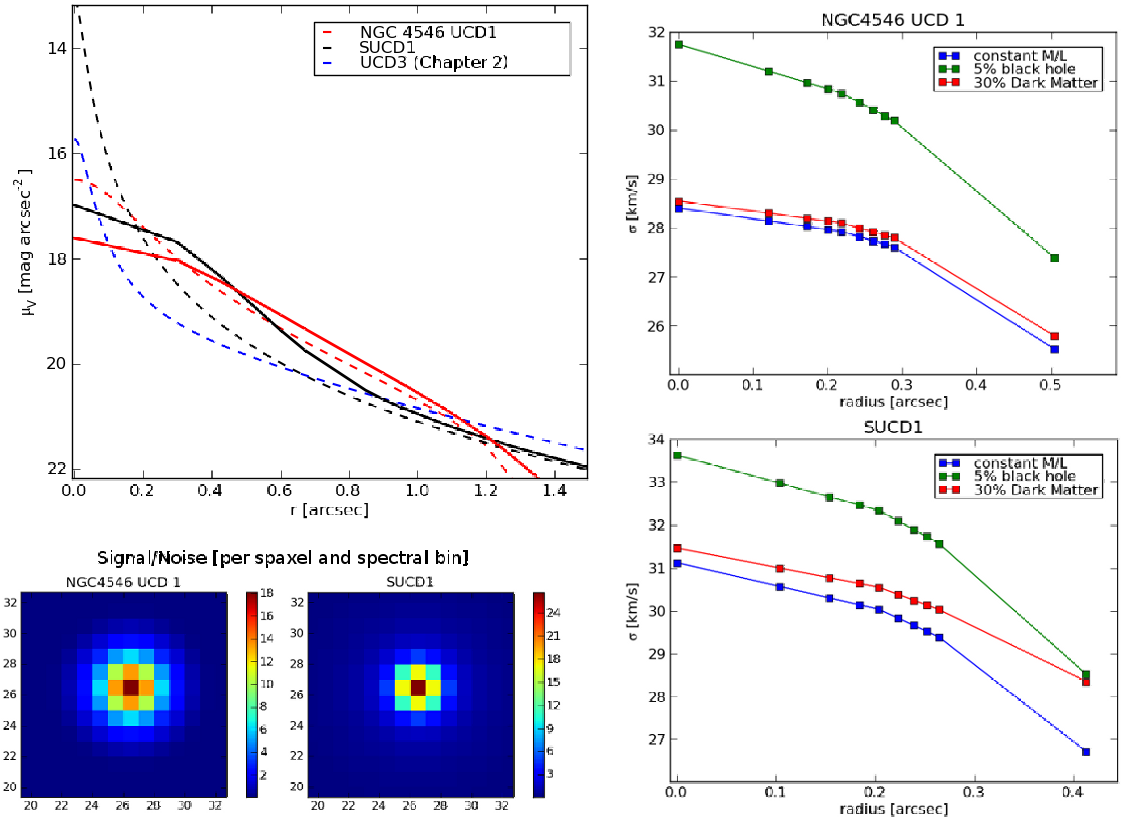

Figure 7.1: Simulations demonstrating the feasibility of obtaining spatially resolved kinematics for two extended UCDs. The upper left panel shows the intrinsic surface brightness profiles of NGC 4546 UCD1 and SUCD1 and of UCD3 for comparison (dashed lines). Solid lines show the surface brightness profile after convolution with the seeing PSF and integrating over 0.3 arcsec spaxels. The signal to noise that can be obtained in 6 hours of VLT observing time is shown in the lower left panels. The right panels show the velocity dispersion expected to be measured in annular segments binned in a similar way as described in Chapter 2 assuming mass follows light, the presence of a dark matter halo, or the presence of a black hole.

of these UCDs, the presence of a black hole contributing 5 percent of the mass would clearly be detectable.

Unfortunately, the most intriguing cases for a kinematical study, the UCDs with the highest M/L ratios, are relatively compact and/or distant. Obtaining spatially resolved kinematics of these UCDs will therefore only come into reach once adaptive-optics integral-field spectrographs are available that have a similarly high spectral resolution as current non-adaptive-optics instruments.

Another approach to answer the question of the origin of UCDs is to study their stellar populations. If multiple stellar populations (differing in age by several Gyr) are present, this would indicate that UCDs are (remnant) galaxies. A more or less coeval stellar population would suggest that they formed similarly to star clusters (cf. Chapter 1). We explore this avenue with two ongoing observational projects (ESO programmes 087.D-0729, PI: Frank; and 087.B-0758, PI: Puzia). The observations, targeting S999, the UCD with the highest M/L (Chapter 3), and several other UCDs in the Virgo cluster and around isolated galaxies with the novel XSHOOTER spectrograph at the VLT, were partially obtained in 2011 in service mode and in visitor mode by Thomas Puzia and the author. The primary goal of these campaigns is to answer the question, whether UCDs contain complex stellar populations. Fig. 7.2 shows the spectral energy distribution of an old, a young and a composite stellar population (based on the GALEV population synthesis models Kotulla et al. 2009)

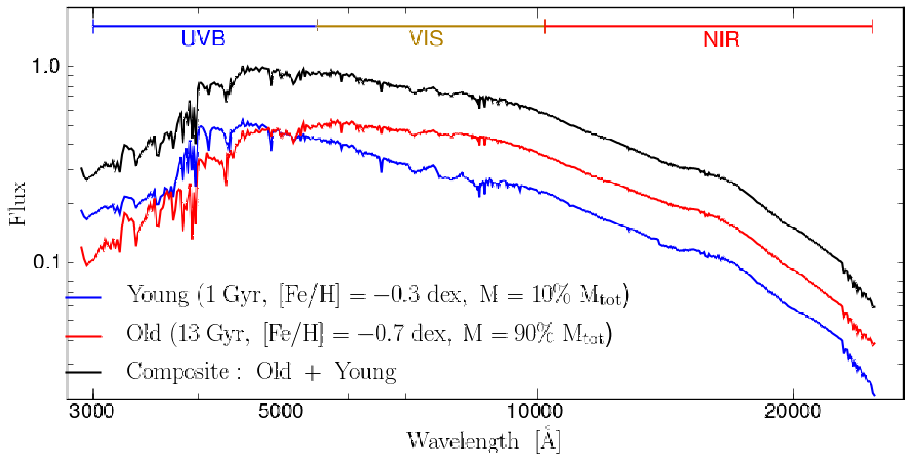

Figure 7.2: Spectral energy distribution of a two-component stellar population in the XSHOOTER wavelength range based on GALEV model spectra (Kotulla et al. 2009). The wavelength ranges covered by the spectrograph's UVB, VIS and NIR arms as indicated at the top. The composite spectral energy distribution (black curve) is composed of an old (13 Gyr; [Fe/H]=−0.7dex; red curve) population constituting 90 per cent of the total stellar mass and a young, more metal-rich component (1 Gyr; [Fe/H]=−0.3 dex, 10 per cent of stellar mass, blue curve). While the younger (hotter) component stands out in the high-excitation features in the UVB range, the old population dominates the molecular bands and the VIS and NIR features.

in the wide wavelength range covered by XSHOOTER's UVB, VIS and NIR arms. The most direct method to search for composite stellar populations will be the fitting of the entire spectral energy distribution with synthetic spectra models, to test whether linear combinations of single stellar populations are required to reproduce the observations. A more indirect approach that is less susceptible to potential flux calibration issues, will be to extract the kinematics separately in the blue and red parts of the spectrum. If multiple stellar populations are present and differ in their kinematics, this would stand out as a difference in the velocity dispersion measured at different wavelengths. In the blue, spectral features, as well as the total flux, are dominated by younger populations, while the red or infrared is dominated by the light from older populations.

The high signal to noise ratio and spectral resolution of these observations ($\sigma_{\rm instrumental} = 15\,{\rm km\,s^{-1}}$ in the optical) may also allow to reliable measure higher order moments of the line-of-sight velocity distributions in these UCDs. These in turn can be used to test for the presence of tidal disturbance (where extended wings of the velocity distribution are expected; Fellhauer & Kroupa 2006) or of massive black holes (cf. Section 2.4.2).

Moreover, with these data, it will be possible to revisit the question of the relative abundance of low-mass stars in UCDs. Measuring the 2.3 μm CO index from these spectra may be problematic, as the signal to noise ratio in the K-band is similar to, or lower than, that of the spectra presented in Chapter 3. However, using a combination of gravity-sensitive features at wavelengths bluer than 1 μm, as done for example by van Dokkum & Conroy (2010), may allow to obtain a significant constraint on the presence of a bottom-heavy stellar mass function.

7.2 Remote Galactic globular clusters

A cosmology based on MOND faces severe problems in explaining the masses of galaxy clusters inferred from gravitational lensing and the third peak of the cosmic microwave background power spectrum that is well understood in ΛCDM, but cannot be explained with baryonic dark matter (e.g.

Famaey & McGaugh 2011; Carroll et al. 2012). On the other hand, MOND is successful as an alternative to dark matter on the galaxy scale. Compared to the indirect cosmological arguments that disfavour MOND, the study of remote Galactic globular clusters offers the possibility to test the very core of MOND: the dynamical behaviour of matter in the regime of small accelerations.

Conclusively distinguishing between Newtonian and MONDian dynamics in remote GCs, and more generally deriving reliable dynamical masses of these clusters, clearly will require larger samples of stellar radial velocities. These would preferentially be obtained in multiple epochs to limit the effect of binaries on the measured velocity dispersions (cf. Section 4.5.2). Since most outer halo clusters are sparsely populated, only a limited number of possible radial velocity target stars can be observed with high-resolution spectrographs on current 8 m-class telescopes. An alternative to larger radial velocity samples in a given cluster is therefore to increase statistics by obtaining moderate numbers of radial velocities in a larger number of clusters.

In this context, an ongoing observational project (ESO programme 089.D-0722, PI: Grebel) aims at the dynamics of the remote halo cluster Pyxis. Using photometry obtained from archival HST and VLT imaging, we selected probable cluster members to be observed with the multi-object FLAMES/Giraffe spectrograph at the VLT. This will allow to obtain precise radial velocities of an estimated 120 probable cluster members and to measure the cluster's velocity dispersion.

The finding of mass segregation in Pal 4 and Pal 14 may mean that primordial, or early dynamical, mass segregation is a common pattern in diffuse GCs. It will therefore be interesting to study the stellar mass function of other diffuse GCs. Alternatively, the present-day half-mass relaxation times of these clusters may not be representative because the clusters were more compact in the past. To answer the question, whether the clusters could have expanded due to disk or tidal shocks, information on their orbits will be required. Measuring the proper motions of these clusters may be feasible with the HST. However, this field of research will also greatly benefit from the upcoming Gaia mission.

A number of authors provided theoretical predictions for the evolution of the slope of the global stellar mass function in GCs with time in the form of fitting functions or as model grids (e.g. Baumgardt & Makino 2003; Kruijssen 2009). However, deep imaging is available almost exclusively for the central parts of Galactic GCs. Therefore, in order to interpret observed stellar mass functions and their radial variation, predictions of the evolution of the mass function of visible stars as a function of projected radius from the cluster centre would be very profitable from an observer's point of view. This would also allow the extrapolation to global mass functions that are independent of the fraction of the cluster covered by imaging, and therefore can be compared among different clusters.

Acknowledgements

It is a pleasure to thank my supervisor in Heidelberg, Eva Grebel. Thank you for the great support in scientific and also administrative things, for good advice, and for the freedom.

I also would like to thank my supervisors at ESO, Michael Hilker and Steffen Mieske. It was a pleasure to spend the two years at ESO Garching and the months at ESO Chile under your guidance. I learnt a great deal about observational astronomy from both of you.

I thank Rainer Spurzem for kindly agreeing to be a referee of my Thesis, and Ulrich Platt and Jochen Heidt for being part of my examination committee.

For their input on this work, I thank Holger Baumgardt (in many ways my fourth advisor), Pat Côté, George Djorgovski, Hosein Haghi, Polo Infante, Andreas Küpper and Pavel Kroupa.

For good scientific advice, I would like to thank Eric Emsellem, Harald Kuntschner, Thorsten Lisker and Marina Rejkuba.

I thank the group at ARI and the ESO gang for helping, sharing fun times and not so fun times and for making both places such pleasant environments. I thank Behrang, Denija, Shoko, Tania and Ulf for long emails, short emails, last-minute proof-reading of conference posters or applications, conference calls, and most of all, for the good conversations.

Ich danke meiner Familie für die Unterstützung all die Jahre. Und ich danke Maria, für vieles.

Bibliography

Aaronson M., Cohen J. G., Mould J., Malkan M., 1978, ApJ, 223, 824 (cited on page 50).

Abazajian K. et al., 2003, AJ, 126, 2081 (cited on page 4).

Abazajian K. N. et al., 2009, ApJS, 182, 543 (cited on pages 14, 42, 73, 90, 93).

Allen K. W., 1977, Astrophysical quantities. (cited on page 48).

An D. et al., 2008, ApJS, 179, 326 (cited on page 73).

Anderson J., van der Marel R. P., 2010, ApJ, 710, 1032 (cited on pages 10, 102).

Armandroff T. E., Da Costa G. S., Zinn R., 1992, AJ, 104, 164 (cited on pages 62, 69, 95).

Arp H., van den Bergh S., 1960, PASP, 72, 48 (cited on page 89).

Bagnulo S., Jehin E., Ledoux C., Cabanac R., Melo C., Gilmozzi R., ESO Paranal Science Operations Team, 2003, ESO Messenger, 114, 10 (cited on page 24).

Barnes J. E., Hernquist L., 1992, Nature, 360, 715 (cited on page 2).

Bassino L. P., Muzzio J. C., 1995, The Observatory, 115, 256 (cited on page 11).

Bassino L. P., Muzzio J. C., Rabolli M., 1994, ApJ, 431, 634 (cited on page 5).

Bastian N., Covey K. R., Meyer M. R., 2010, ARAA, 48, 339 (cited on pages 39, 90).

Bastian N., Konstantopoulos I., Smith L. J., Trancho G., Westmoquette M. S., Gallagher J. S., 2007, MNRAS, 379, 1333 (cited on page 40).

Baumgardt H., Côté P., Hilker M., Rejkuba M., Mieske S., Djorgovski S. G., Stetson P., 2009, MNRAS, 396, 2051 (cited on pages 11, 14, 61, 83).

Baumgardt H., De Marchi G., Kroupa P., 2008, ApJ, 685, 247 (cited on pages 13, 86, 102).

Baumgardt H., Grebel E. K., Kroupa P., 2005, MNRAS, 359, L1 (cited on pages 13, 14, 62, 90).

Baumgardt H., Makino J., 2003, MNRAS, 340, 227 (cited on pages 12, 13, 89, 112).

Baumgardt H., Makino J., Hut P., McMillan S., Portegies Zwart S., 2003, ApJ, 589, L25 (cited on page 10).

Baumgardt H., Mieske S., 2008, MNRAS, 391, 942 (cited on pages 10, 17, 33).

Baumgardt H., Parmentier G., Gieles M., Vesperini E., 2010, MNRAS, 401, 1832 (cited on page 103).

Beasley M. A., Bridges T., Peng E., Harris W. E., Harris G. L. H., Forbes D. A., Mackie G., 2008, MNRAS, 386, 1443 (cited on pages 8, 41, 44).

Beccari G., Sollima A., Ferraro F. R., Lanzoni B., Bellazzini M., De Marchi G., Valls-Gabaud D., Rood R. T., 2011, ApJ, 737, L3 (cited on pages 87, 89, 90, 93, 96, 99, 101, 102, 107).

Bedin L. R., Piotto G., Anderson J., Cassisi S., King I. R., Momany Y., Carraro G., 2004, ApJ, 605, L125 (cited on page 11).

Begeman K. G., Broeils A. H., Sanders R. H., 1991, MNRAS, 249, 523 (cited on page 13).

Bekenstein J., Milgrom M., 1984, ApJ, 286, 7 (cited on page 13).

Bekki K., Couch W. J., Drinkwater M. J., 2001, ApJ, 552, L105 (cited on page 4).

Bekki K., Couch W. J., Drinkwater M. J., Shioya Y., 2003, MNRAS, 344, 399 (cited on pages 4, 5, 17, 33).

Bekki K., Freeman K. C., 2003, MNRAS, 346, L11 (cited on page 11).

Bell R. A., Tripicco M. J., 1991, AJ, 102, 777 (cited on page 41).

Bellazzini M., Dalessandro E., Sollima A., Ibata R., 2012, preprint (arXiv:1203.3024) (cited on page 102).

Belokurov V., Evans N. W., Irwin M. J., Hewett P. C., Wilkinson M. I., 2006a, ApJ, 637, L29 (cited on page 13).

Belokurov V. et al., 2007, ApJ, 654, 897 (cited on page 61).

Belokurov V. et al., 2006b, ApJ, 647, L111 (cited on page 1).

Bender R., Burstein D., Faber S. M., 1993, ApJ, 411, 153 (cited on page 3).

Berg M. d., 2008, Computational geometry, 3rd edn. Springer, Berlin ; Heidelberg, pp. XII, 386 S. (cited on page 68).

Binney J., Merrifield M., 1998, Galactic Astronomy (cited on page 74).

Binney J., Tremaine S., 2008, Galactic Dynamics: Second Edition. Princeton University Press (cited on pages 12, 13).

Blecha A., Cayatte V., North P., Royer F., Simond G., 2000, in SPIE Conf. Ser., Iye M., Moorwood A. F., eds., Vol. 4008, pp. 467–474 (cited on page 19).

Böker T., Sarzi M., McLaughlin D. E., van der Marel R. P., Rix H.-W., Ho L. C., Shields J. C., 2004, AJ, 127, 105 (cited on page 3).

Bonnell I. A., Bate M. R., Clarke C. J., Pringle J. E., 2001a, MNRAS, 323, 785 (cited on page 102).

Bonnell I. A., Clarke C. J., Bate M. R., Pringle J. E., 2001b, MNRAS, 324, 573 (cited on page 102).

Bradford J. D., Geha M., Muñoz R. R., Santana F. A., Simon J. D., Côté P., Stetson P. B., Kirby E., Djorgovski S. G., 2011, ApJ, 743, 167 (cited on pages 9, 85).

Brodie J. P., Larsen S. S., 2002, AJ, 124, 1410 (cited on page 1).

Brodie J. P., Romanowsky A. J., Strader J., Forbes D. A., 2011, AJ, 142, 199 (cited on pages 2, 4, 5, 7).

Bromm V., Larson R. B., 2004, ARAA, 42, 79 (cited on page 39).

Bruzual G., Charlot S., 2003, MNRAS, 344, 1000 (cited on pages 7, 8, 42).

Burbidge E. M., Sandage A., 1958, ApJ, 127, 527 (cited on page 77).

Çalışkan Ş., Christlieb N., Grebel E. K., 2012, A&A, 537, A83 (cited on pages 95, 103).

Cappellari M., 2002, MNRAS, 333, 400 (cited on page 109).

Cappellari M., 2008, MNRAS, 390, 71 (cited on pages 33, 109).

Cappellari M., Copin Y., 2003, MNRAS, 342, 345 (cited on page 24).

Cappellari M., Emsellem E., 2004, PASP, 116, 138 (cited on page 24).

Cappellari M. et al., 2011, MNRAS, 413, 813 (cited on pages 17, 40).

Cappellari M. et al., 2012, Nature, 484, 485 (cited on page 40).

Carraro G., Seleznev A. F., 2011, MNRAS, 412, 1361 (cited on page 102).

Carroll S., Plaga R., McGaugh S., 2012, Dark Matter vs. Modified Gravity: A Trialogue. http://blogs.discovermagazine.com/cosmicvariance/2012/05/09/dark-matter-vs-modified-gravity-a-trialogue/, retrieved 10 May 2012 (cited on page 112).

Catelan M., 2000, ApJ, 531, 826 (cited on page 62).

Chabrier G., 2003, PASP, 115, 763 (cited on pages 7, 40).

Chiboucas K., Tully R. B., Marzke R. O., Phillipps S., Price J., Peng E. W., Trentham N., Carter D., Hammer D., 2011, ApJ, 737, 86 (cited on page 4).

Chies-Santos A. L., Larsen S. S., Cantiello M., Strader J., Kuntschner H., Wehner E. M., Brodie J. P., 2012, A&A, 539, A54 (cited on page 6).

Chilingarian I. V., Bergond G., 2010, MNRAS, 405, L11 (cited on page 3).

Chilingarian I. V., Cayatte V., Bergond G., 2008a, MNRAS, 390, 906 (cited on pages 18, 33).

Chilingarian I. V., Cayatte V., Durret F., Adami C., Balkowski C., Chemin L., Laganá T. F., Prugniel P., 2008b, A&A, 486, 85 (cited on page 3).

Chilingarian I. V., Mamon G. A., 2008, MNRAS, 385, L83 (cited on page 3).

Chilingarian I. V., Mieske S., Hilker M., Infante L., 2011, MNRAS, 412, 1627 (cited on pages 4, 6, 7, 33, 37, 105).

Chilingarian I. V., Prugniel P., Sil'Chenko O. K., Afanasiev V. L., 2007, MNRAS, 376, 1033 (cited on page 24).

Christian C. A., Heasley J. N., 1986, ApJ, 303, 216 (cited on page 77).

Chu Y., Zhao Y.-H., 1998, in New Horizons from Multi-Wavelength Sky Surveys, McLean B. J., Golombek D. A., Hayes J. J. E., Payne H. E., eds., Vol. 179, p. 131 (cited on page 4).

Chun S.-H., Kim J.-W., Sohn S. T., Park J.-H., Han W., Kim H.-I., Lee Y.-W., Lee M. G., Lee S.-G., Sohn Y.-J., 2010, AJ, 139, 606 (cited on page 13).

Clark J. S., Negueruela I., Crowther P. A., Goodwin S. P., 2005, A&A, 434, 949 (cited on page 11).

Cohen J. G., Blakeslee J. P., Ryzhov A., 1998, ApJ, 496, 808 (cited on page 44).

Cohen J. G., Huang W., Kirby E. N., 2011, ApJ, 740, 60 (cited on page 12).

Conroy C., Loeb A., Spergel D. N., 2011, ApJ, 741, 72 (cited on page 11).

Conroy C., van Dokkum P., 2012, ApJ, 747, 69 (cited on page 41).

Côté P., Djorgovski S. G., Meylan G., Castro S., McCarthy J. K., 2002, ApJ, 574, 783 (cited on pages 9, 62, 63).

Côté P., Marzke R. O., West M. J., Minniti D., 2000, ApJ, 533, 869 (cited on page 11).

Côté P. et al., 2006, ApJS, 165, 57 (cited on page 3).

Da Costa G. S., 2012, ApJ, 751, 6 (cited on page 11).

Da Costa G. S., Grebel E. K., Jerjen H., Rejkuba M., Sharina M. E., 2009, AJ, 137, 4361 (cited on page 1).

Da Rocha C., Mieske S., Georgiev I. Y., Hilker M., Ziegler B. L., Mendes de Oliveira C., 2011, A&A, 525, A86 (cited on pages 4, 7).

Dabringhausen J., Fellhauer M., Kroupa P., 2010, MNRAS, 403, 1054 (cited on pages 10, 17, 40).

Dabringhausen J., Hilker M., Kroupa P., 2008, MNRAS, 386, 864 (cited on pages 10, 17, 40).

Dabringhausen J., Kroupa P., Baumgardt H., 2009, MNRAS, 394, 1529 (cited on pages 10, 17, 40).

Dabringhausen J., Kroupa P., Pflamm-Altenburg J., Mieske S., 2012, ApJ, 747, 72 (cited on page 40).

Dalessandro E., Lanzoni B., Ferraro F. R., Vespe F., Bellazzini M., Rood R. T., 2008, ApJ, 681, 311 (cited on page 102).

De Marchi G., Paresce F., Pulone L., 2007, ApJ, 656, L65 (cited on page 80).

De Propris R., Phillipps S., Drinkwater M. J., Gregg M. D., Jones J. B., Evstigneeva E., Bekki K., 2005, ApJ, 623, L105 (cited on pages 5, 17).

de Zeeuw P. T. et al., 2002, MNRAS, 329, 513 (cited on page 17).

Dehnen W., Odenkirchen M., Grebel E. K., Rix H.-W., 2004, AJ, 127, 2753 (cited on pages 103, 107).

Dekker H., D'Odorico S., Kaufer A., Delabre B., Kotzlowski H., 2000, in SPIE Conf. Ser., Iye M., Moorwood A. F., eds., Vol. 4008, pp. 534–545 (cited on page 24).

Dolphin A. E., 2000, PASP, 112, 1383 (cited on pages 64, 91).

Dotter A., Chaboyer B., Jevremović D., Kostov V., Baron E., Ferguson J. W., 2008a, ApJS, 178, 89 (cited on pages 77, 92, 95, 99).

Dotter A. et al., 2010, ApJ, 708, 698 (cited on page 11).

Dotter A., Sarajedini A., Yang S.-C., 2008b, AJ, 136, 1407 (cited on pages 91, 95).

Drinkwater M. J., Gregg M. D., Couch W. J., Ferguson H. C., Hilker M., Jones J. B., Karick A., Phillipps S., 2004, PASA, 21, 375 (cited on page 5).

Drinkwater M. J., Gregg M. D., Hilker M., Bekki K., Couch W. J., Ferguson H. C., Jones J. B., Phillipps S., 2003, Nature, 423, 519 (cited on page 5).

Drinkwater M. J., Jones J. B., Gregg M. D., Phillipps S., 2000, PASA, 17, 227 (cited on page 4).

Drukier G. A., Slavin S. D., Cohn H. N., Lugger P. M., Berrington R. C., Murphy B. W., Seitzer P. O., 1998, AJ, 115, 708 (cited on page 14).

Duc P.-A., Mirabel I. F., 1998, A&A, 333, 813 (cited on page 2).

Eggen O. J., Lynden-Bell D., Sandage A. R., 1962, ApJ, 136, 748 (cited on page 11).

Eisenhauer F. et al., 2003, in SPIE Conf. Ser., Iye M., Moorwood A. F. M., eds., Vol. 4841, pp. 1548–1561 (cited on page 17).

Evstigneeva E. A., Drinkwater M. J., Peng C. Y., Hilker M., De Propris R., Jones J. B., Phillipps S., Gregg M. D., Karick A. M., 2008, AJ, 136, 461 (cited on pages 5, 17, 18).

Evstigneeva E. A., Gregg M. D., Drinkwater M. J., Hilker M., 2007, AJ, 133, 1722 (cited on pages 6, 7, 9, 20, 26, 30, 36).

Famaey B., McGaugh S., 2011, preprint (arXiv:1112.3960) (cited on pages 13, 112).

Fellhauer M., Kroupa P., 2002, MNRAS, 330, 642 (cited on pages 5, 17).

Fellhauer M., Kroupa P., 2005, MNRAS, 359, 223 (cited on page 5).

Fellhauer M., Kroupa P., 2006, MNRAS, 367, 1577 (cited on pages 10, 30, 111).

Ferrarese L. et al., 2006, ApJS, 164, 334 (cited on page 3).

Ferraro F. R., Beccari G., Dalessandro E., Lanzoni B., Sills A., Rood R. T., Pecci F. F., Karakas A. I., Miocchi P., Bovinelli S., 2009, Nature, 462, 1028 (cited on page 89).

Ferraro F. R., Sollima A., Rood R. T., Origlia L., Pancino E., Bellazzini M., 2006, ApJ, 638, 433 (cited on page 102).

Filippenko A. V., 1982, PASP, 94, 715 (cited on page 23).

Firth P., Evstigneeva E. A., Drinkwater M. J., 2009, MNRAS, 394, 1801 (cited on pages 4, 7, 33, 35).

Fischer P., Pryor C., Murray S., Mateo M., Richtler T., 1998, AJ, 115, 592 (cited on pages 86, 102).

Fischer P., Welch D. L., Cote P., Mateo M., Madore B. F., 1992, AJ, 103, 857 (cited on page 75).

Forbes D. A., Bridges T., 2010, MNRAS, 404, 1203 (cited on page 11).

Forbes D. A., Kroupa P., 2011, PASA, 28, 77 (cited on page 2).

Foster C., Spitler L. R., Romanowsky A. J., Forbes D. A., Pota V., Bekki K., Strader J., Proctor R. N., Arnold J. A., Brodie J. P., 2011, MNRAS, 415, 3393 (cited on page 4).

Frank M. J., Hilker M., Baumgardt H., Côté P., Grebel E. K., Haghi H., Küpper A. H. W., Djorgovski S. G., 2012, MNRAS in press, arXiv:1205.2693 (cited on page 61).

Frank M. J., Hilker M., Mieske S., Baumgardt H., Grebel E. K., Infante L., 2011, MNRAS, 414, L70 (cited on page 17).

Freedman W. L. et al., 2001, ApJ, 553, 47 (cited on pages 18, 30).

Frogel J. A., Becklin E. E., Neugebauer G., Matthews K., Persson S. E., Aaronson M., 1975, ApJ, 200, L123 (cited on page 49).

Frogel J. A., Persson S. E., Matthews K., Aaronson M., 1978, ApJ, 220, 75 (cited on page 49).

Frogel J. A., Stephens A., Ramírez S., DePoy D. L., 2001, AJ, 122, 1896 (cited on pages 50, 51, 58, 59).

Frommert H., Kronberg C., McArthur G., Elowitz M., 2006, The SEDS Messier Catalog Webpages. http://messier.seds.org/, retrieved 21 April 2012 (cited on page 1).

Fruchter A. S., Hook R. N., 2002, PASP, 114, 144 (cited on page 23).

Gebhardt K., Rich R. M., Ho L. C., 2002, ApJ, 578, L41 (cited on page 10).

Geha M., Guhathakurta P., van der Marel R. P., 2003, AJ, 126, 1794 (cited on page 7).

Geller A. M., Mathieu R. D., 2011, Nature, 478, 356 (cited on page 90).

Gentile G., Famaey B., Angus G., Kroupa P., 2010, A&A, 509, A97 (cited on pages 14, 61, 82, 90).

Gerssen J., van der Marel R. P., Gebhardt K., Guhathakurta P., Peterson R. C., Pryor C., 2002, AJ, 124, 3270 (cited on page 10).

Gilmore G., Wilkinson M. I., Wyse R. F. G., Kleyna J. T., Koch A., Evans N. W., Grebel E. K., 2007, ApJ, 663, 948 (cited on page 10).

Glatt K. et al., 2008, AJ, 135, 1106 (cited on page 95).

Glatt K. et al., 2011, AJ, 142, 36 (cited on pages 80, 102).

Gnedin O. Y., Lee H. M., Ostriker J. P., 1999, ApJ, 522, 935 (cited on page 103).

Gnedin O. Y., Ostriker J. P., 1997, ApJ, 474, 223 (cited on page 13).

Goerdt T., Moore B., Kazantzidis S., Kaufmann T., Macciò A. V., Stadel J., 2008, MNRAS, 385, 2136 (cited on pages 10, 17, 33, 34, 109).

Goodwin S. P., Bastian N., 2006, MNRAS, 373, 752 (cited on page 40).

Graham A. W., Spitler L. R., 2009, MNRAS, 397, 2148 (cited on pages 10, 35).

Gratton R. G., Carretta E., Bragaglia A., 2012, A&A Rev., 20, 50 (cited on page 11).

Gregg M. D., Drinkwater M. J., Evstigneeva E., Jurek R., Karick A. M., Phillipps S., Bridges T., Jones J. B., Bekki K., Couch W. J., 2009, AJ, 137, 498 (cited on pages 4, 5).

Grillmair C. J., Johnson R., 2006, ApJ, 639, L17 (cited on page 13).

Grillo C., Gobat R., 2010, MNRAS, 402, L67 (cited on page 40).

Gürkan M. A., Freitag M., Rasio F. A., 2004, ApJ, 604, 632 (cited on pages 12, 86).

Haşegan M. et al., 2005, ApJ, 627, 203 (cited on pages 4, 7, 33, 44).

Haghi H., Baumgardt H., Kroupa P., 2011, A&A, 527, A33 (cited on pages 14, 61, 62, 81, 83, 90).

Haghi H., Baumgardt H., Kroupa P., Grebel E. K., Hilker M., Jordi K., 2009, MNRAS, 395, 1549 (cited on pages 14, 61, 90).

Hankey W. J., Cole A. A., 2011, MNRAS, 411, 1536 (cited on page 11).

Hanson M. M., Conti P. S., Rieke M. J., 1996, ApJS, 107, 281 (cited on page 49).

Harris G. L. H., Geisler D., Harris H. C., Hesser J. E., 1992, AJ, 104, 613 (cited on page 44).

Harris W. E., 1996, AJ, 112, 1487 (cited on pages 10, 50, 61, 73, 77, 89).

Hasan P., Hasan S. N., 2011, MNRAS, 413, 2345 (cited on pages 86, 102).

Hau G. K. T., Spitler L. R., Forbes D. A., Proctor R. N., Strader J., Mendel J. T., Brodie J. P., Harris W. E., 2009, MNRAS, 394, L97 (cited on pages 4, 6, 109).

Hesser J. E., Harris H. C., Harris G. L. H., 1986, ApJ, 303, L51 (cited on page 44).

Hilker M., 2006, A&A, 448, 171 (cited on pages 65, 93, 95).

Hilker M., 2009, UCDs - A Mixed Bag of Objects, Richtler T., Larsen S., eds., p. 51 (cited on page 7).

Hilker M., Baumgardt H., Infante L., Drinkwater M., Evstigneeva E., Gregg M., 2007, A&A, 463, 119 (cited on pages 4, 9, 17, 30).

Hilker M., Infante L., Vieira G., Kissler-Patig M., Richtler T., 1999, A&AS, 134, 75 (cited on pages 4, 18).

Hilker M., Richtler T., 2000, A&A, 362, 895 (cited on page 11).

Hillenbrand L. A., 1997, AJ, 113, 1733 (cited on pages 86, 102).

Hillenbrand L. A., Hartmann L. W., 1998, ApJ, 492, 540 (cited on page 86).

Hills J. G., Day C. A., 1976, ApL, 17, 87 (cited on page 89).

Holland S., Côté P., Hesser J. E., 1999, A&A, 348, 418 (cited on page 44).

Holtzman J. A., Burrows C. J., Casertano S., Hester J. J., Trauger J. T., Watson A. M., Worthey G., 1995, PASP, 107, 1065 (cited on pages 68, 75, 94).

Horne K., 1986, PASP, 98, 609 (cited on pages 46, 47, 48).

Hudson D. J., 1971, J. R. Stat. Soc. B, 33, pp. 256 (cited on page 96).

Hughes J., Wallerstein G., 2000, AJ, 119, 1225 (cited on page 11).

Hurley J. R., Tout C. A., Pols O. R., 2002, MNRAS, 329, 897 (cited on page 85).

Huxor A. P., Tanvir N. R., Irwin M. J., Ibata R., Collett J. L., Ferguson A. M. N., Bridges T., Lewis G. F., 2005, MNRAS, 360, 1007 (cited on page 1).

Ibata R., Sollima A., Nipoti C., Bellazzini M., Chapman S. C., Dalessandro E., 2011a, ApJ, 738, 186 (cited on pages 14, 61, 83, 90).

Ibata R., Sollima A., Nipoti C., Bellazzini M., Chapman S. C., Dalessandro E., 2011b, ApJ, 743, 43 (cited on pages 14, 61, 83, 90).

Ibata R. A., Gilmore G., Irwin M. J., 1995, MNRAS, 277, 781 (cited on page 11).

Ivanov V. D., Kurtev R., Borissova J., 2005, A&A, 442, 195 (cited on page 10).

Jalali B., Baumgardt H., Kissler-Patig M., Gebhardt K., Noyola E., Lützgendorf N., de Zeeuw P. T., 2012, A&A, 538, A19 (cited on page 102).

Jones J. B., Drinkwater M. J., Jurek R., Phillipps S., Gregg M. D., Bekki K., Couch W. J., Karick A., Parker Q. A., Smith R. M., 2006, AJ, 131, 312 (cited on page 4).

Jordán A. et al., 2005, ApJ, 634, 1002 (cited on page 61).

Jordán A., Peng E. W., Blakeslee J. P., Côté P., Eyheramendy S., Ferrarese L., Mei S., Tonry J. L., West M. J., 2009, ApJS, 180, 54 (cited on page 3).

Jordi K., Grebel E. K., 2010, A&A, 522, A71 (cited on pages 13, 14, 61, 73, 76, 90).

Jordi K., Grebel E. K., Hilker M., Baumgardt H., Frank M., Kroupa P., Haghi H., Côté P., Djorgovski S. G., 2009, AJ, 137, 4586 (cited on pages 14, 61, 80, 81, 83, 86, 87, 90, 91, 95, 98).

Kaiser N. et al., 2002, in SPIE Conf. Ser., Tyson J. A., Wolff S., eds., Vol. 4836, pp. 154–164 (cited on page 4).

Kaufer A., Pasquini L., Castillo R., Schmutzer R., Smoker J., 2003, ESO Messenger, 113, 15 (cited on page 18).

Khalisi E., Amaro-Seoane P., Spurzem R., 2007, MNRAS, 374, 703 (cited on page 12).

Kim Y.-C., Demarque P., Yi S. K., Alexander D. R., 2002, ApJS, 143, 499 (cited on page 95).

King I., 1962, AJ, 67, 471 (cited on pages 74, 75, 76, 77).

King I. R., 1966, AJ, 71, 64 (cited on pages 13, 73, 75, 76, 77, 80, 106).

Kissler-Patig M., 2004, in The Formation and Evolution of Massive Young Star Clusters, Lamers H. J. G. L. M., Smith L. J., Nota A., eds., Vol. 322, p. 535 (cited on page 4).

Koch A., Côté P., 2010, A&A, 517, A59 (cited on pages 62, 63, 77, 82).

Koch A., Grebel E. K., Odenkirchen M., Martínez-Delgado D., Caldwell J. A. R., 2004, AJ, 128, 2274 (cited on pages 86, 102).

Koekemoer A. M., Fruchter A. S., Hook R. N., Hack W., Hanley C., 2006, in The 2005 HST Calibration Workshop: Hubble After the Transition to Two-Gyro Mode, Koekemoer A. M., Goudfrooij P., Dressel L. L., eds., p. 423 (cited on pages 64, 93).

Kotulla R., Fritze U., Weilbacher P., Anders P., 2009, MNRAS, 396, 462 (cited on pages 110, 111).

Kouwenhoven M. B. N., de Grijs R., 2008, A&A, 480, 103 (cited on page 85).

Kroupa P., 1995, MNRAS, 277, 1507 (cited on page 85).

Kroupa P., 1998, MNRAS, 300, 200 (cited on page 5).

Kroupa P., 2001, MNRAS, 322, 231 (cited on pages 7, 13, 14, 39, 80, 90, 97, 98).

Kroupa P., 2002, Science, 295, 82 (cited on page 39).

Kroupa P., Gilmore G. F., 1994, MNRAS, 269, 655 (cited on page 51).

Kruijssen J. M. D., 2009, A&A, 507, 1409 (cited on pages 12, 80, 89, 112).

Kruijssen J. M. D., Mieske S., 2009, A&A, 500, 785 (cited on pages 7, 9, 17).

Kuntschner H., 2000, MNRAS, 315, 184 (cited on page 7).

Küpper A. H. W., Kroupa P., 2010, ApJ, 716, 776 (cited on pages 14, 61, 90).

Küpper A. H. W., Kroupa P., Baumgardt H., Heggie D. C., 2010a, MNRAS, 407, 2241 (cited on pages 14, 77, 86, 103, 106).

Küpper A. H. W., Kroupa P., Baumgardt H., Heggie D. C., 2010b, MNRAS, 401, 105 (cited on page 103).

Küpper A. H. W., Maschberger T., Kroupa P., Baumgardt H., 2011a, MNRAS, 417, 2300 (cited on page 85).

Küpper A. H. W., Mieske S., Kroupa P., 2011b, MNRAS, 413, 863 (cited on pages 14, 86, 90).

Landolt A. U., 1992, AJ, 104, 340 (cited on page 63).

Lane R. R., Kiss L. L., Lewis G. F., Ibata R. A., Siebert A., Bedding T. R., Székely P., 2010a, MNRAS, 401, 2521 (cited on page 14).

Lane R. R., Kiss L. L., Lewis G. F., Ibata R. A., Siebert A., Bedding T. R., Székely P., Balog Z., Szabó G. M., 2010b, MNRAS, 406, 2732 (cited on page 14).

Lanzoni B., Dalessandro E., Ferraro F. R., Mancini C., Beccari G., Rood R. T., Mapelli M., Sigurdsson S., 2007, ApJ, 663, 267 (cited on page 89).

Larsen S. S., Brodie J. P., 2000, AJ, 120, 2938 (cited on page 1).

Law D. R., Majewski S. R., 2010, ApJ, 718, 1128 (cited on page 62).

Layden A. C., Sarajedini A., 2000, AJ, 119, 1760 (cited on page 11).

Lee Y.-W., Gim H. B., Casetti-Dinescu D. I., 2007, ApJ, 661, L49 (cited on page 11).

Lee Y.-W., Joo J.-M., Sohn Y.-J., Rey S.-C., Lee H.-C., Walker A. R., 1999, Nature, 402, 55 (cited on page 11).

Londrillo P., Nipoti C., 2009, Memorie della Societa Astronomica Italiana Supplementi, 13, 89 (cited on page 81).

Longmore A. J., Kurtev R., Lucas P. W., Froebrich D., de Grijs R., Ivanov V. D., Maccarone T. J., Borissova J., Ker L. M., 2011, MNRAS, 416, 465 (cited on page 10).

Lützgendorf N., Kissler-Patig M., Noyola E., Jalali B., de Zeeuw P. T., Gebhardt K., Baumgardt H., 2011, A&A, 533, A36 (cited on page 10).

Mackey A. D., Gilmore G. F., 2004, MNRAS, 355, 504 (cited on page 11).

Madrid J. P., 2011, ApJ, 737, L13 (cited on page 4).

Madrid J. P., Graham A. W., Harris W. E., Goudfrooij P., Forbes D. A., Carter D., Blakeslee J. P., Spitler L. R., Ferguson H. C., 2010, ApJ, 722, 1707 (cited on page 4).

Majewski S. R., Patterson R. J., Dinescu D. I., Johnson W. Y., Ostheimer J. C., Kunkel W. E., Palma C., 2000, in Liege International Astrophysical Colloquia, Noels A., Magain P., Caro D., Jehin E., Parmentier G., Thoul A. A., eds., Vol. 35, p. 619 (cited on page 11).

Mapelli M., Sigurdsson S., Ferraro F. R., Colpi M., Possenti A., Lanzoni B., 2006, MNRAS, 373, 361 (cited on page 89).

Maraston C., 2005, MNRAS, 362, 799 (cited on pages 7, 8, 42, 53).

Maraston C., Bastian N., Saglia R. P., Kissler-Patig M., Schweizer F., Goudfrooij P., 2004, A&A, 416, 467 (cited on page 6).

Marigo P., Girardi L., Bressan A., Groenewegen M. A. T., Silva L., Granato G. L., 2008, A&A, 482, 883 (cited on page 95).

Marín-Franch A. et al., 2009, ApJ, 694, 1498 (cited on page 95).

Marks M., Kroupa P., Baumgardt H., 2008, MNRAS, 386, 2047 (cited on page 90).

Mármol-Queraltó E., Cardiel N., Cenarro A. J., Vazdekis A., Gorgas J., Pedraz S., Peletier R. F., Sánchez-Blázquez P., 2008, A&A, 489, 885 (cited on page 49).

Marsh T. R., 1989, PASP, 101, 1032 (cited on page 47).

Martell S. L., Grebel E. K., 2010, A&A, 519, A14 (cited on page 13).

Martin N. F., Ibata R. A., Irwin M. J., Chapman S., Lewis G. F., Ferguson A. M. N., Tanvir N., McConnachie A. W., 2006, MNRAS, 371, 1983 (cited on page 1).

Mateo M., 1996, in Formation of the Galactic Halo...Inside and Out, Morrison H. L., Sarajedini A., eds., Vol. 92, p. 434 (cited on page 11).

McConnachie A. W., Côté P., 2010, ApJ, 722, L209 (cited on page 85).

McCrea W. H., 1964, MNRAS, 128, 147 (cited on page 89).

McGregor P. J. et al., 2003, in SPIE Conf. Ser., Iye M., Moorwood A. F. M., eds., Vol. 4841, pp. 1581–1591 (cited on page 17).

McLaughlin D. E., van der Marel R. P., 2005, ApJS, 161, 304 (cited on pages 3, 73, 74, 76).

McMillan S. L. W., Vesperini E., Portegies Zwart S. F., 2007, ApJ, 655, L45 (cited on page 102).

Merritt D., Schnittman J. D., Komossa S., 2009, ApJ, 699, 1690 (cited on pages 10, 17, 31, 35).

Messier C., 1774, Mémoires de l'Académie Royale des Sciences, 435 (cited on page 1).

Mieske S., Gieles M., 2011, ESO Messenger, 144, 44 (cited on page 2).

Mieske S., Hilker M., Infante L., 2002, A&A, 383, 823 (cited on pages 4, 5).

Mieske S., Hilker M., Infante L., 2004, A&A, 418, 445 (cited on pages 5, 17).

Mieske S., Hilker M., Infante L., Jordán A., 2006a, AJ, 131, 2442 (cited on pages 5, 6, 33).

Mieske S., Hilker M., Infante L., Mendes de Oliveira C., 2007a, A&A, 463, 503 (cited on pages 4, 6).

Mieske S., Hilker M., Jordán A., Infante L., Kissler-Patig M., 2007b, A&A, 472, 111 (cited on page 4).

Mieske S. et al., 2008, A&A, 487, 921 (cited on pages 3, 9, 17, 39).

Mieske S., Hilker M., Misgeld I., 2012, A&A, 537, A3 (cited on pages 5, 7).

Mieske S., Infante L., Hilker M., Hertling G., Blakeslee J. P., Benítez N., Ford H., Zekser K., 2005, A&A, 430, L25 (cited on page 3).

Mieske S. et al., 2006b, ApJ, 653, 193 (cited on page 6).

Mieske S. et al., 2010, ApJ, 710, 1672 (cited on page 6).

Mieske S., Kroupa P., 2008, ApJ, 677, 276 (cited on pages 4, 7, 8, 10, 17, 40, 41, 42, 44, 59).

Mighell K. J., 1999, ApJ, 518, 380 (cited on page 96).

Milgrom M., 1983a, ApJ, 270, 371 (cited on page 13).

Milgrom M., 1983b, ApJ, 270, 365 (cited on page 13).

Minniti D. et al., 2011, A&A, 527, A81 (cited on page 10).

Minor Q. E., Martinez G., Bullock J., Kaplinghat M., Trainor R., 2010, ApJ, 721, 1142 (cited on page 9).

Misgeld I., Hilker M., 2011, MNRAS, 414, 3699 (cited on page 3).

Misgeld I., Mieske S., Hilker M., 2008, A&A, 486, 697 (cited on page 3).

Misgeld I., Mieske S., Hilker M., Richtler T., Georgiev I. Y., Schuberth Y., 2011, A&A, 531, A4 (cited on page 4).

Moni Bidin C. et al., 2011, A&A, 535, A33 (cited on page 10).

Moore B., Quinn T., Governato F., Stadel J., Lake G., 1999, MNRAS, 310, 1147 (cited on page 10).

Moorwood A. et al., 1998, ESO Messenger, 94, 7 (cited on page 42).

Murray N., 2009, ApJ, 691, 946 (cited on page 10).

Navarro J. F., Frenk C. S., White S. D. M., 1997, ApJ, 490, 493 (cited on page 10).

Norris M. A., Kannappan S. J., 2011, MNRAS, 414, 739 (cited on pages 4, 7, 109).

Noyola E., Gebhardt K., Bergmann M., 2008, ApJ, 676, 1008 (cited on page 10).

Ocvirk P., 2010, ApJ, 709, 88 (cited on page 9).

Odenkirchen M., Grebel E. K., Dehnen W., Rix H.-W., Yanny B., Newberg H. J., Rockosi C. M., Martínez-Delgado D., Brinkmann J., Pier J. R., 2003, AJ, 126, 2385 (cited on page 103).

Odenkirchen M. et al., 2001, ApJ, 548, L165 (cited on page 13).

Oke J. B. et al., 1995, PASP, 107, 375 (cited on page 62).

Olczak C., Spurzem R., Henning T., 2011, in IAU Symposium, Brummell N. H., Brun A. S., Miesch M. S., Ponty Y., eds., Vol. 271, pp. 389–390 (cited on page 102).

Pasquini L. et al., 2002, ESO Messenger, 110, 1 (cited on page 18).

Paudel S., Lisker T., Janz J., 2010, ApJ, 724, L64 (cited on pages 6, 17).

Paust N. E. Q. et al., 2010, AJ, 139, 476 (cited on page 80).

Peebles P. J. E., 1984, ApJ, 277, 470 (cited on page 11).

Penny S. J., Forbes D. A., Conselice C. J., 2012, MNRAS, 422, 885 (cited on page 4).

Pérez F., Granger B. E., 2007, Comput. Sci. Eng., 9, 21 (cited on page 47).

Persson S. E., Aaronson M., Frogel J. A., 1977, AJ, 82, 729 (cited on page 49).

Phillipps S., Drinkwater M. J., Gregg M. D., Jones J. B., 2001, ApJ, 560, 201 (cited on page 4).

Pickles A. J., 1998, PASP, 110, 863 (cited on page 49).

Piotto G., Bedin L. R., Anderson J., King I. R., Cassisi S., Milone A. P., Villanova S., Pietrinferni A., Renzini A., 2007, ApJ, 661, L53 (cited on page 11).

Press W. H., Teukolsky S. A., Vetterling W. T., Flannery B. P., 2007, Numerical recipes, 3rd edn. Cambridge University Press, Cambridge (cited on pages 33, 55).

Price J. et al., 2009, MNRAS, 397, 1816 (cited on pages 3, 4).

Pryor C., Meylan G., 1993, in Structure and Dynamics of Globular Clusters, Djorgovski S. G., Meylan G., eds., Vol. 50, p. 357 (cited on pages 68, 69).

Rejkuba M., Dubath P., Minniti D., Meylan G., 2007, A&A, 469, 147 (cited on pages 4, 41, 42, 44).

Robin A. C., Reylé C., Derrière S., Picaud S., 2003, A&A, 409, 523 (cited on pages 66, 94).

Rossa J., van der Marel R. P., Böker T., Gerssen J., Ho L. C., Rix H.-W., Shields J. C., Walcher C.-J., 2006, AJ, 132, 1074 (cited on page 3).

Russell H. N., 1934, ApJ, 79, 317 (cited on page 41).

Sagar R., Miakutin V. I., Piskunov A. E., Dluzhnevskaia O. B., 1988, MNRAS, 234, 831 (cited on pages 86, 102).

Saha A., Dolphin A. E., Thim F., Whitmore B., 2005, PASP, 117, 37 (cited on pages 63, 68).

Saha A., Shaw R. A., Claver J. A., Dolphin A. E., 2011, PASP, 123, 481 (cited on page 65).

Salaris M., Cassisi S., 2005, Evolution of stars and stellar populations. Wiley, Chichester (cited on page 6).

Salinas R., Jílková L., Carraro G., Catelan M., Amigo P., 2012, MNRAS, 421, 960 (cited on page 102).

Salpeter E. E., 1955, ApJ, 121, 161 (cited on pages 39, 90).

Sanders R. H., 2012a, MNRAS, 419, L6 (cited on pages 14, 61, 90).

Sanders R. H., 2012b, MNRAS, 422, L21 (cited on pages 14, 61, 90).

Sanders R. H., McGaugh S. S., 2002, ARAA, 40, 263 (cited on pages 13, 61).

Sarajedini A., 1997, AJ, 113, 682 (cited on page 95).

Sarajedini A., Layden A. C., 1995, AJ, 109, 1086 (cited on page 11).

Sarazin M., Melnick J., Navarrete J., Lombardi G., 2008, ESO Messenger, 132, 11 (cited on page 19).

Scarpa R., Falomo R., 2010, A&A, 523, A43 (cited on page 13).

Scarpa R., Marconi G., Carraro G., Falomo R., Villanova S., 2011, A&A, 525, A148 (cited on page 13).

Scarpa R., Marconi G., Gilmozzi R., 2003, A&A, 405, L15 (cited on page 13).

Scarpa R., Marconi G., Gilmozzi R., Carraro G., 2007, A&A, 462, L9 (cited on page 13).

Schlegel D. J., Finkbeiner D. P., Davis M., 1998, ApJ, 500, 525 (cited on page 77).

Searle L., Zinn R., 1978, ApJ, 225, 357 (cited on page 11).

Shapley H., Curtis H. D., 1921, Bull. Nat. Res. Council, 2, 171 (cited on page 1).

Shara M. M., Saffer R. A., Livio M., 1997, ApJ, 489, L59 (cited on page 90).

Sirianni M., Nota A., De Marchi G., Leitherer C., Clampin M., 2002, ApJ, 579, 275 (cited on pages 86, 102).

Smith L. J., Gallagher J. S., 2001, MNRAS, 326, 1027 (cited on page 40).

Smith Castelli A. V., Bassino L. P., Richtler T., Cellone S. A., Aruta C., Infante L., 2008, MNRAS, 386, 2311 (cited on page 3).

Sohn Y.-J., Park J.-H., Rey S.-C., Lee Y.-W., Kim H.-I., Oh S. J., Lee S.-G., Lee M. G., Han W., 2003, AJ, 126, 803 (cited on pages 62, 73, 76).

Sollima A., Ferraro F. R., Bellazzini M., 2007, MNRAS, 381, 1575 (cited on page 102).

Sollima A., Martínez-Delgado D., Valls-Gabaud D., Peñarrubia J., 2011, ApJ, 726, 47 (cited on pages 3, 13, 14, 90, 95, 96, 103).

Sollima A., Nipoti C., 2010, MNRAS, 401, 131 (cited on pages 13, 90).

Sollima A., Nipoti C., Mastrobuono Battisti A., Montuori M., Capuzzo-Dolcetta R., 2012, ApJ, 744, 196 (cited on pages 14, 61, 83, 85, 86, 90).

Spiniello C., Koopmans L. V. E., Trager S. C., Czoske O., Treu T., 2011, MNRAS, 417, 3000 (cited on page 40).

Spitzer, Jr. L., Hart M. H., 1971, ApJ, 164, 399 (cited on page 103).

Sternberg A., 1998, ApJ, 506, 721 (cited on page 40).

Stetson P. B., 1993, in IAU Colloq. 136: Stellar Photometry - Current Techniques and Future Developments, Butler C. J., Elliott I., eds., p. 291 (cited on page 63).

Stetson P. B., 2000, PASP, 112, 925 (cited on page 95).

Stetson P. B. et al., 1999, AJ, 117, 247 (cited on pages 62, 64, 77, 78).

Stoehr F. et al., 2007, STECF, 42, 4 (cited on pages 26, 43).

Strader J., Smith G. H., Larsen S., Brodie J. P., Huchra J. P., 2009, AJ, 138, 547 (cited on page 8).

Tammann G. A., 1994, in European Southern Observatory Conference and Workshop Proceedings, Meylan G., Prugniel P., eds., Vol. 49, p. 3 (cited on page 1).

Taylor M. A., Puzia T. H., Harris G. L., Harris W. E., Kissler-Patig M., Hilker M., 2010, ApJ, 712, 1191 (cited on pages 4, 6, 7, 8, 17, 41, 42, 44).

Thomas D., Johansson J., Maraston C., 2011, MNRAS, 412, 2199 (cited on page 6).

Tonry J., Davis M., 1979, AJ, 84, 1511 (cited on pages 63, 64).

Trager S. C., King I. R., Djorgovski S., 1995, AJ, 109, 218 (cited on pages 73, 75).

Trager S. C., Worthey G., Faber S. M., Burstein D., Gonzalez J. J., 1998, ApJS, 116, 1 (cited on page 7).

Tsuchiya T., Dinescu D. I., Korchagin V. I., 2003, ApJ, 589, L29 (cited on page 11).

Unsöld A., Baschek B., 2005, Der neue Kosmos, 7th edn. Springer, Berlin ; Heidelberg [u.a.], pp. XIV, 577 S. (cited on page 41).

van de Ven G., van den Bosch R. C. E., Verolme E. K., de Zeeuw P. T., 2006, A&A, 445, 513 (cited on pages 11, 102).

van den Bergh S., 1999, A&A Rev., 9, 273 (cited on page 11).

van den Bergh S., 2008, MNRAS, 390, L51 (cited on page 11).

van den Bergh S., Mackey A. D., 2004, MNRAS, 354, 713 (cited on page 11).

van der Marel R. P., Anderson J., 2010, ApJ, 710, 1063 (cited on page 10).

van der Marel R. P., Franx M., 1993, ApJ, 407, 525 (cited on page 24).

van Dokkum P. G., 2001, PASP, 113, 1420 (cited on page 19).

van Dokkum P. G., Conroy C., 2010, Nature, 468, 940 (cited on pages 40, 111).

van Dokkum P. G., Conroy C., 2011, ApJ, 735, L13 (cited on page 40).

VandenBerg D. A., 2000, ApJS, 129, 315 (cited on pages 62, 77, 78).

Verde L., Oh S. P., Jimenez R., 2002, MNRAS, 336, 541 (cited on page 2).

Vesperini E., Heggie D. C., 1997, MNRAS, 289, 898 (cited on pages 12, 89, 103).

Vesperini E., McMillan S. L. W., Portegies Zwart S., 2009, ApJ, 698, 615 (cited on page 87).

Vogt S. S. et al., 1994, in SPIE Conf. Ser., Crawford D. L., Craine E. R., eds., Vol. 2198, p. 362 (cited on page 63).

Vogt S. S., Mateo M., Olszewski E. W., Keane M. J., 1995, AJ, 109, 151 (cited on page 63).

Walker M. G., 2012, preprint (arXiv:1205.0311) (cited on page 11).

Wehner E. M. H., Harris W. E., 2007, ApJ, 668, L35 (cited on page 4).

Weidner C., Kroupa P., 2005, ApJ, 625, 754 (cited on page 39).

Willman B., Blanton M. R., West A. A., Dalcanton J. J., Hogg D. W., Schneider D. P., Wherry N., Yanny B., Brinkmann J., 2005, AJ, 129, 2692 (cited on page 1).

Willman B., Strader J., 2012, preprint (arXiv:1203.2608) (cited on page 2).

Woodley K. A., Harris W. E., Beasley M. A., Peng E. W., Bridges T. J., Forbes D. A., Harris G. L. H., 2007, AJ, 134, 494 (cited on page 44).

Yanny B. et al., 2009, AJ, 137, 4377 (cited on page 4).

Zonoozi A. H., Küpper A. H. W., Baumgardt H., Haghi H., Kroupa P., Hilker M., 2011, MNRAS, 411, 1989 (cited on pages 86, 90, 102, 107).

Zucker D. B. et al., 2004, ApJ, 612, L121 (cited on page 1).